

# **Crossed beam scattering with a Stark-decelerated molecular beam**

vorgelegt von  
Diplom-Chemiker  
Ludwig Scharfenberg  
(Berlin)

Von der Fakultät II - Mathematik und Naturwissenschaften  
der Technischen Universität Berlin  
zur Erlangung des akademischen Grades  
Doktor der Naturwissenschaften  
Dr. rer. nat.

genehmigte Dissertation

Promotionsausschuss:

Vorsitzende: Prof. Dr. Sabine Klapp

Gutachter: Prof. Dr. Gerard Meijer

Gutachter: Prof. Dr. Thomas Möller

Tag der wissenschaftlichen Aussprache: 27. Februar 2012

Berlin 2012

D 83



# Zusammenfassung

Die in den letzten Jahren stetig weiterentwickelte Methode der mehrstufigen Stark-Abbremsung von Molekularstrahlen wurde benutzt, um OH-Radikale in wohldefinierten Quantenzuständen zu präparieren. Bei dieser Methode wird ein gepulster Molekularstrahl mit Hilfe von inhomogenen und zeitabhängigen elektrischen Feldern stufenweise gefiltert, fokussiert und gleichzeitig abgebremst oder beschleunigt. Ein Stark-Abbremsen für polare – aber elektrisch neutrale – Moleküle funktioniert in vielerlei Hinsicht wie ein Linearbeschleuniger für geladene Teilchen. Stark-Abbremsen wurden bisher hauptsächlich verwendet, um Moleküle zum Stillstand zu bringen und in einer Molekülfalle zu speichern.

Der wesentliche Vorzug der Methode liegt darin, daß die mittlere Endgeschwindigkeit der gefilterten Moleküle in einem gewissen Bereich willkürlich festgelegt werden kann und daß man gleichzeitig auch die Geschwindigkeitsverteilung kontrolliert. Wie in der vorliegenden Arbeit gezeigt wird, sind die auf diesem Wege präparierten Moleküle hervorragend geeignet, um damit Streuexperimente bei variabler Stoßenergie durchzuführen. Insbesondere kann man die inelastische Streuung vom gegebenen anfänglichen Quantenzustand in andere Zustände als Funktion der Stoßenergie untersuchen.

Mit diesem Ziel vor Augen wurde zunächst eine neue Stark-Abbremsen Apparatur aufgebaut, welche für Streuexperimente mit gekreuzten Molekularstrahlen optimiert ist. Nach deren Fertigstellung konnte durch ausführliche Charakterisierung des Instruments gezeigt werden, daß die neue Apparatur in der Tat den bisher verwendeten deutlich überlegen ist (siehe Kapitel 5). Im Anschluss an diesen erfolgreichen Test wurde der Stark-Abbremsen mit einer (konventionellen) Molekularstrahlquelle gekoppelt. Mit Hilfe dieser Quelle wurden Atomstrahlen aus der Reihe der Edelgase (He bis Xe) erzeugt, welche als Streumedium für die präparierten OH-Radikale dienten. Nun konnten relative, integrale Streuquerschnitte für die Rotationsanregung des OH-Radikals mit voller Zustandsauflösung, sowohl vor als auch nach dem Stoß, bestimmt werden (siehe Kapitel 7 und 8). Aufgrund der hohen Stoßenergieauflösung war es außerdem möglich, die Energieabhängigkeit der relativen Streuquerschnitte mit bisher unerreichter Genauigkeit zu messen (siehe Seite 118 und 133-134).

Zum einen konnte somit gezeigt werden, daß die Methode der Stark-Abbremsung auch bei Streuexperimenten sehr gute Ergebnisse liefern kann und

somit den bisher üblichen Methoden der Zustandsselektion vorzuziehen ist. Zum anderen ergaben die gemessenen Daten neue Erkenntnisse über das Streuverhalten bei den unterschiedlichen Stoßpartnern He, Ne, Ar, Kr und Xe. Durch Vergleich mit *ab-initio* Streurechnungen konnte außerdem untersucht werden, inwiefern die bisher publizierten Wechselwirkungspotentiale für die verschiedenen Stoßpartner die Daten korrekt reproduzieren können, wenn man sie bei Streurechnungen verwendet. Dabei ergaben sich nützliche Aufschlüsse über die Qualität der Potentiale und der Streurechnungen selbst. Die Rechnungen zeigen allerdings auch, daß immer noch Verbesserungsbedarf von experimenteller Seite besteht, denn nicht alle Strukturen in der Energieabhängigkeit der Streuquerschnitte kann man bisher auflösen. Um dies in Zukunft zu erreichen, wurde eine Modifikation des Experiments vorgeschlagen, welche die Energieauflösung erheblich verbessert (siehe Kapitel 9).



# Contents

<b>Zusammenfassung</b>	<b>i</b>
<b>1 Introduction</b>	<b>5</b>
<b>2 The OH radical</b>	<b>9</b>
2.1 The rigid rotor and its Stark effect . . . . .	10
2.1.1 The energy spectrum . . . . .	10
2.1.2 The rigid rotor wavefunctions . . . . .	12
2.1.3 The Stark effect . . . . .	14
2.2 Energy levels of OH . . . . .	16
2.2.1 Stark effect of OH . . . . .	18
2.2.2 The Stark effect and hyperfine structure . . . . .	21
2.3 Production of a pulsed OH beam . . . . .	24
2.4 Detection of OH radicals . . . . .	26
<b>3 Stark deceleration of OH radicals</b>	<b>29</b>
3.1 Introduction . . . . .	30
3.2 The potential . . . . .	31
3.3 Longitudinal motion . . . . .	31
3.4 Transverse motion . . . . .	38
3.5 Other loss mechanisms . . . . .	44
<b>4 Construction of the Stark decelerator</b>	<b>47</b>
4.1 Description of the mechanical parts . . . . .	48
4.1.1 Design of the modules . . . . .	48
4.1.2 Alignment . . . . .	50
4.1.3 Surface preparation . . . . .	51
4.2 The maximum field strength at the surface . . . . .	51
4.3 Vacuum . . . . .	52
4.4 High voltage conditioning and testing . . . . .	53
4.4.1 The conditioning procedure . . . . .	54
4.5 Safety measures . . . . .	55

4.6	High voltage switching . . . . .	55
4.6.1	Basic requirements . . . . .	55
4.6.2	Components and design . . . . .	56
<b>5</b>	<b>Operation of a decelerator with optimum acceptance</b>	<b>59</b>
5.1	Introduction . . . . .	60
5.2	Experiment . . . . .	62
5.2.1	Experimental setup . . . . .	62
5.2.2	Comparing the $s = 1$ and $s = 3$ modes of operation . . . .	66
5.2.3	The $s = 1$ mode of operation at low phase angles . . . . .	68
5.2.4	Excessive focusing at low velocities . . . . .	69
5.3	Numerical trajectory calculations . . . . .	72
5.4	Conclusions . . . . .	75
5.5	Appendix . . . . .	76
<b>6</b>	<b>Crossed beam scattering with decelerated molecules</b>	<b>81</b>
6.1	Introduction . . . . .	82
6.2	Collision kinematics and classical dynamics . . . . .	83
6.2.1	Conservation laws . . . . .	83
6.2.2	Newton diagram for elastic and inelastic collisions . . . .	87
6.3	The cross section . . . . .	87
6.3.1	Definition of the cross section . . . . .	87
6.3.2	The scattering probability of a molecule . . . . .	90
6.3.3	Determination of the absolute total inelastic cross section	91
6.4	State-to-state inelastic scattering . . . . .	92
6.4.1	The experiment . . . . .	92
6.4.2	Generation of collision products with time . . . . .	95
6.4.3	Detection of collision products . . . . .	99
6.4.4	Excitation functions . . . . .	103
<b>7</b>	<b>Inelastic scattering of OH radicals with Ar atoms</b>	<b>105</b>
7.1	Introduction . . . . .	106
7.2	Experiment . . . . .	108
7.2.1	Experimental setup . . . . .	108
7.2.2	Variation of the collision energy . . . . .	110
7.2.3	Experimental procedure and data analysis . . . . .	112
7.3	Theory . . . . .	114
7.3.1	Potential Energy Surfaces . . . . .	114
7.3.2	Scattering Calculations . . . . .	116
7.4	Results and Discussion . . . . .	117
7.5	Conclusions and outlook . . . . .	120

---

<b>8</b>	<b>Scattering of OH radicals with rare-gas atoms</b>	<b>123</b>
8.1	Introduction . . . . .	124
8.2	Experiment . . . . .	125
8.2.1	Experimental setup . . . . .	125
8.2.2	Measurement procedure and data analysis . . . . .	126
8.3	Theory . . . . .	127
8.4	Results and discussion . . . . .	131
8.4.1	Scattering of OH radicals with Ne, Kr, and Xe atoms . . . . .	131
8.4.2	Comparison between the various collision partners . . . . .	135
8.5	Conclusions . . . . .	137
<b>9</b>	<b>Scattering with optimized energy resolution</b>	<b>139</b>
9.1	Introduction . . . . .	140
9.2	Collision kinematics . . . . .	142
9.3	Overview and applications . . . . .	145
9.3.1	$v_1$ and $v_2$ constant, $\phi$ variable . . . . .	145
9.3.2	$v_2$ and $\phi$ constant, $v_1$ variable . . . . .	147
9.3.3	Variation of $v_1$ , $v_2$ , and $\phi$ for a fixed energy . . . . .	148
9.3.4	Applications . . . . .	148
9.4	Resonances in OH-He and OD-He collisions . . . . .	153
9.5	Conclusion . . . . .	155
9.6	Appendix (estimation of $\sigma_\phi$ ) . . . . .	155
	<b>Bibliography</b>	<b>157</b>
	<b>List of publications</b>	<b>173</b>
	<b>Danksagung</b>	<b>175</b>
	<b>Lebenslauf</b>	<b>179</b>



# Chapter 1

## Introduction

Most natural processes that are of interest to us do not happen in an isolated environment, they usually occur in some condensed phase. But in this state, many of the intrinsic (quantum) properties of molecules and atoms do not manifest themselves very clearly. Only in the gas phase and under certain particularly artificial conditions does it become possible to study in detail how atoms and molecules interact and what their intrinsic properties are. It is one of the ultimate goals of the experimentalists to set up experiments that yield clear and unambiguous information about atoms and molecules with as few additional assumptions as possible and with a minimum of practical and theoretical complexity. In the best case, an experiment does not only yield new information which can be used by others, but is also a beautiful demonstration itself.

Atomic and molecular beams provide a first step towards obtaining such clean and well controlled conditions in particular if additional state-preparation procedures follow before the intended experiment takes place. With the help of external fields – be they electric or magnetic – atoms and molecules in specific quantum states can be prepared. The groundbreaking experiments on the magnetic moment of silver atoms by Otto Stern and Walther Gerlach<sup>1</sup> conducted in Frankfurt in 1922 were the first demonstration of this kind. In their experiment, the external field modifies only the *transverse* velocity components of the atoms or molecules while the velocity component in the beam propagation direction remains unchanged.

However, it is useful to gain better control over the forward velocity as well. In fact, in the past years it has become a kind of competition among several groups of researchers to devise ever more original methods which allow atoms and molecules that originate from supersonic gas expansions to be slowed down to laboratory frame velocities around zero. These relatively new *deceleration* methods have been the subject of several review articles e.g. [3, 4].

---

<sup>1</sup>For interesting and amusing facts about the protagonists see [1] and [2].

In this thesis, the so called multistage *Stark-deceleration* method is used, which is probably the most tried and tested of the currently available ones for the slowing of a molecular beam. This technique exploits the interaction of a polar molecule with a strong and inhomogeneous electric field. The used field is periodic and time dependent and the method is in effect analogous to the acceleration of charged particles in linear accelerators. In 1999, the first demonstration of a decelerator for polar molecules was described in a paper by Bethlem, Berden and Meijer [5]. While their principle design prevails until today, many technical problems have meanwhile been located and eliminated. In particular, the used electric fields became stronger. While some researchers increased the size of the apparatus [6], others tried to miniaturise their machines [7, 8]. The development continues and a very promising route towards higher efficiencies has been demonstrated recently [9].

A Stark decelerated beam is obtained as follows. One first creates a molecular beam by expanding a gas from a reservoir at a high pressure (typically 1-5 bar) into the vacuum through a nozzle using a pulsed valve [10]. During the expansion, the energy of the random thermal motion and also that of the internal degrees of freedom of the particles is converted into kinetic energy of motion in the beam propagation direction through the approximately isentropic expansion. Even if the molecule of interest is in the gaseous state, it is usually added in small concentrations to a carrier gas which is typically one of the rare gases. A few centimeters behind the expansion nozzle, a skimmer is located which extracts the central part of the beam and which separates the beam-source vacuum chamber from the experimental chamber. Right behind the skimmer, many deceleration stages (sometimes hundreds of them) are located which become electrically charged or grounded in a specifically tailored sequence so as to allow a deceleration or acceleration to a specified velocity.

In the first years after their introduction, Stark decelerators were mainly used to slow down molecules and to subsequently load them into a trap [6, 11, 12, 13, 14, 15, 16, 17]. In 2006, Gilijamse and coworkers [18] showed that state-to-state inelastic scattering experiments are also feasible with Stark-decelerated pulses of molecules. However, the machine that was used in the experiment was not well suited for beam scattering studies and a better instrument was designed and built. The first scattering experiments conducted with this new machine are described in the present thesis.

The field of molecular beam scattering has a long history with the first experiments appearing approximately 10 years after the Stern-Gerlach experiment [19]. After Stern had moved to Hamburg in 1923, he continued to cultivate the method of molecular beams further [20, 21]. It is not surprising that one of the first molecular beam scattering studies was carried out in his laboratory, by Friedrich Knauer [22]. Knauer was able to measure differential cross sections for the scattering of He, O<sub>2</sub>, H<sub>2</sub> and H<sub>2</sub>O beams from their respective vapors and also for the scattering of He and H<sub>2</sub> from Hg vapor. Similar experiments were carried out by L.F. Broadway [23] who reported on the scattering of Na

and K atoms from Hg vapor effusing from an oven, in 1933. This appears to be the first crossed beam experiment with neutral particles ever conducted. In the same year R.M. Zabel studied the scattering of He and H<sub>2</sub> and was able to determine differential cross sections for the scattering with He, H<sub>2</sub> and Hg. Further experiments, using alkali atoms, were reported in the following years [24, 25, 26] – until the beginning of the Second World War. One of the main objectives of these early scattering experiments was to detect diffraction phenomena which were expected on the basis of wave mechanics. However, clear indications of diffraction were not seen, because the available beams had too broad a velocity distribution. Later experiments which made use of velocity selectors could clearly show typical quantum effects; rather noteworthy in that respect is the work by Feltgen et al. [27] on the glory oscillations in the integral scattering cross sections for the systems <sup>3</sup>He – <sup>3</sup>He, <sup>3</sup>He – <sup>4</sup>He and <sup>4</sup>He – <sup>4</sup>He.

The technological developments in the past decades have led to more and more refined investigations of the scattering properties of atoms and molecules. Experiments with state-selection before the collision and full state-resolution after the collision have become possible. In particular, ion-imaging techniques together with state-selective ionization enable us to determine, in one stroke, the post-collision quantum state together with the velocity vector of the ionized molecule or atom [28, 29]. Using this so-called *Velocity Map Imaging* technique, it has become possible to efficiently measure quantum state resolved differential cross sections; even the preferred sense of rotation of a molecule after a collision can be determined if suitably polarized laser radiation is used [30].

While it is indeed of interest to control the exact initial and to determine the final state distributions, it is also important to have control over the relative velocity of the colliding particles. An established method to tune the relative velocity, and hence the collision energy, is to change the crossing angle between the two beams [31], but this technique is difficult to combine with a state-selector. By using a Stark decelerator, it is now becoming possible to achieve the ultimate resolution as far as the state-preparation before the collision is concerned: we can tune the initial mean velocity continuously and control the velocity distribution, select the initial internal quantum state (often including the hyperfine level, see p.22) and fix the initial angular momentum projection quantum number  $M$ , since the decelerated molecules are oriented. If a suitable guiding field is used to retain the orientation of the molecules up to the collision zone, it becomes possible to study the effect of orientation on the collision process.

In the following four chapters, the basic principles of operation and the construction of the machine are described. In the subsequent chapters, the instrument is characterized and several scattering experiments are presented. In these experiments, the rotationally inelastic scattering of OH radicals with rare gas atoms is studied and state-to-state cross sections are determined as a function of the collisions energy. That the collision energy can be precisely adjusted is one of the main benefits of this technique and has led to a very

detailed mapping of the energy dependence of the cross sections (see p. 118, 133 and 134). The scattering of OH with argon atoms is studied in chapter 7, the scattering with all other rare gas atoms and D<sub>2</sub> molecules is described in chapter 8. In the final chapter 9, it is analysed how the collision energy resolution can be improved further by using a suitable beam crossing angle that differs from the hitherto used 90°.



## Chapter 2

# The OH radical

The interactions between electrons and protons are well known and consequently one can formulate a Schrödinger equation for any molecule which then in principle describes the system with the desired degree of accuracy. However, even for a small molecule like OH with only two nuclei and 9 electrons the determination of the wavefunctions and energies is already quite a complicated task. In order to solve the problem and also in order to gain physical insight, several approximations need to be introduced which break down the problem into tractable pieces. One usually begins with the separation of the electronic motion from the motion of the nuclei and then separates the vibration, rotation and spin degrees of freedom. A systematic treatment of this procedure can be found for example in [32]. In the following, only the most relevant aspects are described. Since our main interest concerns the Stark effect, particular emphasis is put on the *rotational* properties of the electronic ground state.

## 2.1 The rigid rotor and its Stark effect

The rotation of a molecule as a whole is correctly described, in the first approximation at least, by the quantum mechanical version of the classical rigid body. The model is based on the classical Hamiltonian:

$$H = \frac{J_a^2}{2I_a} + \frac{J_b^2}{2I_b} + \frac{J_c^2}{2I_c} \quad (2.1)$$

with the three principle moments of inertia  $I_a, I_b, I_c$  and the scalar products  $J_a := \mathbf{J} \cdot \mathbf{a}$  etc. between the angular momentum vector  $\mathbf{J}$  and the three orthogonal (body fixed) unit vectors  $\mathbf{a}, \mathbf{b}, \mathbf{c}$  which point along the principle axes of inertia of the body. In the quantum mechanical description, one may think of these axes as defined relative to the position of the molecule's nuclei. Strictly speaking, this model is incompatible with the fundamental principles of quantum mechanics. It is to be regarded as the limiting case in which the positions of the nuclei are fixed relative to each other by a strong interaction potential which is, in the spirit of the Born-Oppenheimer approximation, created by the surrounding electrons. The energy eigenfunctions belonging to the above Hamiltonian determine the relative probabilities for specific orientations of the body in space.

### 2.1.1 The energy spectrum

If the rigid rotor has an axis of symmetry, the possible energies follow from the transformation properties of the involved vectors  $\mathbf{a}, \mathbf{b}, \mathbf{c}$ . In the quantum mechanical description, the  $\mathbf{a}, \mathbf{b}, \mathbf{c}$  become vector operators with respect to the angular momentum  $\mathbf{J}$  which is itself a vector operator.

By definition, the components of a vector operator have to transform like those of an ordinary geometrical vector under rotations (see e.g. [33]). An active rotation of the considered object about a space fixed axis  $\mathbf{e}$  by the angle  $\phi$  is implemented by a unitary transformation which we write as  $R_{\mathbf{e}}(\phi) := e^{-i\phi \mathbf{e} \cdot \mathbf{J}}$  which acts on the respective state vector (we set  $\hbar = 1$ ). The transformation which rotates the operator around the same axis and with the same angle is then  $\mathbf{a}' = R\mathbf{a}R^\dagger$ , the infinitesimal version of which is

$$\mathbf{a}' \approx \mathbf{a} - i\delta\phi[\mathbf{e} \cdot \mathbf{J}, \mathbf{a}]. \quad (2.2)$$

For  $\mathbf{a}$  to be vector operator we require that

$$\delta\mathbf{a} = \mathbf{a}' - \mathbf{a} \approx -i\delta\phi[\mathbf{e} \cdot \mathbf{J}, \mathbf{a}] = -\delta\phi \mathbf{e} \times \mathbf{a} \quad (2.3)$$

and therefore:

$$[\mathbf{e} \cdot \mathbf{J}, \mathbf{a}] = -i \mathbf{e} \times \mathbf{a}. \quad (2.4)$$

For any two space fixed unit vectors  $\mathbf{e}_1$  and  $\mathbf{e}_2$  this becomes

$$[\mathbf{e}_1 \cdot \mathbf{J}, \mathbf{e}_2 \cdot \mathbf{a}] = i (\mathbf{e}_1 \times \mathbf{e}_2) \cdot \mathbf{a}. \quad (2.5)$$

Since  $\mathbf{J}$  is itself a vector operator the commutation rules for the components of  $\mathbf{J}$  with respect to different axes are:

$$[\mathbf{e}_1 \cdot \mathbf{J}, \mathbf{e}_2 \cdot \mathbf{J}] = i (\mathbf{e}_1 \times \mathbf{e}_2) \cdot \mathbf{J}. \quad (2.6)$$

Does this relationship remain true if  $\mathbf{e}_1$  and  $\mathbf{e}_2$  are replaced by vector operators? Not quite. One may show that (2.4) remains true when  $\mathbf{e}$  is replaced by a vector operator:

$$[\mathbf{a} \cdot \mathbf{J}, \mathbf{b}] = -i \mathbf{a} \times \mathbf{b} \quad (2.7)$$

provided  $\mathbf{a}$  and  $\mathbf{b}$  commute. Since  $\mathbf{J}$  commutes with the scalar  $\mathbf{a} \cdot \mathbf{J}$  we have:

$$[\mathbf{a} \cdot \mathbf{J}, \mathbf{b} \cdot \mathbf{J}] = -i (\mathbf{a} \times \mathbf{b}) \cdot \mathbf{J} \quad (2.8)$$

so that compared to (2.6) the sign of  $i$  is now inverted. The three orthogonal vectors used in the description of the rigid rotor therefore have to satisfy these same relationships, which means that the projections of  $\mathbf{J}$  onto the body fixed axes satisfy:

$$[\mathbf{a} \cdot \mathbf{J}, \mathbf{b} \cdot \mathbf{J}] = -i \mathbf{c} \cdot \mathbf{J}. \quad (2.9)$$

If we choose space fixed unit vectors  $\mathbf{e}_1, \mathbf{e}_2, \mathbf{e}_3$  along a given  $x, y, z$  axis system, the commutation relationships become:

$$[J_x, J_y] = +iJ_z \quad (2.10)$$

$$[J_a, J_b] = -iJ_c \quad (2.11)$$

which is not surprising if one recalls that successive rotations about body fixed axes are equivalent to rotations about space fixed axes carried out in reverse order, provided the space and body fixed axes coincide initially. Since scalar products like  $\mathbf{J} \cdot \mathbf{a}$  are invariant under rotations, the components  $J_x, J_y, J_z$  commute with the  $J_a, J_b, J_c$  and therefore common eigenfunctions of  $\mathbf{J} \cdot \mathbf{J}$ ,  $J_z$  and  $J_c$  can be found. The eigenvalue spectrum of  $J_c$  is the same as that of  $J_z$  because the commutation relationships differ only by a sign. We denote the eigenvectors by  $|JMK\rangle$ , so that  $\mathbf{J}^2 |JMK\rangle = J(J+1) |JMK\rangle$ ,  $J_z |JMK\rangle = M |JMK\rangle$  and  $J_c |JMK\rangle = K |JMK\rangle$ .

If the rigid rotor has an axis of symmetry along the  $\mathbf{c}$ -axis, the Hamiltonian becomes:

$$H = \frac{\mathbf{J} \cdot \mathbf{J} - J_c^2}{2I_a} + \frac{J_c^2}{2I_c} \quad (2.12)$$

which is diagonal in the  $|JMK\rangle$  basis and the energy eigenvalues are:

$$H = \frac{J(J+1) - K^2}{2I_a} + \frac{K^2}{2I_c}, \quad (2.13)$$

where  $K = -J, -J+1, \dots, J$  so that states with opposite  $K$  have the same energy. Moreover, all  $2J+1$   $M$ -states have the same energy. The overall degeneracy for the energy levels is therefore  $2(2J+1)$  if  $K \neq 0$  and  $2J+1$  if  $K = 0$ . States of opposite  $K$  have the same energy because the Hamiltonian is invariant under space inversion while  $J_c$  changes sign under inversion<sup>1</sup>. In contrast,  $J_z$  does not change sign under inversion and therefore only states with  $K = 0$  have definite parity.

### 2.1.2 The rigid rotor wavefunctions

A wavefunction for the state  $|JMK\rangle$  must yield the amplitude for a specific orientation of the body fixed system  $\mathbf{a}, \mathbf{b}, \mathbf{c}$  with respect to the space fixed system. The orientation is usually specified by the three Euler angles  $(\phi, \theta, \chi)$ , which define three successive rotations that carry a copy of the space fixed  $x, y, z$ -axis system into the body fixed  $\mathbf{a}, \mathbf{b}, \mathbf{c}$  system; we denote any rotation by  $\omega$  and we write  $\omega\omega'$  for two successive rotations with  $\omega'$  applied first. Following common convention, we rotate first by  $\phi$  about  $z$ , then by  $\theta$  about the new axis  $y'$  and finally by  $\chi$  around  $z''$  so that  $\theta$  and  $\phi$  determine the orientation of the body fixed  $\mathbf{c}$ -axis. The wavefunction of the symmetric rigid body is completely determined by the known transformation laws for angular momentum eigenstates. Under any rotation  $\omega$  such a state must change as

$$R(\omega) |jm\rangle = \sum_{m'} D_{m'm}^{(j)}(\omega) |jm'\rangle \quad (2.14)$$

$$= \sum_{m'} e^{-im'\phi} d_{m'm}^{(j)}(\theta) e^{-im\chi} |jm'\rangle, \quad (2.15)$$

where  $D_{m'm}^{(j)}(\omega)$  is the unitary Wigner rotation matrix and  $d_{m'm}^{(j)}$  is the reduced rotation matrix. The wavefunctions must form basis functions for an irreducible representation of the rotation group, which is given by the matrices  $D^{(j)}(\omega)$ . The wavefunction argument is itself a rotation, namely the rotation specified by the Euler angles and the wavefunction labels are the time independent quantum numbers, in this case  $J, M$  and  $K$ . Hence we denote the wavefunction by  $\Psi_{JMK}(\omega)$ . To rotate such a function, rotations (i.e. group elements) must be combined in the function's argument. An active rotation  $\omega$  of the function with respect to the space-fixed frame is carried out via

---

<sup>1</sup>While  $\mathbf{J}$  remains unchanged under inversion, an operator like  $\mathbf{c}$  changes sign under inversion and therefore  $\mathbf{J} \cdot \mathbf{c}$  changes sign.

$R(\omega)\Psi_{JMK}(\omega') = \Psi_{JMK}(\omega^{-1}\omega')$ . As pointed out in [34]<sup>2</sup>, the group property of the rotation matrices requires that

$$D_{mm'}^{(j)}(\omega^{-1}\omega') = \sum_{m''} D_{mm''}^{(j)}(\omega^{-1}) D_{m''m'}^{(j)}(\omega'). \quad (2.16)$$

But the group representation is unitary and therefore

$$D_{mm'}^{(j)}(\omega^{-1}\omega') = \sum_{m''} D_{m''m}^{(j)*}(\omega) D_{m''m'}^{(j)}(\omega') \quad (2.17)$$

$$D_{mm'}^{(j)*}(\omega^{-1}\omega') = \sum_{m''} D_{m''m}^{(j)}(\omega) D_{m''m'}^{(j)*}(\omega'). \quad (2.18)$$

Hence it is the function  $\Psi_{JMK}(\omega') = D_{MK}^{(J)*}(\omega')$  which transforms as required by (2.14). The second index  $K$  does not change under the rotation, it specifies the “spin” of the rotor. The reason for this is the following. After an arbitrary rotation of the system, a state of definite  $m$  becomes a superposition of various  $m$  states with respect to the space-fixed frame. However, in a reference frame which undergoes the same rotation, the eigenvalue of the  $J_z$  operator with respect to the rotated frame will still be  $m$ . This rotated operator is actually  $J_c$  and therefore it is appropriate to write

$$D_{mm'}^{(j)}(\omega) = \langle jm | R | jm' \rangle = \langle jm | j k := m' \rangle = D_{mk}^{(j)}(\omega) \quad (2.19)$$

which means that the probability amplitude to find the state  $R | jk \rangle$  in an eigenstate of  $J_z$  in the space-fixed frame is proportional to  $D_{mk}^{(j)}(\omega)$ . The properly normalized wavefunction is then

$$\Psi_{JMK}(\phi, \theta, \chi) = \left( \frac{2J+1}{8\pi^2} \right)^{\frac{1}{2}} D_{MK}^{(J)*}(\phi, \theta, \chi) \quad (2.20)$$

provided the integration  $\int \Psi d\phi \sin \theta d\theta d\chi$  is carried out in the range  $0 \leq \phi \leq 2\pi$ ,  $0 \leq \theta \leq \pi$ ,  $0 \leq \chi \leq 2\pi$ . Wavefunctions which differ in  $J$ ,  $M$  or  $K$  are orthogonal. The proper derivation of integrals over rotation matrices is actually a somewhat subtle matter [35]. Care must be taken if integrals over products of rotation matrices are calculated in which integer and half integer values of  $J$  occur at the same time – an integration over either  $\phi$  or  $\chi$  between  $0 \dots 4\pi$  must then be used instead of  $0 \dots 2\pi$  and the normalization factor for the wavefunction is then  $\sqrt{(2J+1)/16\pi^2}$  (see e.g. [33, 36]).

In the case that the rotor is asymmetric,  $K$  is not conserved and therefore no suitable label for the wavefunction. Nevertheless, the wavefunction can be

---

<sup>2</sup>This derivation, given by Biedenharn and Louck [34], clarifies the origin of the seemingly bizarre convention to use complex conjugate matrix elements for the rigid rotor wavefunction.

expressed by a superposition of states with definite  $K$ . This follows from:

$$\Psi_{JM}(\omega\omega') = R(\omega^{-1})\Psi_{JM}(\omega') \quad (2.21)$$

$$= \sum_{M'} D_{M'M}^{(J)}(\omega^{-1})\Psi_{JM'}(\omega') \quad (2.22)$$

$$= \sum_{M'} D_{MM'}^{(J)*}(\omega)\Psi_{JM'}(\omega'). \quad (2.23)$$

If we now consider  $\omega'$  as a fixed reference orientation we get

$$\Psi_{JM}(\omega) = \sum_K D_{MK}^{(J)*}(\omega)A_{JK} \quad (2.24)$$

with the expansion coefficients  $A_{JK}$  which remain to be determined.

### 2.1.3 The Stark effect

The interaction energy between a body fixed dipole moment  $\mathbf{d} := \mu\mathbf{c}$  directed along the  $\mathbf{c}$ -axis and an externally applied electric field  $\mathbf{E}$  is given by the *Stark interaction energy*  $H_S := -\mathbf{d} \cdot \mathbf{E}$ . We let the external field be directed along the space fixed  $z$ -axis, so that

$$H_S := -\mathbf{d} \cdot \mathbf{E} = -\mu E \mathbf{c} \cdot \mathbf{e}_z = -\mu E c_z. \quad (2.25)$$

To determine the new spectrum, the matrix elements of  $H_S$  are needed, which amounts to finding  $\langle J'M'K'|c_z|JMK\rangle$ , where in the Euler angle parametrization  $c_z = \cos\theta$ .  $H_S$  does not connect states with different  $M$  or  $K$  because  $H_S$  is invariant under rotations about the  $z$  and  $c$ -axis:  $[J_z, c_z] = 0$  by (2.5) and  $[J_c, c_z] = 0$  by (2.7). In spherical tensor language, one says that  $c_z$  transforms as the  $m = 0$  component of a spherical tensor operator  $T$  of rank 1, i.e.  $T_0^{(1)} = c_z =: c_0$ . As such it may however connect states with  $\Delta J = 0, \pm 1$  as will be seen below.

To obtain the matrix elements, it is useful to realize that  $c_z$  is an element of a rotation matrix that belongs to  $J = 1$  angular momentum states:  $\cos\theta = D_{00}^{(1)}(\omega)$ . This follows from the transformation properties of  $c_z$ : the  $m = 0$  component of any vector operator transforms as

$$Rc_0R^\dagger = \sum_{m=0,\pm 1} D_{m0}^{(1)}(\omega)c_m \quad (2.26)$$

under a rotation. But, the  $z$ -component of any vector operator is multiplied by  $\cos\theta$  when the rotated  $z$ -component is written as a superposition:

$$Rc_0R^\dagger = D_{-10}^{(1)}(\omega)c_{-1} + \cos(\theta)c_0 + D_{+10}^{(1)}(\omega)c_{+1}. \quad (2.27)$$

The sought matrix elements are therefore

$$\langle J' M' K' | c_z | J M K \rangle = \frac{\sqrt{2J'+1}\sqrt{2J+1}}{8\pi^2} \int d\omega D_{M'K'}^{(J')}(\omega) D_{00}^{(1)}(\omega) D_{MK}^{(J)*}(\omega). \quad (2.28)$$

The Clebsch-Gordon series formula applied to the present case

$$D_{M'K'}^{(J')} D_{00}^{(1)} = \sum_{J''} D_{M'K'}^{(J'')} \left( \begin{array}{cc|c} J' & 1 & J'' \\ K' & 0 & K' \end{array} \right) \left( \begin{array}{cc|c} J' & 1 & J'' \\ M' & 0 & M' \end{array} \right). \quad (2.29)$$

is useful now to evaluate this integral. The used symbol

$$\left( \begin{array}{cc|c} j_1 & j_2 & j_3 \\ m_1 & m_2 & m_3 \end{array} \right) \quad (2.30)$$

is the usual Clebsch-Gordon (CG) coefficient (not a 3j-symbol). Inserting this into (2.28) one obtains:

$$\langle J' M' K' | c_z | J M K \rangle = \frac{\sqrt{2J'+1}}{\sqrt{2J+1}} \left( \begin{array}{cc|c} J' & 1 & J \\ K' & 0 & K \end{array} \right) \left( \begin{array}{cc|c} J' & 1 & J \\ M' & 0 & M \end{array} \right) \quad (2.31)$$

which confirms the selection rules for  $\Delta J$ ,  $\Delta M$  and  $\Delta K$ . The non-zero CG-coefficients are:

$$\left( \begin{array}{cc|c} J+1 & 1 & J \\ M & 0 & M \end{array} \right) = - \left[ \frac{(J+M)(J-M)}{J(2J+1)} \right]^{\frac{1}{2}} \quad (2.32)$$

$$\left( \begin{array}{cc|c} J & 1 & J \\ M & 0 & M \end{array} \right) = \frac{M}{[J(J+1)]^{\frac{1}{2}}} \quad (2.33)$$

$$\left( \begin{array}{cc|c} J-1 & 1 & J \\ M & 0 & M \end{array} \right) = \left[ \frac{(J+1+M)(J+1-M)}{(J+1)(2J+1)} \right]^{\frac{1}{2}} \quad (2.34)$$

as given e.g. in [36]. For  $J' = J$  we obtain the famous formula:

$$\langle J M K | H_S | J M K \rangle = -\mu E \frac{M K}{J(J+1)}, \quad (2.35)$$

which at the same time yields directly the first order energy change of the respective levels with given  $M$  and  $K$ . As mentioned above, for  $K = 0$ , the states have definite parity and therefore no first order Stark effect since  $c_z$  changes sign under inversion. We also learn that to have an average orientation in space (i.e. non-zero expectation value for  $c_z$ ), a non-zero spin around the symmetry axis is required.

## 2.2 Energy levels of OH

In a diatomic molecule, rotations about the internuclear axis are meaningless as long as only the nuclei and not the electrons are considered. The rotational energies of a rigid OH molecule are therefore obtained in the limit  $I_c \rightarrow 0$  so that the energy remains finite only for  $K = 0$ . Despite of this, a diatomic molecule may still have a nonzero projection of  $\mathbf{J}$  onto  $\mathbf{c}$ , if the total orbital  $\mathbf{L}$  and spin  $\mathbf{S}$  angular momentum of the electrons is included in  $\mathbf{J}$ . The operator which generates rotations of the two nuclei is now  $\mathbf{R} := \mathbf{J} - \mathbf{L} - \mathbf{S}$  and its projection onto  $\mathbf{c}$  is zero by definition.

The electrons are moving in an axially symmetric field and therefore the projection of  $\mathbf{L}$  onto the internuclear axis  $\mathbf{c}$  can be considered as conserved, as long as non-axial interactions and the rotation of the reference frame can be neglected. The absolute value of this projection is denoted by  $\Lambda$  and hence a state of definite  $\Lambda$  must transform as  $e^{\pm i\Lambda\chi}$  under a rotation about the internuclear axis by an angle  $\chi$ , i.e. for every  $\Lambda > 0$  there are two degenerate states with projections of  $\mathbf{L}$  given by  $\pm\Lambda$ . If the total spin is zero, the transformation properties of the wavefunction are the same as for the symmetric rigid rotor and therefore, for a fixed electronic state, one may set  $K = \pm\Lambda$ .

The case of non-zero total spin adds another complication. It now depends on the strength of the spin-orbit interaction, whether it is useful to consider the spin as “locked” to the internuclear axis. If it is, one denotes definite projections of  $\mathbf{S}$  on the internuclear axis  $\mathbf{c}$  by  $\Sigma$  and defines another (approximately) conserved quantum number by  $\Omega := \Lambda + \Sigma$ . Eigenstates with definite  $\Omega$  transform as  $e^{\pm i\Omega\chi}$  under a rotation about the internuclear axis and hence we can still use the rigid rotor wavefunction where now  $K = \pm\Omega$ . States with definite  $\Omega$  are still doubly degenerate (apart from the degeneracy in  $M$ ). This scheme is usually referred to as “Hund’s case (a)”, while in case (b), the spin is not considered as locked to the internuclear axis. As the rotational quantum number  $J$  increases, the electron spin projection no longer follows the nuclear framework adiabatically and hence as  $J$  increases, Hund’s case (b) must become the more useful description. By definition, a so called case (a) set of basis functions is constructed of products of basis functions with *definite* values of  $\Lambda$ , total spin  $S$ ,  $\Sigma$ ,  $J$ ,  $\Omega$  and laboratory projection  $M$  of  $\mathbf{J}$  [37].

The characteristic angular momentum quantum numbers for the electronic ground state can be obtained from the electron configuration of the (almost) united atoms, which is  $(1s\sigma)^2(2s\sigma)^2(2p\sigma)^2(2p\pi)^3$ . This configuration gives rise to only a single molecular state with  $\Lambda = 1$  and  $S = 1/2$  (see e.g. [38]) so that the appropriate term symbol is  ${}^2\Pi$ . The possible  $\Omega$  values are  $\Omega = 1 \pm 1/2$  and these are appended as a subscript to the term symbol which means that there are two electronic states:  ${}^2\Pi_{3/2}$  and  ${}^2\Pi_{1/2}$ . These states are not degenerate because of the spin-orbit interaction that gives rise to the so called *fine-structure*. This interaction can be approximated by  $H_{SO} = \mathbf{A}\mathbf{L} \cdot \mathbf{S} \approx A\mathbf{L}_c \cdot \mathbf{S}_c$  where  $A$  is the spin-orbit coupling constant, which can be negative or positive (see e.g. [39]). For



OH, the spin-orbit coupling constant is negative and hence states with  $\Omega = 3/2$  are lower in energy than those with  $\Omega = 1/2$ . The rotational levels with definite  $\Omega$  are labeled  $J = \Omega, \Omega + 1, \Omega + 2, \dots$ .

Each of these levels is doubly degenerate (disregarding the degeneracy in  $M$ ) as long as the rotation of the reference frame is ignored. In reality, there occurs a splitting of every rotational level which is called  $\Lambda$ -type doubling and which increases with the rotational quantum number. The lowest rotational state of OH with  $J = 3/2$  is split into two components that are separated by  $0.055 \text{ cm}^{-1}$ . These components must have definite parity and therefore it is necessary to construct basis functions of definite parity from the case (a) basis functions to obtain the correct zero order basis functions. Details about the behaviour of Hund's case (a) states under inversion can be found in [37, 40, 41]. Here, only the rotational part of the wavefunction is needed and the basis functions of definite parity are given by the symmetric and antisymmetric linear combinations of rigid rotor states with  $K = \pm\Omega$ . Denoting the parity by  $\epsilon$  with  $\epsilon = \pm 1$ , the definite parity states are:

$$|JM\Omega, \epsilon\rangle = \frac{|JM\Omega\rangle + \epsilon(-1)^p |JM-\Omega\rangle}{\sqrt{2}} \quad (2.36)$$

where for states with  $\Lambda > 0$

$$p := J - S \quad (2.37)$$

and hence for the rotational levels of OH  $^2\Pi$  the value of  $p$  is indeed always an integer. It is common convention to denote states with a definite parity of  $(-1)^{J-1/2}$  as  $e$  and states with  $(-1)^{J+1/2}$  as  $f$  provided  $J$  itself is half integer. For integer values of  $J$  the  $e$  and  $f$  levels have the respective parities  $(-1)^J$  and  $(-1)^{J+1}$ . With this convention, all lower components of a  $\Lambda$ -doublet are either  $e$  or  $f$ , independent of  $J$ , likewise for the upper components (see Fig. 2.1 p. 20).

If the Hund's case (a) description is not exactly valid, every level is a mixture of  $|^2\Pi_{3/2}\rangle$  and  $|^2\Pi_{1/2}\rangle$  states. For OH, this complication must also be taken into account by diagonalizing the rotational Hamiltonian

$$H_{rot} = A_v \mathbf{L} \cdot \mathbf{S} + B_v (\mathbf{J} - \mathbf{L} - \mathbf{S})^2 \quad (2.38)$$

in the Hund's case (a) basis, where the spin-orbit coupling constant  $A_v$  and the rotational constant  $B_v$  depend on the vibrational quantum number  $v$ . The result is given in [39, 42]:

$$|(F_1)JM, \epsilon\rangle = a_J |^2\Pi_{1/2}\epsilon\rangle + b_J |^2\Pi_{3/2}\epsilon\rangle \quad (2.39)$$

$$|(F_2)JM, \epsilon\rangle = -b_J |^2\Pi_{1/2}\epsilon\rangle + a_J |^2\Pi_{3/2}\epsilon\rangle, \quad (2.40)$$

The spin-orbit (fine-structure) manifolds  $F_1$  and  $F_2$  are labeled in order of increasing energy. For OH in the electronic ground state  $A_v < 0$  and therefore the  $F_1$  states resemble more closely the basis states with  $\Omega = 3/2$  whereas those

labeled  $F_2$  resemble the  $\Omega = 1/2$  states; in fact, for  $J = 1/2$  we have  $b_J = 0$  exactly and within the used approximations we have a true Hund's case (a) state. The coefficients are:

$$a_J = \sqrt{\frac{X + (Y - 2)}{2X}} \quad (2.41)$$

$$b_J = \sqrt{\frac{X - (Y - 2)}{2X}} \quad (2.42)$$

with the definitions

$$X := \sqrt{4(J + 1/2)^2 + Y(Y - 4)} \quad (2.43)$$

$$Y := \frac{A_v}{B_v}. \quad (2.44)$$

For the vibrational ground state of OH, the values are  $A_v = -139.73 \text{ cm}^{-1}$  and  $B_v = 18.515 \text{ cm}^{-1}$  as determined by Dieke and Crosswhite [43]. For the lowest rotational state of  $F_1$ , which has  $J = 3/2$ , the mixing coefficients and the respective probabilities are:

$$a_{3/2} = 0.1739 \quad (a_{3/2})^2 = 0.03 \quad (2.45)$$

$$b_{3/2} = 0.9848 \quad (b_{3/2})^2 = 0.97 \quad (2.46)$$

so that also this state is quite well described by a pure Hund's case (a) state. It is therefore common practice to denote the  $F_1$ -manifold by  ${}^2\Pi_{3/2}$  and the  $F_2$ -manifold by  ${}^2\Pi_{1/2}$  even though this assignment is not exact.

### 2.2.1 Stark effect of OH

The states of interest here are the upper and lower  $\Lambda$ -doublet component of the lowest rotational ( $J = 3/2$ ) state in the  $F_1$  manifold which we denote by  $|JM, f\rangle$  and  $|JM, e\rangle$  respectively. To determine the Stark effect for these states, the matrix elements of  $H_s$  are needed. If there was no  $\Lambda$ -doubling and if we had a pure Hund's case (a) state, the first order energies would be given by (2.35) where  $K$  is replaced by  $+\Omega$  or  $-\Omega$ . However, the "true" states are given by (2.39):

$$\begin{aligned} |JM, f\rangle &= \frac{a_J}{\sqrt{2}} \left( |JM + \tfrac{1}{2}\rangle - |JM - \tfrac{1}{2}\rangle \right) \\ &+ \frac{b_J}{\sqrt{2}} \left( |JM + \tfrac{3}{2}\rangle - |JM - \tfrac{3}{2}\rangle \right) \end{aligned} \quad (2.47)$$

$$\begin{aligned} |JM, e\rangle &= \frac{a_J}{\sqrt{2}} \left( |JM + \tfrac{1}{2}\rangle + |JM - \tfrac{1}{2}\rangle \right) \\ &+ \frac{b_J}{\sqrt{2}} \left( |JM + \tfrac{3}{2}\rangle + |JM - \tfrac{3}{2}\rangle \right). \end{aligned} \quad (2.48)$$

The diagonal matrix elements of  $H_s$  between these states are

$$\langle JM, e | H_s | JM, e \rangle = \langle JM, f | H_s | JM, f \rangle = 0, \quad (2.49)$$

as it must be, because  $H_s$  does not connect states of identical parity. The two off-diagonal elements are real and given by:

$$\langle JM, e | H_s | JM, f \rangle = -\mu E \frac{M}{J(J+1)} \left( \frac{1}{2}(a_J)^2 + \frac{3}{2}(b_J)^2 \right) =: Q, \quad (2.50)$$

in which the weighted average of  $\Omega = 1/2$  and  $\Omega = 3/2$  occurs which is referred to as the “effective” value of  $\Omega$ :

$$\Omega_{\text{eff}} := \left( \frac{1}{2}(a_J)^2 + \frac{3}{2}(b_J)^2 \right) = \langle JM, e | J_c | JM, f \rangle, \quad (2.51)$$

so that only in the exact case (a) limit  $\Omega_{\text{eff}} = \Omega$ .

The Hamiltonian matrix for the molecule, including  $H_S$ , in the  $\Lambda$ -doublet subspace of definite  $J$  is therefore

$$\begin{pmatrix} E_\Lambda/2 & Q \\ Q & -E_\Lambda/2 \end{pmatrix} \quad (2.52)$$

where  $E_\Lambda$  denotes the energy splitting of the  $\Lambda$ -doublet and therefore the energies of the unperturbed levels are  $\pm E_\Lambda/2$ . The eigenvalues of this matrix give the energy to first order:

$$E_{f/e} = \pm \sqrt{\left( \frac{E_\Lambda}{2} \right)^2 + Q^2} \quad (2.53)$$

where the upper sign refers to the  $f$ -component and the lower to the  $e$ -component.

As the energy  $Q$  becomes significantly larger than the  $\Lambda$ -doublet separation, the Stark effect becomes linear. The Stark shift for levels with  $\pm M$  is the same. For  $J = 3/2$ , we have  $M = -3/2, -1/2, 1/2, 3/2$  and therefore every  $\Lambda$ -doublet component splits into two doubly degenerate levels with either  $|M| = 3/2$  or  $|M| = 1/2$ .

The state  $|\Psi, f\rangle$  which correlates adiabatically with the field free  $|JM, f\rangle$  state can now also be determined, the result is:

$$|\Psi, f\rangle = \alpha |JM, f\rangle + \beta |JM, e\rangle \quad (2.54)$$

where the ratio of the coefficients is

$$\frac{\beta}{\alpha} = \frac{Q}{A + \sqrt{A^2 + Q^2}} = \quad \text{with} \quad A := E_\Lambda/2. \quad (2.55)$$

If for example  $Q = 10A$ , the ratio is  $\beta/\alpha \approx 10/11$  so that the state is already close to being a 1 : 1 mixture of states with opposite parity.

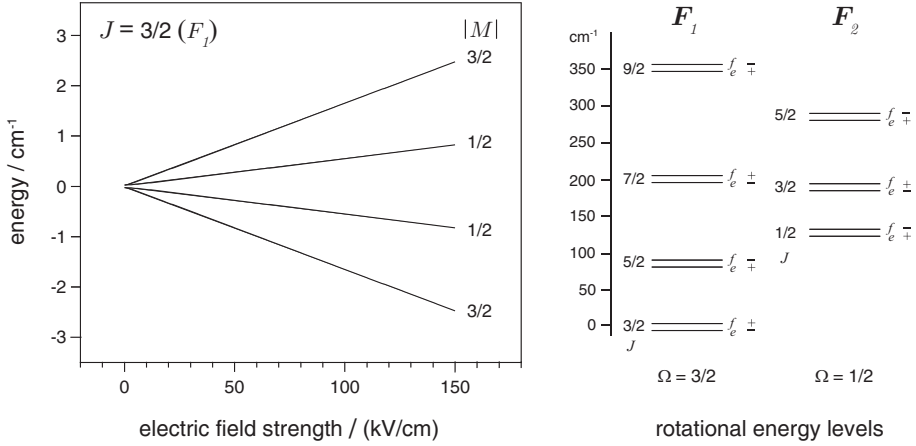


**Figure 2.1:** Right: rotational energy levels of OH ( $^2\Pi_{3/2}$  and  $^2\Pi_{1/2}$ ); the  $\Lambda$ -doublet splittings are magnified. Left: the adiabatic energy change due to the Stark effect for the upper  $J = 3/2$   $f$  and lower  $J = 3/2$   $e$   $\Lambda$ -doublet component. The absolute values for the projection  $M$  of  $\mathbf{J}$  on the laboratory  $z$ -axis are indicated.

To calculate the Stark effect for the  $F_1, J = 3/2$  level, the dipole moment  $\mu$ ,  $\Omega_{\text{eff}}$  and the  $\Lambda$ -doublet splitting  $E_\Lambda$  are needed. The electric dipole moment of OH depends only very slightly on the rotational and vibrational level. For the  $F_1, J = 3/2, v = 0$  state, the value is  $\mu = 1.655$  D as given in ref. [44]. For the purpose of Stark deceleration, the tiny variations in the dipole moment with the rotational state can be ignored. As noted before  $E_\Lambda = 0.055 \text{ cm}^{-1}$ . For  $\Omega_{\text{eff}}$  the above formulae yield  $\Omega_{\text{eff}} = 1.47$  which is identical to the value given in [44]. The value of  $Q$  in units of  $\text{cm}^{-1}$  is given by the following equation

$$Q = -1.679 \cdot 10^{-2} \mu E \frac{M \Omega_{\text{eff}}}{J(J+1)} [\text{cm}^{-1}] \quad (2.56)$$

in which the electric field strength is in  $\text{kV/cm}$  and the dipole moment in Debye. In **Fig. 2.1** a plot of the Stark effect for the  $J = 3/2e, f$  levels is shown. It is seen that the energy of all  $M_J$ -states of the upper  $\Lambda$ -doublet component ( $\epsilon = +$ ,  $f$ -parity) increases in an electric field whereas for states in the lower  $\Lambda$ -doublet component ( $\epsilon = -$ ,  $e$ -parity) the energy decreases. The former type of states are referred to as “low field seeking” states whereas the latter are “high field seeking” states. A low field seeking molecule is thus a molecule which experiences a force in the direction towards lower field strengths due to its Stark interaction upon traversing an electric field gradient.

## 2.2.2 The Stark effect and hyperfine structure

The most abundant isotopic variant  $^{16}\text{OH}$  has a total nuclear spin of  $I = 1/2$  which is due to the nuclear spin of the hydrogen proton alone. This non-zero nuclear spin gives rise to hyperfine structure in the spectrum of OH due to the magnetic dipole moment of the proton. This leads to a splitting of every  $\Lambda$ -doublet component into two states with definite total angular momentum  $\mathbf{F} := \mathbf{J} + \mathbf{I}$ . For the  $J = 3/2$  rotational level, the possible values for  $F$  are therefore  $F = 2$  and  $F = 1$  with a degeneracy of  $2F + 1$ . The splittings are rather small, as shown in **Fig. 2.2** for the  $J = 3/2$  level of  $F_1$ . Many  $\Lambda$ -doublet hyperfine transition frequencies have been measured and are tabulated in ref. [45].

To determine the adiabatic change of the energy levels due to the Stark interaction, we proceed in the same way as above. We use zero order basis functions together with the measured energy splittings and diagonalize the resulting Hamiltonian matrix. The completely general matrix elements are given in [46], but as such the result is not very illuminating. If one decides to ignore  $\Delta J = \pm 1$  contributions anyway, it is quite simple to derive the matrix elements. Since  $H_S$  does not connect states with different  $M_F$ , the matrices are at most  $4 \times 4$  for all  $J$ . We use the following notation for the matrix elements:

$$\begin{array}{c|cccc}
 & \epsilon & + & + & - & - \\
 \hline
 \epsilon & F & 2 & 1 & 2 & 1 \\
 \hline
 + & 2 & E_1 & 0 & Q_1 & Q_3 \\
 + & 1 & 0 & E_2 & Q_3 & Q_2 \\
 - & 2 & Q_1 & Q_3 & E_3 & 0 \\
 - & 1 & Q_3 & Q_2 & 0 & E_4
 \end{array} \tag{2.57}$$

For every  $M_F$ , the off-diagonal elements  $Q_i$  have to be determined. All states with definite  $F$  and  $M_F$  are linear combinations of at most two direct product states of the type  $|J M_J \epsilon\rangle \otimes |I M_I\rangle$  with  $I = 1/2$ :

$$\begin{aligned}
 |F M_F \epsilon\rangle &= |J M_F - \tfrac{1}{2} \epsilon\rangle \otimes |\tfrac{1}{2} + \tfrac{1}{2}\rangle \begin{pmatrix} J & \tfrac{1}{2} \\ M_F - \tfrac{1}{2} & \tfrac{1}{2} \end{pmatrix} \begin{pmatrix} F \\ M_F \end{pmatrix} + \\
 &\quad |J M_F + \tfrac{1}{2} \epsilon\rangle \otimes |\tfrac{1}{2} - \tfrac{1}{2}\rangle \begin{pmatrix} J & \tfrac{1}{2} \\ M_F + \tfrac{1}{2} & -\tfrac{1}{2} \end{pmatrix} \begin{pmatrix} F \\ M_F \end{pmatrix}. \tag{2.58}
 \end{aligned}$$

For  $J = 3/2$  the required CG-coefficients are given in **Fig. 2.2**. Because  $H_S$  does not act on the nuclear spin degree of freedom, the sought matrix elements

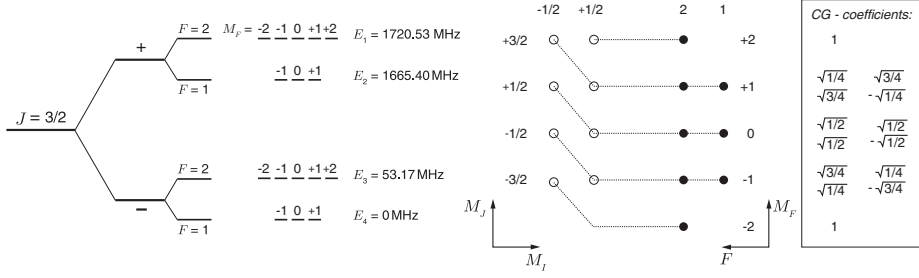


**Figure 2.2:** Left: the splittings of the  $F_1, J = 3/2$  level into two  $\Lambda$ -doublet components of positive and negative parity and the hyperfine splitting of each component (not to scale). Note that in contrast to the definition of eq.(2.52), the zero in energy is not at the center of the  $\Lambda$ -doublet. Right: angular momentum coupling scheme for the case  $3/2 \times 1/2$  and the corresponding Clebsch-Gordon coefficients. The coefficient pairs in the left column belong to  $F = 2$  and those in the right to  $F = 1$ ; for each pair, the upper number belongs to  $M_I = -\frac{1}{2}$  and the lower number to  $M_I = +\frac{1}{2}$ . For example, if  $F = 1, M_F = 1$  the expansion is  $|FM_F\rangle = \sqrt{3/4}|\frac{3}{2}M_J\rangle|\frac{1}{2}M_I\rangle - \sqrt{1/4}|\frac{3}{2}M_J'\rangle|\frac{1}{2}M_I'\rangle$ , with  $M_J = \frac{3}{2}, M_I = -\frac{1}{2}, M_J' = \frac{1}{2}, M_I' = \frac{1}{2}$ .

are:

$$\begin{aligned}
 \langle F' M_F' \epsilon' | H_S | F M_F \epsilon \rangle &= -\mu E \frac{\Omega_{eff}}{J(J+1)} \delta_{\epsilon\epsilon'} \delta_{M_F M_F'} \times \\
 &\left\{ (M_F - \frac{1}{2}) \begin{pmatrix} J & \frac{1}{2} \\ M_F - \frac{1}{2} & +\frac{1}{2} \end{pmatrix} \begin{pmatrix} F' & \frac{1}{2} \\ M_F & +\frac{1}{2} \end{pmatrix} + \right. \\
 &\left. (M_F + \frac{1}{2}) \begin{pmatrix} J & \frac{1}{2} \\ M_F + \frac{1}{2} & -\frac{1}{2} \end{pmatrix} \begin{pmatrix} F' & \frac{1}{2} \\ M_F & -\frac{1}{2} \end{pmatrix} \right\}. \quad (2.59)
 \end{aligned}$$

The Hamiltonian matrix may therefore be written as

$$H = \begin{pmatrix} E_1 & 0 & 0 & 0 \\ 0 & E_2 & 0 & 0 \\ 0 & 0 & E_3 & 0 \\ 0 & 0 & 0 & E_4 \end{pmatrix} - \mu E \frac{\Omega_{eff}}{J(J+1)} \begin{pmatrix} 0 & 0 & q_1 & q_3 \\ 0 & 0 & q_3 & q_2 \\ q_1 & q_3 & 0 & 0 \\ q_3 & q_2 & 0 & 0 \end{pmatrix}. \quad (2.60)$$

For  $J = 3/2$ , the states with  $F = 2, M_F = \pm 2$  consist of only a single component (see Fig. 2.2) and the resulting matrix can be diagonalized in a two dimensional subspace. The matrix elements  $Q_i(M_F)$  for  $M_F = \pm 2$  are:

$$Q_1(\pm 2) = \langle 2 2 \epsilon' | H_S | 2 2 \epsilon \rangle = -\mu E \frac{\Omega_{eff}}{\frac{3}{2}(\frac{3}{2}+1)} \delta_{\epsilon\epsilon'} \times \left( \pm \frac{3}{2} \right) \quad (2.61)$$

$$Q_2(\pm 2) = 0 \quad (2.62)$$

$$Q_3(\pm 2) = 0. \quad (2.63)$$

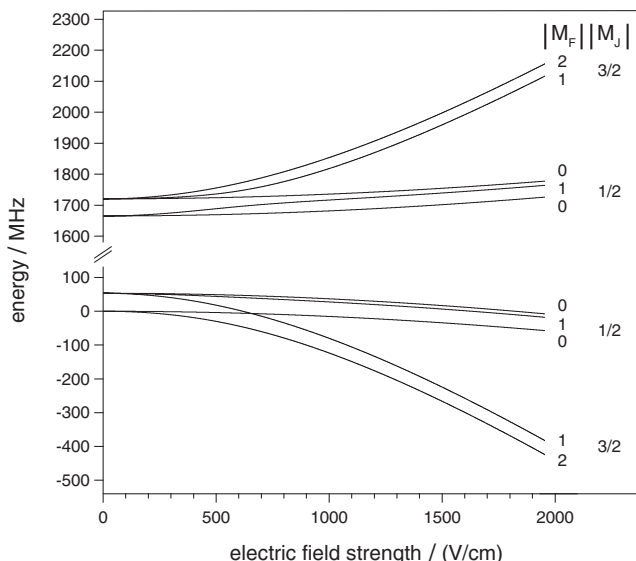


**Figure 2.3:** Adiabatic energy change of the hyperfine resolved energy levels of OH as a function of field strength. The values for  $|M_F|$  are indicated at each curve, likewise for the high-field limit values of  $|M_J|$ .

The matrix elements in the notation of equation (2.60) are:

$M_F :$	0	$\pm 1$	$\pm 2$	(2.64)
$q_1$	0	$\pm 3/4$	$\pm 3/2$	
$q_2$	0	$\pm 5/2$	0	
$q_3$	$1/2$	$\sqrt{3}/4$	0	

The eigenvalues in the cases where  $|M_F| = 1, 0$  are more difficult to obtain analytically as the polynomial  $\det(H - \lambda I) = 0$  is of 4th degree. Numerical methods are useful in this case as provided e.g. by the program package [47]. The result of such a calculation is shown in **Fig. 2.3**, which agrees with previously published data [44, 48]. As before, all  $M_F$ -states of the upper  $\Lambda$ -doublet component are low field seeking whereas all states in the lower  $\Lambda$ -doublet component become high field seeking if subjected to an electric field. For higher electric fields, the hyperfine splittings do not significantly alter the energies obtained before when the hyperfine structure was simply ignored. The result is important nevertheless: all  $M_F$  states in the upper  $\Lambda$ -doublet component belonging to  $F = 1$  have the high field behaviour of the states which were previously labeled  $|M_J| = 1/2$ . In contrast, the  $F = 2$  states with  $|M_F| = 2, 1$  correlate with  $|M_J| = 3/2$  while  $|M_F| = 0$  correlates with  $|M_J| = 1/2$ . The Stark effect for molecules with  $|M_J| = 3/2$  is three time stronger than for those

with  $|M_J| = 1/2$  and therefore under appropriate deceleration conditions (i.e. at high “phase angles” – see chapter 3) it is possible to prepare molecules which are in the low field seeking  $F = 2$  states exclusively while it is not possible to prepare a pure  $F = 1$  ensemble. Of course, this requires that the molecules traverse the adiabatic energy curves during the whole deceleration process.

The described correlations between the hyperfine levels and the high field behaviour are easy to establish *without* setting up and diagonalizing the Hamiltonian matrix. All that is needed are the CG-coefficients. In the limit where the hyperfine splitting approaches zero, the coupled basis is as good as the uncoupled basis, because  $H_S$  does not act on the nuclear spin. All curves shown in Fig. 2.3 would change continuously as the hyperfine splitting decreases to zero to finally merge with the previously obtained curves of Fig. 2.1. If the problem is set up in the coupled basis, the diagonalization of the matrix only gives us back the uncoupled (mixed parity) set as the result when either the splitting is small enough or the field is strong enough! The  $M_J$  states contained in the coupled states are given by the CG-coefficients. The state  $F = 2, M_F = 2$  consists only of  $M_J = 3/2$  and therefore, it must also correlate with this state in higher fields. The states with  $F = 1, 2$  and  $M_F = 0$  consist of  $M_J = +1/2$  and  $-1/2$ , therefore these states must correlate with  $|M_J| = 1/2$ . The only ambiguity occurs for  $F = 1, 2$  with  $M_F = 1$ : here it seems unclear whether  $F = 1$  or  $F = 2$  correlates with  $M_J = 3/2$  or  $1/2$ . However, the  $F = 1$  state is lower in energy than  $F = 2$ , and both curves would have to cross if  $F = 1, M_F = 1$  were to correlate with  $M_J = 3/2$ . Such a crossing is not possible however, because both states have the same value of the only exact constant of motion  $M_F$  (see e.g. [35]) and therefore the correlations can be unambiguously established. The same holds for other values of  $J$ .

## 2.3 Production of a pulsed OH beam

The OH radical is chemically unstable and therefore has to be produced in situ during the supersonic expansion. Several routes are possible for this, the most popular methods being electric discharge and photolysis. Both methods have their benefits and shortcomings. The discharge method is inexpensive and in principle easy to implement, unfortunately it produces many undesired species, especially ions, and the resulting gas expansion does not cool to the lowest possible temperatures. In contrast, the photolysis method is clean and well controlled with small pulse to pulse fluctuations if used correctly. Furthermore, the spatial extension of the produced OH pulse is smaller and to some extent under control.

In both cases, the most common OH precursor molecules are  $\text{H}_2\text{O}$ ,  $\text{HOOH}$  and  $\text{HNO}_3$ . For all experiments described in this work, OH was produced by 193 nm photolysis of  $\text{HNO}_3$  using a compact ArF excimer laser<sup>3</sup>. Nitric acid is a

---

<sup>3</sup>PSX-501, Neweks Ltd., 19 Akadeemia tee, Tallinn, Estonia



very suitable precursor molecule because its absorption cross section at 193 nm is quite large ( $\approx 1200 \cdot 10^{-20} \text{cm}^2$ ) and the OH yield is moderately good<sup>4</sup>.

A thoroughly tested recipe for the production of an intense OH beam is described in the following. First, a few ml of pure nitric acid are loaded into a reservoir – the so called “bubbler” – through which a carrier gas may be passed and become saturated with nitric acid vapor. About half of the inner volume of the bubbler is filled with glass wool to increase the overall surface area of the liquid-gas interface. A well suited material for the bubbler is titanium because it does not react with nitric acid (and many other acids). A PTFE O-ring is used to seal the bubbler. The bubbler is cooled by a thermostat so that the reservoir is always lower in temperature than all other components which are connected to it and therefore no condensation can occur outside the bubbler.

To expand the gas mixture into the vacuum, a commercial solenoid valve (General Valve, Ser. 99) is used. This valve is reasonably resistant towards nitric acid vapor as long as condensation inside the valve is avoided. The gas mixture is expanded into the vacuum at a typical stagnation pressure of 1.5 – 3 bar. The photolysis laser beam intersects the gas jet right behind the nozzle orifice. Usually a short quartz capillary ( $\approx 5 \text{ mm}$  long) is mounted onto the flat front plate of the valve and the photolysis occurs mainly inside this capillary just before the gas starts to expand. Whether a capillary is useful or not depends on the desired beam characteristics. The laser beam is focussed by a cylindrical lens. The so created beam of OH radicals has a high state purity: almost all molecules reside in the  $J = 3/2, \Omega = 3/2$  level (see table 7.1 on page 112). Since the  $\Lambda$ -doublet splitting is only  $0.055 \text{ cm}^{-1}$ , both  $\Lambda$ -doublet components are populated equally in the beam.

The vapor pressure of pure nitric acid at 20°C is about 64 mbar. In the experiment one finds the surprising result that the OH yield does not decrease when the temperature of the  $\text{HNO}_3$ -reservoir is lowered. Even a vapor pressure of 2.4 mbar at  $-30^\circ\text{C}$  is still sufficient to produce a good OH beam. It therefore seems that the chemical reactions which occur after the photolysis always lead to a certain equilibrium concentration of OH radicals which is to a large extent independent of the initial OH concentration<sup>5</sup>.

For practical reasons it is advisable to use low nitric acid concentrations. First, the beam quality improves because there is less energy released during the expansion by chemical reactions, that is the resulting beam temperature is lower. Secondly, the corrosion of the valve and the vacuum system is greatly reduced which is important for experiments which run for more than just a few days. The vapor pressure  $p$  of an ideal gas in equilibrium with its fluid phase

---

<sup>4</sup>Apparently it is not far below 0.5, see IUPAC *Subcommittee on Gas Kinetic Data Evaluation - Data Sheet PNOx2*, where also absorption cross sections are tabulated.

<sup>5</sup>I have obtained these insights thanks to the commitment of Prof. David Nesbitt who was visiting our laboratory in the spring of 2008.

as a function of temperature is given by the relation

$$p = A e^{-\frac{\Delta H_e}{RT}}. \quad (2.65)$$

A derivation of the formula is given in textbooks on thermodynamics, e.g. [49]. The enthalpy of evaporation of nitric acid is  $\Delta H_e = 39.1 \text{ kJ/mol}$  [50]. The pre-exponential factor is determined if a single measured value for the vapor pressure is known. Several are tabulated in [50] and the result is  $A = 592.58 \cdot 10^6 \text{ mbar}$ . The universal gas constant is  $R = 8.3145 \text{ J/(K mol)}$ . The following values result:

$T/^{\circ}\text{C}$	-40	-30	-20	-10	0	10	20	30
$p/\text{mbar}$	1.0	2.4	5.1	10.3	19.8	36.3	64.0	108.6

Another important observation is that highly concentrated nitric acid of least 90%<sub>wt</sub> should be used, even better is close to 100%. One might think that instead of cooling down the reservoir, one could simply dilute the nitric acid. While indeed, the nitric acid partial pressure is reduced in this way, experiment shows that the so produced OH beam density suffers strongly – for as yet unknown reasons.

A final remark regarding beam sources for deceleration machines is in order. Since the apparatus behind the skimmer is on high voltage, it is also quite prone to discharges if droplets or solid particles deposit on the surface. Therefore it is quite important to use only sufficiently clean beam preparation techniques and to avoid condensation in the valve. Substances which tend to polymerize should be avoided e.g. formaldehyde ( $\text{H}_2\text{CO}$ ) and the typical precursor for NH radicals isocyanic acid ( $\text{HNCO}$ ).

## 2.4 Detection of OH radicals

OH radicals are detected by laser induced fluorescence (LIF) using a commercial pulsed dye laser system. The fluorescence is collected by a quartz lens (50 mm focal length, 50 mm diameter) and imaged onto a photomultiplier tube (PMT). Stray light is largely eliminated by use of Brewster windows, baffles and filters.

All rotational levels indicated in Fig. 2.1 can be selectively detected, even if the transition is saturated. Molecules are pumped to the first electronically excited state by using rotational transitions of the  $A^2\Sigma^+, v = 1 \leftarrow X^2\Pi, v = 0$  band which occur at around 282 nm. Measured values can be found in [43], calculated values are available e.g. from the LIFBASE program [51]. The typically used transitions are tabulated on page 113 table 7.2. The radiative lifetime of the  $A^2\Sigma^+, v = 1$  state is 717 ns [52].

The emitted off-resonant fluorescence (to final states with  $v = 1$ ) occurs at longer wavelengths and can thus be separated easily from the excitation wavelength by a filter which transmits at slightly longer wavelengths. One should be aware however that besides true stray light, which has the wavelength

of the excitation laser, also *spurious fluorescence* from the Brewster windows, baffles or any other component can occur and this light naturally also has a longer wavelength<sup>6</sup>. Therefore it is advisable to create a transmission window in the range where the molecular fluorescence mainly occurs. To that end, four filters are used. One UG11 (Schott, 1 mm thickness, transmission 90%) to absorb light in the visible range and three filters which create a transmission window as shown in **Fig. 2.4**. Filter A is a dichroic filter (Omega Optical, USA) of which two are used, filter B (Laser Optik, Germany) is also a dichroic filter. This filter combination (UG11+2A+B) yields a maximum transmission of about 55% in the desired range.

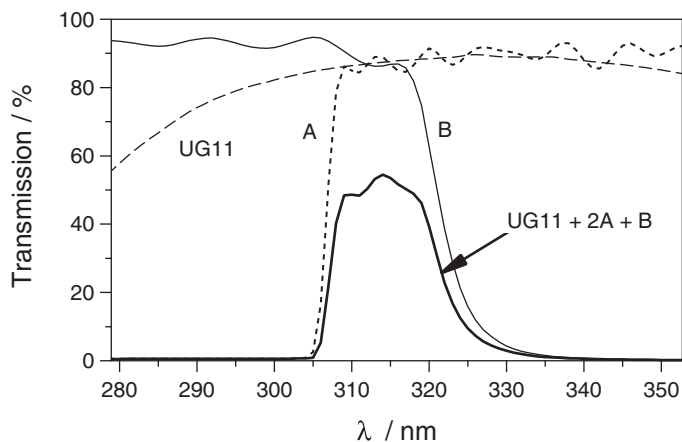


**Figure 2.4:** Transmission curves of the used filters. The transmission curve of the combination (UG11+2A+B) is also shown.

---

<sup>6</sup>An essential fact pointed out to me by Dr. Steven Hoekstra.



## Chapter 3

# Stark deceleration of OH radicals

The Stark effect provides a handle for the state selection and further manipulation of polar molecules in a molecular beam. In this chapter it is explained how an array of time dependent field gradients can be used to prepare molecules in specific low field seeking quantum states and with a specific mean forward velocity. The different modes of operation which are possible are discussed in some detail.

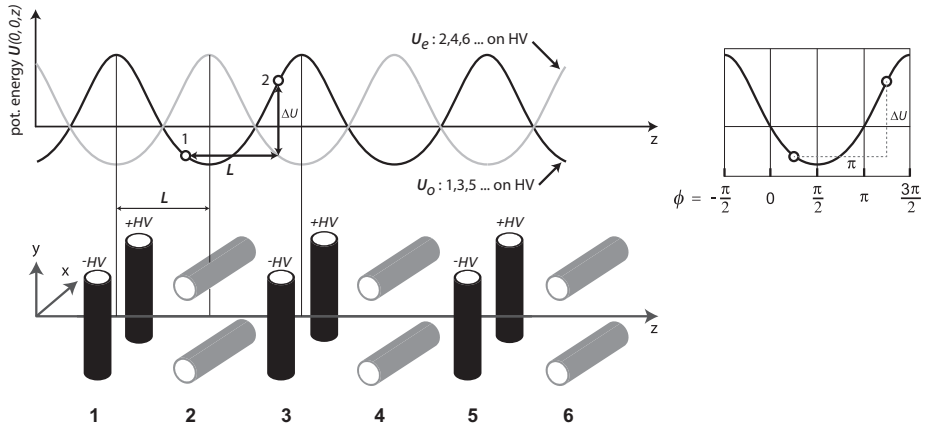


**Figure 3.1:** Scheme of the two possible on-axis potential energy curves  $U_{e/o}(0, 0, z)$  for a molecule in the decelerator together with the electrode geometry and the definition of the coordinate system. For the instrument used in this work,  $L = 8.25$  mm, the electrode gap is 3 mm wide yielding a  $3 \times 3$  mm<sup>2</sup> opening. The inset shows the reference potential which defines the *phase*  $\phi$  of the molecule. A more detailed view of the machine is provided by the pictures on p.49 and 50.

### 3.1 Introduction

The principle design of the deceleration apparatus is very simple: parallel pairs of cylindrical metal rods, that is *electrodes*, are combined into a periodic array as it is shown schematically in **Fig. 3.1**, more detailed views of the machine can be found on p. 49 and 50. The orientation of the pairs alternates between horizontal and vertical, i.e. successive pairs are aligned at a right angle. A likewise periodic electric field is created by applying a voltage to only the vertical (odd numbered) electrodes while the horizontal (even numbered) electrodes remain uncharged at ground potential. The voltages applied to the electrodes of a pair have the same magnitude but opposite polarity. This is one of the two field configurations which are needed. The other configuration is obtained by charging, in the same manner, all horizontal pairs and connecting all vertical ones with ground. During operation one rapidly switches between these two states. The so created time dependent periodic field gradients allow a fairly precise adjustment of the mean forward velocity and also of the velocity distribution (for representative time-of-flight measurements see Fig. 5.3 on p. 65).

The electrodes of the used decelerator have a diameter of 4.5 mm and the center to center distance between electrodes of a pair is 7.5 mm, while the center to center distance  $L$  between neighboring pairs is 8.25 mm. The free opening for the passage of the molecular beam is a 3 mm  $\times$  3 mm square. The aspect ratios are the same as the ones used in earlier experiments by Crompvoets et al. [53] in 2002, which was a slight modification of the very first design by Bethlem

et al. in 1999 [5]. The present instrument has 317 electrode pairs in total, for further technical details see chapter 4.

## 3.2 The potential

As described in chapter 2, the energy levels of a polar molecule change with the applied field strength. If the change of the field direction and strength is slow enough, i.e. if it is *adiabatic*, then the energy shift due to the Stark effect gives rise to a definite force on the molecule. This force then has a potential which in our case depends on the position  $(x, y, z)$  and time  $t$ . We denote this potential by  $U(x, y, z, t)$ . If the state of the molecule is low field seeking, i.e. if the energy increases with increasing field strength, the potential  $U(0, 0, z, t)$  along  $z$  will resemble the curve shown in **Fig. 3.1**.

At a certain time either the odd or the even numbered electrode pairs are charged and therefore either  $U(x, y, z, t) = U_o(x, y, z)$  or  $U(x, y, z, t) = U_e(x, y, z)$ . Both potentials are related by a coordinate transformation where the transverse coordinates  $(x, y)$  undergo a  $90^\circ$  rotation  $R$  and the  $z$ -coordinate is shifted by the electrode distance  $L$ :  $U_e(x, y, z) = U_o(Rx, Ry, z \pm L)$ . One pair of grounded and one pair of charged electrodes make up an “elementary cell” or simply *deceleration stage*. In the present instrument there are 316 stages (the first electrode pair is usually not used to decelerate, because there the field is not well defined).

## 3.3 Longitudinal motion

In the following, the molecules will be treated as mass points upon which external forces act and for which the classical equations of motion hold. No quantum mechanical treatment is necessary because at the given velocities the external potential changes but little over the distance of a few de Broglie wavelengths.

For symmetry reasons, the transverse force components  $F_x = -\partial_x U$  and  $F_y = -\partial_y U$  vanish on axis ( $x = y = 0$ ). The  $z$ -dependence of the potential, i.e. the force component  $F_z$ , does not change much when the transverse position  $(x, y)$  is varied except for points very close to the electrodes. To analyse the longitudinal motion of a molecule through the decelerator one may therefore ignore the  $x, y$ -dependence of the longitudinal force so that  $F_z(x, y, z, t) \approx F_z(z, t)$ .

That it is possible to change the longitudinal velocity of a single molecule is easy to see. In the simplest mode of operation, a molecule with initial velocity  $v_1$  starts at some position  $z_1$  and advances exactly a distance  $L$  on the potential  $U = U_o$  to reach its final position  $z_2$ , as it is shown in **Fig. 3.1**. During its travel, the molecule is first accelerated slightly and then decelerated. The total change in kinetic energy  $\Delta T$  is equal to  $-\Delta U$ , in this case  $\Delta U > 0$  and therefore  $v_2 < v_1$ . Now the field configuration is switched to  $U = U_e$  and the

molecule travels the same distance  $L$ , again changing its kinetic energy by  $-\Delta U$  as before. Because the change in kinetic energy is quite small (on the order of a wavenumber), the process must be repeated many times to significantly change the energy of the molecule<sup>1</sup>. In this mode of operation the considered molecule has the same initial position with respect to the potential at the beginning of every time interval. We call this molecule the *synchronous molecule* because it moves synchronously with the force field. The motion of the synchronous molecule is particularly simple because the kinetic energy change  $\Delta T$  is constant in time by assumption:

$$\Delta T = \frac{m}{2}(v_2^2 - v_1^2) = \frac{m}{2}(v_2 + v_1)(v_2 - v_1) \quad (3.1)$$

$$=: m \frac{v_1 + v_2}{2} \Delta v \quad (3.2)$$

$$=: m\bar{v}\Delta v, \quad (3.3)$$

where the average  $(v_1 + v_2)/2 =: \bar{v}$  is the arithmetic mean of the velocities at the boundaries of the considered time interval. The value of  $\bar{v}$  must be approximately equal to the time average of the molecule's velocity  $\langle v \rangle$  during the time interval of duration  $\tau$  because the velocities attained during a time interval remain close to the velocities at switch time. Since  $\langle v \rangle = L/\tau \approx \bar{v}$  we obtain:

$$\begin{aligned} \Delta T &= m\bar{v}\Delta v \\ &\approx mL \frac{\Delta v}{\tau} \\ \frac{\Delta T}{mL} &\approx \frac{\Delta v}{\tau} =: a = \text{constant}. \end{aligned} \quad (3.4)$$

Of course, the parabolic trajectory  $z(t) = z_0 + v_0 t + at^2/2$  so obtained coincides with the real trajectory only at the beginning and at the end of each time interval but not in between. To describe the motion of non synchronous molecules we proceed similarly in that we ignore the exact trajectory during a time interval and focus only on the position and velocity when the field is switched.

The potential is periodic with period  $2L$  and may be written as a Fourier series. Therefore it is more convenient to map the  $z$ -position onto the angle variable  $\varphi = \pi z/L$ . What has been called above "position with respect to the potential" is also known as the *phase*. We denote this position by  $\phi$  with  $\phi = -\pi/2 \dots 3\pi/2$  as shown in the inset of **Fig. 3.1**. A molecule can locate its phase uniquely at any time by determining the current value of  $U(\varphi)$  and the value of the derivative  $U'(\varphi)$ . The only ambiguity occurs at the time when the field is switched, to remove it we define that the field is already present at the beginning of each time interval. Alternatively, we can define the phase without

---

<sup>1</sup>For instance, an OH radical moving at a speed of 400 m/s has a kinetic energy of about  $114 \text{ cm}^{-1}$ .



reference to the potential: since switching the field corresponds to shifting the position of the molecule by a distance  $+\pi$  or  $-\pi$ , we can define the phase by  $\phi = (\varphi + k\pi) \bmod 2\pi$  where  $k = 0, 1, 2, \dots$  is the index of the time intervals.

If we consider only those modes of operation for which a synchronous molecule exists, we can obtain a simple equation of motion for all other (non synchronous) molecules relative to the synchronous one because the average force acting upon the synchronous molecule is constant. The time averaged acceleration is given approximately by (3.4), therefore the force required to produce this acceleration is approximately  $-\Delta U/L$ . From now on we will refer to one of the time independent on-axis potentials  $U_{e/o}$  simply by  $U(\varphi)$  with the origin of coordinates as defined in the inset of **Fig. 3.1**. If at the start of a time interval the phase is  $\phi$  and the molecule moves a distance  $\xi$  then the force is

$$F(\phi, \xi) := -\frac{U(\phi + \xi) - U(\phi)}{\xi}. \quad (3.5)$$

The phase of the synchronous molecule at the beginning of a time interval shall be denoted exclusively by  $\phi_s$ . For the molecule to be synchronous we have to require that  $\xi = s\pi$  with  $s$  being an odd integer. For even integers  $s$  the molecule is synchronous only every second time the field is switched, moreover, no kinetic energy change results for the synchronous molecule in this case. Hence the average force upon the synchronous molecule is:

$$F(\phi_s, s\pi) = -\frac{U(\phi_s + s\pi) - U(\phi_s)}{s\pi} \quad s = 1, 3, 5, \dots \quad (3.6)$$

The phase of the synchronous molecule at switch time  $\phi_s$  is often simply referred to as the *phase angle*. For  $0^\circ < \phi_s \leq 90^\circ$  the molecules are decelerated whereas for  $-90^\circ \leq \phi_s < 0^\circ$  they are accelerated; if the phase angle is exactly zero ( $\phi_s = 0^\circ$ ), the molecules are guided through the apparatus at a constant mean velocity. The average acceleration and the potential energy change of an OH molecule in the ( $X^2\Pi_{3/2}, J = 3/2f, |M_J| = 3/2$ ) state are shown in **Fig. 3.2** as a function of the phase angle. The acceleration is calculated for  $s = 1$ . The maximum kinetic energy which can be removed or added between switch times is approximately  $1.7 \text{ cm}^{-1}$ . *All of the following examples will pertain to that same state of the OH radical.*

We now consider the start of a time interval. Let the velocity of the synchronous molecule be denoted by  $v_s$  and its position by  $\varphi_s$ ; a non synchronous molecule has at least a different position  $\varphi \neq \varphi_s$  or a different velocity  $v \neq v_s$ . We denote the relative position  $\varphi - \varphi_s$  by  $\theta$ . The non synchronous molecule travels a distance  $s\pi + \delta$  where  $\delta$  is a small correction, provided one considers only molecules with a velocity close to that of the synchronous molecule. This correction is given by  $\delta = s\pi(\langle v \rangle - \langle v_s \rangle) / \langle v_s \rangle$  where the time averages are taken over the considered time interval. For the force upon the non-synchronous

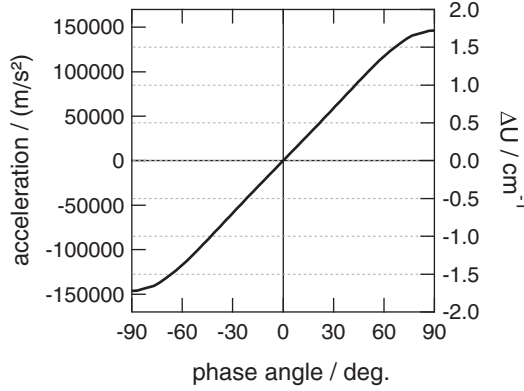


**Figure 3.2:** The acceleration and potential energy change as a function of the phase angle for an OH molecule in ( $X^2\Pi_{3/2}, J = 3/2f, |M_J| = 3/2$ ) state with  $\pm 20$  kV on the electrodes of the decelerator. The acceleration is given for  $s = 1$ ,  $L = 8.25$  mm.

molecule we hence obtain:

$$F(\phi_s + \theta, s\pi + \delta) = -\frac{U(\phi_s + \theta + s\pi + \delta) - U(\phi_s + \theta)}{s\pi + \delta}. \quad (3.7)$$

The phase of the non synchronous molecule is given by  $\phi = (\phi_s + \theta) \bmod 2\pi$  and since  $U$  has periodicity  $2\pi$  the above formula is correct. In the first approximation, one may set  $\delta = 0$  to obtain the equation of motion for the relative position:

$$\begin{aligned} m \frac{d^2\theta}{dt^2} &= F(\phi_s + \theta, s\pi) - F(\phi_s, s\pi) \\ m \frac{d^2\theta}{dt^2} &= \frac{1}{s\pi} [U(\phi_s + \theta) - U(\phi_s + \theta + s\pi) + U(\phi_s + s\pi) - U(\phi_s)]. \end{aligned} \quad (3.8)$$

This differential equation for the relative position at the time the field is switched conserves the energy, since it depends on the relative position only. Therefore the analysis of the motion becomes quite simple. Had we included the correction  $\delta$ , we would have obtained a differential equation involving the velocities as well and then the energy is no longer conserved. This way of writing the equation of motion was first used by Bethlem et al. as described in [54]. To proceed, an analytic expression for the potential is required, which can be obtained from the Fourier series:

$$U(\varphi) = \sum_{n=1}^{\infty} a_n \cos(n(\varphi + \pi/2)), \quad a_n = \frac{1}{\pi} \int_0^{2\pi} d\varphi U(\varphi) \cos(n(\varphi + \pi/2)).$$

The constant term  $a_0$  is the spatial average of the potential and may be set to zero by definition. We locate the origin at  $-\pi/2$  to conform with the definition

of the phase – although it somewhat inconvenient. The resulting series is then:

$$U(\varphi) = -a_1 \sin(\varphi) - a_2 \cos(2\varphi) + a_3 \sin(3\varphi) + a_4 \cos(4\varphi) - \dots \quad (3.9)$$

the alternation of the signs being  $-, -, +, +, -, -, +, +, \dots$ . To evaluate the force in equation (3.9) it is advisable to use the complex series

$$U(\varphi) = \sum_{-\infty}^{\infty} \frac{a_{|n|}}{2} e^{in(\varphi+\pi/2)}, \quad (3.10)$$

so that the shifts of the function arguments become phase factors and the force can be determined quite effortlessly:

$$F_{s,\phi_s}(\theta) = -\frac{1}{s\pi} \sum_{-\infty}^{\infty} \frac{a_{|n|}}{2} e^{in(\phi_s+\pi/2)} (e^{in\theta} - 1) [(-1)^{ns} - 1]. \quad (3.11)$$

From this formula we easily see that positive odd integer values of  $s$  lead to non vanishing terms only if  $n$  is odd, whereas for even integer values of  $s$  the force vanishes identically – which is not surprising in view of the periodicity of  $U$ . Finally, the force for odd integers of  $s$  is obtained from the previous equation:

$$F_{s,\phi_s}(\theta) = -\frac{1}{s\pi} \sum_{n=1,3,5,\dots} i^{n+1} a_n \left( \sin(n[\phi_s + \theta]) - \sin(n\phi_s) \right). \quad (3.12)$$

The potential function  $V$  of this force is obtained via integration:

$$\begin{aligned} V_{s,\phi_s}(\theta) &= \frac{1}{s\pi} \sum_{n=1,3,5,\dots} i^{n+1} a_n \left( \frac{1}{n} \cos(n[\phi_s + \theta]) + \sin(n\phi_s) \theta \right) \\ &\approx -\frac{1}{s\pi} a_1 (\cos(\phi_s + \theta) + \sin(\phi_s) \theta) \end{aligned} \quad (3.13)$$

where in the last equation only the  $n = 1$  term has been kept. For the electrode geometry used in this work, and for an OH radical in the ( $X^2\Pi_{3/2}, J = 3/2f, |M_J| = 3/2$ ) state, the coefficients in units of  $\text{cm}^{-1}$  are:

$$a_1 = 0.8872 \quad a_2 = 0.2308 \quad a_3 = 0.0814 \quad a_4 = 0.0341 \quad a_5 = 0.0173,$$

if  $\pm 20 \text{ kV}$  are applied to the electrodes. These coefficients are determined numerically from the potential  $U(x, y, z)$  which in turn is also determined by numerical methods.

To gain further insight about the relative motion, one need not bother to solve the equation of motion numerically for the given force. The possible trajectories in the phase space spanned by  $v := \dot{\theta}L/\pi$  and  $\theta$  are already determined completely through energy conservation. The implicit function for the trajectories is thus:

$$\frac{m}{2} v^2 + V_{s,\phi_s}(\theta) = E(\theta', v') \quad (3.14)$$

where any phase space point  $(\theta', v')$  suffices to define the traversed curve in phase space uniquely. For an OH molecule in the low field seeking  $|M_J| = 3/2$  state, the possible phase space trajectories for  $s = 1$  and  $\phi_s = 0^\circ, 25^\circ$  are shown in **Fig. 3.3**. All bound trajectories around the synchronous molecule are enclosed by the so called *separatrix*. Therefore, only those molecules with initial relative positions and velocities inside the separatrix are trapped in the potential  $V_{s,\phi_s}(\theta)$  during the passage through the apparatus and undergo stable oscillations in this potential. One says that the decelerator exhibits *phase stability* since the phase at switch time of all trapped molecules never exceeds a certain value which is determined by the phase angle  $\phi_s$ . The area inside the separatrix is an important quantity – the longitudinal *phase space acceptance*.

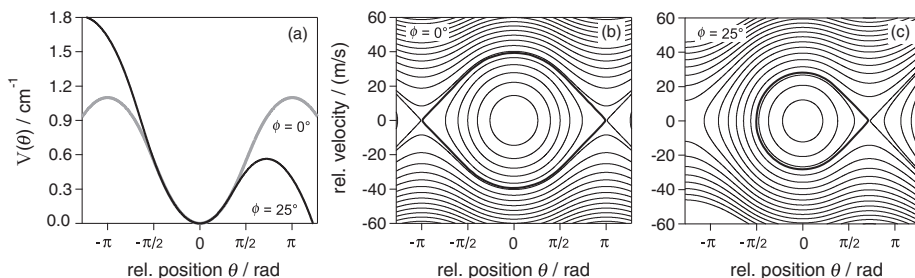


**Figure 3.3:** The potential energy  $V(\theta)_{s,\phi_s}$  in units of  $\text{cm}^{-1}$  of the relative motion for the parameters  $s = 1, \phi_s = 0^\circ, 25^\circ$  (panel a) and the corresponding contours of constant energy (panel b, c) according to equation (3.14). A molecule oscillates around the synchronous molecule only if its initial relative position and velocity lies inside the so called *separatrix*.

For reasons to be explained in the following section, the most useful mode of operation for our purposes is actually the mode where  $s = 3$  instead of  $s = 1$ . In the  $s = 3$  mode, the longitudinal force component is three times weaker and accordingly the longitudinal phase space acceptance is reduced. Since the maximal kinetic energy is a factor of 3 smaller, the maximal velocity is a factor of  $\sqrt{3}$  smaller and so is the longitudinal phase space acceptance. A detailed analysis of the  $s = 3$  mode was first given by van de Meerakker et al. [55].

In **Fig. 3.4** the separatrices for different values of the phase angle are shown for the  $s = 3$  mode. Also shown is the longitudinal oscillation period for the contours of constant energy when the decelerator is operated in the guiding ( $\phi_s = 0^\circ$ ) mode. For example, a molecule with an initial relative position of  $\pm\pi/2$  and zero initial relative velocity traverses the highlighted contour. The period of oscillation is plotted as function of the maximum potential energy, in this case the period is  $\approx 1.5$  ms. The decelerator used in this work has a total length of 2.6 m, if the molecules are guided at e.g. 400 m/s, then the time of flight is 6.5 ms and the molecule traverses the contour 4.3 times.

While the  $s = 1$  and  $s = 3$  mode are the ones usually used in experiments, one might wonder how many possible other modes of operation actually exist.

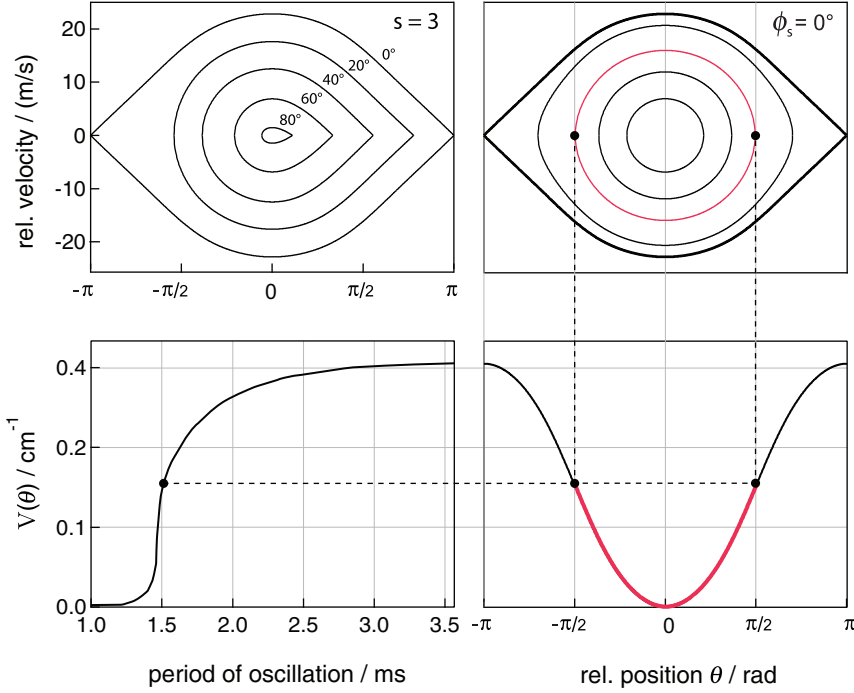


**Figure 3.4:** Top left: separatrixes for different values of the phase angle for  $s = 3$ . Top right: contours of constant energy for  $\phi_s = 0^\circ$ ,  $s = 3$ . Bottom: potential energy  $V(\theta)$  for  $\phi_s = 0^\circ$ ,  $s = 3$  and the corresponding period of oscillation as a function of the potential energy at the turning point (zero relative velocity). For the indicated contour, the period is  $\approx 1.5$  ms.

The above considered scheme where a molecule is synchronous every time the field is switched can be generalised further. If the molecule travels a number of  $Q$  possibly distinct distances  $s_k\pi$  with  $k = 1 \dots Q$  between switch times, then the phase is the same after  $Q$  switch times provided:

$$\left( \sum_{k=1}^Q s_k\pi + Q\pi + \phi_s \right) \bmod 2\pi = \phi_s \quad (3.15)$$

where now  $\phi_s$  is the phase after  $Q$  switch times and  $s_k$  is a positive real number. This condition is equivalent to:

$$\sum_{k=1}^Q s_k + Q = 2n, \quad n = 0, 1, 2, \dots \quad (3.16)$$

As before one may calculate an average force upon the molecule by summing the  $\Delta U$ 's for one cycle  $k = 1, \dots, Q$  which is then divided by the distance

traveled. To give a very simple example, instead of using  $s = 1$ , we could also use  $s_1 = 0.8, s_2 = 1.2$ . In this case  $Q = 2$  and the phase is the same every second time the field is switched. Note that for this example, the average transverse force is asymmetric for the  $x$  and  $y$  directions.

Cycles for which  $s_k$  is always a constant rational number have been analysed first by van de Meerakker et al. [55] and later by Gubbels et al. [56]. The latter Ref. is especially remarkable because the authors do not only use a Fourier analysis of the field's spatial dependence, as is done here, they also use the Fourier analysis of its *time* dependence.

### 3.4 Transverse motion

The components of the force in the transverse direction are given by the derivatives  $F_{x(y)} = -\partial_{x(y)}U(x, y, z, t)$ , but they are time dependent. As in the previous section, it would be convenient if the explicit time dependence could be eliminated. Under the usual operation conditions, all molecules fly approximately a distance  $\Delta z = sL$ , that is  $\Delta\varphi = s\pi$ , within every time interval. Therefore one can determine an approximate average transverse force for the considered interval and use only this force to analyse the molecule motion. During a time interval  $\tau$ , the molecules move transversally from  $(x_0, y_0)$  to  $(x_0 + \delta_x, y_0 + \delta_y)$ . If the longitudinal velocity is high enough, the change  $(\delta_x, \delta_y)$  is small and we may compute the spatially averaged force components by:

$$\bar{F}_y(x, y, \phi) := \frac{1}{s\pi} \int_{\phi}^{\phi+s\pi} d\varphi F_y(x, y, \varphi), \quad (3.17)$$

with the phase  $\phi$  of the molecule at the start of the considered time interval. This approximation, which was first used by Bethlem et al. [57], works better than it may seem at first sight because one can think of the average as being computed for the intermediate point  $(x, y) = (x_0 + \delta_x/2, y_0 + \delta_y/2)$  which is the approximate position at  $\tau/2$ . Denote the potential from which the force is derived by  $U(x, y, \varphi)$ , then

$$\bar{F}_y(x, y, \phi) = -\frac{1}{s\pi} \partial_y \int_{\phi}^{\phi+s\pi} d\varphi U(x, y, \varphi) \quad (3.18)$$

$$=: -\partial_y \langle U \rangle. \quad (3.19)$$

The averaged force is the same every second time interval because the electrode orientation alternates between horizontal and vertical. Therefore we have to use two averaged potentials  $\langle U \rangle^{(1)}$  and  $\langle U \rangle^{(2)}$  for the odd and even numbered time intervals. Both are related by a  $90^\circ$  rotation  $R$  of the coordinates:  $\langle U(x, y, \phi) \rangle^{(1)} = \langle U(Rx, Ry, \phi) \rangle^{(2)}$ . For sufficiently high longitudinal velocities, we may even take the average over both potentials  $\langle U \rangle := (\langle U \rangle^{(1)} + \langle U \rangle^{(2)})/2$ .

This potential is still time dependent for all non synchronous molecules through the phase  $\phi$ .

In **Fig. 3.5**, the contours of the potential  $\langle U \rangle$  are shown for  $s = 1$  and  $s = 3$ . The average potential for  $s = 1$  varies strongly with  $\phi$ . Therefore, a molecule which oscillates longitudinally around the synchronous molecule with a large amplitude is subjected to large variations of the transverse force. Moreover, if the phase of the synchronous molecule  $\phi_s$  is close to zero, the transverse force along the  $x$  or the  $y$  axis is very small during the time when the molecule's relative position  $\theta$  lies within the interval  $-0.25\pi \dots + 0.25\pi$ , and therefore molecules will “leak out” along the  $x$  and  $y$ -axis. For higher absolute values ( $|\phi_s| > 45^\circ$ ) of the phase angle, that is for large accelerations, these escape channels of the potential start to close and the transverse confinement improves – at the cost of the longitudinal confinement.

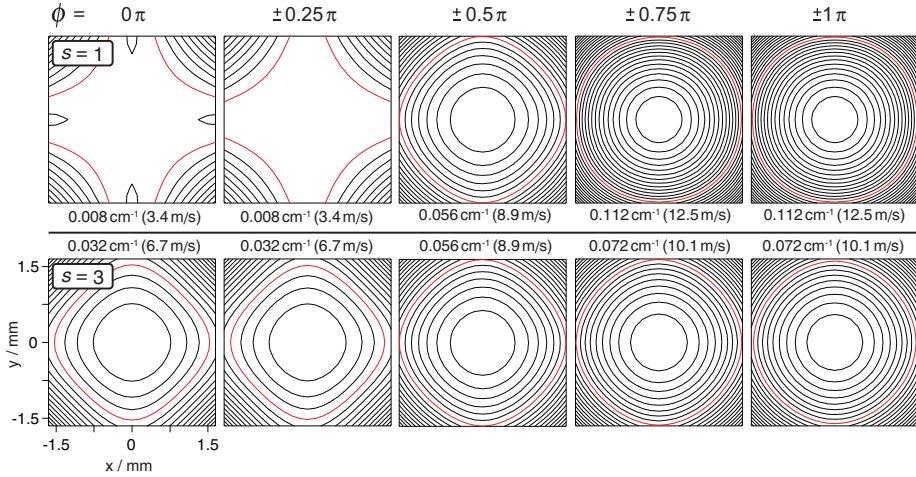


**Figure 3.5:** The transverse potential  $\langle U \rangle$  for  $s = 1$  and  $s = 3$  averaged over two successive time intervals and for a given value of the phase  $\phi$ . The potential has the value  $0 \text{ cm}^{-1}$  at  $x = y = 0 \text{ mm}$ , the contour lines indicate steps of  $0.008 \text{ cm}^{-1}$ . The red contours correspond to the given values for the potential energy (and transverse velocity). The orientation of the coordinate system is the same as given in Fig. 3.1.

For the  $s = 3$  mode, the potential  $\langle U \rangle$  is closed for any relative position, because, for all values of  $\phi$ , the averaging includes twice the full distance  $2\pi$  which corresponds to  $\langle U \rangle_{s=2}$  and which is independent of  $\phi$ . Therefore, the potentials shown for  $s = 3$  are in fact equal to  $\frac{1}{3} \langle U(\phi) \rangle_{s=1} + \frac{2}{3} \langle U \rangle_{s=2}$ . Also,  $\langle U \rangle_{s=2} = \langle U(\pi/2) \rangle_{s=1} = \langle U(\pi/2) \rangle_{s=3}$  is valid for reasons of symmetry.

At  $\phi = 0$ , the potential is deep enough to confine molecules with transverse velocities of at least  $\approx 6.7 \text{ m/s}$ . The depth of the potential increases with increasing relative position, but the change is now much more modest as compared to the  $s = 1$  mode – for sufficiently high longitudinal velocities, the transverse

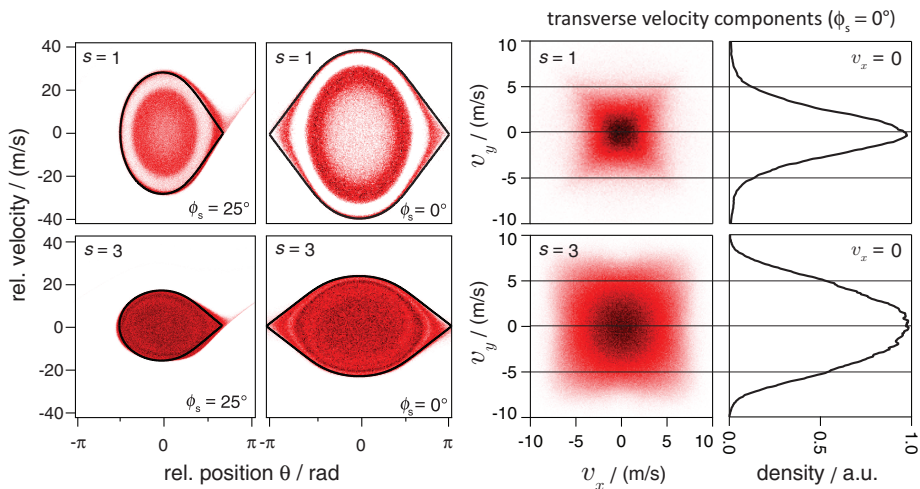


**Figure 3.6:** Projections of the phase space density distributions after a guiding or deceleration sequence for  $s = 1$  and  $s = 3$  as determined from numerical trajectory calculations. The initial mean forward velocity is 350 m/s in all cases, the final mean velocity for  $\phi_s = 25^\circ$  is 190 m/s. The separatrix as determined from the one dimensional model is shown as a black solid curve.

motion is therefore approximately independent of the longitudinal motion and may be treated separately.

The functional form of the potential is a sum of a two dimensional harmonic potential and a part which has reduced (4-fold) rotational symmetry. It is approximated quite well by the simple formula:

$$\langle U(x, y, \phi) \rangle = c_2(x^2 + y^2) + c_4x^2y^2, \quad (3.20)$$

where  $c_2$  and  $c_4$  depend on  $s$  and  $\phi$ . For  $s = 1$ , the potential becomes more and more harmonic as  $\phi$  increases, whereas for values close to zero the harmonic part disappears almost completely. The potential does not conserve the angular momentum and therefore it is not easy to analyse the motion analytically.

The model which has been discussed so far can be tested with the help of numerical trajectory calculations. In **Fig. 3.6**, different projections of the resulting phase space distribution are shown for both modes of operation and for two different values of the phase angle. In all cases, the initial mean velocity in the  $z$ -direction is 350 m/s; the mean final velocities are 350 m/s ( $\phi_s = 0^\circ$ ) and 190 m/s ( $\phi_s = 25^\circ$ ). The number of electrode pairs in the  $\phi_s = 0^\circ$  case is 301, i.e. we use 300 deceleration stages. For the case  $\phi_s = 25^\circ$  case 300 stages are used for  $s = 3$  and 100 stages for  $s = 1$  to obtain the same final velocities. For all simulations, the initial position and velocity components of a molecule are chosen at random from within a 6 dimensional “box” with  $a_x < x < b_x, a_{v_x} < v_x < b_{v_x}$  and so on. This box must be chosen large enough



so that it completely contains the 6 dimensional phase space volume from which molecules are accepted, that is from which stable trajectories result.

We find that the separatrices which are determined from the simple model fit quite well to the observed boundaries. For the  $s = 1$  mode, one can clearly make out two separate areas for which the *transverse* motion is not stable. The central area which represents molecules with small longitudinal oscillation amplitudes is unstable because the transverse potential hardly confines molecules which move close to and along the  $x$  and  $y$ -axis, as discussed above. Obviously this leaking out cannot be immediate and therefore the area is somewhat diffuse. The second unstable phase space area closer to the separatrix arises from the oscillation of the potential with time as the molecules traverse along their longitudinal contour of constant energy. This kind of instability can be analysed with well known and simple methods, provided the non-harmonic terms of the potential are neglected. An analysis of this kind has been given by van de Meerakker et al. in Ref. [58]. Both instabilities are almost absent<sup>2</sup> in the  $s = 3$  mode, because the time variation is smaller and the potential provides much better transverse confinement for all relative positions. The projections onto the  $v_x, v_y$ -plane show that the transverse velocity acceptance at small phase angles is larger for  $s = 3$ . Under which conditions which mode is preferable is described in detail in chapter 5.

As the mean forward velocity of the molecules becomes smaller and smaller, one might expect that the approximation of an average potential should become less and less suitable – in particular for the  $s = 3$  mode where the averaging is over a large distance of  $6L$ . Below a certain velocity, one should therefore consider the transverse potential as alternating between the two states  $\langle U \rangle^{(1)}$  and  $\langle U \rangle^{(2)}$ . The potentials  $\langle U \rangle_{s=1}^{(1)}$  and  $\langle U \rangle_{s=3}^{(1)}$  are shown in **Fig. 3.7** for two values of the phase ( $0^\circ$  and  $180^\circ$ ). The contour lines given in red color indicate values  $\leq 0$  whereas the black contours indicate positive values. For  $\phi \approx 0$  and  $s = 1$ , the defocusing force (i.e. away from the central axis) is about as large as the focusing force (i.e. toward the central axis). The maximum focusing and minimum defocusing force is found for  $180^\circ$ . In the case of  $s = 3$  the focusing force is always larger than the defocusing force.

We see that focusing and defocusing forces are present in successive time intervals. One might imagine that especially in the case of  $s = 3$ , a slow molecule may get lost e.g. in the  $x$ -direction during the time interval in which there is a defocusing force in this direction. Furthermore, it is possible that even before this can happen, the alternation of direction and magnitude of the transverse forces can cause an (unlimited) increase of the transverse oscillation amplitude over time.

---

<sup>2</sup>A very thin unstable band close to the separatrix can be found.

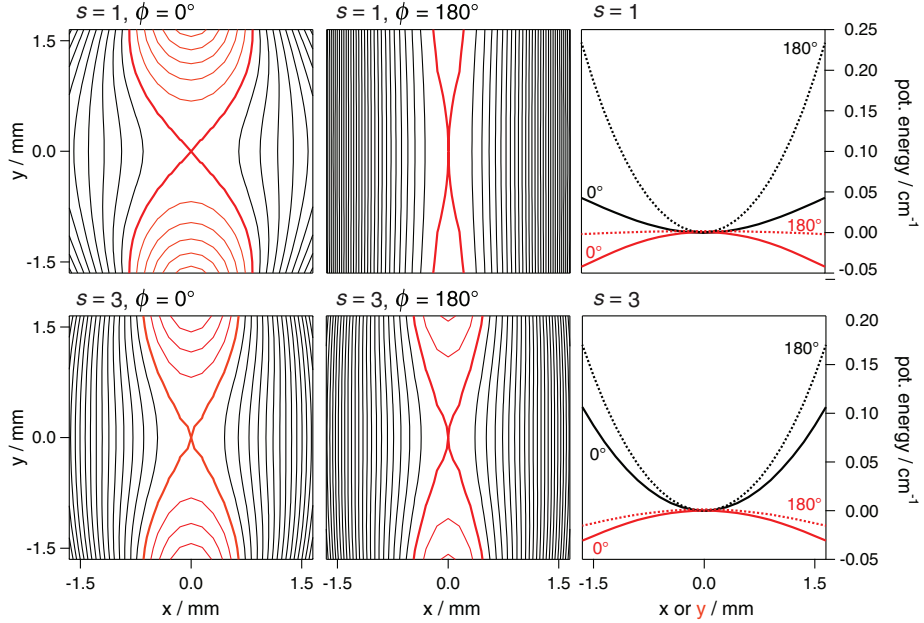


**Figure 3.7:** Contour plots of the transverse potential averaged over a distance  $s\pi$  for  $\phi = 0^\circ$  and  $180^\circ$ . The red contour lines indicate values  $\leq 0$ , the black contours positive values. The potential difference between two contours is  $0.008 \text{ cm}^{-1}$ , cuts through the potentials are shown on the right hand side for  $x = 0$  and  $y = 0$  where the dashed lines belong to  $\phi = 180^\circ$  and the solid lines to  $\phi = 0^\circ$ . Cuts for  $x = 0$  are indicated by the red curves, those for  $y = 0$  by the black curves.

If the non-harmonic part is neglected, the potentials are:

$$\langle U(x, y, \phi) \rangle^{(1)} = a(\phi)x^2 + b(\phi)y^2 \quad (3.21)$$

$$\langle U(x, y, \phi) \rangle^{(2)} = b(\phi)x^2 + a(\phi)y^2 \quad (3.22)$$

for the potentials in two successive time intervals. The equation of motion for the  $y$ -direction is then

$$m\ddot{y} = f(t)y \quad (3.23)$$

with either  $f(t) = -a/2$  or  $f(t) = -b/2$ , depending on the time interval considered.

One can now start to tackle the problem with increasing degree of difficulty. The simplest case is the one where the phase  $\phi$  is approximately constant (small longitudinal oscillation amplitude) and where the absolute change of the forward velocity over time is small. In this case the time intervals have constant duration  $\tau = sL/v_z$  and the function  $f(t)$  is periodic in time with period  $2\tau$ . If the phase is not constant, but the velocity  $v_z$  is, then  $f(t)$  is also approximately periodic but the period is now the period of the longitudinal oscillation. In both cases

(periodic  $f$ ) the differential equation is known as *Hill's differential equation*<sup>3</sup>. Techniques to solve the problem are well known and described in detail e.g. in Refs. [59, 60].

The method uses a  $(2 \times 2)$  *transfer matrix* to propagate the initial phase space point  $\mathbf{u}(0) := (y(0), v_y(0))$  in time steps of  $2\tau$  by taking powers of this matrix. To obtain the matrix one has to solve the differential equations for the individual time intervals (in this case 2) which make up the whole period of  $f$ . If the matrix for the first period is  $\mathbf{M}_1$  and for the second  $\mathbf{M}_2$  then the transfer matrix is  $\mathbf{M} = \mathbf{M}_2\mathbf{M}_1$ . To propagate the point  $\mathbf{u}(0)$  in time steps of  $2\tau$  we use powers of  $\mathbf{M}$ :  $\mathbf{u}(n2\tau) = \mathbf{M}^n\mathbf{u}(0)$ . To see whether the motion is bound or not, one diagonalizes the matrix so that powers of  $\mathbf{M}$  become powers of the eigenvalues. The motion can be bound only if the eigenvalues are complex (conjugate) numbers of unit modulus (the case where the eigenvalues are real and both smaller than unity does not occur). One can show that this requirement is equivalent to the condition that  $|tr(\mathbf{M})| < 2$  because the eigenvalues  $\lambda_{1/2}$  are determined by:

$$\lambda_{1/2} = \frac{tr(\mathbf{M})}{2} \pm \sqrt{\frac{tr(\mathbf{M})^2}{4} - |\mathbf{M}|} \quad (3.24)$$

which follows from the requirement that  $|\mathbf{M} - \lambda\mathbf{I}| = 0$ . For the determinant  $|\mathbf{M}| = 1$  always holds, which can be shown directly from the differential equation, but it is actually Liouville's theorem for the motion in one dimension. For the case considered, the differential equations for both time intervals are

$$\ddot{y} = \alpha^2 y, \quad \alpha > 0 \quad (3.25)$$

$$\ddot{y} = -\beta^2 y, \quad \beta > 0 \quad (3.26)$$

where  $\alpha$  and  $\beta$  depend on the phase  $\phi$ . After solving these equations, one finds that the trace is given by:

$$tr(\mathbf{M}) = 2 \cosh(\beta\tau) \cos(\alpha\tau) + \left(\frac{\beta}{\alpha} - \frac{\alpha}{\beta}\right) \sinh(\alpha\tau) \sin(\alpha\tau) \quad (3.27)$$

where  $\tau = sL/v_z$ . For  $\phi = 0$  and  $s = 3$  one finds that  $|tr(\mathbf{M})| < 2$  as long as  $v_z > 103$  m/s. From computer simulations and also from the experiment we find that instabilities start to manifest for velocities below 150 m/s and that almost no molecules can pass the decelerator for velocities below 100 m/s. To efficiently decelerate OH molecules below 150 m/s, it is better to switch the mode of operation to  $s = 1$  somewhere before the critical velocity is reached. More details can be found in chapter 5.

The various transverse instabilities can be circumvented only, if the transverse potential well is approximately constant in time. Such a decelerator has

---

<sup>3</sup>George William Hill, *Acta Mathematica*, **8**, 1-36 (1886), *On the part of the motion of the lunar perigee which is a function of the mean motions of the sun and moon*

been demonstrated already by Osterwalder, Meek and co workers [9]. Their decelerator provides a true 3-dimensional trapping potential which propagates along the beam axis and which can be used to slow down a packet of molecules. This new principle might turn out to become the deceleration method of choice in the near future.

### 3.5 Other loss mechanisms

The so far mentioned mechanisms which lead to a loss of particles during deceleration can be described by classical mechanics alone, provided the potentials are known. These effects are however not the only ones we have to worry about, there are three more possibilities to lose molecules.

Probably the most obvious loss mechanism are collisions with the background gas. Whether a molecule is really lost or not after a collision depends on the details. If the collision is elastic, i.e. if the internal state remains the same, the scattering angle and the depth of the transverse trapping potential determine whether a molecule is lost. Inelastic collisions to states with a different Stark effect, in particular to high field seeking states, also lead to losses. Collisions which change only the projection quantum number(s), are particularly important since the cross sections for such collisions can be large (see for example Paterson et al. [61] for the case OH/Xe). In-beam collisions, that is collisions among molecules which are being decelerated, are of course also possible. Hogan et al. have considered this problem in some detail in Ref. [4] and they find the effect to be irrelevant for most practical purposes.

The second important process which can cause a change of the internal quantum state is optical pumping by black body radiation. This type of loss mechanism has been studied in detail for OH radicals trapped in an electrostatic trap by Hoekstra et al. in 2007 [16]. On the time scale of a deceleration/acceleration sequence, this loss mechanism is unimportant for OH, but one should still be aware of its presence, especially if one is interested in obtaining a very pure ensemble of molecules for state-to-state scattering experiments.

The third mechanism which can lead to a loss of molecules is somewhat more intrinsic and fundamental. One usually calculates the energies of the molecule as a function of a given static field strength. To apply this calculation to the Stark deceleration process, one needs another assumption: adiabaticity. Hence we assume that the state changes continuously and that the system remains in a single *instantaneous* eigenstate of the Hamiltonian at any time. But the Stark effect changes with the projection quantum number  $M$  of the total angular momentum on the external quantization axis and as the field strength approaches zero, these states are particularly sensitive to a rotation of the field (by definition of the angular momentum states). In fact, the smaller the energy difference is between states of different  $M$  for a given field strength, the more difficult it is to rotate the field adiabatically. If the change of the external field magnitude or

direction is too fast, a low field seeking state can acquire components of other, possibly high field seeking, instantaneous eigenstates. During a deceleration sequence, a molecule experiences a time varying field simply because it travels through a field which is inhomogeneous – but usually this causes no problems. More important is the abrupt change when the decelerator switches: now the field vectors rotate and change their magnitude as a function of time while the molecules barely move forward. During this time, the field strength is reduced and states with a different Stark effect can get rather close in energy. It is then necessary to use time dependent perturbation theory to determine whether the considered state can acquire amplitudes of other instantaneous states of different energy by extracting quanta from the field. Such nonadiabatic transitions during deceleration have been observed and quantified by Tarbutt et al. in 2010 [62] for a conventional decelerator and for the molecule LiH. Meek et al. [63] have also thoroughly studied such effects in 2011 for a microchip based decelerator and the molecules  $^{12}\text{CO}$  and  $^{13}\text{CO}$ . Nonadiabatic transitions of electrostatically trapped ammonia molecules were studied by Kirste et al. in 2009 [64].

For a conventional decelerator, a bias field can be used to ensure that the field strength does not drop below a critical level. However, it depends on the molecule whether this is necessary. For OH in the considered state, nonadiabatic effects have not yet been noticed during normal operation in the decelerators hitherto used and no bias voltage is necessary. The absence of these effects calls for provoking them actively. This can be done in several ways. One possibility is to introduce a gap in the switching sequence which normally is not there, for example one may switch off the horizontal electrodes at the regular time and switch on the vertical ones only after a certain delay. In **Fig. 3.8** the result of such an experiment is shown. Here the molecules have been guided at constant velocity for 2/3 of the whole sequence, and then a single delay of 1, 2, 3... microseconds is introduced. It is seen that the measured OH signal drops to about 75% and stays approximately constant after that. If one tries to reproduce this

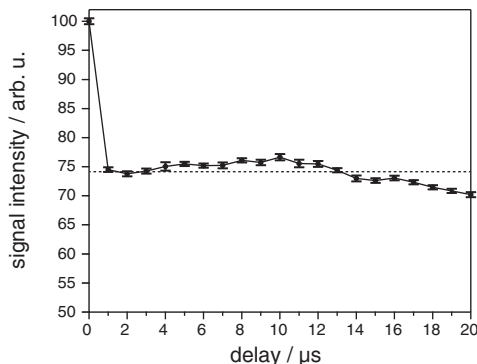


**Figure 3.8:** The signal for guided OH as a function of the delay time.

result with numerical trajectory calculations, one gets very good agreement by assuming that molecules with  $|M_J| = 3/2$  and those with  $|M_J| = 1/2$  (because a mixture is present) redistribute among both states homogeneously during the delay. These states are degenerate as long as the hyperfine structure is ignored. Yet, if we assume that the hyperfine splitting can prevent transitions between the hyperfine states of the upper  $\Lambda$ -doublet component, we obtain a drop to  $\approx 88\%$ .

From hyperfine resolved experiments one knows that it is possible to prepare an ensemble which is exclusively in the  $F = 2$  state, provided high phase angles are used (see sect. 2.2.2 and the remarks on p. 23). Therefore the nonadiabatic transitions observed here probably occur during the rapid switching on of the field – from almost zero to a high voltage – at the end of the delay.

## Chapter 4

# Construction of the Stark decelerator

During the operation of a Stark decelerator, strong electric fields have to be switched on and off at a rapid pace. With the advent of transistor based high voltage switches, the switching itself has become less problematic and is nowadays straightforward to implement – provided a few tricks of the trade are known. It is more demanding to design and manufacture the electrode arrays, because several hundred electrodes are usually required. In this chapter, the construction of the used apparatus is layed out in some detail and on several occasions a few pertinent but more general remarks are given.

## 4.1 Description of the mechanical parts

A multi-stage Stark decelerator for low field seeking molecules consists of a periodic array of high voltage (HV) electrode pairs. The electrodes need to be securely suspended and precisely aligned inside a vacuum chamber that is capable to support a vacuum of about  $10^{-8}$  mbar. Furthermore, all components which are on high voltage during operation need to be well insulated from the surrounding ground potential.

The main parts of the apparatus are shown in **Fig. 4.1**. In the present instrument the total number of electrodes is 634. The cylindrical electrodes are made of stainless steel with a diameter of 4.5 mm and are capped by a half-sphere. The vacuum gap between the electrodes of a pair is 3 mm wide, the gap between neighboring pairs is 3.75 mm (see **Fig. 4.1**). The total length from the centerline of the first electrode to the last electrode is  $316 \times 8.25 \text{ mm} = 2607 \text{ mm}$ . To construct the machine as a single unit is unfeasible and therefore it is split into three independent modules – in this way the handling of the apparatus during construction becomes much easier; the modules can be subjected to independent high voltage conditioning and testing prior to their final installation.

### 4.1.1 Design of the modules

It has been found empirically that suitable HV electrode materials are stainless steel, molybdenum, tantalum and titanium [65]. In the present instrument all parts which are on HV during operation are made of stainless steel. Each of the four arrays of electrodes is held in place by a cylindrical mounting rod with a diameter of 25 mm; every electrode is securely fixed to this rod by two screws. The mounting rods are suspended by a support-frame and electrically insulated therefrom by ceramic cylinders ( $\text{Al}_2\text{O}_3$ , alumina) which are clamped by doughnut shaped holders (see also **Fig. 4.2**). It is documented in the HV-engineering literature, and also tested experimentally in our lab, that the risk of surface flashovers across the ceramics is reduced if the so called *triple joint*<sup>1</sup> is slightly recessed in this way. The length of the insulators required to securely hold a certain voltage difference cannot be calculated, but a rule of thumb dictates a distance of 1 cm for every 5 kilovolts. Under favorable conditions, it is possible that a much smaller distance suffices, but this distance can only be determined through experiment. In the present setup, the insulators can securely hold voltages well above the required  $\pm 20 \text{ kV}$ . The support-frame consists of two parallel discs (294 mm in diameter) which are held together by four hardened steel rods of absolutely accurate straightness. Onto these discs, the clamps, which hold the insulators, are mounted.

The first and last four electrodes in each array are made from a single slab of stainless steel with the help of a CNC milling machine. The electrodes merge

---

<sup>1</sup>The “triple joint” is the point where metal, ceramic and vacuum meet. For details see e.g. [65].



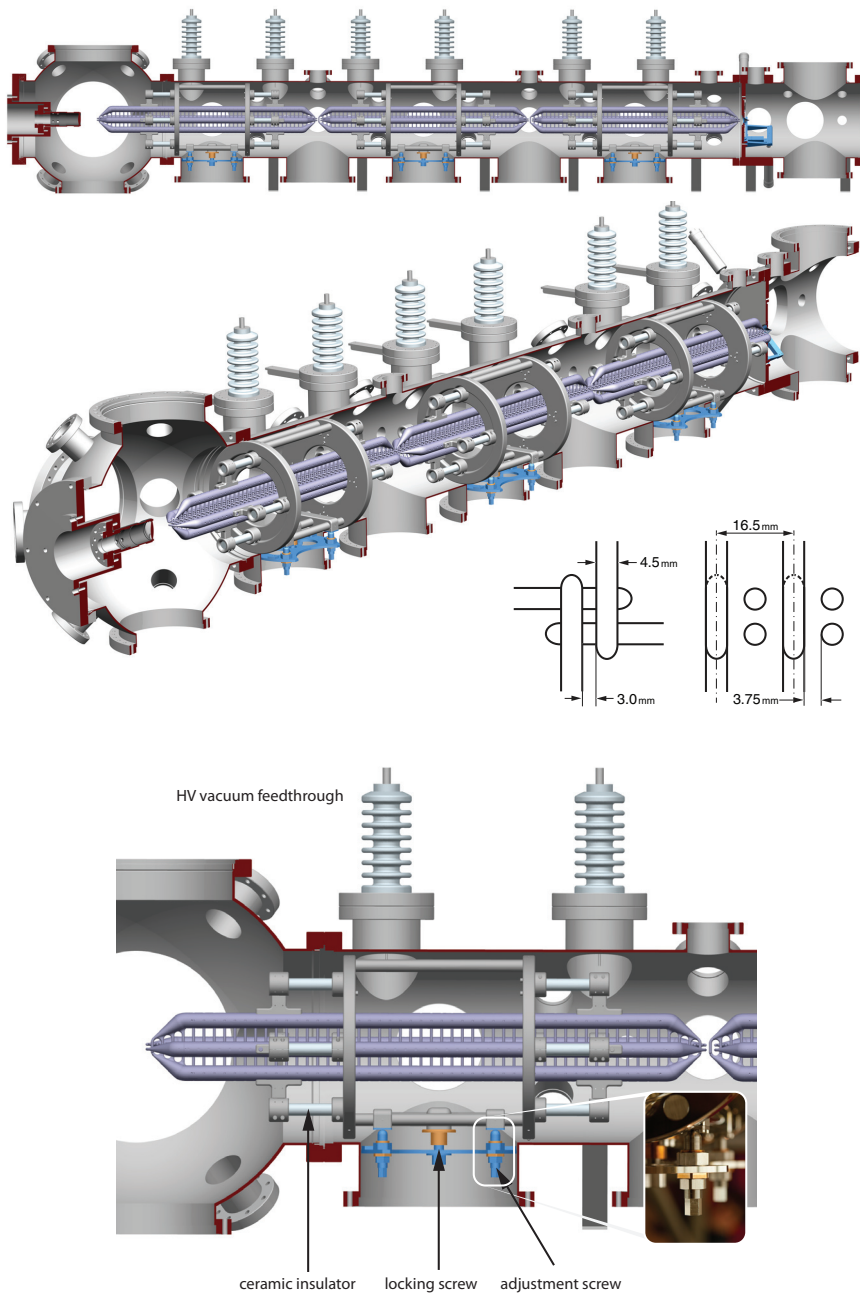


**Figure 4.1:** Schematic views of the Stark deceleration machine and its electrode dimensions. The molecular beam pulses propagate from the source chamber on the right hand side to the (spherical) experiment-chamber on the left hand side.

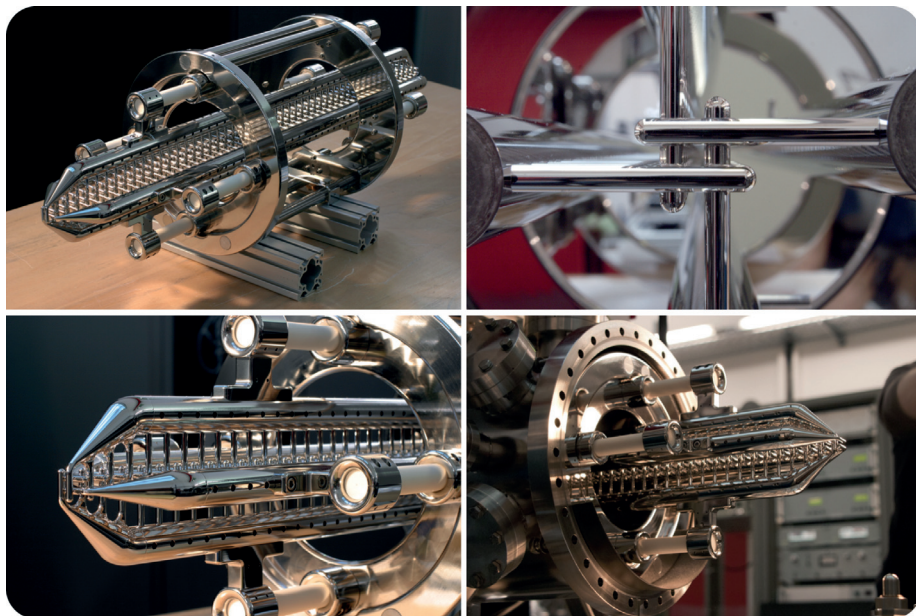


**Figure 4.2:** Photos of a single decelerator module.

seamlessly with the tapered support rod. The reason for implementing such intricate electrode arrangements is twofold. First, the coupling of the decelerator to the molecular beam source is improved because the distance to the skimmer exit can be reduced, and also the coupling of the decelerator exit to a secondary beam for crossed beam scattering is facilitated. The second benefit is that the optical access in between two modules becomes more efficient, which is important if it is desired to detect molecules after the first or the second module (see Fig. 5.1 on p. 62).

#### 4.1.2 Alignment

To achieve a precise alignment of all electrodes within a single module, a specially designed scaffold is used which first defines the correct position of the mounting rods (to which the electrodes are attached) with respect to the frame. The connecting elements between the rods and the frame (T-piece, first clamp, insulator, second clamp) are then fixed using conventional screws. After removing the scaffold, some relaxation can occur and the width of the gap between opposite electrodes often needs some re-adjustment. Through tiny rotations of the clamp on the insulator, a fairly precise adjustment of this gap is possible and an accuracy of  $\pm 0.05$  mm may be readily achieved.

The support-frame rests on four fine thread screws. These screws are screwed

into a support that is made of brass. The use of (soft) brass together with (hard) stainless steel makes lubricants superfluous. With the help of these screws, the whole module can be tilted and adjusted such that the molecular beam propagation axis coincides with the central axis defined by the HV-electrodes. A *theodolite* is used to accurately define the central beam propagation axis with respect to the vacuum chamber. After the alignment, the module is locked in place by a centrally positioned locking screw (see **Fig. 4.1**).

### 4.1.3 Surface preparation

It is well known that the maximum voltage difference supported by a vacuum gap depends quite strongly on the surface quality, i.e. on its smoothness. Therefore all parts which need to support strong electric fields are to be polished to some extent. The polishing quality which is necessary depends on the electric field strength that is locally present during operation.

In the present instrument, the electrodes are highly polished by mechanical means<sup>2</sup> to a final sub-micron “mirror finish”. Prior to its installation, each electrode is inspected under a microscope and here it is a matter of experience to be able to judge by eye if the surface is sufficiently smooth. Before an electrode is mounted, it is cleaned by thoroughly wiping it with an iso-propanol soaked cloth. All other parts are cleaned in several steps before installation. All inner threads are first freed of any remaining metal particles and grease using plenty of iso-propanol and a bottle brush or a pipe cleaner. Subsequently, the parts are immersed in the same solvent and put into the ultrasonic bath, preferably at slightly elevated temperature. If the solvent becomes markedly dirty, one more cleaning step with fresh solvent is advisable.

The ceramic insulators require special attention. It is important to keep them as clean as possible since any material deposited on the surface promotes surface flashovers. In that respect metallic abrasions are particularly problematic.

## 4.2 The maximum field strength at the surface

Discharges become more likely with increasing electric field strength at the surface. It is therefore important to determine the field between two parallel cylindrical electrodes with given radius as a function of position between the

---

<sup>2</sup>It has been reported by other researchers that additional electro-polishing further improves the surface quality. For the present instrument, the mechanical polishing was largely sufficient. In fact, during a HV-test a single pair of electrodes could be subjected to a voltage of  $\pm 30$  kV across a distance of 1 mm.

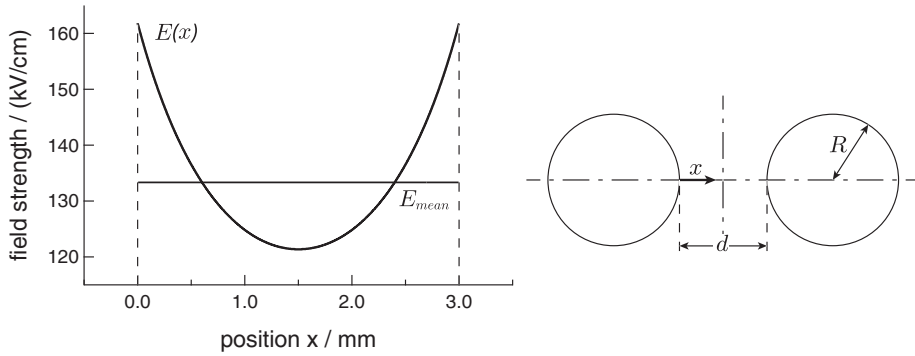


**Figure 4.3:** Electric field strength  $E$  for parallel charged cylinders as a function of position  $x$  for  $U = 40$  kV,  $R = 2.25$  mm and  $d = 3$  mm. The mean electric field is 133 kV/cm as indicated by the horizontal line.

electrodes. As described in Ref. [66] the sought function is:

$$E(x) = \frac{U}{d} \frac{\sqrt{\left(\frac{d}{2R}\right)^2 + \left(\frac{d}{R}\right)}}{\left[1 + \frac{x}{R} - \frac{x^2}{Rd}\right] \ln\left(1 + \frac{d}{2R} + \sqrt{\left(\frac{d}{2R}\right)^2 + \left(\frac{d}{R}\right)}\right)}, \quad (4.1)$$

where  $R$  is the radius of the electrodes and  $d$  is their separation. The position  $x$  is equal to the distance from the surface of the left electrode as defined in **Fig. 4.3**. The mean value of the electric field strength is given by  $E_{mean} = |U|/d$  where  $U$  is the potential difference between both electrode surfaces. In **Fig. 4.3** the function  $E(x)$  is plotted for the present case with  $U = 40$  kV,  $R = 2.25$  mm and  $d = 3$  mm; the mean field strength of 133 kV/cm is indicated by the horizontal line. The maximum field strength at the surface is 162 kV/cm. With increasing electrode radius (at constant  $d$ ) the curve  $E(x)$  becomes flatter and approaches the line  $E(x) = E_{mean}$ .

In the real electrode configuration every charged pair of electrodes has two grounded pairs as neighbors at a distance of 3.75 mm which in principle must be taken into account as well. Furthermore, every electrode terminates with a spherical endcap and there the maximum field strength is higher because of the additional curvature at the transition between the cylinder and half-sphere.

### 4.3 Vacuum

The main vacuum chamber which houses the decelerator is separated from the source chamber where the molecular beam is created. The connection between both chambers is provided by a skimmer with a 2 mm diameter opening. It would be very inconvenient if regular maintenance of the beam source would

always require a venting of the whole apparatus. In our setup therefore, the source chamber can be isolated from the main chamber with the help of specially designed gate-valve [67] so that both chambers can be vented independently.

The main chamber is pumped by two magnetically levitated turbo molecular pumps (TMU 1600M P, *Pfeiffer Vacuum GmbH*) each backed by a membrane fore-pump (MVP 055-3C, *Pfeiffer Vacuum GmbH*). The membrane pumps are highly durable and able to run for several years without maintenance. For the source chamber the same type of turbo pump is used but here the membrane fore-pump is specifically adapted to pump corrosive gases which are often used in experiments. If such gases are to be pumped, it is advisable to reduce their residence time inside the apparatus. To that end, an inert gas (usually nitrogen) is introduced via a special leak-valve, which is connected directly to the turbo pump, to establish a higher gas flow through the fore-vacuum system.

The pressure is monitored at several positions by cold cathode gauges. Gauges based on hot cathodes (e.g. Bayard-Alpert ionization gauges) are not suitable because the emitted electrons can induce discharges – unless a suitable shielding is installed. Without the gas load of the molecular beam, the vacuum in the main chamber is in the low  $10^{-8}$  mbar range without any bake-out.

During operation, the molecular beam valve introduces pulses of gas into the source chamber, usually at a rate of 10 Hz. Only the central part of the so-created beam passes the skimmer and propagates directly into the main chamber, the remaining gas gives rise to a background pressure in the source chamber and a flow of this background gas through the skimmer into the main chamber. The pressure in the main chamber rises by at least an order of magnitude after the molecular beam valve is switched on. Currently there is no need to further improve the situation by an additional differential pumping stage behind the skimmer.

## 4.4 High voltage conditioning and testing

Before the decelerator can be put into operation, the whole system is subjected to a DC high-voltage testing and *conditioning* procedure to make sure that the *break-down voltage* lies well above the voltage which is applied during normal operation. In the present instrument the maximal operating voltages are  $\pm 20$  kV, i.e. 40 kV across a minimum distance of 3 mm. During the conditioning procedure small discharges may occur which, in the favorable case, do not cause any damage but rather improve the quality of the surface so that no further discharges occur at the given voltage. In the less favorable case, a constant electrical current remains after a discharge and the part which could not hold the voltage has to be located and replaced or repolished.

Often it is not so clear what has actually triggered a sparkover across the vacuum gap, but commonly cited reasons are surface defects or adsorbed materials (“dirt”). If the insulators are the limiting factor, the mechanism is different

again. A useful overview about these problems is given in [65].

All field configurations which are planned to occur during normal operation need to be tested. Furthermore, a certain safety margin should be allowed for: here the voltage is raised to  $\pm 23$  kV during conditioning, while the highest switched voltage used in the experiment is only  $\pm 20$  kV. It is necessary to apply the voltage with the same polarity on the electrodes during conditioning as during normal operation. However, it can be beneficial to test from the beginning whether the systems can hold the voltage in both polarities. If a serious sparkover has caused irreversible damage to the electrodes and a lowering of the break-down voltage, the chance is high that the system can still hold the voltage after switching the polarity. In this machine, a discharge occurred once and severely lowered the break-down voltage. After switching the polarities, the ongoing experiments could be resumed without opening the instrument. Later on the faulty electrodes were located and repolished.

#### 4.4.1 The conditioning procedure

To condition the system, a HV-power supply of positive polarity is connected with the desired electrodes via a  $300\text{ M}\Omega$  resistor and an ampere meter; the HV-power supply of negative polarity is connected in the same way. Since the current on the negative and the positive polarity can be monitored independently, it is possible to determine whether a sparkover occurs among charged HV-electrodes or between a charged component and any other grounded component of the system. The resistor is in place to limit the current in the case of a sparkover. The vacuum conditions are monitored by cold cathode gauges.

The conditioning proceeds as follows. At first, the voltage is raised slowly but steadily to  $\pm 5$  kV. Subsequently it is raised in increments of  $|\Delta U| \approx 1$  kV per minute. The process is slowed down a bit as the absolute voltage approaches the maximum. The rationale behind this procedure is that a sparkover, if it occurs, should happen at the lowest possible voltage (often the sparkover occurs with some delay after the voltage was raised). If a sparkover occurs, it is usually accompanied by a short increase in the pressure; if no such increase can be detected the chance is high that the discharge actually involved parts somewhere outside the vacuum chamber – a common problem especially if the humidity of the air is high.

In the present instrument, only very few discharges occurred during the initial conditioning procedure which means the electrodes were well polished and clean. If the vacuum chamber is vented, and especially if the installed parts are exposed to ambient air, it is necessary to repeat the HV-testing and conditioning procedure. Depending on the degree of exposure, the voltage can be raised somewhat more quickly as compared to the initial conditioning run.

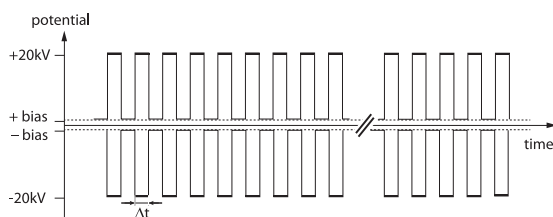


**Figure 4.4:** HV pulses on either the even or odd numbered electrode pairs for the guiding of molecules. If the molecules are decelerated or accelerated the time  $\Delta t$  increases or decreases with time, respectively. If desired, one may switch between high voltage and a small bias voltage (below 1 kV) instead of ground potential (0 V).

## 4.5 Safety measures

All electrical components which are on high voltage and outside the vacuum need to be properly insulated. Permanent connections between cables and other components like resistors should be casted in synthetic resin to inhibit corona discharges or sparkovers to other components. Sharp tips of conductive material must not occur anywhere. When soldering, a seemingly excessive amount of solder should be used to achieve a smooth and nicely rounded off connection. All insulating surfaces need to be properly cleaned to reduce the surface conductivity.

A device which is of central importance is the *interlock unit*, it automatically disables the power supplies and stops the HV-switches if a serious system fault occurs. In the present instrument, the interlock unit monitors the pressure of the chambers and of the fore-vacuum system. Faults reported by the HV-switches are also monitored. In this way it is possible to avert or at least reduce the chance of a complete destruction of the apparatus by a gas discharge which would occur after uncontrolled venting of the system during operation. If discharges happen to occur during seemingly normal operation, they are usually also registered because of the accompanying rise in pressure. Therefore it is advisable to set the threshold for the maximally allowed pressure as low as possible.

## 4.6 High voltage switching

### 4.6.1 Basic requirements

For the present deceleration machine, a potential of  $\pm 20$  kV has to be switched rapidly between ground or bias and high voltage. If molecules are guided, the pulses are of constant duration  $\Delta t$  as shown in **Fig. 4.4**; if molecules with a mean forward velocity of e.g. 400 m/s are to be guided through the decelerator, then  $\Delta t = (0.00825/400) \text{ s} = 20.6 \mu\text{s}$ . If the  $s = 1$  mode of operation is used,



each module has to be charged about 100 times, which means that every switch needs to switch on and off 50 times. In order to supply the required charge during a sequence of high voltage pulses (a *burst* sequence) a buffer capacitor must be used. As the experiment typically runs at 10 Hz, there is enough time available between the bursts for the capacitors to be reloaded. The short rise and fall times of less than 100 ns can be realized with commercial high voltage transistor switches (see below).

#### 4.6.2 Components and design

Shown in **Fig. 4.5** is the circuit diagram of the basic electronic assembly that is used to run a single module of the deceleration machine. In the center of the figure, the decelerator electrodes are sketched. These are connected via their support rods and via the vacuum feedthroughs (compare Fig. 4.1) to the high voltage switches. The used switches are commercial transistor based switches (HTS 301-03-GSM, *Behlke Electronic GmbH*) which can be operated at a maximum absolute voltage of 30 kV. The same type of switch is used for both polarities. For voltages up to 20 kV it is sufficient to cool the switches by air-flow alone – for higher voltages an oil cooling system would be required. In the present instrument, every switch is positioned directly below a small fan.

The *driver control unit* supplies the switch with the required +5 VDC operating voltage and with a control input signal: a +10 V trigger pulse for positive polarity, an inverted pulse for negative polarity. Fault signals from the switch are transmitted by a 50  $\Omega$ -driver to the *system and control unit*. A fault signal occurs in the case of overfrequency, thermal overload or incorrect voltage supply. In these three cases<sup>3</sup> the switch connects the electrodes with the ground or bias potential. If the +5 VDC supply is cut off, the electrodes become isolated (floating). To ensure a short rise time, the high voltage power supply is not directly connected to the switch, but used to constantly load a 500 nF high voltage buffer capacitor (30 kV, PPR300-504 *HiVolt Capacitors Ltd.*). The capacitive load behind a single switch is approximately 100 pF. If during a typical burst one switch has to switch e.g. 50 times, a charge of about  $50 \times 100 \text{ pF} \times 20 \text{ kV}$  is drawn from the capacitor. If the recharging of the capacitor during the burst is negligible, a total voltage drop of 1% or 200 V results. To avoid ringing, two 330  $\Omega$  resistors are placed in series: one resistor is placed before the input and one behind the output of the HV-switch ( $R_1$  and  $R_2$ , see detail of Fig. 4.5).

The *system and control unit* supplies 24 V for the *driver control unit* and transmits the trigger signals from the *burst unit*. This unit also interprets the fault signals from all 4 switches. In case of a fault, the +5 V at the fault output,

---

<sup>3</sup>One should not assume that these are all possible faults which can occur. It once happened that under normal operating conditions a single switch suffered from a strong discharge right through its own insulation. The event didn't result in an error signal at the fault output, however, the accompanying apocalyptic noise was easy to notice and the system was then shut down by hand.



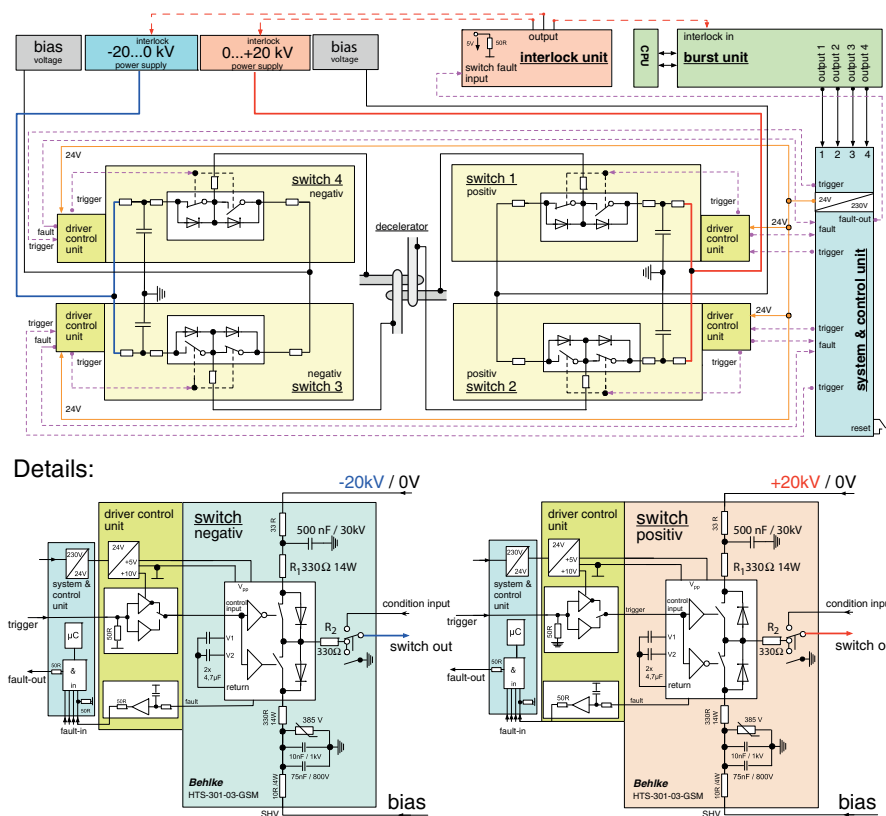


**Figure 4.5:** The HV circuitry and auxiliary instrumentation for the deceleration machine.

which is connected to the *interlock unit*, drops to 0 V. The interlock unit then shuts down the HV power supplies and it also brings the burst unit to a halt.

As may be seen from **Fig. 4.6**, the switch units are mounted directly onto the top of the vacuum chamber. A metal housing encloses each unit and provides shielding against leakage of high frequency radiation originating from the fast switching of the high voltages. Onto each housing, 10 fans are mounted to establish a steady air flow for the cooling of the switches and the resistors.

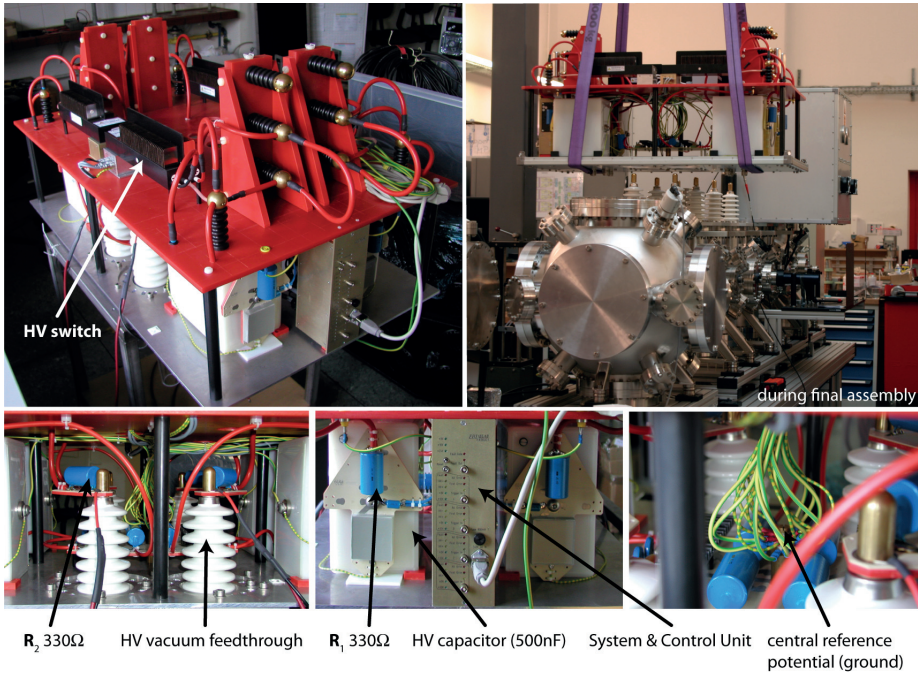


**Figure 4.6:** Top left: a switch unit corresponding to the circuit diagram of Fig. 4.5. Top right: a single unit during its installation on the vacuum chamber. Bottom: details for a single unit. For HV connections, (red) silicone clad cables without shielding are used. All other cables are shielded, except those leading to the central ground potential point.

## Chapter 5

# Operation of a Stark decelerator with optimum acceptance

With a Stark decelerator, beams of neutral polar molecules can be accelerated, guided at a constant velocity, or decelerated. The effectiveness of this process is determined by the 6D volume in phase space from which molecules are accepted by the Stark decelerator. Couplings between the longitudinal and transverse motion of the molecules in the decelerator can reduce this acceptance. These couplings are nearly absent when the decelerator operates such that only every third electric field stage is used for deceleration, while extra transverse focusing is provided by the intermediate stages. For many applications, the acceptance of a Stark decelerator in this so-called  $s = 3$  mode significantly exceeds that of a decelerator in the conventionally used ( $s = 1$ ) mode. This has been experimentally verified by passing a beam of OH radicals through a 2.6 meter long Stark decelerator. The experiments are in quantitative agreement with the results of trajectory calculations, and can qualitatively be explained with a simple model for the 6D acceptance. These results imply that the 6D acceptance of a Stark decelerator in the  $s = 3$  mode of operation approaches the optimum value, i.e. the value that is obtained when any couplings are neglected.

---

Based on: *Operation of a Stark decelerator with optimum acceptance*  
L. Scharfenberg, H. Haak, G. Meijer and S.Y.T. van de Meerakker  
Phys. Rev. A **79**, 023410, (2009)

## 5.1 Introduction

Since its introduction in 1999, the method of Stark deceleration has developed into an established method for taming molecular beams [5, 3]. The Stark deceleration technique combines molecular beam technology with concepts from charged particle accelerator physics. In essence, a part of a beam of neutral molecules is selected and decelerated utilizing the force that polar molecules experience in inhomogeneous electric fields. A Stark decelerator produces bunches of state-selected molecules with a computer-controlled velocity and with narrow velocity distributions. These beams are ideally suited for a variety of experiments in which the velocity of the molecules is an important parameter. Applications include the use of slow molecular beams to enhance the interaction time in spectroscopic experiments [68, 69] and scattering studies as a function of the collision energy [18]. When the molecules are decelerated to a near standstill, they can be loaded and confined in traps [11, 6]. This allows the observation of molecules in complete isolation for times up to several seconds, and enables the investigation of molecular properties in great detail [13, 16, 15].

For many of these applications it is crucial that the number density of the decelerated packets of molecules is further increased. Higher densities of decelerated molecules will improve the statistics in metrology experiments and can be decisive, for instance, for the observation of (in)elastic scattering or reactive collisions in crossed molecular beam experiments. Higher densities in traps are also a prerequisite for the future application of cooling schemes like evaporative cooling, needed to reach the regime of degenerate dipolar quantum gases [70].

The number density of decelerated molecules that can be reached at the exit of the decelerator is limited by the initial phase space density in the molecular beam and by the 6D phase space acceptance of the decelerator. The latter is defined as the volume in 6D phase space – the product of the volume in real space and in velocity space – from which stable trajectories through the decelerator originate<sup>2</sup>. In most Stark deceleration experiments to date, molecular beams with a low initial velocity are slowed down using decelerators with a rather limited number of electric field stages. Hence, molecular beams are typically released from a cooled pulsed valve using Xe or Kr as a carrier gas. The use of Xe or Kr and the cooling of the pulsed valve strongly enhances cluster formation, however, and is generally regarded to be non-ideal for a molecular beam expansion. Moreover, these decelerators are usually operated at large phase angles. The phase angle  $\phi_0$  is defined by the position of the synchronous molecule at the moment the fields are switched [57] and determines the deceleration rate per electric field stage. It ranges from  $0^\circ < \phi_0 < 90^\circ$  for deceleration, while acceleration occurs from  $-90^\circ < \phi_0 < 0^\circ$ . While for increasing values of  $|\phi_0|$

---

<sup>2</sup>More precisely, if a specific (small) volume in phase space is denoted by  $(\Delta x \Delta y \Delta z \Delta v_x \Delta v_y \Delta v_z)_i$ , and if all particles which originate from this volume can be decelerated or accelerated without being lost, then the total phase space acceptance is obtained by summing all these volumina:  $\sum_i (\Delta x \Delta y \Delta z \Delta v_x \Delta v_y \Delta v_z)_i$ .

the deceleration rate gets larger, the longitudinal phase space acceptance gets smaller.

An obvious route to higher number densities of decelerated molecules is thus the use of seed gases of lower mass (preferably Ne or Ar) in room-temperature expansions and the use of low phase angles in the decelerator. Together this implies, however, that (much) longer Stark decelerators need to be constructed to compensate for both the higher initial velocity and the lower deceleration rate. It is not *a priori* clear whether one can actually transport molecules through such long decelerators without significant losses. If only molecular trajectories along the molecular beam axis are considered, the length of the decelerator is inconsequential, as the deceleration process is subject to phase stability [54, 57]. In reality the molecules in the beam have off-axis position and velocity components, however. The transverse electric field gradients in the decelerator drive the molecules back towards the molecular beam axis. The resulting transverse oscillatory motion is strongly coupled to the longitudinal (forward) motion and can result in a reduction of the 6D phase space acceptance of the decelerator [58]. Numerical simulations indicate that this coupled motion does not affect the overall performance of the relatively short Stark decelerators that have been used and operated at high phase angles thus far, but that it can severely affect the performance of longer decelerators that are operated at low phase angles. In the ideal case, the longitudinal and transverse motions in the Stark decelerator are completely uncoupled. This can be achieved by constructing decelerators with dedicated, spatially separated, elements for focusing and deceleration [71, 72], as is common practice in charged particle accelerators [73]. The required electrode geometries make the decelerator rather complex, however [74, 72].

In this work we exploit that in a Stark decelerator with the original electrode geometry, i.e., the geometry as used in reference [5], the coupling between the longitudinal and transverse motion can be significantly reduced when the decelerator is operated in the so-called  $s = 3$  mode (see [55] and chapter 3). In this mode, only every third electric field stage is used for deceleration, while extra transverse focusing is provided by the intermediate stages. We demonstrate and quantify that for many applications, the acceptance of the Stark decelerator in the  $s = 3$  mode significantly exceeds that of a decelerator in the conventionally used ( $s = 1$ ) mode of operation. The improved performance of the  $s = 3$  operation mode was demonstrated earlier for guiding at a constant velocity ( $\phi_0 = 0^\circ$ ) [58] and for deceleration in a relatively short decelerator at high phase angles [72]. However, the latter experimental arrangement did not allow for a direct comparison between the  $s = 1$  and  $s = 3$  modes of operation, and the advantages of the  $s = 3$  mode of operation for a wide range of parameters cannot be inferred from these studies. Here we present experiments in which a beam of OH radicals passes through a 2.6 meter long Stark decelerator consisting of 316 electric field stages. In this machine, the OH radicals can be detected either after 103 or after 316 electric field stages, enabling a direct comparison between

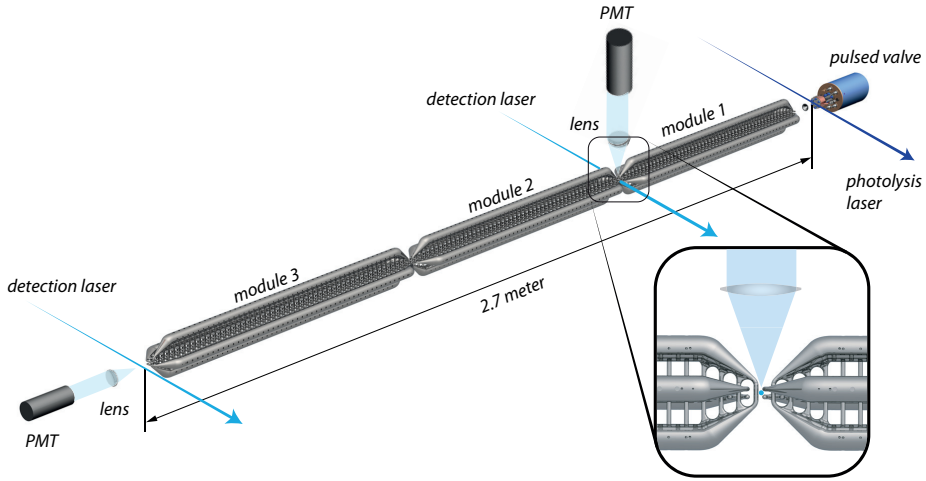


**Figure 5.1:** Scheme of the experimental setup. A pulsed beam of OH radicals is produced via photolysis of  $\text{HNO}_3$  seeded in Xe, Kr, or Ar. The beam of OH radicals passes through a 2.6 m long Stark decelerator that consists of three modules of  $\sim 100$  stages each. The OH radicals can be state-selectively detected using a laser induced fluorescence scheme at the end of the decelerator, and in the region between the first two modules. In the top inset, a photograph of a decelerator module is shown.

the  $s = 1$  and  $s = 3$  modes of operation under otherwise identical conditions, in particular using the same phase angle  $\phi_0$ . This direct comparison allows us to draw firm conclusions on the usefulness of the  $s = 3$  mode of operation for a wide range of experimental parameters. The experimental results are in quantitative agreement with the results of trajectory calculations, and can qualitatively be explained with a simple model for the 6D acceptance.

## 5.2 Experiment

### 5.2.1 Experimental setup

The experimental setup is schematically shown in **Fig. 5.1**. A pulsed beam of OH radicals is produced via ArF-laser (193 nm) dissociation of  $\text{HNO}_3$  seeded in an inert gas. The dissociation is carried out inside a quartz capillary that is mounted on the orifice of a pulsed valve (General Valve, Series 99). The experiment runs at a repetition frequency of 10 Hz. Details about the production of OH radicals can be found on p. 24.

During the supersonic expansion, the majority of the OH radicals cool to the lowest rotational and vibrational level of the  $X^2\Pi_{3/2}$  spin-orbit manifold of the electronic ground state. This population is equally distributed over the two  $\Lambda$ -doublet components of the  $J = 3/2$  level. Only OH molecules in the

upper  $\Lambda$ -doublet component are low-field-seeking, and are of relevance to the experiments discussed here. This component splits into an  $|M_J| = 1/2$  and an  $|M_J| = 3/2$  component in an electric field (see Fig. 2.1 on p. 20). Molecules in the  $|M_J| = 3/2$  component experience a Stark shift that is a factor of three larger than the Stark shift experienced by molecules in the  $|M_J| = 1/2$  component.

After passage through a skimmer with a 2 mm diameter opening, the molecular beam enters the differentially pumped decelerator chamber. The skimmer is mounted on a compact gate valve [67], enabling the venting of the source chamber while keeping the decelerator chamber under vacuum. The beam enters the Stark decelerator 60 mm from the nozzle orifice. The Stark decelerator consists of three modules that are mechanically and electrically decoupled from each other. The first two modules consist of 104 electrode pairs (i.e. 103 electric field stages) each, whereas the last module contains 109 electrode pairs. These electrode pairs consist of two parallel 4.5 mm diameter stainless steel electrodes that are placed symmetrically around the molecular beam axis, providing a 3 mm gap for the molecular beam to pass through. Adjacent electrode pairs are alternately horizontally and vertically oriented, such that a  $3 \times 3 \text{ mm}^2$  opening area remains for the molecular beam. The electrodes of all horizontal (vertical) pairs within each module are electrically connected and switched simultaneously to high voltage. The center-to-center distance ( $L$ ) of electrodes of adjacent pairs is 8.25 mm, and the three modules are carefully aligned to also maintain this distance between the electrode pairs of adjacent modules. The first and last eight electrode pairs of each module are mounted on conically shaped rods, as shown enlarged in Fig. 5.1 and in Fig. 4.1 on p. 49. This design provides excellent optical access for fluorescence collection in between adjacent decelerator modules. It also allows the exits of two Stark decelerators in a crossed beam arrangement to be brought close together.

The electric field in the decelerator is switched back and forth between two different configurations, that are schematically shown in **Fig. 5.2**. In each configuration, the opposing electrodes of every other electrode pair are at  $\pm 20 \text{ kV}$ , while the remaining electrodes are grounded. Switching between the two configurations is performed using fast air-cooled high voltage switches (see p. 55). To minimize the power dissipation per switch, each module is connected to four separate high voltage switches. Each switch is connected to its power supply via a  $0.5 \mu\text{F}$  capacitor bank, limiting the voltage drop during a deceleration cycle to less than 5%. For the conventional mode of operation of a Stark decelerator, the  $s = 1$  mode, the voltages are switched every time the molecules approach the pair of electrodes that are on high voltage. In this case, the molecules are simultaneously decelerated and transversally focussed in every electric field stage. When the decelerator is operated in the  $s = 3$  mode, the voltages are switched only after every third stage. In this case, only every third stage is used for combined deceleration and transverse focusing, while the intermediate stages provide additional focusing.

The OH radicals can be state-selectively detected using an off-resonant Laser



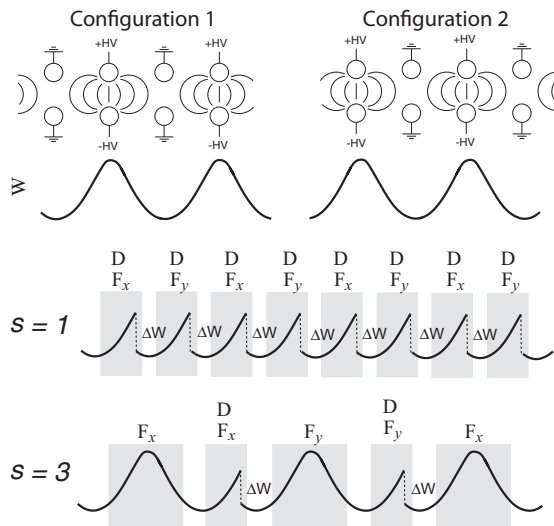


**Figure 5.2:** Schematic representation of the two electric field configurations that are used in the deceleration process, together with the potential energy  $W$  for an OH molecule along the molecular beam axis. By switching between the two field configurations when the molecules are at the positions indicated by the vertical dashed lines, an amount of kinetic energy  $\Delta W$  is removed from the molecules. In the conventional ( $s = 1$ ) mode of operation, each electric field stage is used simultaneously for deceleration (D) and focusing in alternating transverse directions ( $F_x, F_y$ ). In the  $s = 3$  mode of operation, only every third stage is used for combined deceleration and transverse focusing, while the intermediate stages provide additional focusing.

Induced Fluorescence (LIF) detection scheme at two different positions along the beam line. The first detection zone is located between the first two modules and the second one is 18 mm downstream from the last module, enabling the detection of OH radicals after 103 or 316 electric field stages, respectively. The 282 nm radiation of a pulsed dye laser crosses the molecular beam in either one of the detection regions at right angles, and saturates the (spectroscopically not resolved)  $Q_{21}(1)$  and  $Q_1(1)$  transitions of the  $A^2\Sigma^+, v = 1 \leftarrow X^2\Pi_{3/2}, v = 0$  band. The fluorescence occurs predominantly on the  $A^2\Sigma^+, v = 1 \rightarrow X^2\Pi, v = 1$  transition around 313 nm. Stray light from the laser is minimized by passing the laser beam through light baffles between the entrance and exit windows, and by using optical filters which are located in front of the photomultiplier tube (PMT).

In the experiments the seed gases Xe, Kr, or Ar are used. The velocity distribution can be determined very accurately by measuring a time-of-flight profile when the decelerator does not switch but is operated in a *static* mode. In this mode, a static high voltage is applied to the horizontal and vertical electrodes simultaneously with the effect that low field seeking molecules are only transversally focused, while their longitudinal velocity remains unchanged. The



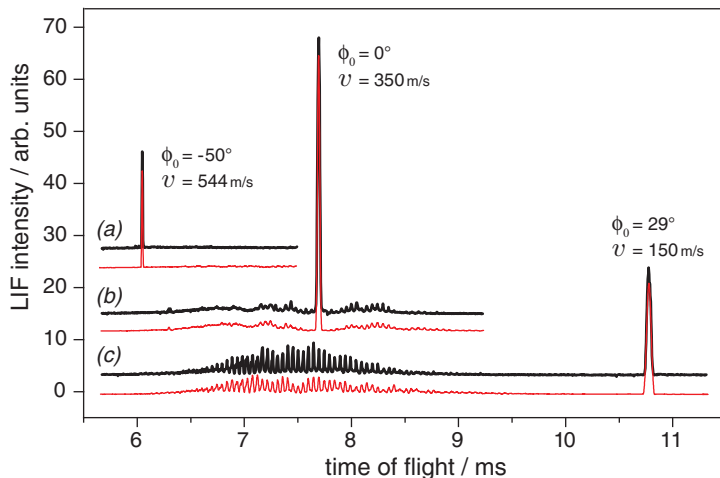


**Figure 5.3:** Time-of-flight profiles of OH radicals, recorded at the exit of the 316 stage Stark decelerator (black curves). The Stark decelerator is operated in the  $s = 3$  mode, and accelerates (curve *a*), guides (curve *b*), or decelerates (curve *c*) a packet of OH radicals with an initial velocity of 350 m/s. The TOF profiles that result from simulations of the experiment are shown underneath the experimental profiles (red curves).

packet of OH radicals is quite short initially and therefore one may directly infer the velocity distribution from the known total distance ( $\approx 2.7$  m, see Fig. 5.1) and the measured time-of-flight profile. The mean velocities for the beam are 350 m/s, 430 m/s, and 590 m/s for Xe, Kr, and Ar, respectively, with a full width at half maximum (FWHM) velocity spread of about 15 – 20 % for all seed gases.

In **Fig. 5.3** the intensity of the LIF signal of a beam of OH ( $J = 3/2$ ) radicals seeded in Xe is shown as a function of time after firing the dissociation laser using different deceleration sequences.

The OH radicals are detected using the second LIF detection unit, and the Stark decelerator is operated in the  $s = 3$  mode. In curve (*b*) the TOF profile is shown that is obtained when the decelerator is operated at a phase angle of  $\phi_0 = 0^\circ$ , corresponding to guiding a packet of OH radicals at a constant velocity. A packet of OH radicals with a mean velocity of 350 m/s is selected, transported through the 2.6 m long decelerator, and arrives in the detection region some 7.6 ms after its production, with a FWHM of the arrival time distribution of 25  $\mu$ s. The measurements shown in curve (*a*) are obtained with the decelerator operating at a phase angle of  $\phi_0 = -50^\circ$ , accelerating a packet of OH radicals from an initial velocity of 350 m/s to a final velocity of 544 m/s. There is no signature of the part of the molecular beam that is not accelerated. This is also expected as the electrodes of the decelerator are switched to ground when the accelerated packet exits the decelerator, about 1.5 ms before the remainder

of the beam pulse would arrive in the detection region. Curve (c) shows the TOF profile that is obtained when the decelerator is operated at a phase angle of  $\phi_0 = 29^\circ$  to decelerate a packet of OH radicals from 350 m/s to 150 m/s. The decelerated molecules exit the decelerator about 10.7 ms after production, about 3 ms after the arrival of the undecelerated part of the beam.

The experimental TOF profiles are in excellent agreement with the profiles that result from three dimensional trajectory simulations of the experiment that are shown underneath the experimental profiles. In these and in all subsequent simulations, the individual contributions of the  $|M_J| = 3/2$  and the  $|M_J| = 1/2$  components to the LIF signal intensity are taken into account.

### 5.2.2 Comparing the $s = 1$ and $s = 3$ modes of operation

In **Fig. 5.4** two series of TOF profiles are shown that allow a direct comparison between the performance of a Stark decelerator in the  $s = 1$  and  $s = 3$  operation mode under otherwise identical conditions. In both series, the Stark decelerator is programmed to accelerate, guide or decelerate a packet of OH radicals with a mean initial velocity of 350 m/s to a final velocity that is in the 70 – 600 m/s range ( $-65^\circ < \phi_0 < 32^\circ$ ). Only that part of each TOF profile that contains the signature of the packet at the final velocity is shown. In the left and right panels the series of profiles are shown that are obtained when the decelerator is operated using the  $s = 1$  and the  $s = 3$  mode, detecting the OH radicals after 103 and 316 stages, respectively. The (almost) factor of three difference in the number of stages results in (almost) identical phase angles for the Stark decelerator to produce a given final velocity in both series. The phase angle that is used, and the final velocity of the packet, is indicated for selected profiles in both panels. To enable a direct comparison between the two modes of operation, both series are plotted on the same vertical scale. For this, the relative detection efficiency in the two LIF zones is experimentally determined by measuring OH radicals at both detection locations when the Stark decelerator is operated at  $s = 3, \phi_0 = 0^\circ$ . The overall scaling factor that is thus determined is correct if we assume that for the  $s = 3, \phi_0 = 0^\circ$  mode of operation the number density of the packet of OH radicals does not decline when progressing from the first to the second LIF zone, and that the relative detection efficiency is independent of the velocity of the OH radicals. The validity of both assumptions is checked experimentally and verified by numerical simulations.

When the decelerator is operated using  $s = 1$ , the signal intensity for  $\phi_0 = 0^\circ$  is about a factor of two-and-a-half lower than the signal intensity for  $s = 3, \phi_0 = 0^\circ$ . The signal intensity for the  $s = 1$  appears rather constant for the different values of  $\phi_0$  that are used. For the  $s = 3$  mode of operation it is observed that the signal intensity for  $\phi_0 \neq 0^\circ$  gradually reduces for increasing absolute values of the phase angle, following the reduced acceptance of the decelerator. For final velocities below 150 m/s, indicated by the dashed line in Fig. 5.4, a sharp reduction of the signal intensity is observed even though the

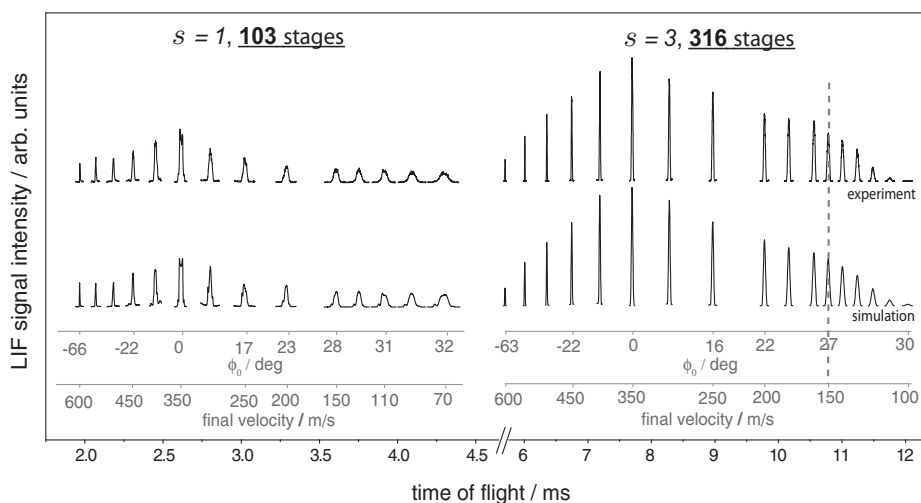


**Figure 5.4:** Time-of-flight profiles of OH radicals that exit the Stark decelerator using the  $s = 1$  and  $s = 3$  mode of operation. The OH radicals are detected after 103 and after 316 electric field stages for  $s = 1$  and  $s = 3$ , respectively. The measurements are recorded under otherwise identical conditions, and are shown on the same vertical scale. The beam of OH radicals has a mean initial velocity of 350 m/s. The mean final velocity of the molecules and the phase angle used, are indicated for selected profiles.

change in phase angle is only very small. This reduction is due to excessive transverse focusing for low velocities, and will be discussed in more detail in section 5.2.4. The signal intensities for the  $s = 1$  and  $s = 3$  modes of operation are about equal for  $\phi_0 = -65^\circ$ . Both series of TOF profiles are in excellent agreement with profiles that result from simulations of the experiment that are shown underneath the experimental profiles (the low field seeking  $|M_J| = 1/2$  component only contributes to the TOF profiles for  $-30^\circ \leq \phi_0 \leq 30^\circ$ ).

The gain of the  $s = 3$  mode with respect to the  $s = 1$  mode of operation, defined as the ratio of the maximum signal intensities of the decelerated packets at a given final velocity, is shown as a function of the final velocity in **Fig. 5.5**. For this, the data presented in Fig. 5.4 are used. For selected velocities, the phase angle that is used for  $s = 3$  operation is indicated; the phase angle that is used for  $s = 1$  operation differs only slightly from this value. It is seen that for  $\phi_0 = 0^\circ$ , i.e. at a final velocity of 350 m/s, the gain is 2.4, consistent with previous studies [55, 72]. When the beam is accelerated to 450 m/s ( $\phi_0 = -21.7^\circ$ ), a gain up to 3 is observed. For higher velocities the gain gradually reduces and reaches 1.2 for 600 m/s ( $\phi_0 = -63.2^\circ$ ). A gain up to 4.2 is observed when the beam is decelerated to 200 m/s ( $\phi_0 = 22.3^\circ$ ). Below 150 m/s ( $\phi_0 = 27.0^\circ$ ), the gain drops fast and reaches 1.0 for a final velocity of about 120 m/s.

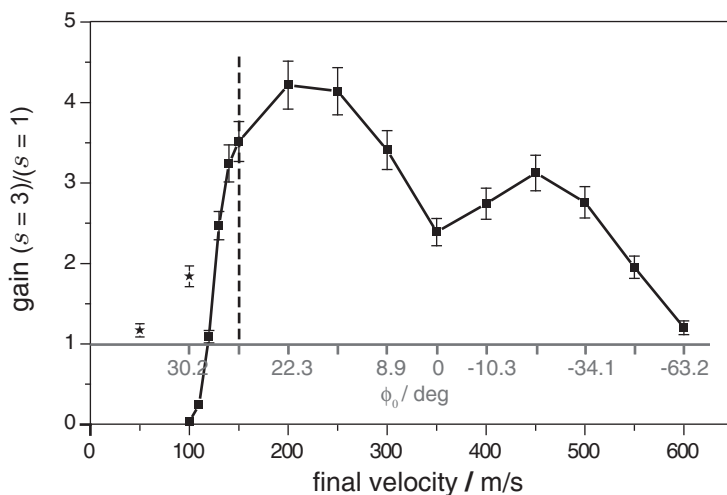


**Figure 5.5:** The ratio of the maximum signal intensities (squares, connected by straight line segments) for  $s = 3$  operation versus  $s = 1$  operation as a function of the final velocity. The two additional data points (stars) apply to a bimodal operation of the decelerator (see text for details).

### 5.2.3 The $s = 1$ mode of operation at low phase angles

In this section we want to address the question whether, for a fixed initial and final velocity, the number density of decelerated molecules can also be increased by using lower phase angles in the  $s = 1$  mode of operation. For this, we compare the deceleration with 103 stages at a certain phase-angle to the deceleration with 316 stages at about one-third of this phase-angle. The data for the deceleration at the  $s = 1$  mode with 103 deceleration stages, have already been shown and discussed in the previous section. The complimentary data for the deceleration at the  $s = 1$  mode with 316 deceleration stages have been measured as well; a beam of OH radicals with the same initial velocity of 350 m/s is decelerated or accelerated to the same final velocities between 70 m/s and 600 m/s. The phase-angles used for these measurements are very low, ranging from  $-21.7^\circ$  to  $10.9^\circ$ . Again, the signal intensity that is observed with guiding at the  $s = 3$  mode, is used to calibrate the measurements with 316 stages relative to the ones with 103 stages.

For the operation in the  $s = 1$  mode, the gain in using 316 stages compared to using 103 stages is shown as a function of the final velocity in the lower curve in **Fig. 5.6**. This gain is determined as the ratio of the signal intensities of the decelerated packets at a given final velocity, and lies between 0.5 and 0.7 throughout. Since this gain stays smaller than one in the considered velocity range, it is evident that for the chosen parameters the number density of decelerated molecules can not be increased by the use of lower phase-angles.

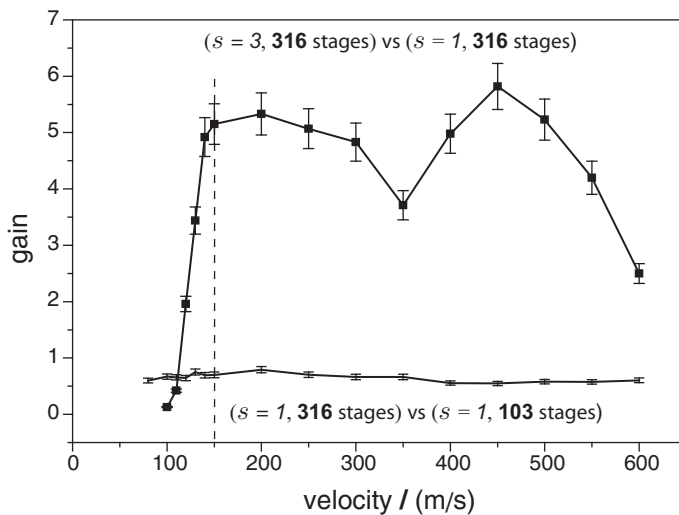


**Figure 5.6:** Lower curve: The ratio of the signal intensity for  $s = 1$  operation of a decelerator with 316 versus 103 stages as a function of the final velocity. Upper curve: The ratio of the signal intensity using a 316 stage decelerator operating on the  $s = 3$  versus the  $s = 1$  mode.

This perhaps counterintuitive finding is explained by the presence of inherent instabilities in the  $s = 1$  mode, which more strongly manifest themselves during the increased time spent in the decelerator.

We can now also address the question whether, given a Stark decelerator of a certain length, the maximum number density of decelerated molecules is obtained using the  $s = 3$  mode at a certain phase-angle or using the  $s = 1$  mode at about one-third of this phase-angle. For the 316 stage decelerator, the resulting gain of the  $s = 3$  versus the  $s = 1$  mode directly follows from the curve shown in Fig. 5.5 and the lower curve in Fig. 5.6, and is shown as the upper curve in the Fig. 5.6. Operation on the  $s = 3$  mode is seen to be about a factor five better than on the  $s = 1$  mode, provided the final velocity is larger than the threshold velocity.

#### 5.2.4 Excessive focusing at low velocities

The rather abrupt decrease in the number density of decelerated molecules for velocities below 150 m/s as shown in the right hand panel of Fig. 5.4 can qualitatively be understood as follows. During their flight through the decelerator, molecules are alternately focused in each transverse direction. When the focusing force acts in one transverse direction, molecules experience to a good approximation no focusing or de-focusing force in the orthogonal transverse direction (the molecules actually experience a small defocusing force in the orthogonal direction). As long as the characteristic wavelength  $\lambda$  of the trans-

verse oscillatory motion is much larger than the periodicity of the transverse focusing force, molecules will follow stable trajectories through the decelerator. The wavelength  $\lambda$  is given by  $\lambda = \langle v_z \rangle 2\pi/\Omega_y$ , where  $\langle v_z \rangle$  and  $\Omega_y$  are the mean longitudinal velocity and the mean transverse oscillation frequency of the packet of molecules, respectively. The periodicity of the focusing force is given by  $2sL$ , where  $L$  is the center-to-center distance of adjacent electrode pairs. For high velocities, therefore, stable trajectories are expected. For low velocities, however,  $\lambda$  becomes ever closer to  $2sL$ , and molecules will get more tightly transversely focused. The molecular trajectories will then exhibit ever larger deviations from the molecular beam axis, and the molecules will eventually crash onto the electrodes. For a given electric field distribution in a Stark decelerator, the resulting loss of molecules is thus expected to strongly depend on the longitudinal velocity of the molecules.

In **Fig. 5.7**, the maximum signal intensity of decelerated packets of OH radicals is shown at the exit of the 316 stage decelerator, operating in the  $s = 3$  mode. Beams of OH radicals with three different initial velocities have been used, and the signal is shown as a function of the final velocity (upper panel) or as a function of the phase-angle (lower panel). When Xe or Kr are used as carrier gas, the Stark decelerator is programmed to select a packet of molecules with an initial velocity that is identical to the mean velocity of the molecular beam, i.e. 350 m/s or 430 m/s, respectively. For Ar, a velocity of 520 m/s is selected from the slow tail of the velocity distribution of the beam. The phase angle  $\phi_0$  is varied to decelerate the selected packet of molecules to final velocities down to 100 m/s. The series of measurements for each seed gas are normalized to the data point that corresponds to  $\phi_0 = 0^\circ$ . The thresholds are found at a velocity of about 150 m/s in each series, and are indicated by the vertical dashed lines. This velocity is reached when  $\phi_0 = 27^\circ$ ,  $\phi_0 = 43^\circ$ , and  $\phi_0 = 67^\circ$  for Xe, Kr, and Ar seeded beams, respectively. The value of the threshold velocity appears independent from the phase angle  $\phi_0$  of the decelerator, consistent with the qualitative picture described above. The intensities that result from numerical trajectory simulations of the experiments are shown as solid lines in **Fig. 5.7**. Excellent agreement is obtained with the experiments and in particular the threshold behavior of the signal intensity is reproduced well.

The threshold velocity below which losses due to excessive transverse focusing occurs, can be approximately determined as described in section 3.4 (pp. 38). The model described there predicts that no stable trajectories exist in the  $s = 3$  mode of operation when  $\lambda \leq (2.6 \cdot 2sL)$ . For the present Stark decelerator, operating on  $s = 3$ , the periodicity of the transverse focusing force  $2sL$  is equal to 49.5 mm. The mean transverse oscillation frequency  $\Omega_y$  follows from the time-averaged transverse force (see the Appendix on p. 76). For  $s = 3$ ,  $\Omega_y$  is rather independent from the phase angle  $\phi_0$ , and a threshold velocity of about 92 m/s is found, consistent with the experimental findings. In the  $s = 1$  mode, there is no clearly defined threshold velocity, but similar losses due to excessive transverse focusing occur for velocities below 30 m/s.

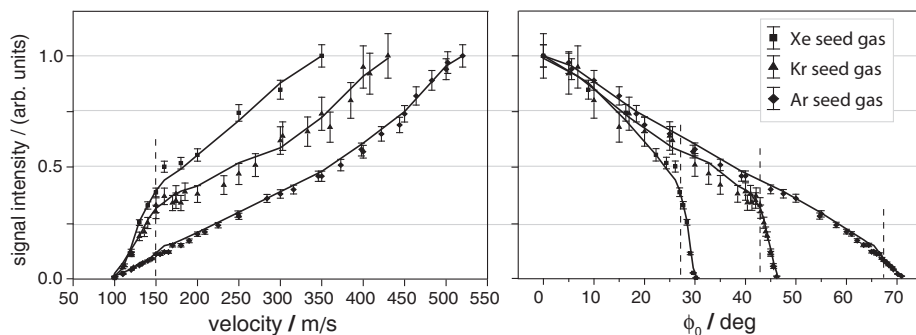


**Figure 5.7:** Maximum signal intensity of decelerated packets of OH radicals as a function of the final velocity (left panel) and as a function of  $\phi_0$  (right panel), using a 316 stage decelerator operating at the  $s = 3$  mode. Beams of OH radicals with three different initial velocities, produced by seeding in Xe, Kr, or Ar, have been used. The intensities that are obtained from numerical simulations of the experiment are shown as solid lines.

The rather high threshold velocity for  $s = 3$  does not severely affect experiments in which Stark-decelerated beams are used for high resolution spectroscopy and collision studies, or in which the decelerated beams are injected into molecular storage rings or synchrotrons. It does affect, however, experiments in which lower final velocities are required, e.g. trap loading experiments. There are several approaches to yet produce decelerated packets at a velocity below the threshold velocity with decelerators that are intended to operate at  $s = 3$ . An electric field geometry for the last section of the decelerator can be designed that permits a gradual reduction of the transverse focusing strength. This can be achieved by a dedicated electrode geometry and/or by a sequential reduction of the voltage that is applied to the electrodes. It is noted that similar strategies have already been implemented in trapping experiments using decelerators in the  $s = 1$  mode [75]. An alternative approach is to develop an electrode geometry for the last segment of the decelerator that allows the confinement of molecules in a genuine traveling potential well. When the velocity of this well is gradually reduced, the packet of molecules can be transferred from the threshold velocity to lower velocities without loss. The trapping of molecules in genuine traveling potential wells has already been demonstrated using optical fields [76] and using electric fields above a micro-structured electrode array [7].

Within the possibilities of the present experimental arrangement, decelerated packets with low final velocities can be produced by changing over from the  $s = 3$  mode to the  $s = 1$  mode before the threshold velocity has been reached. The number of molecules that exit the decelerator at velocities below the threshold velocity strongly depends on the details of the change-over, i.e., the velocity after which  $s = 1$  operation is used, and the phase angles that are used before and after the transition. The influence of the choice of these parameters on the number of molecules that exit the decelerator has experimentally

been studied, decelerating a packet of OH radicals with an initial velocity of 350 m/s. The velocity and position of the packet in the decelerator at which the change-over from  $s = 3$  to  $s = 1$  is made is systematically varied for the target (final) velocities of 100 m/s and 50 m/s. For both velocities the maximum signal intensity is observed when the transition to  $s = 1$  is made when the first  $\sim 300$  stages are operated at  $s = 3$ ,  $\phi_0 \sim 26^\circ$  and when the molecular packet has reached a velocity of 170 m/s. The remaining 12 and 15 stages are then used at  $s = 1$ ,  $\phi_0 = 43.2^\circ$  and  $s = 1$ ,  $\phi_0 = 48.3^\circ$  to produce the final velocities of 100 m/s and 50 m/s, respectively. The gain of this bimodal operation of the Stark decelerator with respect to  $s = 1$  operation is shown in Fig. 5.5 as separate data points. It is observed that for a final velocity of 100 m/s the gain is about a factor of 2, and is close to one for a final velocity of 50 m/s. These measurements demonstrate that low final velocities can be produced with Stark decelerators that are designed to operate at  $s = 3$ , although the efficiency approaches the efficiency of conventional Stark decelerators when the target velocity is much lower than the  $s = 3$  threshold velocity.

### 5.3 Numerical trajectory calculations

The measurements presented thus far demonstrate the performance of the  $s = 1$  and  $s = 3$  modes of operation of Stark decelerators in the (limited) range of parameters that is accessible to the experiment. In this section, both modes of operation are studied in a wider parameter range using numerical trajectory simulations. The electrode geometry that is used in the simulations is the same as used in the experiments, but the decelerator is allowed to have an arbitrary length.

Trajectories of OH radicals through the decelerator are numerically calculated as a function of the phase angle  $\phi_0$  for both the  $s = 1$  and the  $s = 3$  mode of operation. In these simulations, a large number of molecules is homogeneously distributed at the entrance of the Stark decelerator over a block in 6D phase space. This block has a dimension of 20 mm  $\times$  90 m/s in the longitudinal direction, and a dimension of 4 mm  $\times$  25 m/s in each transverse direction. The molecular distribution has a mean forward velocity of 550 m/s at the entrance of the decelerator, and is decelerated or accelerated to a final velocity of 180 m/s or 755 m/s, corresponding to a change in the kinetic energy of 90%. These values are arbitrary and can be chosen without loss of generality, as the phase-space acceptance of a Stark decelerator is in principle independent of the absolute initial and final velocity. The rather high final velocity of 180 m/s for deceleration is chosen to stay away from the velocities for which excessive transverse focusing occurs, as discussed in section 5.2.4. Decelerators containing 781, 388, 256, 190, 151, 126, 111, 102, and 99 electric field stages are simulated that are operated using  $|\phi_0| = 10^\circ, 20^\circ, 30^\circ, 40^\circ, 50^\circ, 60^\circ, 70^\circ, 80^\circ$ , and  $90^\circ$ , respectively. These numbers apply to  $s = 1$ ; for simulations that apply to  $s = 3$  the number of



stages is three times as large. For both values of  $s$ , additional simulations were performed for  $\phi_0 = 0^\circ$  using a 2500 stages long decelerator. In each simulation, a sufficient number (5,000,000 for  $s = 1$  and 500,000 for  $s = 3$ ) of molecules is generated to obtain good statistics. The number of molecules that are within the phase-space distributions of the decelerated packet are counted, and the corresponding 6D volume in phase-space is calculated. In the lower part of **Fig. 5.8**, the simulated longitudinal phase-space distributions for  $\phi_0 = -10^\circ$  are shown both for  $s = 1$  and for  $s = 3$ , together with the separatrices that follow from the 1D model for phase stability [55]. These distributions are representative for the distributions at low phase angles in general, and are shown here to exemplify the simulation method only. The phase-space distribution for  $\phi_0 = -10^\circ, s = 1$  is highly structured with alternating stable and unstable regions. In the distribution for  $\phi_0 = -10^\circ, s = 3$  no clear structure is present. The area within the longitudinal separatrix – the longitudinal acceptance – is a factor  $\sqrt{3}$  smaller for  $s = 3$  than for  $s = 1$  [55].

In the upper panel of **Fig. 5.8**, the resulting simulated 6D phase-space acceptance is shown as a function of  $\phi_0$  for both  $s = 1$  and  $s = 3$ . For  $s = 1$  the phase-space acceptance is maximum for  $\phi_0 = 0^\circ$ , and drops significantly for  $\phi_0 \neq 0^\circ$ . It has a minimum at  $|\phi_0| = 10^\circ$ , is rather constant for  $20^\circ \leq |\phi_0| \leq 50^\circ$ , and drops again for  $|\phi_0| \geq 50^\circ$ , consistent with the experiments in section 5.2.3. Note that the Stark decelerator has a nonzero acceptance for  $|\phi_0| = 90^\circ$ , as discussed before [58]. It is interesting to note that the phase-space acceptance is not symmetric around  $\phi_0 = 0^\circ$ . The phase-space acceptance for  $\phi_0 < 0$  is larger than the acceptance for the same positive phase-angle; molecules spend less time in the decelerator when they are accelerated than when they are decelerated, reducing the loss due to instabilities.

The calculated acceptance for  $s = 3$  shows a rather different trend, and is generally larger for smaller values of  $|\phi_0|$ . Although the longitudinal phase-space acceptance for  $s = 3$  is a factor  $\sqrt{3}$  smaller than for  $s = 1$ , the 6D phase-space acceptance exceeds the acceptance for  $s = 1$  for  $0^\circ \leq |\phi_0| \leq 70^\circ$ . When  $|\phi_0| = 70^\circ$ , the acceptance in both modes of operation is equal, consistent with the experimental findings discussed in section 5.2.2. For  $|\phi_0| \geq 70^\circ$  the acceptance for  $s = 1$  is slightly larger than the acceptance for  $s = 3$ . Although less pronounced, the  $|\phi_0|$  dependence of the acceptance for  $s = 3$  is again asymmetric around  $\phi_0 = 0^\circ$ .

It is interesting to compare the calculated phase-space acceptance with the phase-space acceptance that is expected for a Stark decelerator in which instabilities are absent. From this comparison one can quantify the presence and severeness of instabilities in the  $s = 1$  and  $s = 3$  mode of operation. The longitudinal phase-space acceptance of a decelerator is given by the area within the separatrix. The equations of motion that govern the transverse trajectories of molecules through the decelerator contain time-dependent forces, for which in general no simple analytical solutions exist. These equations, together with the equation for the longitudinal motion, can be used to estimate the volume

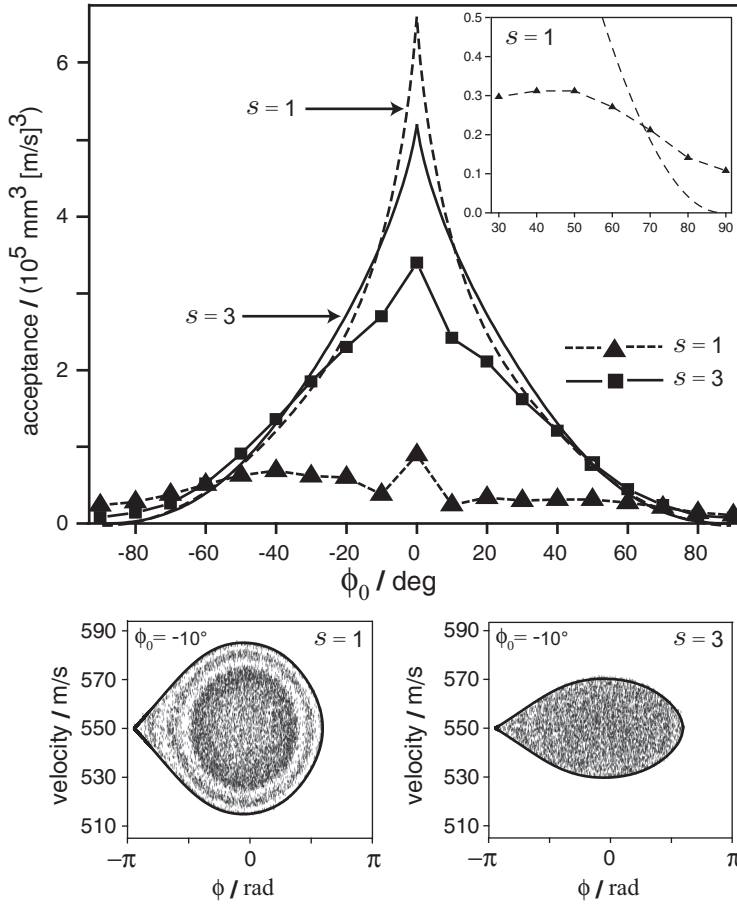


**Figure 5.8:** 6D phase space acceptance of a decelerator as a function of the phase-angle  $\phi_0$ , resulting from numerical trajectory calculations (squares connected with solid lines for  $s = 3$ ; triangles connected with dashed lines for  $s = 1$ ), together with the model predictions (solid line for  $s = 3$ ; dashed line for  $s = 1$ ). In the inset, the  $s = 1$  data is shown enlarged. In the lower part, the longitudinal phase-space distributions that result from the simulations are shown for  $\phi_0 = -10^\circ$ , both for  $s = 1$  and  $s = 3$ .

in phase space from which stable trajectories can originate. This procedure is outlined in detail in the Appendix to this chapter on p. 76, and the resulting 6D phase-space acceptance is shown as a function of  $\phi_0$  for both  $s = 1$  and  $s = 3$  in Fig. 5.8. It is seen that for  $s = 1$  the phase-space acceptance predicted by the model deviates significantly from the calculated acceptance; for  $|\phi_0| \leq 20^\circ$  the deviation is at least an order of magnitude. For larger angles the discrepancy gets less, and both curves cross around  $|\phi_0| = 70^\circ$ . From this comparison it is once more evident that instabilities are present when the decelerator operates

in the  $s = 1$  mode [58], and that these instabilities severely limit the obtainable acceptance.

For the  $s = 3$  mode, the acceptance predicted by the model reproduces the calculated acceptance much better. The agreement for  $|\phi_0| > 40^\circ$  is good, and the deviations are in the 5-20% range for  $20^\circ \leq |\phi_0| \leq 40^\circ$  and about 30 % for  $|\phi_0| < 20^\circ$ . These minor deviations can be taken as an indication for the presence of small instable regions, as have indeed been observed close to the separatrix for  $\phi_0 = 0^\circ$  [58]. The overall agreement, however, demonstrates that the 6D acceptance of a Stark decelerator in the  $s = 3$  mode of operation approaches the optimum value, i.e. the value that is predicted from the model that neglects any instabilities.

## 5.4 Conclusions

The studies presented in this chapter address the question how one can get the highest number density of decelerated molecules with a certain velocity at the exit of a decelerator. Rather than discussing a variety of electrode geometries that one might use to decelerate a beam of polar molecules, these studies focus on a Stark decelerator in the conventional, experimentally proven design. This decelerator can run at different phase-angles and operate in different modes, and can be built with a variable length. The number density of accelerated and decelerated OH radicals has been experimentally studied as a function of these three parameters. Quantitative comparisons of these number densities, obtained using Stark decelerators with different parameter sets, have been made. The measurements have been substantiated by numerical simulations, from which comparisons for a much wider range of parameters can be made. These studies provide quantitative arguments for the design criteria of Stark decelerators for specific applications.

Based on the one-dimensional description of a Stark decelerator, one would expect more molecules at the end of the decelerator for longer decelerators that run at lower phase-angles. This description neglects the coupling between the longitudinal and transverse motion, however, which limits the actual 6D acceptance of a decelerator. A first important conclusion from the present study is that, for a decelerator operating in the  $s = 1$  mode, a strategy to optimize the number of decelerated molecules by using low phase angles and a large number of deceleration stages is only of limited use. There is a maximum of the 6D acceptance for a phase-angle of around  $50^\circ$ , and the optimum number of molecules is obtained when the length of the decelerator (for a given initial and final velocity) is adjusted such that this phase-angle can be used. A decelerator of 150 stages that is operated at  $50^\circ$ , for instance, produces more decelerated molecules than a decelerator of 250 stages that runs at a phase angle of  $30^\circ$ .

A second important conclusion is that a decelerator that operates in the  $s = 3$  mode outperforms a decelerator in the  $s = 1$  mode in almost all cases.

In the  $s = 3$  mode, coupling between the longitudinal and transverse motion is nearly absent, and lower phase angles always result in a larger acceptance. For small phase angles, a gain up to a factor of ten can be obtained. The gain depends strongly on the phase angle that is used and for phase angles above  $70^\circ$ , the acceptance for the two modes of operation is very similar. An intrinsic disadvantage of the  $s = 3$  mode is that there are large losses for final velocities below around 150 m/s. Lower velocities can still be produced, however, and different schemes have been discussed and demonstrated for this.

A third important conclusion is that the acceptance of a Stark decelerator operating in the  $s = 3$  mode approaches the optimum value. This conclusion is based on a comparison between the outcome of numerical trajectory calculations and the 6D acceptance that is derived from a model. In this model, couplings between the longitudinal and transverse motion are neglected.

To make use of the advantages that the  $s = 3$  mode of operation offers, a considerably longer Stark decelerator is needed than for the  $s = 1$  mode. This indeed requires more electrode pairs and a longer vacuum chamber, but it should be realized that there is no additional requirement on the high voltage electronics. Compared to the decelerators that have been commonly used so far ( $s = 1$ ,  $\approx 100$  stages,  $\phi_0 = 50 - 60^\circ$ ) a five times longer version operating in the  $s = 3$  mode at somewhat lower phase angles will typically result in a factor five higher number density at the exit. Moreover, this gain in number density is accompanied by a reduction in the longitudinal translational temperature.

## 5.5 Appendix

In chapter 3 (pp. 38), we studied the transverse stability in a Stark decelerator. Here we adapt the model for the transverse motion of molecules through a Stark decelerator, with the goal to derive the 6D phase-space acceptance as a function of the phase angle  $\phi_0$ .

In the description of the motion of the OH radicals through the decelerator, the  $z$  coordinate describes the position of the molecule along the molecular beam axis, while  $x$  and  $y$  are the transverse coordinates. The forces in the  $x$  and the  $y$  direction are assumed to be uncoupled from each other and identical. The alternating focussing in either one of the transverse directions (say  $y$ ) is represented by an average transverse force  $\bar{F}_y(\phi, y)$  that depends on the phase  $\phi$  of the molecule and on  $y$ -position, as described on pp. 38. We therefore define:

$$\begin{aligned}\bar{F}_y(\phi, y) &= \frac{1}{2T} \int_t^{t+2T} F_y(y(t'), z(t'), t') dt' \\ &\approx \frac{1}{2sL} \int_{\phi L/\pi}^{(\phi+2s\pi)L/\pi} F_y(y, z) dz,\end{aligned}\tag{5.1}$$

where  $2T$  is the time during which the synchronous molecule travels a distance  $2sL$ .

To a reasonable approximation, the transverse force  $\bar{F}_y$  is linear in the displacement  $y$  from the molecular beam axis. The strength of the transverse force can be expressed in terms of a frequency  $\omega_y(\phi)/2\pi$ , referred to hereafter as the natural transverse oscillation frequency, using the relation:

$$\bar{F}_y(\phi, y) = -m\omega_y^2(\phi)y, \quad (5.2)$$

where  $m$  is the mass of the OH radical. In **Fig. 5.9**, the natural transverse oscillation frequency is shown for an OH ( $X^2\Pi_{3/2}, J = 3/2, |M_J| = 3/2$ ) radical as a function of its phase  $\phi$ . For  $s = 1$ , the natural transverse oscillation frequency has a strong dependence on the phase  $\phi$ . For molecules close to  $\phi = 0^\circ$ , the transverse frequency is very low and focussing forces are almost absent. For  $s = 3$ , the natural transverse oscillation frequency is rather independent from the phase  $\phi$ .

The transverse phase-space acceptance for a given mode of operation of the decelerator is evaluated as schematically illustrated in **Fig. 5.10**. The decelerator is operated at  $\phi_0 = 30^\circ$  and  $s = 1$  in this example. Let's consider a molecule with a maximum deviation  $z_i$  from the synchronous molecule. The frequency  $\omega_y(t)$  of this molecule can be constructed from its phase  $\phi(t)$  as it revolves around the synchronous molecule in longitudinal phase-space. Let's now consider an ensemble of molecules that is enclosed by this contour, and by a contour that is displaced by an infinitesimal value  $\Delta z_i$ . All these molecules experience the same temporal dependence of the transverse focusing force, and the transverse trajectories of the molecules are governed by the equation:

$$\frac{d^2y}{dt^2} + \omega_y^2(t)y = 0. \quad (5.3)$$

The transverse phase-space acceptance is easily calculated only if  $\omega_y^2(t)$  is con-

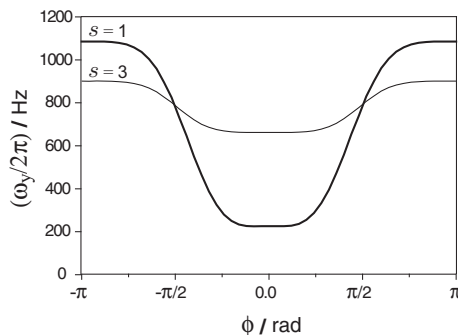


**Figure 5.9:** Natural transverse oscillation frequency  $\omega_y/2\pi$  for an OH ( $X^2\Pi_{3/2}, J = 3/2, |M_J| = 3/2$ ) radical as a function of its phase  $\phi$  in a Stark decelerator, for the operation modes  $s = 1$  and  $s = 3$ .

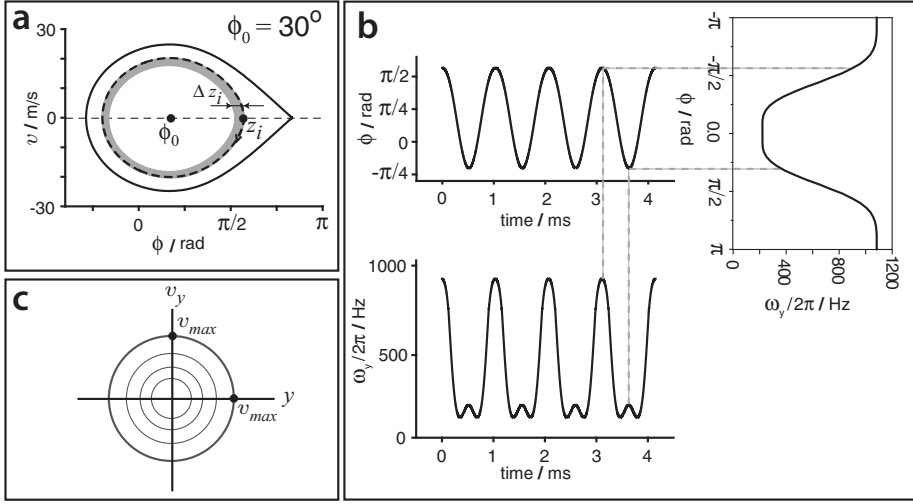


**Figure 5.10:** Schematic representation of the method used to calculate the transverse phase-space acceptance. (a) The trajectory of a molecule in longitudinal phase-space, shown as a dashed line. (b) The time dependence of the natural transverse oscillation frequency is constructed from the time dependence of the phase  $\phi(t)$ , and the phase dependence of the natural transverse oscillation frequency  $\omega_y(\phi)/2\pi$ . (c) The time-averaged transverse focusing force results in elliptical orbits in transverse phase-space.

stant. In this case, in which  $\omega_y(t)$  is written as  $\omega_y$ , the longitudinal and transverse motions are uncoupled, and in each transverse direction the molecules orbit ellipses in transverse phase-space, as is shown in **Fig. 5.10**. The phase space acceptance  $(A_y)_{z_i}$  and  $(A_x)_{z_i}$  in each transverse direction is given by the maximum extension  $y_{max} = x_{max} = 1.5$  mm from the molecular beam axis, and by the maximum transverse velocity  $v_{y,max} = v_{x,max} = \omega_y \times y_{max}$  that can be captured. The 4D volume  $(A_t)_{z_i}$  of the transverse phase-space acceptance is then given by

$$(A_t)_{z_i} = (A_x)_{z_i} (A_y)_{z_i} = (\pi \omega_y (y_{max})^2)^2. \quad (5.4)$$

If  $\omega_y^2(t)$  is not constant, as is actually the case in a Stark decelerator, the molecules experience a transverse frequency  $\omega_y(t)$  that oscillates between the minimum value  $\omega_y^{\min}$  and the maximum value  $\omega_y^{\max}$ . The time-averaged value of  $\omega_y^2$  for this molecule is given by:

$$\langle \omega_y^2 \rangle_{z_i} = \frac{1}{\tau} \int_0^\tau \omega_y^2(t) dt, \quad (5.5)$$

where  $\tau$  is the time it takes the molecule to revolve the contour in longitudinal phase-space. The transverse phase-space acceptance cannot be calculated anymore, but the values of  $\omega_y^{\min}$ ,  $\omega_y^{\max}$ , and  $\sqrt{\langle \omega_y^2 \rangle_{z_i}}$  can nevertheless be used to

characterize the transverse phase-space acceptance of the ensemble of molecules in three limiting cases. When the longitudinal oscillation frequency is much larger than the transverse oscillation frequency,  $\omega_y$  can be taken as  $\sqrt{\langle \omega_y^2 \rangle_{z_i}}$ . In that case, one obtains the 4D transverse acceptance for the molecules in this shell in longitudinal phase-space. This 4D acceptance can be interpreted as the best estimate for the true transverse acceptance. When  $\omega_y^{\max}$  is used, a transverse acceptances results that can be interpreted as a strict upper limit for the true acceptance.

The total 6D phase-space acceptance  $A(\phi_0)$  is obtained by integrating over all shells with area  $dA_z$  within the separatrix in longitudinal phase-space:

$$A(\phi_0) = \int (A_y)_{z_i} (A_x)_{z_i} dA_z. \quad (5.6)$$

In **Fig. 5.11**, the longitudinal (2D), transverse (2D) and total (6D) phase-space acceptances are shown for the operation modes  $s = 1$  and  $s = 3$ . The transverse acceptance  $A_y(\phi_0)$  is calculated from the total 6D acceptance  $A(\phi_0)$  and the longitudinal acceptance  $A_z(\phi_0)$  via  $A_y(\phi_0) = \sqrt{A(\phi_0)/A_z(\phi_0)}$ . For each mode of operation three curves are shown; the lower, center, and upper curve correspond to the choice of  $\omega_y^{\min}$ ,  $\sqrt{\langle \omega_y^2 \rangle_{z_i}}$ , and  $\omega_y^{\max}$  for  $\omega_y$  in equation (5.4), respectively. The longitudinal acceptance  $A_z(\phi_0)$  is a factor  $\sqrt{3}$  smaller for  $s = 3$  than for  $s = 1$ . The transverse acceptance for  $s = 3$  is somewhat larger than for  $s = 1$  and is almost independent of  $\phi_0$ . Furthermore, the three different curves predict a rather similar transverse acceptance for  $s = 3$ . The three curves for the transverse acceptance for  $s = 1$  differ much more among each other. The center curves that are shown in Fig. 5.11(c), and that have been used in Fig. 5.8 of section 5.3, predict a rather similar total 6D phase-space acceptance for  $s = 1$  and  $s = 3$ . For almost all phase angles, the lower longitudinal phase-space acceptance for  $s = 3$  is compensated for by the larger transverse acceptance of  $s = 3$ .

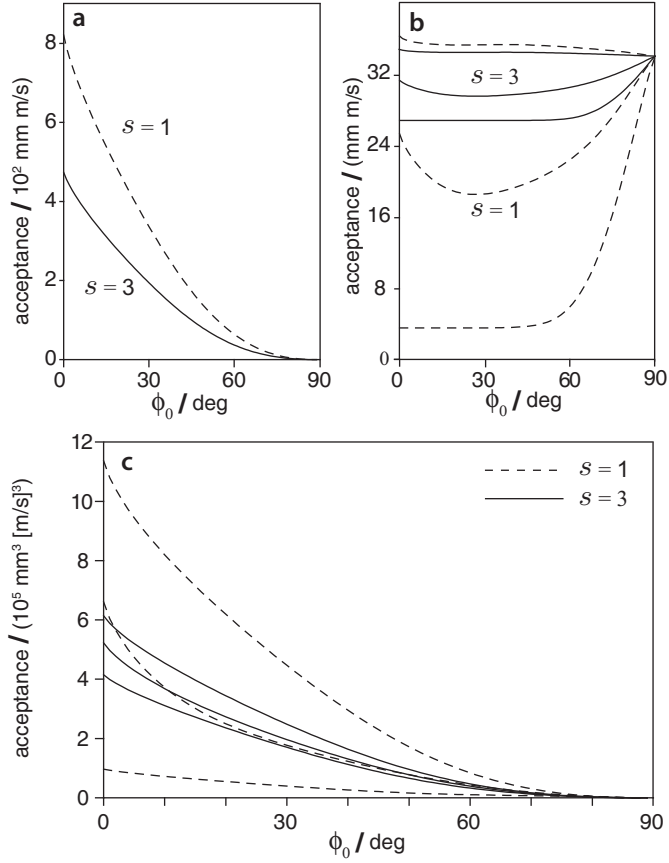


**Figure 5.11:** Prediction for the longitudinal (a), transverse (b) and total 6D (c) phase-space acceptance of a Stark decelerator for the operation modes  $s = 1$  (dashed curves) and  $s = 3$  (solid curves) as a function of the phase angle  $\phi_0$ . For the transverse and 6D acceptances, three curves are shown for each mode of operation that predict the phase space acceptance in three limiting cases, as explained in the text. The center curves describe the best estimate for the acceptance in the limit that instabilities in the decelerator can be neglected, and have been used in Fig. 5.8 of section 5.3.



## Chapter 6

# Crossed beam scattering with Stark-decelerated molecules

As explained in detail in the previous chapters, polar molecules in specific quantum states can be picked up from a supersonic expansion to be decelerated or accelerated. Multi-stage Stark deceleration is often highly state selective and therefore a natural application for such a beam is state-to-state inelastic scattering at a precisely defined and also tunable collision energy. In the present work, the Stark-deceleration machine is combined with a standard pulsed beam source which provides a supersonic beam of rare gas atoms. In the following it is analysed in detail what type of scattering cross sections can be determined with such a setup and what is required to reliably extract the cross sections from measurements.

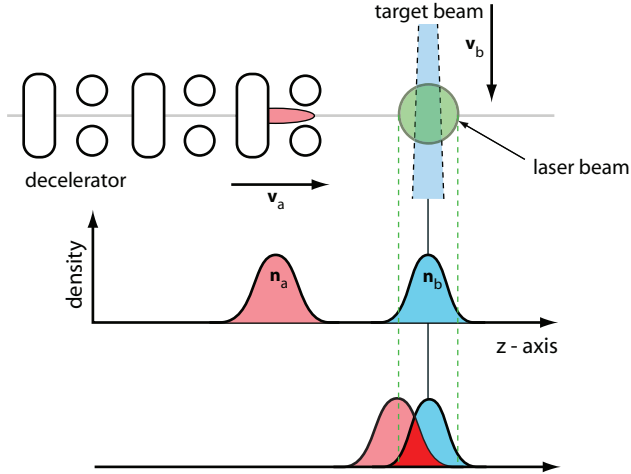


**Figure 6.1:** Scheme of the experimental setup used for the scattering experiments.

## 6.1 Introduction

The scattering experiment proceeds as sketched in **Fig. 6.1**: an incoming pulse of state-selected OH molecules with mean velocity  $\mathbf{v}_a$  and number density  $n_a(\mathbf{r}, t)$  is supplied by the decelerator and propagates freely towards a target beam of rare gas atoms with mean velocity  $\mathbf{v}_b$  and density  $n_b(\mathbf{r}, t)$ . Both particle sources are pulsed and therefore the number densities are functions of position  $\mathbf{r}$  and time  $t$ . The central axes of both beams cross at a right angle. While passing through the target beam, some of the OH molecules are scattered and their internal quantum state changes (*inelastic* scattering). To detect such events, the scattered molecules are excited state sensitively by a pulsed laser beam which propagates orthogonally to both molecular beam axes. The subsequently emitted fluorescence is imaged onto a photo multiplier tube by a lens and hence provides a signal that is proportional to the number of molecules in a specific state at a certain time and within a certain volume, provided suitable conversion factors are taken into account. This signal is henceforth referred to as the *collision signal*. With this experimental configuration one can in principle determine the following quantities:

1. the cross section ratios for different inelastic scattering channels for a fixed collision energy, so-called *relative* cross sections
2. the energy dependence of the cross sections up to an energy independent scaling factor, i.e. the shape of the so called *excitation functions*
3. the total absolute cross section for inelastic scattering for a given energy.

During the time interval in which the density functions  $n_a$  and  $n_b$  have spatial overlap, collisions occur at a rate that is proportional to the cross section for the considered inelastic transition. Hence, the total number of molecules that are scattered into a specific state until a certain time is strictly proportional to the corresponding cross section. While the incoming molecules have a well defined mean velocity with a narrow distribution, the scattered molecules have, in general, a broad velocity distribution. Since slow molecules tend to reside longer within the detection volume as compared to fast ones there is the possibility that the relative collision signals are not exactly proportional to the respective cross sections. Hence, if cross sections pertaining to case (1) are to be accurately measured, the detection probability for all states which are monitored also has to be determined.

For case (2), we have the same requirement as for (1) but additionally, all factors (apart from the cross section itself) which determine the collision product creation as a function of the collision energy must also be known. The main difficulty here lies in the precise determination of the spatial beam overlap as a function of time.

For measurements of type (3), no knowledge about the detection probabilities is required because it is merely the decrease of the initial population that has to be determined. What is required, but difficult to measure, is the target beam density.

Before these three cases are discussed in detail, we review the most essential aspects of the classical two body collision problem and we derive some pertinent formulae which relate the scattering cross section to experimentally accessible quantities. The discussion given in the following sections is to some extent specialized to the considered experimental setup, but it is with obvious modifications also applicable to cases where more conventional pulsed beams are used.

## 6.2 Collision kinematics and classical dynamics

### 6.2.1 Conservation laws

The classical two-body problem is special insofar as for this case the conservation laws alone impose fairly severe constraints upon the possible post collision velocities and thereby on the possible particle trajectories. The following detailed analysis will show how this information can be used to design the crossed

beam experiment in such a way that cross sections can be determined with the least possible error.

Let two point particles  $a$  and  $b$  with masses  $m_{a(b)}$  approach each other with laboratory position  $\mathbf{r}_{a(b)}$  and velocity  $\mathbf{v}_{a(b)}$ , as shown in **Fig. 6.2**. We denote the relative position by  $\mathbf{r}$  and the relative velocity by  $\mathbf{g}$ ; the position of the center of mass is  $\mathbf{R}$  and its corresponding velocity  $\mathbf{V}$ . For later reference the used kinematic variables are collected in the following:

**reduced mass:**

$$\mu := \frac{m_a m_b}{m_a + m_b} \quad (6.1)$$

**position:**

$$\mathbf{R} := \frac{m_a \mathbf{r}_a + m_b \mathbf{r}_b}{m_a + m_b} \quad (6.2)$$

$$\mathbf{r} := \mathbf{r}_a - \mathbf{r}_b \quad (6.3)$$

$$\mathbf{r}_a = \mathbf{R} + \frac{m_b}{m_a + m_b} \mathbf{r} = \mathbf{R} + \frac{\mu}{m_a} \mathbf{r} \quad (6.4)$$

$$\mathbf{r}_b = \mathbf{R} - \frac{m_a}{m_a + m_b} \mathbf{r} = \mathbf{R} - \frac{\mu}{m_b} \mathbf{r} \quad (6.5)$$

**velocity:**

$$\mathbf{V} := \dot{\mathbf{R}} = \frac{m_a \dot{\mathbf{r}}_a + m_b \dot{\mathbf{r}}_b}{m_a + m_b} \quad (6.6)$$

$$\mathbf{g} := \dot{\mathbf{r}} = \dot{\mathbf{r}}_a - \dot{\mathbf{r}}_b \quad (6.7)$$

$$\mathbf{v}_a := \dot{\mathbf{r}}_a = \dot{\mathbf{R}} + \frac{\mu}{m_a} \mathbf{g} \quad (6.8)$$

$$\mathbf{v}_b := \dot{\mathbf{r}}_b = \dot{\mathbf{R}} - \frac{\mu}{m_b} \mathbf{g} \quad (6.9)$$

$$\mathbf{u}_a := \mathbf{v}_a - \dot{\mathbf{R}} = \frac{\mu}{m_a} \mathbf{g} \quad (6.10)$$

$$\mathbf{u}_b := \mathbf{v}_b - \dot{\mathbf{R}} = -\frac{\mu}{m_b} \mathbf{g} \quad (6.11)$$

If the particle velocities are given relative to the the center of mass velocity  $\mathbf{V}$ , as in (6.10) and (6.11), then the corresponding momenta  $m_a \mathbf{u}_a$  and  $m_b \mathbf{u}_b$  have equal magnitudes and point into opposite directions at any time *by definition*, i.e. regardless of whether or not the total momentum is conserved.

It remains to be seen in which cases the equations of motion for the center of mass  $\mathbf{R}$  and for the relative position  $\mathbf{r}$  will be independent. Assume that particle  $a$  experiences a force  $\mathbf{F}_{ab}$  due to particle  $b$ , which in turn experiences a force  $\mathbf{F}_{ba}$  due to the presence of particle  $a$ . In general, external (or inertial) forces  $\mathbf{F}_a^e$  and  $\mathbf{F}_b^e$  can also be present, as e.g. the gravitational or the Coriolis force. If the collisions happen in external electric or magnetic fields, as present in a trap or a storage ring, quantum state specific external forces must be included

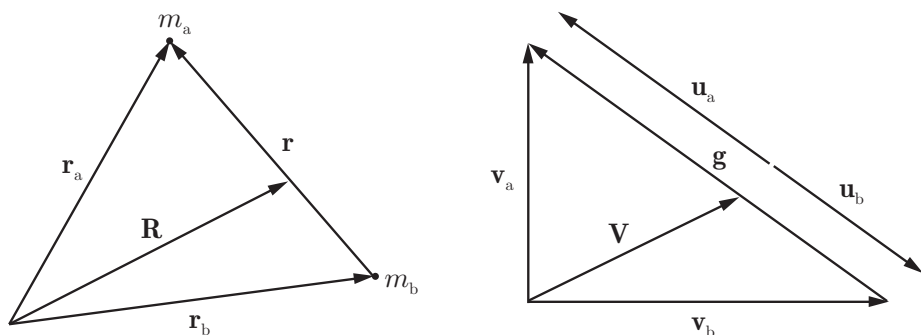


**Figure 6.2:** Definition of coordinates and velocities.

as well. The equations of motion are:

$$\ddot{\mathbf{R}} = \frac{\mathbf{F}_{ab} + \mathbf{F}_{ba}}{m_a + m_b} + \frac{\mathbf{F}_a^e + \mathbf{F}_b^e}{m_a + m_b} \quad (6.12)$$

$$\ddot{\mathbf{r}} = \frac{\mathbf{F}_{ab}}{m_a} - \frac{\mathbf{F}_{ba}}{m_b} + \frac{\mathbf{F}_a^e}{m_a} - \frac{\mathbf{F}_b^e}{m_b}. \quad (6.13)$$

If the interaction forces are equal in magnitude and point into opposite directions so that  $\mathbf{F}_{ab} = -\mathbf{F}_{ba}$ , the equations simplify to:

$$\ddot{\mathbf{R}} = \frac{\mathbf{F}_a^e + \mathbf{F}_b^e}{m_a + m_b} \quad (6.14)$$

$$\ddot{\mathbf{r}} = \frac{\mathbf{F}_{ab}}{\mu} + \frac{\mathbf{F}_a^e}{m_a} - \frac{\mathbf{F}_b^e}{m_b}. \quad (6.15)$$

If no external forces are present, the relative motion is influenced only by the mutual force and the total momentum  $(m_a + m_b)\mathbf{V}$  is conserved. The gravitational force, if it is included, is proportional to the masses and (6.15) shows that it disappears from the equation for the relative motion, but it does of course lead to an acceleration of the center of mass. The equations we have to consider are therefore:

$$\ddot{\mathbf{R}} = \mathbf{a}_{gr} \quad (6.16)$$

$$\ddot{\mathbf{r}} = \frac{\mathbf{F}_{ab}}{\mu} \quad (6.17)$$

where  $\mathbf{a}_{gr}$  is the gravitational acceleration. We see that the total momentum given by  $(m_a + m_b)\mathbf{V}$  changes linearly in time. On the time scales considered here the gravitational force has no significant effect upon the particle trajectories.

All collisions conserve the energy. The total kinetic energy  $T$ , as calculated in the laboratory frame, can be related to the velocity of the center of mass and

to the relative velocity using the above definitions:

$$T = \frac{m_a + m_b}{2} V^2 + \frac{\mu}{2} g^2 =: T_{cm}(V) + T_{rel}(g). \quad (6.18)$$

This formula implies no assumptions about the forces, it is merely a result of the coordinate transformation; the kinetic energy splits into two parts which are independent in our case because  $V$  and  $g$  are independent. The interesting part is the kinetic energy of the relative motion  $T_{rel} = \mu g^2/2$ , the so called *collision energy*. If before and after the collision this part remains the same, the collision is said to be *elastic*, whereas otherwise it is said to be *inelastic*. If at least one of the particles has internal degrees of freedom, internal energy can be taken up from or released into the relative motion. Using energy conservation alone, only the length of the relative velocity vector after the collision, denoted by  $g'$ , can be inferred if the change of the internal energy  $\Delta E_{int}$  is given:

$$g' = g \sqrt{\frac{T_{rel} + \Delta E_{int}}{T_{rel}}}, \quad (6.19)$$

where  $\Delta E_{int}$  is positive if energy is released into the relative motion and negative in the opposite case. If the beams cross at a right angle (other angles are discussed in chapter 9 in connection with the overall energy resolution), the collision energy is a linear combination of the laboratory translational energies  $T_a$  and  $T_b$  of particle  $a$  and  $b$  given by:

$$T_{rel}^{90^\circ} = \frac{\mu}{2} g^2 = \frac{\mu}{2} (v_a^2 + v_b^2) = \frac{\mu}{m_a} T_a + \frac{\mu}{m_b} T_b. \quad (6.20)$$

Another important quantity to consider is the total angular momentum. For two point particles it is given by:

$$\mathbf{L} = m_a(\mathbf{r}_a \times \mathbf{v}_a) + m_b(\mathbf{r}_b \times \mathbf{v}_b) \quad (6.21)$$

$$= (m_a + m_b)\mathbf{R} \times \mathbf{V} + \mu \mathbf{r} \times \mathbf{g} \quad (6.22)$$

$$= \mathbf{L}_{cm} + \mathbf{L}_{rel}. \quad (6.23)$$

Again, this formula is valid for any type of force. The angular momentum vector *of the relative motion* does not change with time, if the external forces are proportional to the masses and if the particles interact via forces which are not only equal in magnitude and point into opposite directions, but are also directed along the relative position  $\mathbf{r}$ ; if this is the case, the relative angular momentum is conserved:

$$\partial_t \mathbf{L} = (m_a + m_b)\mathbf{R} \times \dot{\mathbf{V}} + \mu \mathbf{r} \times \dot{\mathbf{g}} \quad (6.24)$$

$$= \mathbf{R} \times (\mathbf{F}_a^e + \mathbf{F}_b^e) + \mathbf{r} \times \mathbf{F}_{ab} \quad (6.25)$$

$$= \mathbf{R} \times (m_a + m_b)\mathbf{a}_{gr}. \quad (6.26)$$

With gravity included, only the angular momentum of the center of mass motion changes in time, while the relative motion is confined to the plane perpendicular to  $\mathbf{L}_{rel}$ . In crossed beam experiments the relative velocity is usually rather well defined. Yet, the relative angular momentum of a particle pair is not well defined. In fact,  $\mathbf{L}_{rel}$  samples all directions and magnitudes because the relative position is not controlled in the experiment. Therefore, even if the forces conserve the relative angular momentum,  $\mathbf{g}'$  does not remain in the plane spanned by the *initial* laboratory velocity vectors  $\mathbf{v}_a$  and  $\mathbf{v}_b$ , unless  $\mathbf{r}$  happens to lie in that same plane initially. Therefore, every interaction between the two particles is bound to rotate the relative velocity vector out of its initial plane.

## 6.2.2 Newton diagram for elastic and inelastic collisions

The magnitude of the relative velocity after the collision is fixed through energy conservation. Its orientation is determined through the scattering dynamics which in turn depend on the initial conditions and the intermolecular potential. The angle between  $\mathbf{g}'$  and  $\mathbf{g}$ , the so called *scattering angle*, is denoted by  $\theta$ . The second angle which is needed to fix the orientation of  $\mathbf{g}'$  will be denoted by  $\phi$ .

If the forces conserve the relative angular momentum, the initial conditions alone determine  $\phi$  while the scattering angle  $\theta$  is determined by the equations of motion and the initial conditions. As noted before, the initial relative position is not controlled in a gas phase scattering experiment and therefore an ensemble of particles scatters in such a way that  $\phi$  is homogeneously distributed between 0 and  $2\pi$  for every given  $\theta$ . Even if the forces do not conserve the relative angular momentum, this is true as well. The only difference is that the initial conditions alone no longer determine  $\phi$ .

The relations discussed so far are conveniently visualized in the *Newton diagram*. In **Fig. 6.3** the relevant velocities and angles are indicated. The final laboratory velocity vector  $\mathbf{v}'_a$  is determined if  $\mathbf{u}'_a$  is known. In the special case where the inelastic collision consumes the total available collision energy,  $\mathbf{v}'_{a(b)} = \mathbf{V}$  holds and the scattering dynamics are defined completely through energy conservation alone. One speaks of *forward*, *sideways* or *backward* scattering if the values of the scattering angle  $\theta$  lie at around  $0^\circ$ ,  $90^\circ$  or  $180^\circ$  respectively.

## 6.3 The cross section

### 6.3.1 Definition of the cross section

The cross section can be defined in the following way (see e.g. [77]). We imagine that a single scattering target is given and held fixed in space. Particles approach this target with identical velocities  $\mathbf{v}$  and pass through a plane of area  $A$  *perpendicular* to  $\mathbf{v}$ . The target is located far enough behind this plane so that there is not yet any influence on the trajectories of the particles and the plane

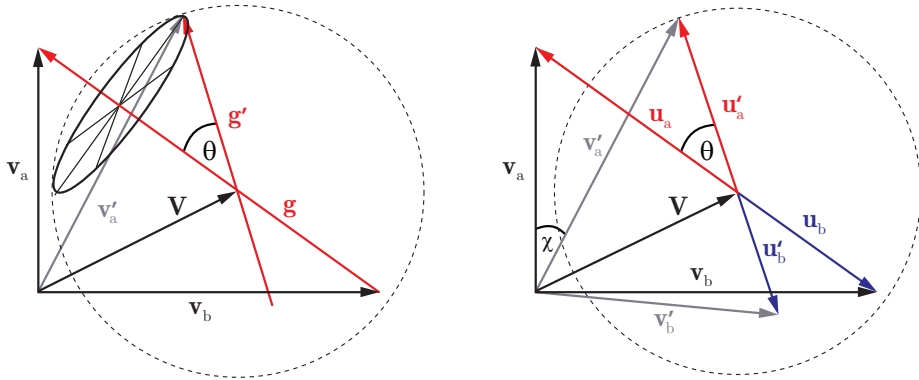


**Figure 6.3:** The Newton diagram for the scattering of two point particles; the *scattering angle* is denoted by  $\theta$ , whereas the laboratory scattering angle of particle  $a$  is denoted by  $\chi$ .

is intersected by the particles at totally random positions. The cross section then relates the number of particles that are scattered by the target  $N_{sc}$  to the number of incoming particles  $N_{inc}$  having passed through area  $A$ :

$$N_{sc} = \sigma \frac{N_{inc}}{A}. \quad (6.27)$$

The collision probability  $N_{sc}/N_{inc}$  is therefore given by the ratio  $\sigma/A$ . What defines a scattering event? Clearly, the event must be countable in some way and this is certainly the case if the collision changes the internal state of the incoming particle. Another possibility is to count particles which are scattered into a specific direction. The magnitude of the cross section is a function of the internal state of the particles and of the collision energy; it may also depend on the presence of external fields.

As such, the given definition of the cross section is still somewhat remote from any measurable quantity. More useful relations are therefore given in the following. Let incoming molecules of type ( $a$ ) form a beam with constant flux  $J_a$ , that is let  $N_a$  molecules pass through a plane with area  $A$  in time  $\Delta t$ . If a number  $N_b$  of fixed targets is present within this beam, the number of scattered molecules per unit time is:

$$\frac{N_{sc}}{\Delta t} = \sigma \frac{N_a}{A \Delta t} N_b = \sigma J_a N_b \quad (6.28)$$

or equivalently

$$\frac{N_{sc}}{\Delta t} \frac{1}{J_a} \frac{1}{N_b} = \sigma, \quad (6.29)$$

which shows that the cross section can be inferred if the number of scattering events per time interval, the number of targets and the incoming flux is known.



Instead of counting *all* scattered particles, we may also count only those that are scattered into a specific direction  $\mathbf{n}$ . Let the cross section for scattering into a solid angle  $d\Omega$  in the direction  $\mathbf{n}$  be denoted by  $G(\mathbf{n})d\Omega$  or by  $G(\theta, \phi) \sin(\theta)d\phi d\theta$  if spherical coordinates are used. The particles scattered into a solid angle  $d\Omega$  at  $\mathbf{n}$  in a given time interval form a flux  $J_{sc}(\mathbf{n})$  in the direction  $\mathbf{n}$ . The angle resolved cross section  $G(\theta, \phi)$ , the so called *differential cross section* (DCS), is therefore related to the outgoing ( $J_{sc}$ ) and incoming flux ( $J_a$ ) by:

$$\frac{N_{sc}(\mathbf{n})}{\Delta t} \frac{1}{d\Omega} \frac{1}{J_a} \frac{1}{N_b} = \frac{J_{sc}(\mathbf{n})}{J_a} \frac{1}{N_b} =: G(\mathbf{n}). \quad (6.30)$$

The incoming flux  $J_a$  refers to a *plane* area with dimension length squared whereas the outgoing flux  $J_{sc}$  refers to a *curved* area given in units of sterad ( $4\pi$  times the fraction of area on the unit sphere). Since the DCS does not depend on  $\phi$  the cross section for scattering with deflection angle  $\theta$  and arbitrary  $\phi$  is  $2\pi \sin(\theta)G(\theta)d\theta$ .

Usually the target molecules are dispersed homogeneously within a scattering volume  $V$ . The scattering events per time and volume are then given by

$$\dot{n}_{sc} := \frac{N_{sc}}{\Delta t V} = \sigma \frac{N_a}{A \Delta t} n_b = \sigma J_a n_b, \quad (6.31)$$

with the number density  $n_b = N_b/V$  within the scattering volume. If the considered incoming molecules of *a*-type approach with speed  $v_a$  along parallel lines, the flux is  $J_a = n_a v_a$  with number density  $n_a$  in the beam. Therefore the scattering rate per scattering volume is:

$$\dot{n}_{sc} = \frac{N_{sc}}{\Delta t V} = \sigma v_a n_a n_b. \quad (6.32)$$

Generalized to inhomogeneous and time dependent number densities the scattering rate per volume is a function of position  $\mathbf{r}$  and time  $t$ :

$$\dot{n}_{sc}(\mathbf{r}, t) = \sigma v_a n_a(\mathbf{r}, t) n_b(\mathbf{r}, t). \quad (6.33)$$

For pulsed beams the total number of scattered molecules as a function of time is therefore determined by an integration over the beam intersection volume and the relevant time interval.

Until now, the target molecules were considered at rest in space. For two crossed beams with laboratory velocities  $\mathbf{v}_a$  and  $\mathbf{v}_b$  the speed  $v_a$  in the previous formulae has to be replaced with the relative speed  $g = |\mathbf{g}| = |\mathbf{v}_a - \mathbf{v}_b|$ :

$$\dot{n}_{sc}(\mathbf{r}, t) = \sigma g n_a(\mathbf{r}, t) n_b(\mathbf{r}, t). \quad (6.34)$$

This replacement is allowed if we think of the plane that is intersected by the *a*-type molecules as perpendicular to  $\mathbf{g}$  rather than  $\mathbf{v}_a$ .

The direct determination of *absolute* state-to-state inelastic cross sections is possible only, if the absolute number of molecules that are scattered into a

specific state within a certain time interval and volume can be measured, and if furthermore the density (distribution) of both beams is known. Usually this kind of information is too difficult to obtain and cross sections are determined up to a scaling factor. If the (absolute) total inelastic cross section is of interest, one may proceed as described in section 6.3.3 – in this case only the target beam density must be known.

### 6.3.2 The scattering probability of a molecule

What is the probability that a given molecule with specified initial position and velocity collides at a certain time while passing through a beam of target molecules? Due to the homogeneous but random distribution of the target molecules there exists a *time independent* chance to collide within a time interval  $dt$ . This quantity, which we shall denote by  $k$ , is the *collision rate*: the probability density to scatter in a time interval  $dt$ . Starting with  $N_a$  molecules at some initial position in the target beam the change of  $N_a$  is:

$$\frac{dN_a(t)}{N_a(t)} = -kdt, \quad (6.35)$$

where  $N_a(t)$  denotes the number of molecules that have not yet collided with a target. To identify the relation between  $k$  and the cross section, we write the previous equation in the form:

$$\frac{N_{sc}}{\Delta t} = -\frac{dN_a}{dt} = kN_a. \quad (6.36)$$

The number of scattering events  $N_{sc}$  is given by (6.28):

$$\frac{N_{sc}}{\Delta t} = \sigma \frac{N_a N_b}{\Delta t A} \quad (6.37)$$

where we think of  $N_a$  stationary molecules being approached by a flux  $N_b/\Delta t A = gn_b$  of  $b$ -molecules moving with velocity  $-\mathbf{g}$ :

$$\frac{N_{sc}}{\Delta t} = \sigma gn_b N_a. \quad (6.38)$$

The relation between the collision rate and the cross section is found by comparing this equation with (6.36):

$$k = \sigma gn_b. \quad (6.39)$$

We may now proceed to calculate the scattering probability for a single  $a$ -molecule moving with speed  $g$  through stationary  $b$ -molecules. Denote the probability for scattering at time  $t$  within a time interval  $dt$  by  $p(t)dt$ , then

$$p(t)dt = -\frac{dN_a(t)}{N_a(0)}. \quad (6.40)$$

Using the time evolution

$$N_a(t) = N_a(0)e^{-kt}, \quad (6.41)$$

the collision probability is therefore

$$p(t)dt = ke^{-kt}dt = \sigma g n_b e^{-\sigma g n_b t} dt. \quad (6.42)$$

If the decline of the initial population is small, that is if the exponential remains close to unity within the time considered, the scattering experiment proceeds under quasi single collision conditions and for the scattering probability we have  $p(t)dt \approx \sigma g n_b dt$ . Since all molecules move with the same speed  $g$ , we can rewrite the probability in terms of the position  $l$  by noting that  $dt = 1/g dl$  where  $dl$  is the distance traveled in time  $dt$  in the direction of  $g$ :

$$p(l)dl = \frac{k}{g} e^{-kl/g} dl = \sigma n_b e^{-\sigma n_b l} dl, \quad (6.43)$$

or we may instead refer to the distance traveled in the direction of  $\mathbf{v}_a$  so that  $dt = dz/v_a$ :

$$p(z)dz = \sigma n_b \frac{g}{v_a} e^{-\sigma n_b g z/v_a} dz. \quad (6.44)$$

Hence, the probability to collide within  $dz$  is proportional to  $g/v_a$ . In general, the target density is position and time dependent. Under single collision conditions, the probability to scatter in a time interval  $dt$  is then given by  $\sigma g n_b(\mathbf{r}, t) dt$ .

### 6.3.3 Determination of the absolute total inelastic cross section

The total inelastic cross section  $\sigma_t$  is the sum over the cross sections for all inelastic scattering channels which are relevant at the considered collision energy. It would be useful if this quantity can be measured, because if  $\sigma_t$  and also the relative inelastic cross sections are known, we can calculate all absolute inelastic cross sections. In order to determine  $\sigma_t$ , a well characterized target beam is needed, i.e.  $n_b(\mathbf{r}, t)$  has to be known. If such a beam can be obtained, one only needs to determine the fraction of molecules which are scattered out of the initial state. The measurement principle is analogous to experiments where a beam is scattered by molecules in a gas-cell.

To accurately determine the depletion of the initial population, an appreciable fraction of molecules has to scatter out of its initial state. This means that the target beam must be rather intense or that the incoming molecules have to be slow enough so that the factor  $g/v_a$  is large. If the depletion is of the order of a few percent, say 1 to 5, it can be determined quite accurately while no effects due to multiple collisions should occur. The most simple and least error prone configuration for such an experiment is shown in **Fig. 6.4**, here the incoming pulse passes through the target beam completely before it is

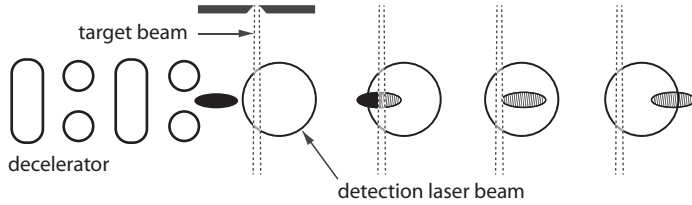


**Figure 6.4:** An experimental configuration for the measurement of total absolute inelastic cross sections. The packet of molecules is detected after having passed the (well collimated) target beam and before it exits the detection volume.

detected. We also assume that the target beam is a function of the  $z$ -position only and homogeneous transversally. In this setting, the profile of the density  $n_b$  is irrelevant because all molecules pass through the whole target beam and the fraction of scattered molecules is given by:

$$\frac{N_0 - N_{sc}}{N_0} = \int p(z) dz \approx \frac{\sigma_t g}{v_a} \int n_b(z) dz \quad (6.45)$$

where the integration is performed over the whole beam width. In this case it is obviously sufficient to know the average density along the  $z$ -interval.

This way of measuring the cross section can also be sensitive to elastic scattering. However, if the detection volume is sufficiently large compared to the size of the packet, the effect should be negligible. A decelerator which can provide a very small packet of molecules is best suited for such an experiment.

## 6.4 State-to-state inelastic scattering

### 6.4.1 The experiment

We proceed with the description of the essential elements of the scattering experiments as they were performed in this work using OH radicals. For perpendicular beams, the collision energy is given by

$$E_{coll} = \frac{\mu}{2}(v_{OH}^2 + v_{target}^2) = \frac{\mu}{m_{OH}}T_{OH} + \frac{\mu}{m_{target}}T_{target}. \quad (6.46)$$

The mean speed of the target beam is adjusted through a variation of the valve temperature and the initial mean speed of the OH beam is set by choosing a specific carrier gas (mixture) for the expansion. The collision energy can then be tuned continuously by deceleration and acceleration of the OH radicals. As a representative example, **Fig. 6.5** shows the time of flight profiles which are obtained when the initially selected mean forward velocity of the OH molecules is 430 m/s which is the mean speed obtained upon seeding OH in Kr. Different final velocities are reached by deceleration (down to 67 m/s) or acceleration

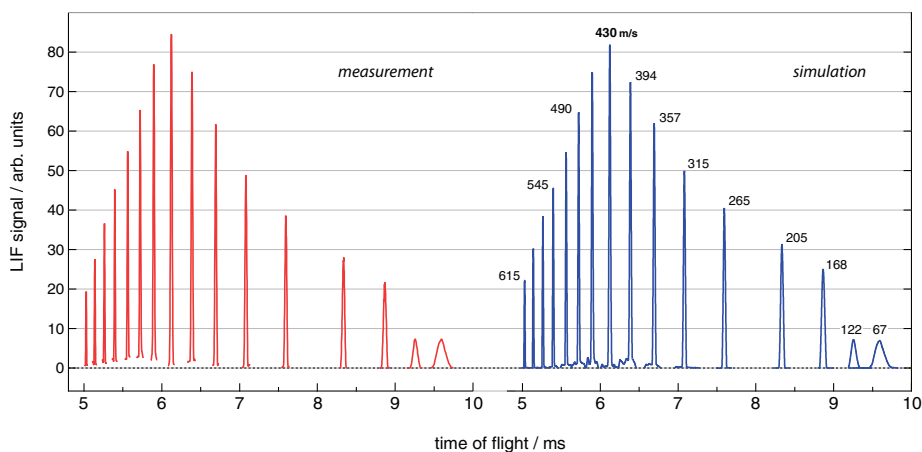


**Figure 6.5:** Left: time-of-flight profiles for the deceleration, guiding or acceleration of OH radicals seeded in krypton. The selected initial velocity in all cases is 430 m/s which is also the mean forward velocity of the input beam. Right: time-of-flight profiles as obtained from 3D trajectory calculations; selected output velocities are indicated. Except for the two lowest velocities (122 and 67 m/s), the  $s = 3$  mode of operation is used. The used parameters are listed in Table 6.1.

(up to 615 m/s). In Table 6.1 the parameters that pertain to the time of flight profiles of Fig. 6.5 are listed. The contribution of the OH molecules to the collision energy is given by  $(\mu/m_{OH})T_{OH}$ . At 67 m/s the remaining laboratory kinetic energy of the OH molecules is only  $3 \text{ cm}^{-1}$  which means that even lower velocities are usually not required in a crossed beam experiment of this kind. If the target beam consists of Ar atoms with a mean speed of 400 m/s, the collision energy range covered by deceleration and acceleration would be 82 - 268  $\text{cm}^{-1}$ .

**Table 6.1:** Parameters pertaining to the 16 time-of-flight profiles shown in Fig. 6.5: phase angle  $\phi_0$ , mean OH velocity  $v_{OH}$  and laboratory kinetic energy  $T_{OH}$ . For the calculation of the quotient  $g/v_{OH}$  and also for the collision energy  $E_{coll}$  a target beam speed of 400 m/s is assumed and the reduced mass for OH/Ar is used. The relative velocity  $g$  is determined by  $g = (v_{target}^2 + v_{OH}^2)^{1/2}$ . For the two lowest velocities, the field is switched 100 times using  $s = 3$ , afterwards the switching continues on  $s = 1$  for 16 switch times; the transition occurs at a velocity of 170 m/s and the phase angles are  $44/28^\circ$  for (a) and  $44/46^\circ$  for (b) where  $44^\circ$  is the phase angle in the  $s = 3$  mode. Units:  $\phi_0$  in deg,  $v_{OH}$  in m/s,  $T_{OH}$  in  $\text{cm}^{-1}$ ,  $E_{coll}$  in  $\text{cm}^{-1}$

$\phi_0$	-51	-44	-37	-30	-22	-15	-8	0	8	16	23	31	38	42	a	b
$v_{OH}$	615	593	562	545	516	490	463	430	394	357	315	265	205	168	122	67
$T_{OH}$	269	250	224	211	189	171	152	131	110	91	70	50	30	20	11	3
$\frac{g}{v_{OH}}$	1.2	1.2	1.2	1.2	1.3	1.3	1.3	1.4	1.4	1.5	1.6	1.8	2.2	2.6	3.4	6.1
$E_{coll}$	268	255	241	228	212	199	187	172	157	143	129	115	101	94	87	82

As analysed in detail in chapter 5, the deceleration process becomes rather inefficient for velocities below 150 m/s. However, the number of molecules which are scattered is proportional to the quotient  $g/v_{OH}$  and this quotient (see Table 6.1) increases significantly as we decelerate the molecules to the lowest velocities. Hence, even though we have less molecules to start with, a larger fraction of them collide. This is indeed beneficial provided the detection probability remains high. Unfortunately, the latter is not the case. The fraction of molecules which can be detected is typically small compared to higher velocities: in every time interval  $\Delta t$  the number of molecules scattered per volume is  $\sigma g n_a n_b \Delta t$ ; during this time the slow incoming molecules move only a small distance  $v_a \Delta t$  into the target beam while the scattered molecules can acquire much higher speeds  $v'_a > v_a$  and therefore cover a larger distance in the same time  $\Delta t$ . Now, as  $v_a$  goes to zero, the possible  $v'_a$  remain approximately the same and therefore the detection probability goes down as  $v_a$  is becoming smaller and smaller. There is only one exception: if the scattering is almost exclusively in the forward direction and almost elastic, the final velocities remain very close to the initial ones and the fraction of all scattered molecules which can be detected remains high.

Because the OH beam is pulsed, the collision signals are time dependent as shown in the first row of **Fig. 6.6**, where collision signals that arise from the scattering of OH with He, Ar and Xe are shown for a few selected scattering channels. In the background the time of flight profile of the incoming OH molecules is also shown for reference. The mean forward OH velocities are 430 m/s (He) and 615 m/s (Ar, Xe) while the target beam velocities are 950, 400 and 300 m/s for He, Ar and Xe respectively. In the second row of the same figure, the collision signals are scaled so that the sum for all channels is equal to 100 for every given detection time, hence they represent the relative populations *within the detection volume* in percent. For collisions with He, the measured relative populations remain approximately constant in time, while for Ar and Xe this is clearly not the case. As can be seen by comparing the respective Newton diagrams, the range of possible final laboratory velocity vectors is rather constrained only in the case of OH/He scattering, here molecules in different states escape from the detection volume at similar rates. For Ar and Xe one expects that a more pronounced effect occurs and this is indeed the case as the measurements clearly show. Before collision signals can be compared with predicted cross sections, it is necessary to model the detection process and to determine the overall detection probability for the different scattering products as a function of the detection time. If it is desired to determine excitation functions, then also the change of the beam overlap for the different collision energies has to be calculated. Both issues are addressed in the following sections.

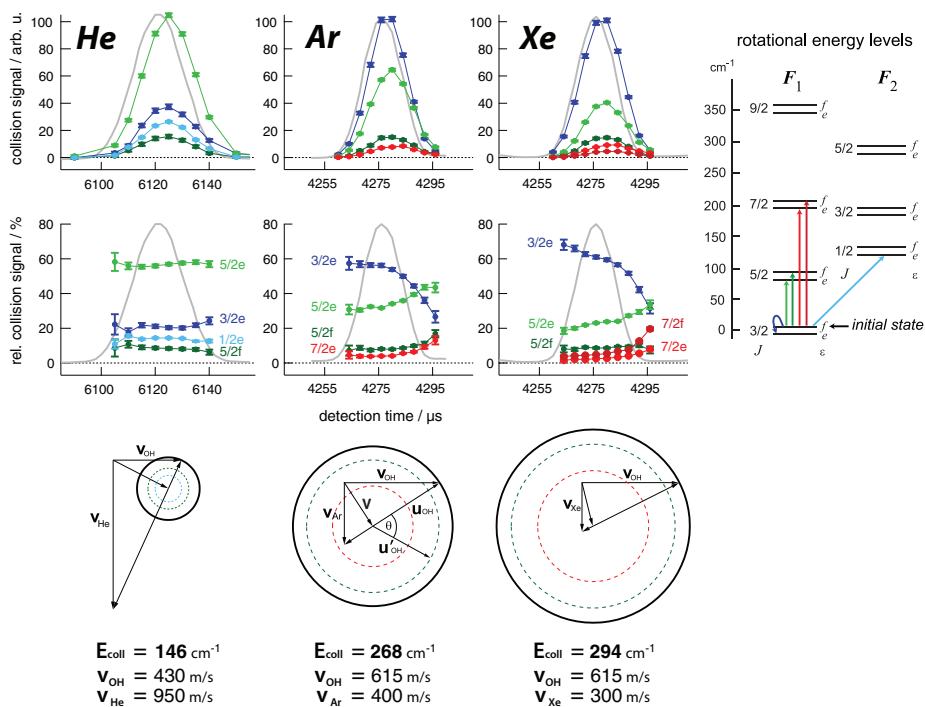


**Figure 6.6:** Collision signals that arise from the scattering of OH radicals in the  $F_1(3/2f)$  state with He, Ar and Xe atoms as a function of time. In the bottom row, a Newton diagram of the respective scattering kinematics is shown; here the outermost circle corresponds to the quasi elastic scattering into the  $F_1(3/2e)$  state, whereas the inner circles (dashed lines) relate to the scattering into the other possible states shown in the energy level diagram.

It is well known in the field that crossed beam experiments often require more or less extensive modelling of the measurement process to extract cross sections from the data. However the literature on this issue is somewhat scarce and the procedures described are not directly applicable here; partly useful sources are [78, 79].

#### 6.4.2 Generation of collision products with time

The total scattering rate at time  $t$  can be obtained from (6.34) by spatial integration over the scattering volume  $V$ :

$$\dot{N}_{sc}(t) = \sigma g \int_V d^3r n_a(\mathbf{r}, t) n_b(\mathbf{r}, t), \quad (6.47)$$

and therefore the total number of molecules scattered between  $t = t_0 \dots \tau$  is given by adding the contributions  $\dot{N}_{sc}(t)dt$  – which are nothing but simple

integrals of the density function product (the “overlap”):

$$N_{sc}(t_0, \tau) = \int_{t_0}^{\tau} dt \dot{N}_{sc}(t). \quad (6.48)$$

This integration is trivial only, because we neglect the change of the density functions due to the collisions.

In the experiment, the incoming pulse  $n_a(\mathbf{r}, t)$  propagates along the  $z$ -direction with a mean speed  $v_a$ . The relative velocity  $\mathbf{g}$  is changed by a variation of  $v_a$  through deceleration or acceleration. What is the influence on the total number of scattered molecules apart from the possible change of the cross section itself? Assume that there is a characteristic position of the density function  $n_a$ , say the peak position, and assume that for  $t = t_0$  this peak is at some position  $z_0$ . At the instant of detection  $\tau$ , the peak shall always be at the position  $z_\tau$ . Upon changing the variable of integration from time to position using  $z = v_a t + z_0$  we get

$$N_{sc}(t_0, \tau) = \frac{1}{v_a} \int_{z_0}^{z_\tau} dz \dot{N}_{sc}((z - z_0)/v_a + t_0). \quad (6.49)$$

If we neglect the velocity distribution of the decelerated beam and simply assume a constant mean velocity for all particles, then the time evolution of  $n_a$  is trivial and given by  $n_a(\mathbf{r}, t) = n_a(\mathbf{r} - \mathbf{e}_z v_a(t - t_0), t_0)$  where  $\mathbf{e}_z$  is the unit vector in the  $z$ -direction. The integral may therefore be expressed by

$$N_{sc}(t_0, \tau) = \frac{\sigma g}{v_a} \int_{z_0}^{z_\tau} dz \int_V d^3r n_a(\mathbf{r} - \mathbf{e}_z(z - z_0), t_0) n_b(\mathbf{r}, (z - z_0)/v_a + t_0). \quad (6.50)$$

As the velocity  $v_a$  is tuned, the value of the integral changes because the function  $n_a$  changes. Furthermore we see that  $N_{sc}$  is proportional to  $g/v_a$ . It would clearly be optimal if the function  $n_a$  would not change with the velocity  $v_a$  and if  $n_b$  would be time independent. In this case, only the factor  $\sigma g/v_a$  changes when  $v_a$  is tuned and therefore one need not evaluate the integral – provided it is ensured that the beam overlap remains constant by choosing appropriate detection times so that the peak intensity is always at the same position when the molecules are detected.

Especially for the case of time independent  $n_b$  it is useful to analyse the above formula a bit further. Assume that at  $t = \tau = 0$  the peak intensity of the incoming pulse  $n_a$  is located exactly in the center of the target beam  $n_b(\mathbf{r})$  for which we assume that  $n_b(\mathbf{r}) = n_b(z) = n_b(-z)$  holds. This implies that  $n_b$  depends only on the longitudinal position, has its center at  $z = 0$  and is symmetric with respect to  $z = 0$ . Assume further that the incoming pulse of molecules has a number density distribution at time  $t = 0$  given by  $N_a f_1(z) f_2(y) f_3(x) dz dy dx$  where  $N_a$  is the total number of particles in the pulse. The total number of molecules scattered until  $t = 0$  is

$$N_{sc}(-\infty, 0) = \sigma g N_a \int_{-\infty}^0 dt \int_{-\infty}^{\infty} dz f_1(z - v_a t) n_b(z). \quad (6.51)$$



By changing the integration variable to  $q = v_a t$  this becomes

$$N_{sc}(-\infty, 0) = \sigma \frac{g}{v_a} N_a \int_{-\infty}^0 dq \int_{-\infty}^{\infty} dz f_1(z - q) n_b(z) \quad (6.52)$$

$$=: \sigma \frac{g}{v_a} N_a \int_{-\infty}^0 dq U(q). \quad (6.53)$$

In the experiment, the shape of  $f_1(z)$  changes as a function of the phase angle, but it remains approximately symmetric also for non zero values of the phase angle. If it would be the case that  $f_1(z) = f_1(-z)$  exactly, then also  $U(q) = U(-q)$  and the above integral yields

$$\int_{-\infty}^0 dq U(q) = \frac{1}{2} \int_{-\infty}^{\infty} dq U(q) \quad (6.54)$$

$$= \frac{1}{2} \int_{-\infty}^{\infty} dz n_b(z) \quad (6.55)$$

which is the same for all collision energies and the evaluation of the integral can be omitted (one half of the scattered molecules collide before  $t = 0$  and the other half after  $t = 0$ , independent of the collision energy).

To determine  $N_{sc}(t_0, \tau)$  for arbitrary functions  $n_a$  and also for arbitrary and possibly time dependent  $n_b$ , the density function  $n_a$  has to be known. However, computer simulations yield only phase space points which sample  $n_a$ . To proceed by *direct* evaluation of (6.48) is possible but inconvenient because a binning procedure is required to first obtain  $n_a$  from the given phase space points. A different approach which requires only single particle phase space coordinates is discussed in the following.

The computer simulations correctly reproduce the relative number of molecules which exit the decelerator for a given output velocity (see Fig. 6.5). Moreover, the phase space density distribution is *represented* with sufficient accuracy by sample points. Let the phase space coordinates for molecule  $i$  at time  $t$  be denoted by  $\mathbf{r}_i(t)$ ,  $\mathbf{v}_i(t)$  or simply by a 6-dimensional vector<sup>1</sup>  $\mathbf{R}_i$ . Denote the number of molecules in an element of volume  $dR = dx dy dz dv_x dv_y dv_z$  in phase space by  $\rho(\mathbf{R}, t) dR$  so that  $\rho$  is the phase space density at time  $t$ . For a given start-time  $t_0$  the packet of molecules shall already be outside of the decelerator but not yet inside the target beam. Now calculate the probability for a molecule originating from  $\mathbf{R}$  to have had a collision in the time interval  $[t_0 \dots \tau]$ , denote this probability by  $w(\mathbf{R}, t_0, \tau)$ . Being given a specific distribution  $\rho(\mathbf{R}, t)$  the number of molecules scattered within the time interval  $[t_0 \dots \tau]$  is given by

$$N_{sc}(t_0, \tau) = \int dR w(\mathbf{R}, t_0, \tau) \rho(\mathbf{R}, t_0). \quad (6.56)$$

---

<sup>1</sup>Here,  $\mathbf{R}_i$  is a member of  $\mathbb{R}^6$  that is used to collect the phase space coordinates – in this case the three Cartesian position and velocity components.

The computer simulation yields sample points  $\mathbf{R}_i$  in phase space, which occur with a frequency that is proportional to  $\rho(\mathbf{R}, t)$  in the considered phase space region. Assume that a sufficiently small region around  $\mathbf{R}_i$  has a certain collision probability  $w(\mathbf{R}_i, t_0, \tau)$  associated with it. This means that if  $N_i$  molecules would actually be inside the considered phase space volume at  $\mathbf{R}_i$  at time  $t_0$ , a number  $w(\mathbf{R}_i, t_0, \tau)N_i$  of them would on average collide until time  $\tau$ . Therefore, the total number of scattered molecules is

$$N_{sc}(t_0, \tau) = \sum_i w(\mathbf{R}_i, t_0, \tau)N_i =: \sum_i w_i(t_0, \tau)N_i. \quad (6.57)$$

We may actually set  $N_i = 1$  and simply sum the  $w_i(t_0, \tau)$  for the molecules in a simulation. If the target beam density  $n_b(\mathbf{r}, t)$  is given,  $w_i$  can be calculated by integration of the collision probability along the path  $\mathbf{r}_i(t)$  that is being traversed:

$$w_i(t_0, \tau) = \sigma g \int_{t_0}^{\tau} dt n_b(\mathbf{r}_i(t), t). \quad (6.58)$$

For our purposes it is of course sufficient to know  $n_b$  up to a scaling factor, provided it is the same function for all relevant collision energies.

The procedure has a peculiar asymmetry: it depends on the availability of a density function for the target beam. If only a limited number of phase space points are given which sample this function, one first needs to determine an approximate density  $n_b$  by binning the spatial density and fitting an analytic function to it. It is somewhat counterintuitive perhaps that one cannot directly simulate the whole collision process by using only phase space sample points from computer simulations for both beams.

If the fraction of all scattered molecules which are detected (the detection probability) does not change with collision energy, then the energy dependence of a collision signal  $S$  is given by

$$S(E, t_0, \tau) = \lambda \sum_{i=1}^{N_E} w_i(t_0, \tau) \quad (6.59)$$

$$= \lambda \sigma(E) g(E) \sum_{i=1}^{N_E} \int_{t_0}^{\tau} dt n_b(\mathbf{r}_i(t), t) \quad (6.60)$$

where the summation index runs over all particles in the packet for the given energy (in total  $N_E$  particles) and  $\lambda$  is an energy independent scaling factor. If we have measured the collision signals for different energies  $E_k$ , we divide them by  $g(E_k)$  and also by the sum over the integrals to obtain the sought energy dependence of  $\sigma$ , again, provided the detection probability is the same for all  $E_k$ . Since the summation runs over all particles in the packet, the relative intensities of the particle numbers in a packet obtained from the simulation must be sufficiently accurate. If they are not, one may try to scale up or down the total particle number in the packet to apply a first order correction.

Finally we note that there is a useful relation between (6.60) and the collision time distribution. This distribution shall be denoted by  $f(E, t_0, t)$  and it is given by

$$f(E, t_0, t) := \partial_t \frac{S(E, t_0, t)}{S(E, t_0, \infty)} =: \partial_t F(E, t_0, t). \quad (6.61)$$

If a particle is certain to be scattered, and if its initial phase space position is chosen at random from one of the vectors  $\mathbf{R}_i$  then  $F(E, t_0, t)$  is the probability to scatter within a specific time interval  $t_0 \dots t$ . For  $F(E, t_0, t)$  we have

$$F(E, t_0, t) = \frac{\sum_{i=1}^{N_E} \int_{t_0}^t dt' n_b(\mathbf{r}_i(t'), t')}{\sum_{i=1}^{N_E} \int_{t_0}^{\infty} dt' n_b(\mathbf{r}_i(t'), t')} \quad (6.62)$$

so that for the collision signal we may write

$$S(E, t_0, \tau) = \lambda \sigma(E) g(E) F(E, t_0, \tau) \sum_{i=1}^{N_E} \int_{t_0}^{\infty} dt n_b(\mathbf{r}_i(t), t). \quad (6.63)$$

If the target density is independent of time, the sum over the integrals is particularly simple:

$$\sum_{i=1}^{N_E} \int_{t_0}^{\infty} dt n_b(\mathbf{r}_i(t), t) = \sum_{i=1}^{N_E} \frac{1}{v_i} \int_{\mathbf{r}_0}^{\infty} ds n_b(\mathbf{r}) \quad (6.64)$$

$$\approx \frac{1}{v_a} \sum_{i=1}^{N_E} \int_{\mathbf{r}_0}^{\infty} ds n_b(\mathbf{r}) \quad (6.65)$$

$$= \frac{N_E}{v_a} \int_{\mathbf{r}_0}^{\infty} ds n_b(\mathbf{r}) \quad (6.66)$$

where  $ds$  is the line element along the particle trajectory  $\mathbf{r}_i(t)$  with speed  $v_i$ . If (6.66) is inserted into (6.63), the integral may be absorbed into  $\lambda$  because it is independent of the collision energy  $E$ . The final result is then:

$$S(E, t_0, \tau) = \lambda \sigma(E) g(E) \frac{N_E}{v_a} F(E, t_0, \tau). \quad (6.67)$$

This particular formulation is useful because  $F(E, t_0, \tau)$  can be obtained on the side while determining the detection probability (see the following section). We expect that  $F \approx 0.5$  – provided the symmetry conditions hold which were discussed above in the derivation of (6.55) and provided the packet is centered around the target beam's central axis at the time the molecules are detected.

### 6.4.3 Detection of collision products

So far the discussion was only concerned with the creation of collision products as a function of time. We now proceed to analyse the detection of these products for a given collision energy.

The post collision velocity distribution relative to center of mass coordinates, that is the distribution of  $\mathbf{u}'_{OH}$ , depends on the scattering channel and can be inferred if the differential cross section is known. Upon adding the velocity of the center of mass itself, we obtain the distribution for the laboratory velocities. Together with a model of the detection system of the used apparatus, we can infer the *detection probability*. This probability depends on the scattering channel, and the detection time, we define it by:

$$P_j(t_0, \tau) := \frac{N_{det}(j, \tau)}{N_{sc}(j, t_0, \tau)} \quad (6.68)$$

where  $N_{det}$  denotes the number of particles that are detected at time  $t = \tau$  in state  $j$  and  $N_{sc}$  is equal to the total number of molecules scattered into state  $j$  in the time interval  $t_0 \dots \tau$ ;  $t_0$  is some time before the beams have significant overlap.

In the best case, the experiment yields a detection probability that is the same for all probed final states at a given collision energy and detection time. If one is interested also in the measurement of excitation functions, it would be optimal if the detection probability is also the same for all probed energies. To achieve this, one can try to design the setup such that  $P_j$  is unity for all  $j$  at least until a certain time. This is possible only, if the detection volume is large compared to the scattering volume and if furthermore the scattering volume is located inside the detection volume (see also [79]). In general this is not always possible; especially if the detection proceeds via state selective ionization the used laser beam is often focussed and the ionization volume is then quite small and somewhat ill defined.

There is also a special case for which the kinematics are constrained enough so that  $P_j$  is not necessarily unity but approximately independent of  $j$  at a given energy. This case occurs if the target has a much smaller mass compared to the considered molecule, because then the velocity vector of the center of mass lies very close to the laboratory velocity  $\mathbf{v}_{OH}$  – an example is the scattering of OH molecules with helium atoms already mentioned above. We proceed to discuss how  $P_j$  can be calculated.

At first, specific assumptions have to be made about the scattering angle distribution. This distribution, denoted by  $g_j(\theta)d\theta$ , can be calculated from the differential cross section  $G_j(\theta)$ . As explained on p.89, the cross section for scattering into a specific solid angle is  $2\pi G_j(\theta) \sin(\theta)d\theta$  and therefore

$$g_j(\theta)d\theta := \frac{G_j(\theta) \sin(\theta)d\theta}{\int_0^\pi G_j(\theta) \sin(\theta)d\theta}. \quad (6.69)$$

In order to separate assumptions about the experiment from assumptions about the differential cross section, we first calculate a scattering angle resolved probability distribution  $W_j$  defined by

$$W_j(t_0, \tau, \theta) := \frac{N_{det}(j, \tau, \theta)}{N_{sc}(j, t_0, \tau, \theta)} \quad (6.70)$$

where  $N_{det}$  and  $N_{sc}$  are defined as before but now the scattering angle  $\theta$  is fixed. With this definition the total detection probability becomes

$$P_j(t_0, \tau) = \int_0^\pi W_j(t_0, \tau, \theta) g_j(\theta) d\theta \quad (6.71)$$

so that we can first determine  $W_j$  which is a function of the experimental configuration alone and then later determine  $P_j$  by making assumptions about the differential cross section.

The function  $W_j$  can be determined by a computer simulation in a straight forward manner provided we have sufficient knowledge about the initial phase space distribution, the target beam density profile – including its time dependence – and also about the detection volume. As shown in the previous section, under single collision conditions, the probability to scatter in a small time interval  $dt$  is given by  $\sigma(E)g(E)n_b(\mathbf{r}(t), t)dt$ . In a direct approach, a molecule with given initial phase space position  $\mathbf{R}_i$  is followed along its straight line trajectory in sufficiently small increments  $dt$  to its final position at  $t = \tau$ . Along the way, scattered molecules are created with numbers that are proportional to  $n_b dt$  and it is determined how many of them reside within the detection volume at  $t = \tau$ . If a molecule is created during the simulation, its propagation direction and speed has to be determined for a fixed scattering angle  $\theta$  and random  $\phi$ . A possible post collision velocity  $\mathbf{v}'_i$  is given by

$$\mathbf{v}'_i = \mathbf{V} + \mathbf{u}'_i(\theta, \phi) \quad (6.72)$$

where  $\mathbf{V}$  is the approximate center of mass velocity<sup>2</sup>. The length of  $\mathbf{u}'_i$  depends on the scattering channel and is given by (6.19), while the correct direction is obtained by a sequence of suitable rotations of the initial velocity  $\mathbf{u}_i$ . Because the length of the final relative velocity vector depends on the scattering channel, the obtained functions  $W_j(t_0, \tau, \theta)$  depend on  $j$ .

For the experiments of this work, the target beam pulse has a sufficient duration to assume that it is approximately constant during the time in which the OH molecules pass through, except maybe for the lowest velocities. Furthermore, the transverse width of the decelerated OH packet is sufficiently narrow compared with the width of the target beam so that  $n_b$  depends only on  $z$  and is constant in  $x$  and  $y$ . A fair amount of simplification is possible in this case. The probability to collide in a small time  $dt$  is  $\sigma(E)g(E)n_b(z)dz/v_a$ , therefore the collision position distribution is obtained by normalizing the density function  $n_b(z)$  along  $z$ . Here, a Gaussian is used for  $n_b$ , the width of which is estimated from a spatial scan of the target beam intensity using a small microphone as a beam detector. To simulate the scattering of a single particle with given phase space coordinate  $\mathbf{R}_i$ , a collision position is determined at random but in accord with the respective distribution and the collision time is inferred from the initial

---

<sup>2</sup>If necessary, an appropriate averaging over the distribution of  $\mathbf{V}$  can be implemented in a straight forward manner.

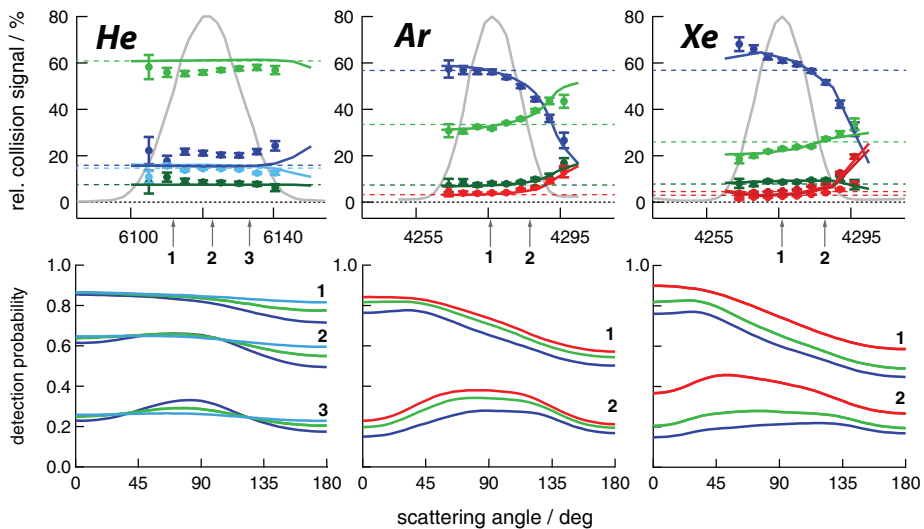


**Figure 6.7:** Top row: the time dependence of the measured and the predicted *apparent* relative cross sections. Bottom row: the functions  $W_j(t_0, \tau, \theta)$  for different values of the detection time  $\tau$ , which are indicated by the arrows and referenced by the associated numbers. The color code corresponds to the channels which are shown in the top row; molecules scattered into the  $e$  or  $f$  component of the same rotational level have equal detection probabilities.

position and velocity of the particle. By recording the collision time we obtain the function  $F(E, t_0, \tau)$  on the side. At a given collision position, molecules have to be released for a given scattering angle  $\theta$  and arbitrary  $\phi$  and the time interval in which they can be detected has to be determined. This is all that is required to determine  $W_j(t_0, \tau, \theta)$ . The main uncertainty lies in the proper specification of the detection volume, which must be estimated from the laser diameter and the properties of the imaging system. Here, a cylinder with a diameter of 8 mm and a height of 10 mm is assumed for the detection volume.

In the bottom row of **Fig. 6.7**,  $W_j$  is plotted for different detection times. The final results of the simulation are shown in the top row as solid lines, together with the measurements; the horizontal dashed lines represent the expected relative cross sections obtained from scattering calculations. In the case of OH – He the functions  $W_j$  are approximately constant for any detection time which means that different scattering angle distributions  $g_j(\theta)d\theta$  yield approximately the same detection probabilities. This is the most favorable case, the collision signals need no further correction.

For OH – Ar the dependence on  $\theta$  and also on  $j$  is a bit more pronounced. At detection time (1), molecules which are scattered in the forward direction are detected more efficiently compared to side and backward scattered ones. For time (2), those molecules which are side scattered have a higher chance of being detected. In the experimental setup the beam intersection volume is

smaller than the detection volume so that for an early detection time most of the scattered molecules can also be detected and the resulting bias is small. In the case of OH – Xe, the situation is somewhat less favorable, even for an early detection time the resulting detection probabilities differ.

The differential cross section that is used in all cases is based on high quality ab-initio scattering calculations which are explained in more detail in chapter 8. The agreement with the measured time dependence of the relative cross sections is remarkably good. It is found that within a reasonable range the results are only modestly sensitive to input parameters which pertain to the geometry of the detection volume and to the target beam width. In contrast, the simulations showed that the vertical position of the detection volume can have a strong influence on the results. For the simulations shown here, it is assumed that the center of the detection laser is located where the central axes of both beams intersect.

### 6.4.4 Excitation functions

To measure the energy dependence of the cross sections up to an energy independent scaling factor is more difficult than determining only relative cross sections at a given energy, because now also the number of particles which collide has to be accurately known. Upon multiplying (6.60) with  $P_j$ , the collision signal  $S_j$  can be related to the cross section  $\sigma_j$ :

$$S_j(E, t_0, \tau) = \lambda P_j(E, t_0, \tau) \sigma_j(E) g(E) \sum_{i=1}^{N_E} \int_{t_0}^{\tau} dt n_b(\mathbf{r}_i(t), t). \quad (6.73)$$

We apply the so far discussed methods to the scattering of OH with Ar atoms at the lowest measured energies. If a constant target beam density is assumed and (6.73) is evaluated, the cross sections shown in **Fig. 6.8**, panel (a) and (b) result. The measurements are scaled so as to give a good match to the predicted cross sections from medium to high energies. It is seen that at low energies, a significant decrease in the ( $3/2f \rightarrow 3/2e$ ) channel occurs, which is actually not

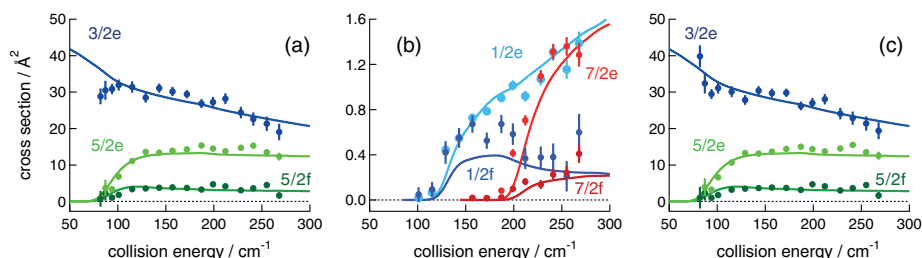


**Figure 6.8:** Measured excitation functions for collisions of OH with Ar atoms, scaled to match theoretical cross sections (solid lines).

predicted: at low velocities the decelerated OH packet probes different parts of the target beam as compared to large velocities. The average density that is probed can be significantly lower for the very slow molecules as now the “early” part of the target beam pulse also participates (in the experiment, the target beam pulse density at the detection time in the crossing region is the same for all energies, therefore slow molecules see more of the front of the beam also). To verify this explanation, the measured time dependence of the target beam density was included in the simulation program and the result is shown in panel (c), yielding a consistent picture. Nevertheless, the need to include such a time dependent beam density in a calculation should be avoided since invariably yet another error prone factor is introduced in this way; if possible a beam source which yields sufficiently long pulses should be used. In the present work, the initial aim was not to measure excitation functions, and the relative cross sections presented in the following chapters are not affected by such problems.



## Chapter 7

# State-to-state inelastic scattering of Stark-decelerated OH radicals with Ar atoms

The Stark deceleration method exploits the concepts of charged particle accelerator physics to produce molecular beams with a tunable velocity. These tamed molecular beams offer interesting perspectives for precise crossed beam scattering studies as a function of the collision energy. The method has advanced sufficiently to compete with state-of-the-art beam methods that are used for scattering studies throughout. This is demonstrated here for the scattering of OH radicals ( $X^2\Pi_{3/2}, J = 3/2, f$ ) with Ar atoms, a benchmark system for the scattering of open-shell molecules with atoms. Parity-resolved integral state-to-state inelastic scattering cross sections are measured at collision energies between 80 and 800  $\text{cm}^{-1}$ . The threshold behavior and collision energy dependence of 13 inelastic scattering channels is accurately determined. Excellent agreement is obtained with the cross sections predicted by close-coupling scattering calculations based on the most accurate *ab initio* OH+Ar potential energy surfaces to date.

---

Based on: *State-to-state inelastic scattering of Stark-decelerated OH radicals with Ar atoms*, L. Scharfenberg, J. Klos, P.J. Dagdigan, M.H. Alexander, G. Meijer and S.Y.T. van de Meerakker; Phys. Chem. Chem. Phys. **12**, 10660 (2010)

## 7.1 Introduction

The detailed understanding of interactions between individual atoms and/or molecules is of fundamental importance in physical chemistry, and is pivotal to the interpretation of the dynamic behavior of macroscopic systems. The study of collisions between neutral atoms and molecules in the gas-phase is a well-established experimental avenue to probe the potential energy surfaces (PES) that govern molecular interactions [80].

The crossed molecular beam technique is ideally suited to obtain detailed information on the PES, and enables the study of molecular encounters under single collision conditions and in complete isolation from the environment. The level of detail that can be reached in these experiments depends on the uniqueness of the pre-collision conditions and on the quality of the detection method to analyze the scattering products. Gaining ever better control over the relevant parameters has thus been a recurrent theme in crossed beam experiments.

A wide variety of sophisticated methods have been developed to control the collision energy [81, 82], the internal quantum states [83, 84, 85], the velocity spreads [86, 87], and the mutual orientation [88, 89] of the scatterers. Powerful laser-based detection techniques have been developed to measure the state, angular and translational energy distribution of the scattering products [90, 28, 29, 91]. Many of these methods have recently yielded new insights in molecular scattering processes, ranging from the role of nonadiabatic dynamics in elementary reactions [92, 93] to product pair correlations in bimolecular reactive scattering [94]. In concert with advances in the theoretical analysis of scattering processes, the wealth of available experimental scattering data has contributed enormously to our present understanding of how intermolecular potentials control molecular reaction dynamics.

Further enhancement of this relationship requires experiments with an increasing level of resolution and detail. In crossed beam experiments the most serious roadblock to further improve the resolution are the molecular beam pulses. A precise level of control over molecules in a beam has become possible with the Stark deceleration technique [3]. A Stark decelerator for neutral polar molecules is the equivalent of a linear accelerator (LINAC) for charged particles [95], and exploits the interaction of a polar molecule with inhomogeneous time-varying electric fields. Compared to conventional molecular beam sources, a Stark decelerator produces beams of molecules with a narrow velocity spread, perfect quantum state purity, and with a computer-controlled velocity that can be tuned between standstill and high velocities. These monochromatic molecular beams offer the possibility of studying molecular encounters under well controlled and unexplored conditions, and offer new prospects to probe molecular interaction potentials with unprecedented detail [96].

The application of Stark-decelerated beams in scattering experiments is still in its infancy, however. In 2006, Gilijamse *et al.* performed the thus far only state-to-state scattering experiment using a Stark decelerated molecular beam

[18]. A Stark-decelerated beam of OH radicals was crossed with a conventional beam of xenon atoms, and the state-to-state rotational inelastic scattering cross sections were measured for a number of scattering channels as a function of the collision energy. This experiment clearly demonstrated the feasibility of the approach; however, the sensitivity of the experiment was limited by the rather low number densities of the decelerated molecules.

During the last years, we have developed a new Stark decelerator that employs the so-called  $s = 3$  mode of operation to eliminate the loss of molecules that occurs in decelerators of earlier designs. With this apparatus (see chapter 4 and 5), packets of molecules can be produced with a superior number density, a narrower velocity spread, and a higher quantum state purity. This Stark decelerator enables state-to-state scattering experiments with a sensitivity that is comparable to (or even exceeds) the level of sensitivity that is obtained in state-of-the-art crossed beam scattering experiments of similar systems. This we demonstrate here for the  $\text{OH}(X^2\Pi)\text{--Ar}$  system.

Rotational inelastic scattering of free radical species such as OH [97, 98], CH [99] and NO [100] with rare gas atoms have always been of special interest in crossed beam scattering experiments. This interest stems from the crucial roles that these species play in many areas of chemistry and physics, ranging from combustion to astrophysics. Because of the unpaired electrons, these radicals have non-zero electronic spin and orbital angular momentum. This renders more complex the rotational energy level structure. In addition, the scattering is dominated by collisions on two (or more) PES's. A detailed understanding of these elementary systems therefore provides a firm basis to understand the dynamics of more complex systems.

The  $\text{OH}(X^2\Pi)\text{--Ar}$  system (together with the similar  $\text{NO}(X^2\Pi)\text{--Ar}$  system) has emerged as the paradigm for the scattering of open shell radicals with rare gas atoms. In a series of crossed beam experiments, ter Meulen and coworkers prepared the OH radicals in the upper  $\Lambda$ -doublet component of the  $X^2\Pi_{3/2}$ ,  $J = 3/2$  level by hexapole state selection [101, 102]. Accurate parity-resolved integral state-to-state cross sections for rotational excitation up to the  $X^2\Pi_{3/2}$ ,  $J = 9/2$  and the  $X^2\Pi_{1/2}$ ,  $J = 5/2$  states were obtained at high collision energies. Preferred excitation to one of the  $\Lambda$ -doublet states of the final rotational and spin-orbit state was observed, in agreement with the general propensity rules that follow from a formal quantum analysis [103, 104]. Steric asymmetries of the inelastic cross sections were measured by orienting the OH radicals with either the O-end or the H-end towards the Ar atom by a static electric field in the collision zone [105]. The collision induced reorientation of the OH radicals was measured by probing the Stark-split states of the products corresponding to different orientations [106]. Under thermal bulk conditions, the evolution of oriented or aligned OH ( $X^2\Pi$ ) radicals was studied in collisions with argon by polarization spectroscopy [107, 108, 109]. Detailed information on the  $\text{OH}(X^2\Pi)\text{--Ar}$  PES has also been obtained from spectroscopic study of the bound states of the OH-Ar van der Waals complex [110, 111].

Here we report the investigation of rotational energy transfer of fully state-selected OH ( $X^2\Pi_{3/2}, J = 3/2, f$ ) radicals in collisions with Ar atoms at collision energies between 80 and 800  $\text{cm}^{-1}$ . Parity-resolved integral state-to-state scattering cross sections for rotational excitation up to the  $^2\Pi_{3/2}, J = 9/2$  and the  $^2\Pi_{1/2}, J = 5/2$  states are accurately measured. The collision energy dependence of the relative integral inelastic scattering cross sections, the threshold behavior of the inelastic channels, and the energy dependence of the state-resolved propensities are accurately determined. Excellent agreement is obtained with cross sections determined by quantum close-coupled calculations based on recent high-quality *ab initio* OH-Ar PES's.

## 7.2 Experiment

### 7.2.1 Experimental setup

The production, Stark deceleration and detection of OH radicals as used in this experiment has been described in the previous chapters. For convenience, we briefly repeat the most important aspects in this section. All details that are relevant to the variation of the collision energy are given in section 7.2.2 and 7.2.3.

A schematic overview of the experimental setup is shown in **Fig. 7.1**. A pulsed supersonic beam of OH radicals is produced by photolysis (193 nm) of nitric acid seeded in an inert carrier gas. During the expansion, nearly all molecules cool to the lowest rotational ( $J = 3/2$ ) and vibrational level of the  $X^2\Pi_{3/2}$  electronic ground state. This level consists of two  $\Lambda$ -doublet components (labelled *e* and *f* [40], see part c of Fig. 7.2) that are separated in energy by only 0.05  $\text{cm}^{-1}$ . Both components are therefore equally populated in the beam, but only the energetically higher lying *f*-component is low field seeking in inhomogeneous electric fields and can be Stark-decelerated. The lower *e*-component is high field seeking and is deflected from the beam axis in the experiment.

After passage through a 2 mm diameter skimmer, the beam enters the 2.6 meter long Stark decelerator that consists of 317 parallel pairs of high-voltage electrodes. Successive pairs are alternately charged or grounded, creating a periodic field along the beam axis [57]. Two distinct field configurations are produced by either charging the electrode pairs on the even or the odd numbered positions. The OH radicals can be decelerated or accelerated by switching back and forth between these two configurations using a sequence of high voltage pulses. Essential in these experiments is the use of the so-called  $s = 3$  operation mode of the decelerator [55]. In this mode, only every third electrode pair is used for deceleration, while extra transverse focusing is provided by the intermediate electrode pairs.

The packet of OH ( $X^2\Pi_{3/2}, J = 3/2, f$ ) molecules that emerges from the

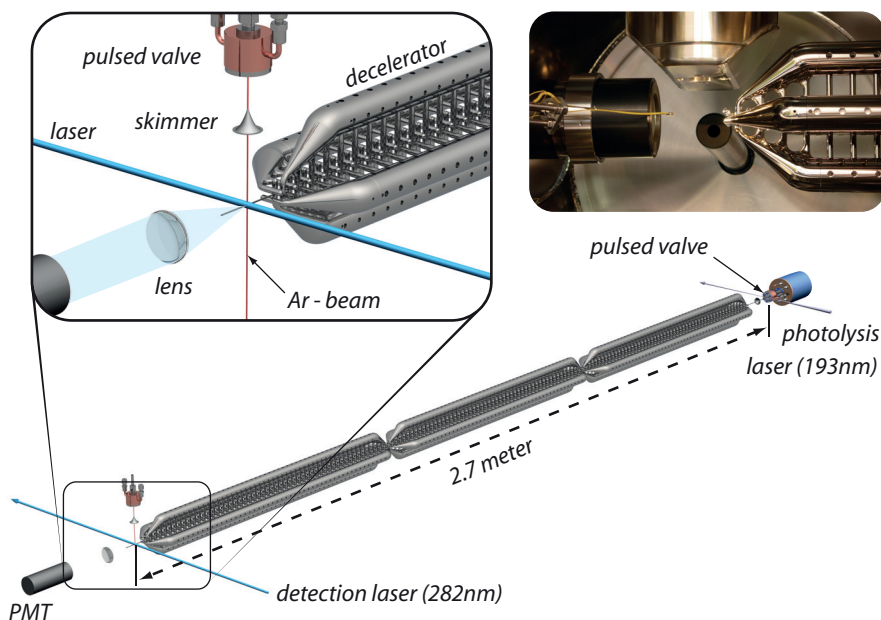


**Figure 7.1:** Scheme of the experimental setup. A pulsed beam of OH radicals is produced via of  $\text{HNO}_3$  seeded in an inert carrier gas. The OH radicals pass through a 2.6-m-long Stark decelerator, and are scattered with a pulsed beam of argon atoms. The OH radicals are state-selectively detected using a laser-induced fluorescence scheme. The fluorescence is imaged onto a PMT. In the inset, a photograph of the beam crossing region is shown.

decelerator intersects with the central axis of the beam of argon atoms at a distance of 16.5 mm from the exit of the decelerator under  $90^\circ$  angle of incidence. The fields are switched off when the OH radicals leave the decelerator, and collisions take place in a field free region. We assume that the uneven distribution over  $M_J$ -components that is present in the decelerator is scrambled completely before collisions occur. A modified commercial solenoid valve (General Valve, Series 99) is used to produce the pulsed supersonic beam of argon. The velocity of this beam can be adjusted by controlling the temperature of the valve. The atoms pass a 2 mm diameter skimmer and intersect the centerline of the OH packet 90 mm from the nozzle orifice. The duration of the gas pulse is long, and the number density of the argon atoms in the crossing region is constant during the passage of the OH packet. Single collision conditions are insured by keeping the decrease of the population in the  $J = 3/2, f$  level due to scattering with the argon atoms below 4 percent. A microphone based beam detector [112] can be moved into the crossing region to probe the spatial density profile of the argon beam. Together with a second microphone that is placed 300 mm further downstream, the mean forward beam velocity is determined from a time of flight measurement of the gas pulse.

The OH radicals are state-selectively detected via saturated laser induced fluorescence when the most intense part of the OH packet is in the center of the beam crossing region. The 282 nm radiation of a pulsed dye laser intersects both beams under  $90^\circ$  angle of incidence, and induces rotational transitions of the  $A^2\Sigma^+, v=1 \leftarrow X^2\Pi, v=0$  band. The off-resonant fluorescence is collected at right angles by a lens and imaged onto a photo multiplier tube (PMT). Stray light from the laser is suppressed by light baffles and by optical filtering in front of the PMT. The radiative lifetime of the  $A^2\Sigma^+, v=1$  state is 717 ns [52], and no collisional quenching of the excited molecules takes place. The diameter of the laser beam is approximately 8 mm, providing a detection volume that is larger than the intersection volume of the OH and Ar beams.

### 7.2.2 Variation of the collision energy

The collision energy is varied by deceleration, guiding, or acceleration of the OH radicals in the Stark decelerator, and by using two different temperatures for the argon valve. The total energy range of 80 to  $800\text{ cm}^{-1}$  is covered using six separate measurement intervals, as is illustrated in **Fig. 7.2 (a)**. The argon valve is operated at 110 K for the collision energy range of 80 to  $500\text{ cm}^{-1}$  (intervals 1 to 4) and at 293 K for energies between 430 and  $800\text{ cm}^{-1}$  (intervals 5 and 6). The corresponding argon beam velocities are determined to be 400 and 565 m/s and stagnation pressures of 2 and 4 bar were used. Lower temperatures for the valve are not possible without the risk of condensation.

For a given velocity of the argon beam, the collision energy range that is accessible by tuning the velocity of the OH radicals is defined by the initial velocity of the OH molecular beam. Molecular beams are produced using Kr, Ar, Ne, a Ne/Ar mixture, and a He/Ne mixture as carrier gas; the gas that is used in each interval is indicated in **Fig. 7.2 (a)** together with the mean initial velocity of the molecular beam pulse. The collision energies that correspond to these mean velocities are indicated by vertical lines in **Fig. 7.2 (a)** for each interval. Within each interval, the argon beam velocity is fixed and the collision energy is continuously scanned from low to high energies by deceleration and acceleration of the OH radicals. The velocity range of the OH radicals was chosen to ensure overlap between successive intervals.

The number density, velocity spread, quantum state purity, and size of the OH packet critically depends on the carrier gas that is used, and on the final velocity of the OH radicals. Within a measurement interval, the number density varies by about a factor of three throughout the range of final velocities. The highest number densities are typically observed for final velocities that are close to the mean velocity of the initial molecular beam, and for beams that are produced with a light carrier gas. The velocity spread depends on the settings of the Stark decelerator, and ranges from 10 to 25 m/s. The size of the packet is confined in the direction perpendicular to the beam axis to the  $3 \times 3\text{ mm}^2$  aperture of the Stark decelerator; the length of the packet in the beam direction

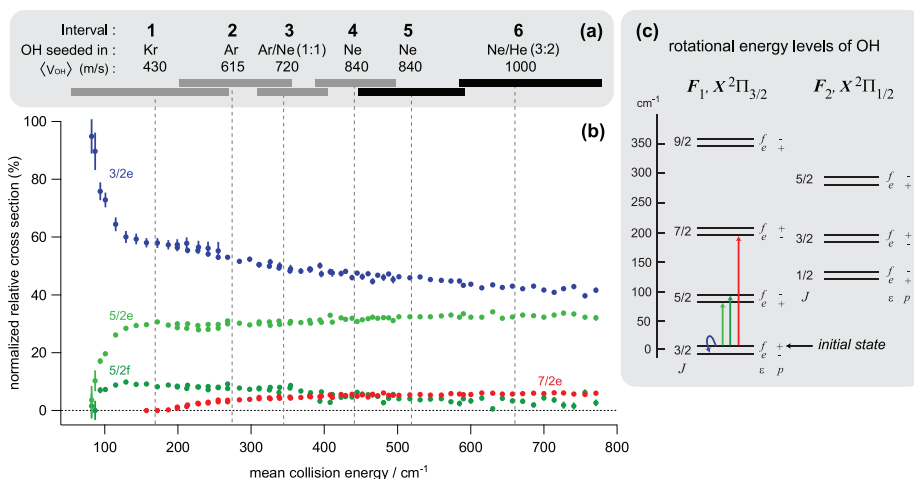


**Figure 7.2:** (a) Collision energy intervals that were used to measure the collision energy dependence of the state-to-state scattering cross sections. The carrier gases that are used to generate OH radical beams with the indicated mean velocities are given above each interval. (b) Measured relative collision induced populations for the four strongest scattering channels, that are indicated in the rotational energy level diagram of the OH radical (c). In this diagram, the energy splitting between both parity components is greatly exaggerated for reasons of clarity.

depends on the settings of the decelerator and is typically 10–15 mm. The state purity of the OH packet strongly depends on the carrier gas that is used and the settings of the Stark decelerator. Representative values of the background populations in levels other than the  $J = 3/2, f$  level are given in Table 7.1 for the different carrier gases that were used. The deceleration/acceleration process is highly quantum state specific, and the quantum state purity of the OH radicals approaches 100 %. The quantum state purity only drops below 99% when helium or neon is used, which reflects the inferior rotational cooling of OH radicals during the supersonic expansion for He and/or Ne containing carrier gases. The contaminating population is mainly in the low-field seeking  $X^2\Pi_{3/2}, J = 5/2, f$  level. Population in high-field seeking levels of  $e$ -parity is negligible for all experimental conditions.

The energy resolution depends on the velocity and angular spreads of both beams. The phase-space distribution of OH radicals that emerge from the decelerator is accurately known from simulations of the deceleration process. The spatial distribution of argon atoms is estimated from the microphone measurements; the velocity distribution is estimated to be 12% of the mean velocity. The collision energy distribution is approximately gaussian with a full width at half maximum of 20 cm<sup>-1</sup> at the lowest collision energies and grows approximately linearly to 33 cm<sup>-1</sup> at 500 cm<sup>-1</sup>.

carrier gas	$F_1(5/2f)$	$F_1(7/2f)$	$F_2(1/2f)$
Kr	0.10 - 0.40	—	—
Ar	0.17 - 0.43	—	—
Ar/Ne (1:1)	0.26 - 0.72	0.01 - 0.04	0.01 - 0.07
Ne	2.40 - 3.40	0.04 - 0.12	0.13 - 0.20
Ne/He (3:2)	1.83 - 2.90	0.02 - 0.15	0.12 - 0.22

**Table 7.1:** Background population in %. All states which are not listed are populated to less than 0.04%.

### 7.2.3 Experimental procedure and data analysis

The experiment runs at a repetition rate of 10 Hz, and all relevant trigger pulses to synchronize the experiment are computer controlled. The argon beam runs at a repetition rate of 5 Hz, and the collision signals are inferred from the signal intensity difference of alternating shots of the experiment. Within each interval of collision energies, the collision energy is varied in a quasi-continuous cycle. The Stark decelerator is programmed to produce a different velocity of the OH radicals every second shot of the experiment. The timing of the argon valve is adjusted automatically to match the arrival time of the OH packet in the collision zone. The collision energy is scanned within an interval using typically 5 – 15 different velocities of the OH packet; a single scan is thus made in 1 – 3 seconds. This scan is cycled 1000 times for every scattering channel, and the scattering signals that correspond to the same collision energies are averaged. Such cycles are made for all inelastic channels, and for all collision energy intervals. This measurement procedure ensures that the collision energy dependence of a given inelastic channel is insensitive to long-term variations in either the beam intensities or the laser wavelength, and can be measured independently from other channels. The relative signal intensities for the inelastic channels are measured for a fixed collision energy in each interval separately. These reference points are measured a few times, and are used to scale the signal intensities that result from the automated cycles with respect to each other.

During all measurements, the fluorescence signals are recorded using dedicated data acquisition software. The signal intensity of the strongest and weakest scattering channels differs by three orders of magnitude, and two modes of signal processing are used. The weakest channels are analyzed using photon counting; an analog mode of detection is used for the strongest channels. Both modes of signal acquisition are calibrated with respect to each other by comparing both modes for several channels with intermediate signal intensity.

With the experimental arrangement used here, only scattering events that change the quantum state of the OH radical, i.e., inelastic scattering events,



	<b>J</b>	<i>e</i>			<i>f</i>		
		transition	<b>ER</b>	<i>E</i> (cm <sup>-1</sup> )	transition	<b>ER</b>	<i>E</i> (cm <sup>-1</sup> )
$F_1$	$\frac{3}{2}$	$P_1$	$\frac{1}{3}$	[0.000]	$Q_1 + Q_{21}$	$\frac{3}{5}$	0.055
	$\frac{5}{2}$	$P_1$	$\frac{2}{5}$	83.723	$Q_1$	$\frac{1}{2}$	83.924
	$\frac{7}{2}$	$P_1$	$\frac{3}{7}$	201.931	$Q_1$	$\frac{1}{2}$	202.379
	$\frac{9}{2}$	$P_1$	$\frac{4}{9}$	355.120	$Q_1$	$\frac{1}{2}$	355.914
$F_2$	$\frac{1}{2}$	$Q_2 + Q_{12}$	$\frac{3}{4}$	126.296	$P_{12}$	$\frac{1}{2}$	126.453
	$\frac{3}{2}$	$Q_2$	$\frac{1}{2}$	187.497	$P_{12} + P_2$	$\frac{3}{5}$	187.757
	$\frac{5}{2}$	$Q_2$	$\frac{1}{2}$	288.776	$P_{12}$	$\frac{1}{2}$	289.048

**Table 7.2:** The rotational states of the OH radical that are of relevance to the experiment. The rotational energy of the levels, the rotational transitions that are used to probe the population in the levels, and the excitation rates that apply to these transitions are given. Rotational energies are adapted from ref. [113].

can be studied. A total of 13 inelastic scattering channels are measured. These channels populate the rotational levels that are shown in the energy level diagram in **Fig. 7.2 (c)**. The rotational levels are referred to hereafter as  $F_i(Je/f)$ , where  $i = 1$  and  $i = 2$  are used to indicate the  $X^2\Pi_{3/2}$  and  $X^2\Pi_{1/2}$  spin-orbit manifolds, respectively, and the parity labels  $e$  and  $f$  correspond to the two  $\Lambda$ -doublet components of each rotational level. The rotational energies of all levels are given in Table 7.2, together with the rotational transitions that are used to probe the individual levels. The transitions are labelled using the nomenclature of Dieke and Crosswhite [43]. A number of rotational levels are probed by inducing both the main and satellite lines of a transition simultaneously. The laser intensity is carefully adjusted to saturate both the main and satellite lines, without causing spectral overlap between the transitions that probe individual levels.

To relate fluorescence signal intensities to collision induced populations, the fraction of molecules that are laser excited and that contribute to the fluorescence intensity must be taken into account. This fraction is referred to as the excitation rate (ER). We assume that for laser excitation under saturated conditions, the population in the rotational level that is probed is equilibrated between all possible  $M_J$  levels of the initial and final levels of the rotational transition [105, 99]. Under this assumption, the ER is given by  $g''/(g' + g'')$ , where  $g'' = (2J'' + 1)$  and  $g' = (2J' + 1)$  denote the degeneracy of the initial and final state, respectively. In case molecules are excited by main and satellite lines simultaneously,  $g'$  is given by the sum over the degeneracies of the two final states. The excitation rates that apply to the rotational transitions to probe the 13 inelastic scattering channels are listed in Table 7.2. The population in

selected rotational levels was probed using different optical transitions, and it was verified that the difference in fluorescence intensities reflect the difference in excitation rates. The laser radiation is linearly polarized, and it was verified that a rotation of the polarization axis does not influence the fluorescence intensities.

In **Fig. 7.2 (b)** the measured relative collision induced populations are shown for the four strongest channels, i.e. channels that populate the  $F_1(3/2e)$ ,  $F_1(5/2e)$ ,  $F_1(5/2f)$ , and  $F_1(7/2e)$  levels. The error bars represent the statistical spread ( $2\sigma$ ) of the data as obtained from repeated runs of the experiment. The  $F_1(5/2e)$ ,  $F_1(5/2f)$ , and  $F_1(7/2e)$  levels open at a collision energy of  $83.7\text{ cm}^{-1}$ ,  $83.9\text{ cm}^{-1}$ , and  $201.9\text{ cm}^{-1}$  respectively, and the energetic thresholds are clearly recognized in the data. The only exoenergetic inelastic channel is scattering to the  $F_1(3/2f)$  level, and all inelastic scattering events populate this level at the lowest collision energies that were probed. We will postpone the discussion of all 13 measured channels to section 7.4; we will first describe the theoretical methods that were used to calculate the inelastic scattering cross sections.

## 7.3 Theory

When a diatomic molecule in a  $\Pi$  electronic state interacts with a spherical target, the degeneracy is lifted, giving rise to two states, one of  $A'$  and one of  $A''$  symmetry, in which the single-occupied  $\pi$  orbital lies, respectively in, or perpendicular to, the triatomic plane [114]. The inelastic scattering can be described in terms of the average  $V_{sum}$  and half-difference  $V_{dif}$  of the potential energy surfaces (PESs) corresponding to these two states [114].

### 7.3.1 Potential Energy Surfaces

In the simulations of the present experiments two sets of PESs are used. The first were the restricted-coupled-cluster [RCCSD(T)] PESs of Toboła *et al.* [107, 115]. Here, the ArOH complex is described by single-determinant restricted Hartree-Fock (RHF) wavefunction with the OH molecular geometry frozen at its equilibrium bondlength  $r_e = 0.96966\text{ \AA}$ . Subsequently, a full single- and double-excitation coupled-cluster calculation was carried out with non-iterative inclusion of triple excitations [RCCSD(T)] [116, 117]. We used the augmented correlation-consistent, quadruple-zeta (aug-cc-avqz) atomic orbital basis sets of Dunning and coworkers [118, 119]. The analytic fit to this RCCSD(T) PES has already been used in scattering studies of the Ar-OH(X) system [107]. For the present investigation we also used a second set of PESs, in which we averaged the interaction potential over the  $v = 0$  vibrational motion of the OH molecule. Here, we used a spin-unrestricted, coupled-cluster method [UCCSD(T)], which allows more flexibility in the description of the wave function of the system by introducing different spatial functions for  $\alpha$  and  $\beta$  spin-orbitals. We used the

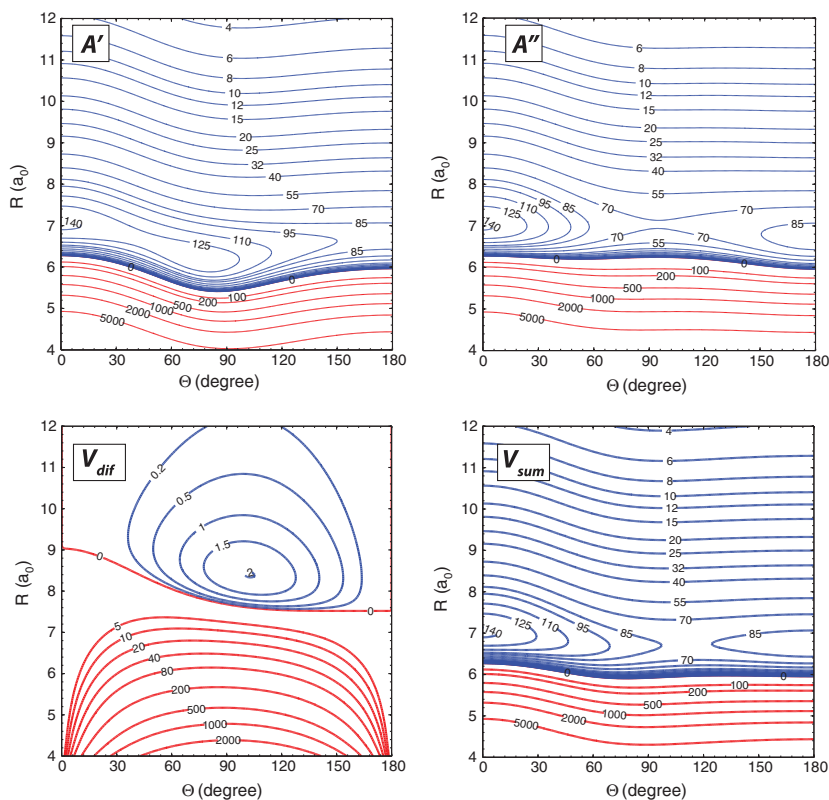


**Figure 7.3:** UCCSD(T) potentials of OH-Ar in  $\text{cm}^{-1}$  averaged over the  $v = 0$  vibrational motion of the OH moiety; for plots of the RCCSD(T) potential see Ref. [115]. Blue contours belong to negative values of the potential energy, red contours belong to positive values.

MOLPRO 2008 program suite [120] to carry out UCCSD(T) calculations on a grid of points specified by, in Jacobi coordinates, 10 equi-spaced values of the Ar-OH angle  $\theta$  (with  $\theta = 0$  corresponding to collinear ArHO), 35 values of the Ar-OH distance ranging from  $3.5 a_0$  to  $25 a_0$ , and five values of the OH bond distance  $r$  [ $0.7, 0.85, 0.96966, 1.15, 1.4 \text{ \AA}$ ]. This range of values of  $r$  spans well the lower vibrational wavefunctions of the OH radical. The interaction energy is determined in a supermolecular, counterpoise corrected approach where the total energies of the dimer and of the monomers are calculated using a dimer centered basis set [121]. At each point on the grid we performed three calculations for the PESs of both the  $A'$  and  $A''$  electronic states, using, successively, aug-cc-pvtz, aug-cc-pvqz and aug-cc-pv5z atomic orbital bases [118, 119]. These were then extrapolated to the complete basis set limit, using the mixed exponential and Gaussian formula of Peterson *et al* [122, 123]. Finally, the resulting three-dimensional  $V_{sum}$  and  $V_{dif}$  PES's were averaged over the  $v = 0$  OH vi-

Method	$\theta_e$	$R_e$	$D_e$
	ArHO, $A'$ , $A''$ , linear		
<b>UMP4</b>	0	7.08	147.3
<b>RCCSD(T)</b>	0	6.98	140.4
<b>UCCSD(T)/CBS</b> $r = r_e$	0	6.97	141.0
<b>UCCSD(T)/CBS</b> $\langle v = 0 \rangle$	0	7.01	141.7
	ArOH, $A'$ , $A''$ , linear		
<b>UMP4</b>	180	6.70	95.5
<b>RCCSD(T)</b>	180	6.71	91.8
<b>UCCSD(T)/CBS</b> $r = r_e$	180	6.70	91.4
<b>UCCSD(T)/CBS</b> $\langle v = 0 \rangle$	180	6.70	92.4
	ArOH, $A'$ , bent		
<b>UMP4</b>	75.1	6.23	135.5
<b>RCCSD(T)</b>	74.4	6.19	137.4
<b>UCCSD(T)/CBS</b> $r = r_e$	73.9	6.19	137.4
<b>UCCSD(T)/CBS</b> $\langle v = 0 \rangle$	74.8	6.18	137.1

**Table 7.3:** Calculated position and depth of the minima in the OH-Ar potential energy surface as predicted by four different *ab initio* surfaces. Energy  $D_e$  in  $\text{cm}^{-1}$ , coordinate  $R_e$  in  $a_0$ , coordinate  $\theta_e$  in degree.

brational wavefunction. As shown in **Fig. 7.3**, the ArOH PESs have minima in both collinear geometries. In addition, the state of  $A'$  reflection symmetry exhibits an additional minimum in bent geometry. The position and depth of these minima are listed in Table 7.3 as predicted by the present UCCSD(T) calculations as well as by the RCCSD(T) [107] and the earlier calculations of Kłos and co-workers [124], based on the application of 4<sup>th</sup>-order Møller-Plesset perturbation theory within an unrestricted (spin-polarized) framework (UMP4). As can be seen, the differences between the three CCSD(T) PESs are very small. Averaging over the  $v = 0$  vibrational motion of the OH moiety results in a slight ( $\sim 1 \text{ cm}^{-1}$ ) lowering of the well depth and a small shift in the minimum.

### 7.3.2 Scattering Calculations

The OH radical in its ground  $X^2\Pi$  electronic state is split into a lower (labelled  $F_1$ ) and upper ( $F_2$ ) spin-orbit manifold [125]. In Hund's case (a) these correspond, for a molecule with a negative spin-orbit constant, such as OH, to projection quantum numbers of the sum of the electronic orbital and spin angular momenta  $\Omega = 3/2$  and  $\Omega = 1/2$ , respectively. Each rotational level  $J$  is further split into two close-lying  $\Lambda$ -doublet levels, which are labelled  $e$  and  $f$ . For a state of doublet multiplicity, the total parity is  $+(-1)^{J-1/2}$  for the  $e$ -labelled states and  $-(-1)^{J-1/2}$  for the  $f$ -labelled states [40]. To define the asymptotic energies of the OH molecule we used the known spectroscopic values of the rotational constant in the lowest vibrational manifold ( $B_0 = 19.5487 \text{ cm}^{-1}$ ),

the spin-orbit constant ( $A_0 = -139.21 \text{ cm}^{-1}$ ), and the two  $\Lambda$ -doubling parameters ( $p = 0.235 \text{ cm}^{-1}$  and  $q = -0.0391 \text{ cm}^{-1}$ ) [126]. We further assume that the value of the spin-orbit constant of the OH is not altered by approach of the Ar atom. We have used the HIBRIDON program suite [127] to carry out fully-quantum, close-coupling calculations [103] of integral cross sections for the scattering of  $\text{OH}(X^2\Pi)$  with Ar on a dense grid of 3270 collision energies ranging from 0.2 to  $2500 \text{ cm}^{-1}$ . We used a channel basis large enough to ensure convergence of the integral and differential cross sections for all  $J, F_i \rightarrow J', F'_i$  transitions with  $J, J' \leq 11.5$ . The rotational basis set of OH was increased gradually with increasing total energy up to a maximum value of  $J = 14.5$ . At each collision energy, the maximum value of the total angular momentum  $\mathcal{J}$  was set large enough ( $\mathcal{J}_{max}^{tot} = 280$  for collision energies between  $2000\text{--}2500 \text{ cm}^{-1}$ ) that the inelastic cross sections were converged to within  $0.01 \text{ \AA}^2$ . We have also calculated differential cross sections, using both sets of PESs, for transitions from the initially prepared  $F_1(3/2f)$  level. These cross sections, which were used in the calculation of the density to flux transformation, were computed on a coarser dense grid of collision energies.

## 7.4 Results and Discussion

The experimental scattering signals are most easily compared with theoretical calculations when relative inelastic scattering cross sections are analyzed. The measured relative collision induced populations do not yield directly the relative scattering cross sections, but must be corrected for the detection probability of the scattered molecules. This probability is not equal for all scattered molecules and depends mostly on the post-collision velocity of the OH radicals. Molecules with a low laboratory velocity reside longer in the detection area, and are thus detected with higher probability than high velocity products which leave the detection area quickly.

The detection probability of a scattered OH radical depends on kinematic factors such as the translational energy of the products and/or the differential cross section (DCS) of the scattering process, and on experimental geometric factors like the spatial and temporal distribution of the colliding molecular beams and the size of the detection laser beam. To obtain the relative scattering cross sections from the raw experimental data, we corrected the scattering signals using a model that is explained in detail in chapter 6 section 6.4.3. Only small corrections are needed for the given experimental conditions, they amount to typically 0.1 to 5 percent. The correction factors are insensitive to small differences in the DCS. Use of DCS's from calculations based on the RCCSD(T) and UCCSD(T) sets of PESs gives rise to correction factors that are virtually identical.

The resulting experimental relative inelastic scattering cross sections for 13 inelastic channels are shown in **Fig. 7.4**. The cross sections for inelastic scat-

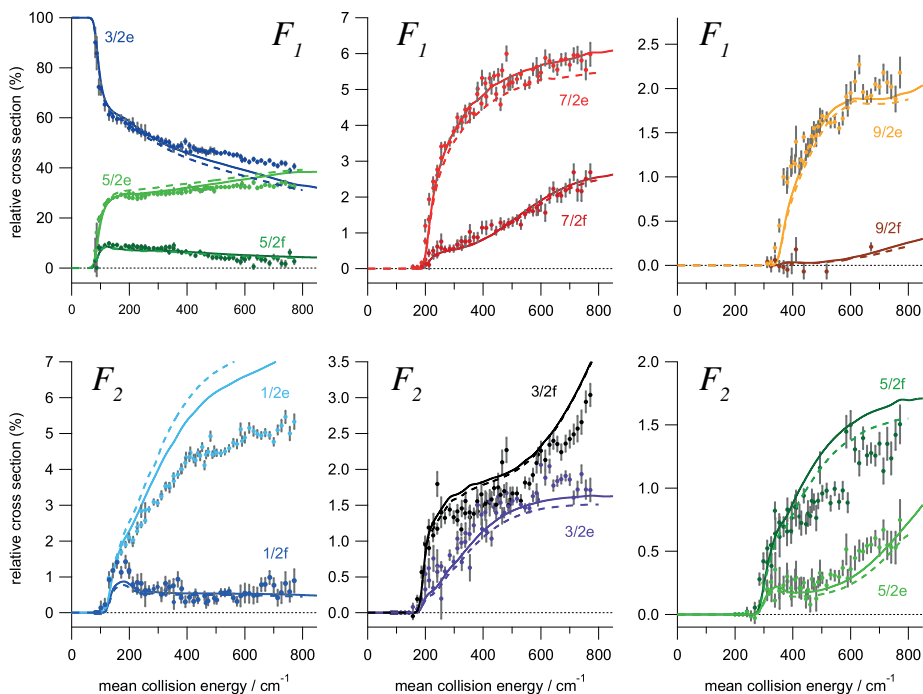


**Figure 7.4:** Measured relative state-to-state inelastic scattering cross sections for the scattering of OH ( $X^2\Pi_{3/2}, J = 3/2, f$ ) radicals with argon atoms as a function of the collision energy. The relative cross sections that result from the RCCSD(T) and the UCCSD(T) potential energy surfaces are given by the dashed and solid curves, respectively.

tering generally rise sharply from the energy threshold, reach a maximum, and become rather insensitive to a variation of the collision energy at higher energies. For fine structure conserving collisions (transitions within the  $F_1$  spin-orbit manifold) there is a strong propensity for final states of  $e$ -parity, while final states of  $f$ -parity are preferred for fine-structure changing collisions. An exception to this general propensity rule is the  $F_2(1/2)$  state for which the  $e$ -component is preferred in collisional excitation. These propensities are consistent with previous state-to-state inelastic scattering studies at high collision energies, and are well understood [102].

To facilitate a direct comparison between experiment and theory, we have also included in Fig. 7.4 the corresponding cross sections computed using the RCCSD(T) and UCCSD(T) PESs, as described in Section 7.3, convoluted with the experimental energy resolution. Excellent agreement is obtained for both potentials for all inelastic channels throughout the entire range of collision energies. Slightly better agreement is found for cross sections computed with the UCCSD(T) potential. However, the differences between cross sections com-

puted for the two sets of PES's are minor. This reflects the minor differences between them, as illustrated by the comparison of well depths and separations in Table 7.3.

For fine-structure-conserving transitions to levels within the  $F_1$  spin-orbit manifold we find excellent agreement between the experimental and computed cross sections. The only exceptions are slight differences for the transitions to the  $F_1(3/2e)$  and  $F_1(5/2e)$  levels for collision energies above  $500\text{ cm}^{-1}$ . For a  $^2\Pi$  molecule described well by Hund's case (a) (which is not, strictly speaking, the case of  $\text{OH}(X)$ ) transitions within a given spin-orbit manifold are induced by the average ( $V_{sum}$ ) of the PESs for  $A'$  and  $A''$  symmetry [103]. Thus the good agreement between experiment and theory for fine-structure conserving transitions seen in Fig. 7.4 is a measure of the quality of the  $V_{sum}$  PES predicted by the CCSD(T) calculations.

Transitions from the  $F_1$  to  $F_2$  spin-orbit manifolds are induced (again, in the Hund's case (a) limit) by the difference PES ( $V_{dif}$ ) [103]. The largest disagreement between experiment and theory occurs for transition to the  $F_2(1/2e)$  level, where the computed cross sections are significantly larger for collision energies greater than  $200\text{ cm}^{-1}$ . We note, however, that these cross sections are considerably smaller in magnitude than those for the spin-orbit conserving transitions. Nonetheless, the disagreement of the cross sections for the transition to the  $F_2(1/2e)$  level suggests that the difference between the  $A'$  and  $A''$  *ab initio* Ar-OH( $X$ ) PESs may be less accurate than their average.

As can be seen in Fig. 7.4, the difference in the cross sections predicted by the earlier RCCSD(T) and the present UCCSD(T) calculations is small. In general, and in particular in the case of the transition into the  $F_2(1/2e)$  level, this difference is considerably smaller than the magnitude of the disagreement between theory and experiment. The present UCCSD(T) PES's represent an average over the zero-point vibrational motion of the OH molecule. Comparison of these vibrationally averaged UCCSD(T) PES's with those calculated for the OH molecule frozen at  $r = r_e$ , the same rigid rotation approximation that was made in the RCCSD(T) calculations, show very little difference. The vibrationally averaged UCCSD(T) PES's, which are extrapolated to the complete basis set limit, represent the best currently achievable potential energy surfaces for a system like OH-Ar. Extending the complexity of the treatment of electron correlation to include full (rather than perturbative) inclusion of triple, and, ultimately, quadruple excitations would be computationally impractical.

We observe in Fig. 7.4 that the disagreement between theory and experiment increases at higher collision energy. At higher collision energy, the classical turning point moves up the repulsive wall. Thus, it is possible that the increasing discrepancy at higher energy indicates a progressively increasing inaccuracy higher on the repulsive wall. It is here, when the three atoms are closest, that a fully correct description of electron correlation becomes increasingly important. Thus, incompleteness in the description of triple excitations, and the neglect of quadruple excitations, may possibly lead to a greater degree of inaccuracy in

the calculated PES's in the repulsive region.

## 7.5 Conclusions and outlook

We have presented measurements of the state-to-state rotational inelastic scattering of OH radicals as a function of the collision energy. The velocity and the initial quantum state of the OH radicals prior to the collision is controlled by passing the OH radicals through a Stark decelerator. The collision energy is varied from 80 to 800  $\text{cm}^{-1}$ , and the relative inelastic scattering cross sections have been accurately determined for 13 inelastic scattering channels. Throughout the range of collision energies that were probed, excellent agreement is found with the results of quantum scattering calculations that are based on the most accurate PES's currently available. These PES's should provide a very good description of the interaction of the OH radical with Ar atoms.

The present experiment has allowed a more comprehensive comparison of experimental and theoretical inelastic cross sections than has been hitherto possible. The implications of the experiments that are presented in this chapter reach beyond the OH-Ar system alone. These experiments also demonstrate that the Stark deceleration technique has matured sufficiently to be applied successfully in a wide range of scattering experiments.

The level of sensitivity that can now be achieved in these experiments is comparable to the sensitivity of conventional crossed beam experiments of similar systems. In the present experiment, the sensitivity allows for the observation of scattering processes with cross sections  $\geq 0.01 \text{ \AA}^2$ . In future experiments one could add many of the well-established methods of the crossed beam experimentalist. For instance, the collision energy dependence of steric effects can be investigated by adding a static orientation field around the beam intersection region. The implementation of a velocity map imaging detector would allow for the measurement of the collision energy dependence of the differential cross sections [90]. The narrow velocity spread of the Stark decelerated beam yields images of the scattering products with a high angular and velocity resolution.

The Stark deceleration technique is applicable to a number of molecular species, and allows for scattering studies involving chemically relevant molecules like OH, NO,  $\text{ND}_3$ ,  $\text{H}_2\text{CO}$ , and  $\text{SO}_2$ . The recent development of the related Zeeman deceleration technique extends this chemical diversity to molecules like NH and  $\text{O}_2$ , all molecular radical species, and all metastable atoms [128, 129].

The study of molecular collisions in the 1–20  $\text{cm}^{-1}$  energy range is another exciting avenue. Cold molecular collisions are governed by rich quantum phenomena such as shape or Feshbach resonances that are less pronounced in collisions at high energies [130, 131]. These resonances are extremely sensitive to the details of the interaction potential, but have thus far escaped experimental observation. Over the energy regime investigated here, molecular collisions are expected to be highly susceptible to externally applied fields, opening the pos-



sibility for controlled chemistry. The Stark deceleration technique offers viable routes to reach experimentally the required energy range and resolution. For instance, in the present experiment the angle between the reagent beams can be made smaller to further reduce the collision energy. Although more challenging, the scattering between *two* Stark-decelerated packets of molecules, either directly or in a molecular synchrotron, would allow us to observe the scattering between fully state-selected and velocity controlled molecules at collision energies down to  $1\text{ cm}^{-1}$  [96, 132].

Although originally conceived as a method to produce cold polar molecules by decelerating molecules to a near-standstill, the Stark deceleration technique offers exciting perspectives for molecular beam scattering experiments as well. These tamed molecular beams add a novel new element to the existing collection of experimental methods to unravel the precise nature of molecular interactions.



## Chapter 8

# Scattering of Stark-decelerated OH radicals with rare-gas atoms

We present a combined experimental and theoretical study on the rotationally inelastic scattering of OH ( $X^2\Pi_{3/2}, J = 3/2, f$ ) radicals with the collision partners He, Ne, Ar, Kr, Xe, and D<sub>2</sub> as a function of the collision energy between  $\sim 60\text{ cm}^{-1}$  and  $400\text{ cm}^{-1}$ . The OH radicals are state selected and velocity tuned prior to the collision using a Stark decelerator, and field-free parity-resolved state-to-state inelastic relative scattering cross sections are measured in a crossed molecular beam configuration. For all OH-rare gas atom systems excellent agreement is obtained with the cross sections predicted by coupled channel scattering calculations based on accurate *ab initio* potential energy surfaces. This series of experiments complements recent studies on the scattering of OH radicals with Xe, Ar, He, and D<sub>2</sub>. A comparison of the relative scattering cross sections for this set of collision partners reveals interesting trends in the scattering behavior.

---

Based on: *Scattering of Stark-decelerated OH radicals with rare-gas atoms*  
L. Scharfenberg, K.B. Gubbels, M. Kirste, G.C. Groenenboom, A. van der Avoird,  
G. Meijer and S.Y.T. van de Meerakker; Eur. Phys. J. D **65**, 189-198 (2011)

## 8.1 Introduction

The study of collisional energy transfer between simple atoms and molecules has been essential for our present understanding of the dynamics of molecular interactions, and for testing our ability to accurately calculate potential energy surfaces that govern these interactions [80]. Rotationally inelastic scattering is one of the simplest scattering processes, and has been studied with ever increasing level of detail during the last decades. Experimental studies at a full state-to-state level are nowadays possible, revealing detailed information on the potential energy surfaces and the resulting motion on these surfaces [133, 134].

Rotationally inelastic scattering of free radical species such as OH or NO with atomic collision partners has been of special interest in molecular scattering experiments [100, 135]. The scattering of these open-shell species in a  $^2\Pi$  electronic state involves more than one Born-Oppenheimer potential surface, resulting in rich multi-surface dynamics with various quantum interference effects [136]. At a state-to-state level, collision induced transitions between rotational, spin-orbit, and  $\Lambda$ -doublet levels have been studied [101, 102, 137]. Sophisticated beam production and product state detection methods have been developed to measure differential cross sections [90, 138], the steric asymmetry of the collision [88], and the alignment or orientation of the collision products [106, 107, 115, 61]. The wealth of scattering data that is available for these systems, together with the spectroscopic data of the bound states of relevant complexes [139, 111], offers stringent tests for *ab initio* potential energy surfaces (PESs) and for quantum scattering calculations.

In recent years, new approaches to perform high-precision inelastic scattering experiments involving radical species have become possible with the development of the Stark-deceleration technique [3]. The Stark deceleration method exploits the concepts of charged-particle accelerator physics to produce molecular beams with a tunable velocity and almost perfect state purity [5]. The method was first applied to molecular scattering studies in 2006, when a Stark-decelerated beam of OH ( $X^2\Pi_{3/2}, J = 3/2, f$ ) radicals was scattered with a conventional beam of Xe atoms [18]. By tuning the velocity of the OH radicals between 33 m/s and 700 m/s prior to the collision, the center-of-mass collision energy was varied between  $60\text{ cm}^{-1}$  and  $400\text{ cm}^{-1}$ . This energy range encompasses the energetic thresholds for inelastic scattering to the first excited rotational levels of the OH radical, and the threshold behavior of the inelastic state-to-state cross sections was accurately determined. Excellent agreement was found with cross sections derived from coupled channel calculations on *ab initio* computed potential energy surfaces.

Since this first proof-of-principle experiment, a new crossed beam scattering apparatus was developed that employs an improved version of the Stark decelerator. With this decelerator, packets of OH radicals can be produced with a superior number density, a narrower velocity spread, and a higher quantum state purity (see chapter 5). This apparatus enables state-to-state scattering experi-

ments as a function of the collision energy with a sensitivity that exceeds that of conventional crossed beam scattering experiments. This was demonstrated on the benchmark OH ( $X^2\Pi$ )-Ar system in chapter 7, for which parity-resolved integral state-to-state scattering cross sections for in total 13 inelastic scattering channels have been determined as a function of the collision energy. The same methodology has also been applied to the scattering of OH radicals with He atoms and D<sub>2</sub> molecules [140].

These experiments challenge the most accurate potential energy surfaces and quantum scattering calculations presently available. For the scattering of OH radicals with Ar and He atoms, excellent agreement was found between experiment and theory, although at high collision energies and for specific inelastic channels deviations were found. For the OH-He system, the almost perfect quantum state purity offered by the Stark decelerator enabled the observation of the strong propensities for preferred excitation into final states of certain parity that had been predicted for this system [101].

In this chapter, we report new measurements on the rotationally inelastic scattering of OH ( $X^2\Pi_{3/2}$ ,  $J = 3/2$ ,  $f$ ) radicals with He, Ne, Kr, and Xe atoms, as well as D<sub>2</sub> molecules, at collision energies between 60 cm<sup>-1</sup> and 400 cm<sup>-1</sup>. The measured cross sections for the OH-Xe system confirm the cross sections that were determined in the earlier work of Gilijamse et al. [18]. For all four systems, excellent agreement is obtained with cross sections that are derived from quantum scattering calculations based on available potential energy surfaces.

These studies complement previous investigations on the scattering of OH radicals with He, Ar and D<sub>2</sub>, and together form a complete data set on the scattering of OH radicals with rare-gas atoms. A comparison of the relative cross sections for the various collision partners is presented that reveals interesting aspects about the scattering behavior.

## 8.2 Experiment

### 8.2.1 Experimental setup

The experiments are performed in a crossed molecular beam apparatus that is schematically shown in Fig. 7.1 on page 109. A detailed description of this machine, as well as of the production, Stark deceleration, and detection of OH radicals can be found in the previous chapters; only the most essential aspects of the experiment are described here.

A pulsed supersonic beam of OH radicals is created by photolysis of nitric acid seeded in either krypton or argon. After the supersonic expansion nearly all OH radicals reside in the lowest rotational ( $J = 3/2$ ) and vibrational level of the  $X^2\Pi_{3/2}$  electronic ground state. The two  $\Lambda$ -doublet components of this level, labeled  $e$  and  $f$ , are populated equally in the beam since their energy difference is only 0.05 cm<sup>-1</sup>. OH radicals that reside in the energetically higher lying

$f$ -component can be focused and velocity tuned using the Stark decelerator, whereas OH radicals in the  $e$ -component are deflected from the beam axis. After passing a skimmer, the packet of OH radicals enters the  $3 \times 3 \text{ mm}^2$  opening of the decelerator. A sequence of high voltage pulses is applied to the decelerator electrodes to generate time-dependent electric field configurations that either decelerate, guide or accelerate the OH radicals.

The packet of OH ( $X^2\Pi_{3/2}, J = 3/2, f$ ) radicals that emerges from the decelerator has a quantum state purity of  $> 99\%$  and intersects the central axis of the secondary beam at an angle of  $90^\circ$  at a distance of 16.5 mm from the decelerator exit. Collisions take place in a field free region and the initially uneven distribution over  $M_J$ -components which is present inside the decelerator is assumed to be scrambled completely while the molecules move towards the collision region.

A temperature controlled solenoid valve produces the secondary beam of rare-gas atoms or  $\text{D}_2$  molecules. The mean forward velocity of this beam is inferred from a time-of-flight measurement using two microphone-based beam detectors that are placed 300 mm apart. To ensure single-collision conditions, the intensity of the secondary beam is kept sufficiently low so that the decrease of the initial population in the  $J = 3/2, f$  level remains below 4 percent.

The collision products are state-selectively detected *via* saturated laser-induced fluorescence when the most intense part of the OH packet is in the center of the collision region. A pulsed dye laser is used to induce various rotational transitions of the  $A^2\Sigma^+, v = 1 \leftarrow X^2\Pi, v = 0$  band. The laser beam intersects both molecular beams under  $90^\circ$  and the off-resonant fluorescence is collected by a lens and imaged onto a photomultiplier tube.

### 8.2.2 Measurement procedure and data analysis

The collision energy range between  $60$  and  $400 \text{ cm}^{-1}$  is covered using two measurement intervals with overlapping energy, as described in chapter 7. For these intervals, molecular beams of OH radicals are produced using Kr and Ar as seed gases, resulting in OH radical beams with mean initial velocities of  $430 \text{ m/s}$  and  $615 \text{ m/s}$ , respectively. Within each interval, the collision energy is varied by tuning the velocity of the OH radicals prior to the collision using the Stark decelerator. For collisions with Ne, Ar, Kr and Xe atoms, the mean velocity of the rare-gas atom beam is kept constant for all measurements. The mean speed and corresponding valve temperatures for the different rare-gas beams are:  $445 \text{ m/s}$  (Ne,  $93 \text{ K}$ ),  $400 \text{ m/s}$  (Ar,  $110 \text{ K}$ ),  $330 \text{ m/s}$  (Kr,  $163 \text{ K}$ ) and  $300 \text{ m/s}$  (Xe,  $220 \text{ K}$ ). For collisions with He atoms and  $\text{D}_2$  molecules, the small reduced mass makes it inconvenient to vary the collision energy by solely tuning the speed of the OH packet. Therefore, the speed of the secondary beam is varied in comparatively large steps by changing the temperature of the valve. For a given valve temperature, the OH velocity is then tuned from  $168$  to  $741 \text{ m/s}$ . The  $\text{D}_2$  molecules are assumed to be distributed between ortho and para rota-

tional levels according to the statistical weights, i.e. 67% of the molecules are expected to populate rotational levels with  $J$  even and 33% levels with  $J$  odd.

The Stark decelerator provides packets of OH radicals at a rate of 10 Hz. The secondary beam is operated at 5 Hz and collision signals are inferred from the fluorescence intensity difference between alternating shots of the experiment. To limit the effects of long-term drifts in the experiment, the collision energy dependence of the scattering channels is measured *via* a quasi-continuous cycle (see chapter 7). In such a cycle, the collision energy is scanned automatically by producing a different velocity of the OH radicals for every shot of the experiment. The collision signals are obtained from typically 1000 runs of the experiment, and quoted error bars represent the statistical fluctuation of the measured mean values. Both photon counting and analog detection are used in the data acquisition.

The experiment is not sensitive to elastic scattering; only scattering events that change the internal quantum state of the OH radical can be detected. Within the studied collision energy range, collisional excitation to at most 13 rotational levels can occur. These levels are labeled as  $F_1(Je/f)$  and  $F_2(Je/f)$ , where  $F_1$  and  $F_2$  denote the  $X^2\Pi_{3/2}$  and the  $X^2\Pi_{1/2}$  spin-orbit manifolds, respectively, and the parity labels  $e$  and  $f$  correspond to the two  $\Lambda$ -doublet components of each rotational level. An energy level diagram with all relevant rotational levels is shown in Fig. 8.2 (p. 133). Note that the  $\Lambda$ -doublet splitting is largely exaggerated in this figure for reasons of clarity. The rotational transitions that are used to probe the individual levels, as well as the excitation rates that are used to convert measured fluorescence intensities to populations, are specified in Table 7.2 on page 113.

The experimental scattering signals are most easily compared with theoretical calculations when relative inelastic scattering cross sections are derived from the observations. The relative scattering cross section for a specific channel is proportional to the total number of molecules that is detected in the corresponding quantum state. However, the detection volume is necessarily limited and in general not all molecules can be detected. A density-to-flux transformation is required to relate the measured relative populations in final states to relative scattering cross sections. Under the given experimental conditions, the resulting correction is small, as is discussed in detail in chapter 6. For the scattering of OH with Ne, Ar, Kr and Xe atoms, we have performed the transformation using the differential cross sections determined from theory. For He and D<sub>2</sub>, the density-to-flux correction can be safely omitted due to the small mass of the collision partner compared to the mass of the OH radical.

## 8.3 Theory

The theory for the scattering of  $^2\Pi$ -state molecules with  $^1S$ -state atoms is well established [103]. In particular, collision studies between OH molecules and

rare-gas atoms at low collision energies have received a lot of attention over the last years [18, 141, 142, 143]. In this section we only give a brief summary of the relevant theory. A more extensive account can be found in Ref. [144].

The Hamiltonian that describes the scattering of ground state OH ( $X^2\Pi$ ) with rare-gas atoms is given by

$$\hat{H} = \frac{-\hbar^2}{2\mu R} \frac{\partial^2}{\partial R^2} R + \frac{\hat{L}^2}{2\mu R^2} + \sum_{\Lambda', \Lambda} |\Lambda'\rangle V_{\Lambda', \Lambda}(R, \theta) \langle \Lambda| + \hat{H}_{\text{OH}}, \quad (8.1)$$

where  $R$  is the length of the vector  $\mathbf{R}$  that connects the center-of-mass of the OH molecule and the rare-gas atom,  $\mu$  is the reduced mass of the atom-OH complex,  $\hat{L}$  is the angular momentum operator corresponding to end-over-end rotation of the OH-rare gas atom complex, and  $\hat{H}_{\text{OH}}$  is the Hamiltonian of the OH molecule in the ( $X^2\Pi$ ) ground state. The  $X^2\Pi$  electronic ground state of the OH radical has two degenerate components with projections  $\Lambda = \pm 1$  of the orbital electronic angular momentum on the internuclear  $\hat{r}$ -axis. The OH-rare gas interaction is represented by the operators  $|\Lambda'\rangle V_{\Lambda', \Lambda}(R, \theta) \langle \Lambda|$  that couple different electronic states  $\Lambda$  and  $\Lambda'$ . The angle  $\theta$  defines the angle between the unit vector  $\hat{R}$  and the OH bond direction  $\hat{r}$ , with  $\theta = 0$  corresponding to collinear atom-HO. The Hamiltonian of OH includes rotation, spin-orbit coupling and  $\Lambda$ -doubling, where we use the OH rotational constant  $B = 18.5487 \text{ cm}^{-1}$ , the spin-orbit coupling constant  $A = -139.21 \text{ cm}^{-1}$ , and  $\Lambda$ -doubling parameters  $p = 0.235 \text{ cm}^{-1}$  and  $q = -0.0391 \text{ cm}^{-1}$  [126]. From Eq. (8.1) it follows that differences in the collisions between OH and the various rare gas atoms originate from the differences in the interaction potential and the reduced mass.

When the rare-gas atom approaches the OH molecule, the electronic degeneracy of the  $\Pi$  state is lifted. The resulting matrix elements  $V_{\Lambda, \Lambda'}$  of the potential are nonzero for  $\Lambda' - \Lambda = 0, \pm 2$ , and two potential energy surfaces are involved in the scattering process. The potential energy surfaces can be expanded in Racah normalized spherical harmonics

$$\begin{aligned} V_{1,1} = V_{-1,-1} &= \frac{V_{A'} + V_{A''}}{2} = \sum_l v_{l,0}(R) C_{l,0}(\theta, 0), \\ V_{1,-1} = V_{-1,1} &= \frac{V_{A''} - V_{A'}}{2} = \sum_l v_{l,2}(R) C_{l,2}(\theta, 0), \end{aligned} \quad (8.2)$$

where  $A'$  and  $A''$  refer to the reflection symmetry of the electronic states. The surfaces  $V_{1,1}$  and  $V_{1,-1}$  are often referred to as the sum  $V_{\text{sum}}$  and difference  $V_{\text{diff}}$  potential energy surface, respectively.

*Ab initio* calculations for the OH-atom interaction energy can be performed using the MOLPRO program package [120], which has resulted in potentials for the OH-He [145], OH-Ne [145, 146], OH-Ar [147] (see also p. 115), OH-Kr [148] and OH-Xe [18] complexes. The most relevant properties of the various interacting systems, such as the reduced mass of the OH-rare gas atom complex,



Atom	$\mu$	$\alpha$	$E$	$R$	$\theta$	PES
<b>He</b>	3.24	0.21	-27.1	6.54	0	$A', A''$
			-21.8	6.09	180	$A', A''$
			-30.0	5.69	68.6	$A'$
<b>Ne</b>	9.22	0.40	-59.34	6.53	0	$A', A''$
			-45.18	6.14	180	$A', A''$
			-59.60	5.82	67.6	$A'$
<b>Ar</b>	11.9	1.64	-141.7	7.01	0	$A', A''$
			-92.4	6.70	180	$A', A''$
			-137.1	6.18	74.8	$A'$
<b>Kr</b>	14.14	2.48	-172.5	7.2	0	$A', A''$
			-110.3	6.8	180	$A', A''$
			-177.0	6.25	78	$A'$
<b>Xe</b>	15.05	4.04	-202.3	7.6	0	$A', A''$
			-117.9	7.3	180	$A', A''$
			-224.4	6.45	84	$A'$

**Table 8.1:** Properties of the Rg-OH interaction. Values for the potential minima adapted from [18, 147, 124, 146, 148]. Reduced mass  $\mu$  in u, polarizability  $\alpha$  in  $10^{-24} \text{ cm}^3$ , potential energy  $E$  in  $\text{cm}^{-1}$ , coordinate  $R$  in  $a_0$ , coordinate  $\theta$  in degree.

the polarizability of the rare gas atom, the minima of the potential energy surfaces in the two different linear configurations of the complex ( $\theta = 0^\circ$  and  $\theta = 180^\circ$ ), as well as the position and energy of the minimum of the  $A'$  potential at a nonlinear geometry, are listed in Table 8.1.

The potential energy surfaces vary in the quality of the basis set used, and the quality of the method. All potentials used the counterpoise procedure to correct for the basis set superposition error [149]. The OH-He and the OH-Ne potentials of Lee *et al.* were both calculated with a spin-restricted coupled-cluster method with single and double excitations and perturbative triples [RCCSD(T)]. The augmented triple-zeta correlation-consistent basis set (aug-cc-pVTZ) was used with an additional ( $3s, 3p, 2d, 2f, 1g$ ) set of bond functions centered in the midpoint of the vector  $\mathbf{R}$  [145]. The Ne-OH potential was also calculated more recently by Sumiyoshi *et al.*, who used an explicitly correlated, spin-unrestricted approach [UCCSD(T)-F12b] with a larger quintuple-zeta basis set (aug-cc-pV5Z) [146]. We calculated the cross sections for both Ne-OH potentials, and we find that the most recent potential gives a clearly better agreement with experiment. This is probably due to the larger basis set and the improved calculation method, which includes explicit electron correlations that particularly enhance the accuracy of the short-ranged behavior of the potential. For the Xe-OH potential, RCCSD(T) was used with a quadruple-zeta basis set (aug-cc-pVQZ) and with a set of ( $3s, 3p, 2d, 1f, 1g$ ) mid-bond orbitals with geometry-dependent exponents [18]. For the Kr-OH potential, the UCCSD(T)-F12b approach was used with the aug-cc-pVQZ basis set [148].

Finally, the Ar-OH potential surface was calculated with a spin-unrestricted approach [UCCSD(T)], where the basis set was extrapolated to the complete basis set limit, and where also an averaging over the  $v = 0$  motion of the OH molecule was performed. For the other systems, the OH molecular geometry was assumed frozen at its equilibrium bond length (OH-He, Ne, Kr) or at its vibrationally averaged distance (OH-Xe).

In order to calculate the OH monomer eigenfunctions it is convenient to use a parity adapted Hund's case (a) basis set, labeled by  $|\Omega, J, M_J, p\rangle$  with  $J$  the total angular momentum of the OH molecule,  $\Omega$  and  $M_J$  the projections on the molecular and space-fixed quantization axes, and  $p$  the parity under inversion. For the exact OH eigenfunctions,  $|\Omega|$  is nearly a good quantum number. The total angular momentum of the OH-atom complex is represented by the operator  $\hat{\mathcal{J}} = \hat{\mathbf{J}} + \hat{\mathbf{L}}$ , whose eigenfunctions are obtained by coupling the monomer basis with the spherical harmonics  $|L, M_L\rangle = Y_{L,M_L}(\vartheta, \varphi)$ , where  $\vartheta$  and  $\varphi$  are the space-fixed spherical coordinates of the vector  $\mathbf{R}$ . Assuming that the OH bond length is fixed, we write the scattering wave functions as products of radial and angular functions,

$$\Psi_{\beta, L}^{\mathcal{J}, M_{\mathcal{J}}, \mathcal{P}} = \frac{1}{R} \sum_{\beta', L'} \chi_{\beta', L' \leftarrow \beta, L}^{\mathcal{J}, M_{\mathcal{J}}, \mathcal{P}}(R) \psi_{\beta', L'}^{\mathcal{J}, M_{\mathcal{J}}, \mathcal{P}}(\hat{R}, \hat{r}), \quad (8.3)$$

where  $\beta$  is a shorthand notation for the monomer quantum numbers ( $F_i, J$ ) with  $i$  to distinguish between the  $F_1$  and  $F_2$  spin-orbit manifolds of the OH eigenstates. Note that the total angular momentum  $\mathcal{J}$ , its space-fixed projection  $M_{\mathcal{J}}$  and the parity of the complex  $\mathcal{P} = p(-1)^L$  are conserved in the collision process. The experimentally relevant scattering properties, that is the cross sections, are conveniently expressed in terms of scattering matrices, which can be obtained using standard asymptotic matching procedures [150]. The obtained  $S$ -matrices are then related to the scattering amplitudes, which in turn determine the differential cross sections [151].

In order to achieve convergence of the calculated cross-sections, we used a basis set that included all OH rotational states up to an angular momentum of  $J = 21/2$ , and took into account all partial wave contributions up to a total angular momentum of  $\mathcal{J} = 241/2$ . For the propagation of the wavefunction, the renormalized Numerov method was used, starting at  $4a_0$  and continuing to  $35a_0$  with  $a_0$  the Bohr radius. The cross sections were evaluated on an energy grid with a  $5 \text{ cm}^{-1}$  interval spacing, well below the experimental energy resolution in all cases. It is noted that this energy grid is too sparse, however, to identify individual scattering resonances that occur at collision energies around the energetic thresholds. In **Fig. 8.1** the total integral inelastic cross sections (the sum of the integral cross sections over all inelastic channels) are shown for collisions of OH ( $X^2\Pi_{3/2}, J = 3/2, f$ ) radicals with the five different rare-gas atoms. In this figure, the contribution to the total cross section of collisions that populate levels within the  $F_1$  manifold are indicated. The total inelastic cross

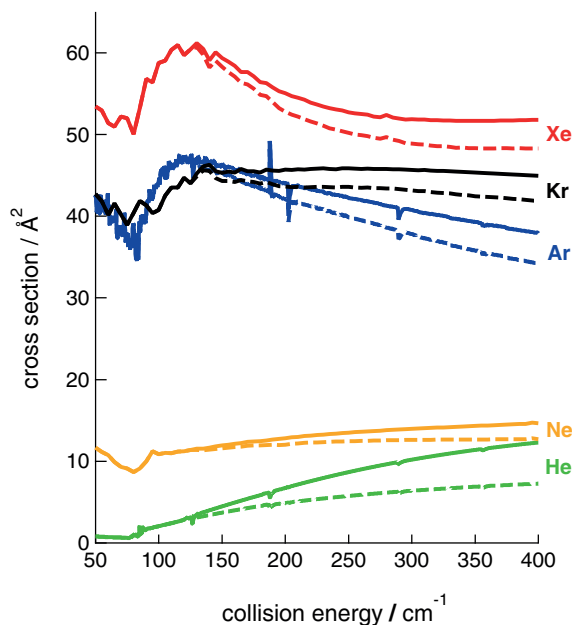


**Figure 8.1:** The calculated total integral cross sections for inelastic scattering of OH ( $X^2\Pi_{3/2}, J = 3/2, f$ ) radicals with He, Ne, Ar, Kr and Xe atoms (solid lines). The contribution to the cross section which is due to transitions into the  $F_1$  spin-orbit manifold are shown by the broken lines.

section is seen to rise with increasing reduced mass, increasing atom polarizability and increasing well depth of the potential. The total inelastic cross sections as presented in Fig. 8.1 can be used to deduce absolute state-to-state inelastic cross sections from the experimentally determined relative state-to-state cross sections. These are presented in the next section.

## 8.4 Results and discussion

### 8.4.1 Scattering of OH radicals with Ne, Kr, and Xe atoms

In this section, we first describe the results on the scattering of OH radicals with Ne, Kr, and Xe atoms. A detailed comparison of the scattering behavior for the various systems is given in section 8.4.2.

The measured relative state-to-state cross sections for the scattering of OH radicals with Ne, Kr, and Xe are shown in **Fig. 8.2** and **Fig. 8.3**. The theoretically computed cross sections, convoluted with the experimental energy resolution, are included as solid curves; in the case of Ne, the cross sections obtained from the most recent potential [146] are shown as solid curves, whereas

the ones obtained from the older potential [145] are shown as dashed curves. For completeness, the experimental and theoretical cross sections from previous work for the OH-He, OH-D<sub>2</sub>, and OH-Ar systems [140, 147] are also shown in these figures. The spin-orbit manifold conserving (transitions within the  $F_1$  spin-orbit manifold) and spin-orbit manifold changing collisions (transitions from the  $F_1$  into the  $F_2$  manifold) are summarized in Fig. 8.2 and Fig. 8.3, respectively. In both figures, the state resolved scattering channels are labeled following the color codes as indicated in the rotational energy level diagrams.

For the scattering of OH( $F_1(3/2f)$ ) with Ne, the  $\Lambda$ -doublet changing channel  $F_1(3/2f) \rightarrow F_1(3/2e)$  dominates at low collision energies; at energies above  $\sim 150 \text{ cm}^{-1}$  the scattering is dominated by rotational excitation to the  $F_1(5/2e)$  state. For spin-orbit manifold conserving transitions, there is a strong propensity for final states of  $e$  parity. For spin-orbit manifold changing collisions, a strong  $\Lambda$ -doublet propensity is only observed for excitation into the  $F_2(1/2)$  states.

The scattering behavior of OH with Kr is observed to be very similar to the scattering of OH with Xe atoms, and dominated by the  $\Lambda$ -doublet changing  $F_1(3/2f) \rightarrow F_1(3/2e)$  channel at all probed collision energies. For rotational excitation, the cross sections generally rise sharply from the energetic threshold, reach a maximum, and become rather insensitive to a variation of the collision energy at higher energies. For spin-orbit manifold conserving collisions, there is a small propensity for excitation into final states of  $e$  parity. For spin-orbit changing collisions, no clear preference for excitation into one of the  $\Lambda$ -doublet components of a final rotational state is observed.

For all three scattering systems, the measured cross sections are compared to the cross sections determined by quantum coupled channel calculations based on high quality *ab initio* PESs. For the scattering of OH with Ne and Kr atoms, excellent agreement is found between the experimentally determined and theoretically computed scattering cross sections. The cross sections for all scattering channels, both for spin-orbit conserving and spin-orbit changing collisions, and for all collision energies are perfectly reproduced by the calculations.

For the scattering of OH radicals with Xe atoms, the measured cross sections confirm the cross sections that were determined in previous work on this system [18]. It is noted that both experiments were performed in different apparatuses and with different levels of sensitivity. For the present experiment, in which state-to-state cross sections for a larger number of final states are measured, excellent agreement is obtained between experimental and theoretical cross sections. The relative scattering cross sections, as well as the threshold behavior of individual channels, are reproduced well. Also the increase in the relative scattering cross section for the  $F_1(3/2f) \rightarrow F_1(5/2e)$  channel at collision energies just above the energetic threshold is perfectly reproduced. The only pronounced difference between experiment and theory is observed for the  $F_2(1/2f)$  channel at energies just above threshold. This discrepancy could possibly be explained by small imperfections in the difference potential. We have observed in the

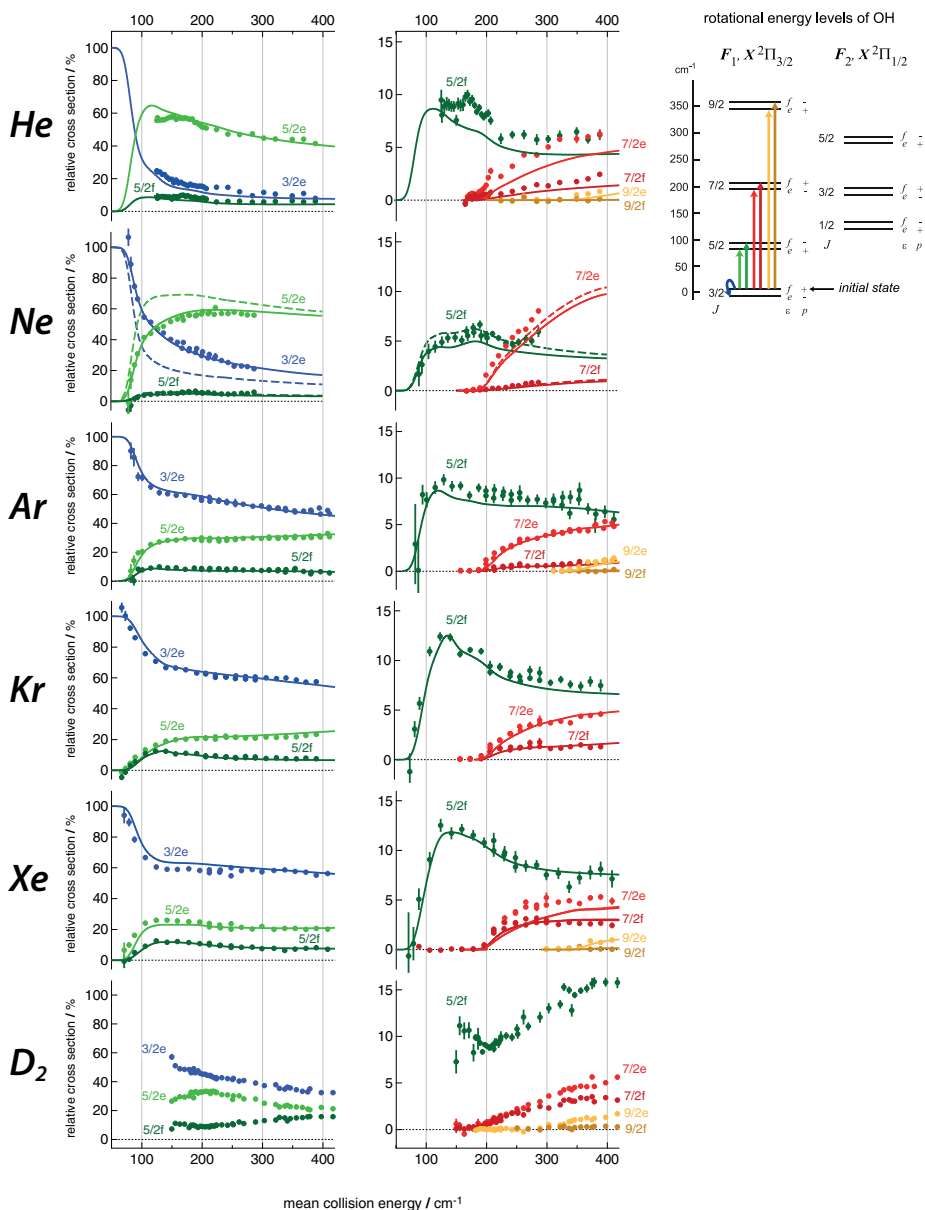


**Figure 8.2:** Relative state-to-state inelastic scattering cross sections for spin-orbit conserving ( $F_1 \rightarrow F_1$ ) collisions of OH ( $X^2\Pi_{3/2}$ ,  $J = 3/2, f$ ) radicals with He, Ne, Ar, Kr, and Xe atoms and  $D_2$  molecules as a function of the collision energy. The theoretically calculated cross sections are included as solid curves. In the case of Ne, the cross sections calculated from the old potential [145] are shown as dashed curves. In the energy-level scheme, the splitting between both parity components of each rotational level is greatly exaggerated for reasons of clarity.

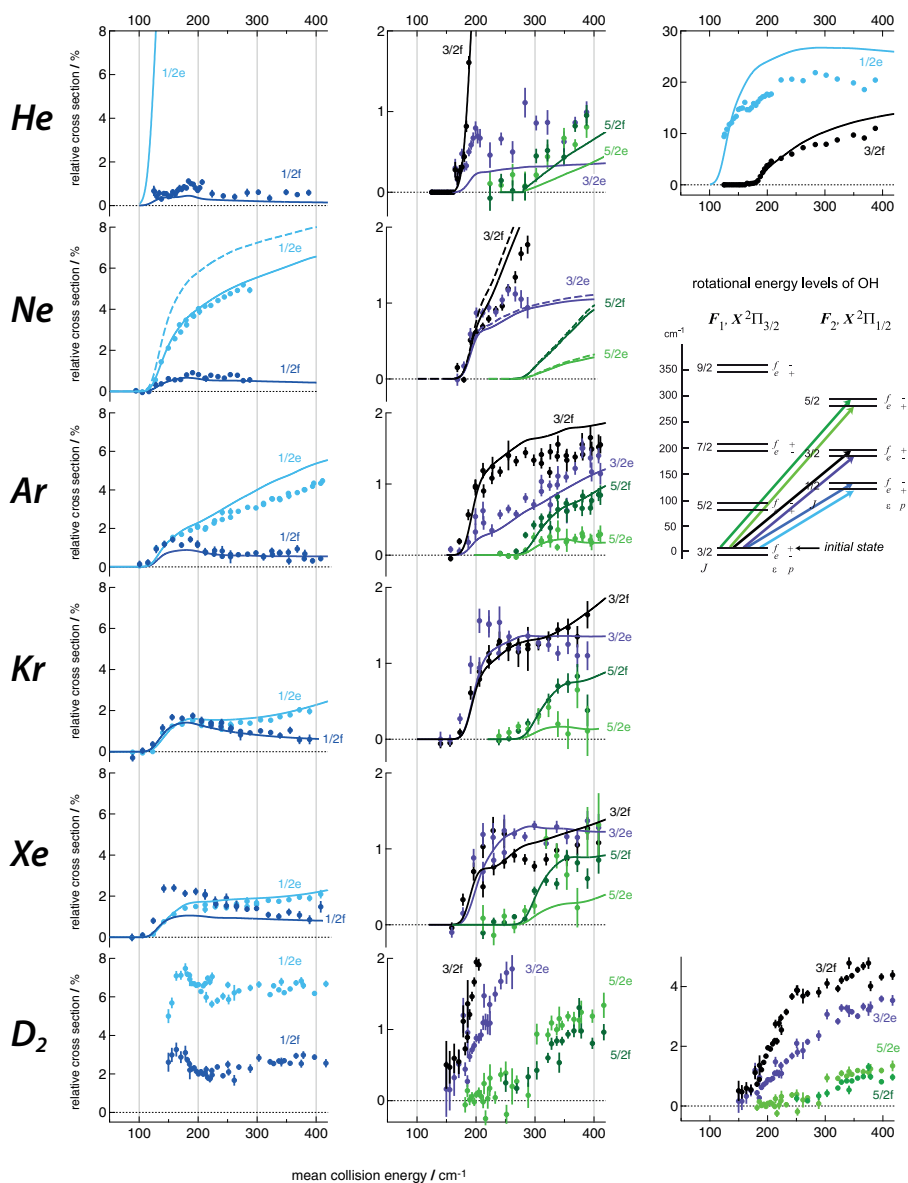


**Figure 8.3:** Relative state-to-state inelastic scattering cross sections for spin-orbit changing ( $F_1 \rightarrow F_2$ ) collisions of OH ( $X^2\Pi_{3/2}, J = 3/2, f$ ) radicals with He, Ne, Ar, Kr, and Xe atoms and  $D_2$  molecules as a function of the collision energy. The theoretically calculated cross sections are included as solid curves. In the case of Ne, the cross sections calculated from the old potential [145] are shown as dashed curves.

calculations that the cross sections for scattering into the  $F_2(1/2)$  channels are particularly sensitive to small variations of  $V_{\text{diff}}$ . At low collision energies, there appears to be a small offset in the collision energy of a few  $\text{cm}^{-1}$  between the experimental and the theoretical values for cross section. The origin of this offset is not known, but could well be the result of an uncertainty in the Xe beam velocity measurements.

### 8.4.2 Comparison between the various collision partners

Interesting trends are observed when the general scattering behavior for the various OH-rare gas atom systems are qualitatively compared with each other. For the series OH-He, Ne, Ar, Kr, Xe it is observed that the role of the  $F_1(3/2f) \rightarrow F_1(3/2e)$  channel gradually increases. At the same time, propensities for preferred scattering into the  $e$  parity state of the other rotational states of the  $F_1$  manifold tend to get weaker. Finally, the contribution of the spin-orbit changing  $F_1(3/2f) \rightarrow F_2(1/2e)$  channel to the scattering is gradually reduced from  $\sim 20\%$  for OH-He to  $\sim 2\%$  for OH-Xe. We note that these qualitative changes are strongest when the collision partner He is replaced by Ne, and when Ne is replaced by Ar. When Ar is replaced by Kr, smaller changes are observed, while hardly any changes occur in going from Kr to Xe. The scattering of OH radicals with  $\text{D}_2$  molecules does not fit entirely in this trend; the overall scattering behavior for this system resembles that of the OH-Ar, OH-Kr and OH-Xe systems.

A qualitative understanding of the inelastic scattering of OH radicals with rare-gas atoms can be obtained from a general analysis given by Dagdigian *et al.* [104]. According to this analysis, the relative strength of the various scattering channels (in particular for low values of  $J$ ) can be estimated from the rotational energy level structure of the OH radical and the different expansion coefficients  $v_{l,0}(R)$  and  $v_{l,2}(R)$  of the sum and difference potential energy surfaces, respectively.

A close inspection of the nature of the interaction potential and the relevant coefficients that determine the state-to-state cross sections can yield a satisfying understanding of the physical origin of general scattering features [152]. As outlined in Ref. [140], for instance, the profound difference in the scattering behavior that is observed for the inelastic scattering of OH with He atoms or  $\text{D}_2$  molecules can be explained by the much larger anisotropy of the OH- $\text{D}_2$  PESs compared to the OH-He PESs. In general, a small  $F_1(3/2f) \rightarrow F_1(3/2e)$   $\Lambda$ -doublet changing cross section, a strong propensity for rotational excitation into the  $e$  parity component of the  $F_1(5/2)$  state, and a strong cross section for scattering into the  $F_2(1/2e)$  level indicates that the scattering is dominated by the symmetric  $l = \text{even}$  terms, whereas the opposite scattering behavior is expected for systems in which the asymmetric  $l = \text{odd}$  terms play a large role. The former is the case for the weakly interacting OH-He system that results in a potential energy surface with small anisotropy; the latter applies to the

strongly interacting OH-D<sub>2</sub> system.

These qualitative arguments can also be used to rationalize the trends that are observed for the scattering of OH with the series of rare-gas atoms He, Ne, Ar, Kr, and Xe. Indeed, with increasing polarizability of the collision partner, the scattering is governed by potential energy surfaces with increasing well depth and larger anisotropy. This results in more dominant  $l = \text{odd}$  expansion coefficients, and hence in a larger  $F_1(3/2f) \rightarrow F_1(3/2e)$   $\Lambda$ -doublet cross section, smaller  $e$  over  $f$  propensities for excitation into the  $F_1(5/2)$  state, and reduced cross sections for the  $F_1(3/2f) \rightarrow F_2(1/2e)$  spin-orbit changing channel.

The trends that are observed are thus consistent with what may be expected from the nature of the OH-rare gas atom interaction potential. However, for the series of collision partners also dynamic effects that are related to the increasing mass of the collision partner may play a role. It is not *a priori* clear which features in the scattering behavior are due to the effect of the PES, and which features result from the effect of the reduced mass.

To study the influence of both parameters on the scattering, we have performed calculations for two hypothetical OH-rare gas atom systems. In the first system, we have used the OH-He PESs, but performed the scattering calculations with the He atom mass replaced by the Xe atom mass. In the second system, we have used the OH-Xe PESs, but performed the scattering calculations with the Xe atom mass replaced by the He atom mass. These model systems thus yield information on the scattering of OH radicals with a weakly interacting but heavy collision partner, and with a strongly interacting but light collision partner. The resulting inelastic scattering cross sections for both systems are shown in **Fig. 8.4**.

For the OH-He interaction potential, significant changes in the cross sections are observed upon replacement of the He atom mass with the Xe atom mass. In particular, the relative cross section for scattering into the  $F_1(3/2e)$  state increases, while the contributions of the  $F_1(5/2e)$  and  $F_2(1/2e)$  channels to the scattering decrease. Note that also the threshold behavior of various channels changes significantly; the cross sections rise less sharply at collision energies above threshold. The resulting state-to-state relative inelastic cross sections closely resemble those for the OH-Ne system, i.e. a weakly interacting system with a larger reduced mass compared to OH-He.

For the OH-Xe interaction potential, opposite changes in the scattering cross sections are observed upon replacement of the Xe mass with the He atom mass. The  $F_1(3/2f) \rightarrow F_1(3/2e)$  channel becomes less dominant, and the  $F_1(5/2e)$  and  $F_2(1/2e)$  channels gain importance. The resulting relative state-to-state cross sections resemble those that are measured for the OH-D<sub>2</sub> system, i.e. of a strongly interacting system with a smaller reduced mass compared to OH-Xe.

These model calculations indicate that the nature of the potential energy surface and the reduced mass of the system can both have a profound and qualitatively similar influence on the scattering cross sections. This suggests that the interesting trends that are observed for the scattering of OH with He,



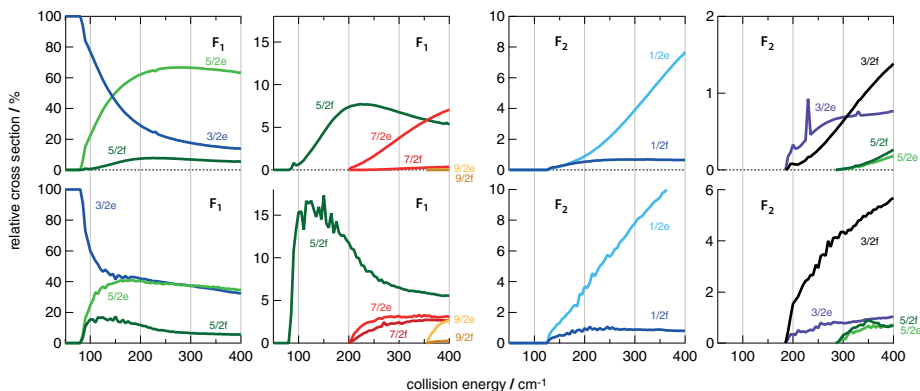


**Figure 8.4:** Calculated relative state-to-state inelastic scattering cross sections for two hypothetical OH ( $X^2\Pi_{3/2}, J = 3/2, f$ )-rare gas atom systems. Top row: calculations are based on the OH-He PESs from Ref. [124], but the scattering calculations are performed with the He atom mass replaced by the Xe atom mass. Bottom row: calculations are based on the OH-Xe PESs from Ref. [18], but the scattering calculations are performed with the Xe atom mass replaced by the He atom mass.

Ne, Ar, Kr, and Xe are in part due to the increasing interaction strength of the OH radical with the collision partner, and in part due to the increasing mass of the rare-gas atom. It is not straightforward to disentangle the influence of both effects using *ab initio* potential energy surfaces and coupled channel scattering calculations as employed here. The individual influence on the scattering of properties such as well depth, anisotropy and reduced mass can be studied best using models for the potential and the scattering dynamics that allow for an independent variation of the relevant parameters [153, 154].

## 8.5 Conclusions

We have presented new measurements on the state-to-state rotational inelastic scattering of Stark-decelerated OH ( $X^2\Pi_{3/2}, J = 3/2, f$ ) radicals with Ne, Kr, and Xe atoms. For each collision system, a total of 13 inelastic scattering channels is studied at collision energies in the 70 – 400  $\text{cm}^{-1}$  range. The collision energy dependence of the relative inelastic scattering cross sections, the threshold behavior of inelastic channels, and the energy dependence of the state-resolved propensities are accurately determined. Excellent agreement is found with the inelastic scattering cross sections determined from quantum coupled channel scattering calculations based on *ab initio* potential energy surfaces.

These measurements complement recent studies on the scattering of the OH radicals with He atoms, Ar atoms, and  $\text{D}_2$  molecules, and confirm the measured cross sections of the original work on the scattering of OH radicals with Xe atoms. Together, these studies represent the most complete combined

experimental and theoretical study of the inelastic scattering of an open shell radical in a  $^2\Pi$  electronic state with rare-gas atoms. The excellent agreement that is obtained with the cross sections that are derived from *ab initio* potential energy surfaces for all OH-rare gas atom systems clearly indicates that the scattering of these systems is well understood.

Significant differences are found in the scattering behavior of OH radicals with the various collision partners, and interesting trends are observed in the relative inelastic scattering cross sections for the series OH-He, Ne, Ar, Kr, and Xe. Replacement of the He atom by heavier rare-gas atoms results in a more dominant  $F_1(3/2f) \rightarrow F_1(3/2e)$   $\Lambda$ -doublet changing cross section, smaller propensities for preferred excitation into one of the  $\Lambda$ -doublet components of excited rotational levels, and reduced cross sections for the  $F_1(3/2f) \rightarrow F_2(1/2e)$  transition. These trends result in part from the increasing strength of the OH-rare gas atom interaction, and in part from the increasing mass of the rare-gas atom.

## Chapter 9

# Crossed beam scattering with optimized energy resolution

Crossed molecular beam scattering experiments in which the energy of the collision is varied can reveal valuable insight in the collision dynamics. The energy resolution that can be obtained depends mainly on the velocity and angular spreads of the molecular beams; often, these are too broad to resolve narrow features in the cross sections like scattering resonances. The collision energy resolution can be greatly improved by making appropriate choices for the beam velocities and the beam intersection angle. This method works particularly well for situations in which one of the beams has a narrow velocity spread, and we here discuss the implications of this method for crossed beam scattering experiments with Stark-decelerated beams.

---

Based on: *Crossed beam scattering experiments with optimized energy resolution*  
L. Scharfenberg, S. Y. T. van de Meerakker and G. Meijer  
Phys. Chem. Chem. Phys. **13**, 8448 (2011)

## 9.1 Introduction

The crossed molecular beam technique is one of the most widely used experimental approaches to study collisions between individual atoms and molecules, and has been seminal to our present understanding of molecular dynamics at a microscopic level [80]. Since its introduction in the 1950's, the technique has witnessed a remarkable and continuous development. Its present level of advancement allows for accurate control over the collision partners prior to the collision event, and for sophisticated detection of the collision products [155, 10, 28].

One of the most important parameters in a collision experiment is the collision energy of the colliding particles. The collision energy can be tuned by controlling the velocity of the particles prior to the collision, or by changing the angle between the intersecting beams. For the latter approach, ingenious crossed molecular beam machines have been engineered to continuously vary the collision energy [81]. These methods have been used to measure, for instance, the threshold behavior of rotational energy transfer [99, 82], or to tune the collision energy over the reaction barrier for reactive scattering [156, 157].

Recently, new molecular beam techniques have become available that allow for detailed control over the velocity of molecules in a beam. This control is obtained by exploiting the interaction of molecules with electric or magnetic fields in a so-called Stark decelerator or Zeeman decelerator, respectively [3, 4]. The tunability of the velocity allows for scanning of the collision energy in a fixed experimental geometry. State-to-state inelastic scattering between Stark-decelerated OH radicals and conventional beams of He, Ne, Ar, Kr, and Xe atoms, as well as D<sub>2</sub> molecules, has been studied. These beam deceleration methods hold great promise for future scattering experiments and offer the possibility to extend the available collision energy range to energies below one wavenumber [96].

Essential in these experiments is the resolution with which the collision energy can be varied. High energy resolutions are particularly important at those collision energies where a detailed structure in the energy dependence of the cross sections is expected. At low collision energies, shape or orbiting resonances can occur that are caused by rotational states of the collision complex that are trapped behind the centrifugal or reaction barrier [158, 159]. At collision energies near the energies of excited states of one of the reagents, also Feshbach resonances can occur [160]. The experimental mapping of these resonances would probe the interaction potentials with unprecedented detail [161].

The energy resolution that can be obtained experimentally depends on the velocity and angular spreads of the molecular beam pulses. Typical molecular beam spreads are too large to reveal narrow features like scattering resonances that often require energy resolutions of about one wavenumber. So far, only in exceptional cases have resonances been observed, mostly for kinematically favorable systems in which a collision partner with low mass has been used

[162, 163, 164, 165]. Recently, crossed beam experiments employing a tunable beam crossing angle have been reported in which the resolution was sufficient to resolve the contribution of individual partial waves to the scattering [166, 167].

Compared to conventional molecular beams, Stark-decelerated molecular beams offer superior velocity spreads that typically range between 1 and 20 m/s [57]. This narrow velocity spread can be exploited in crossed beam scattering experiments to yield a high energy resolution. Indeed, energy resolutions of about  $13\text{ cm}^{-1}$  have already been achieved for the OH-Xe and OH-Ar systems, which is particularly good in view of the relatively large reduced mass of these systems. This energy resolution was sufficient to accurately measure the threshold behavior of the rotational inelastic cross sections and to resolve broader features in the collision energy dependence of the cross sections (see p.118 and p.133,134). The sharp resonances that are predicted by *ab initio* calculations remained elusive, however.

To further improve the energy resolution in these experiments, the velocity spread of the collision partner needs to be reduced. This can be achieved by using a second Stark decelerator to obtain control over a molecular collision partner, or by using mechanical velocity selectors to reduce the velocity spread of the atomic collision partner. However, both approaches would reduce the number density in the colliding beams.

Here we describe a simple yet effective method to improve the collision energy resolution that does not rely on velocity selection of the target beam. We show that for beam crossing angles smaller than  $90^\circ$ , kinematically favorable situations can occur in which the velocity spread of the target beam does not contribute to the collision energy spread. This enables high collision energy resolutions without having to sacrifice the number density of the target beam that is available to the scattering. Furthermore, it is experimentally more convenient because it avoids the use of a mechanical velocity selector for the target beam.

This method has been exploited before to improve the resolution in scattering experiments. It was described for the first time in a book chapter by H. Pauly and J.P. Toennies [168] in 1968 and it was part of the dissertation [169] of R. Feltgen (a student of Pauly) in 1970. The method was used in an experiment by Scoles and coworkers, in which orbiting resonances were observed in the integral elastic scattering cross sections for the scattering of velocity selected H atoms by Hg atoms [162, 163]. A beam intersection angle of  $73^\circ$  was used in order to improve the velocity resolution. A similar investigation was performed by Toennies and coworkers, who used a beam intersection angle of  $46^\circ$  to resolve orbiting resonances in the scattering of H atoms by various rare gas atoms [164]. Finally, we note that under well chosen kinematic conditions, one may produce molecules which are standing still (in the laboratory frame) after the collision [170, 171].

The approach discussed in this chapter is particularly advantageous, if one of the beams has a narrow velocity spread and if the overall angular spread of the beams is sufficiently small. For collisions between Stark-decelerated beams

and conventional beams of rare gas atoms, for instance, a very high energy resolution can be obtained that may well be sufficient to experimentally resolve scattering resonances, even for systems with a relatively large reduced mass.

This chapter is organized as follows. In section 9.2 the method itself is explained in more detail, and the beam properties that are used throughout in the examples are introduced. In section 9.3 we describe different experimental approaches that can be followed to vary the collision energy, and their implications for the collision energy resolution are analyzed. The description will be held rather general, although we will emphasize the experimental arrangement of one Stark-decelerated beam colliding with a conventional molecular beam. In section 9.4 we illustrate the potential of the method using a recent crossed beam experiment as an example. In this experiment, a Stark decelerated beam of OH radicals was scattered with a beam of He atoms at a  $90^\circ$  crossing angle, and we show that the future implementation of the method may well lead to the experimental observation of scattering resonances for this system. In section 9.5 we will draw conclusions, again with an emphasis on the advantages this method can have for crossed beam collision experiments in which Stark-decelerated beams are employed.

## 9.2 Collision kinematics

Consider two colliding particles with mass  $m_1$  and  $m_2$  and with respective laboratory velocity vectors  $\mathbf{v}_1$  and  $\mathbf{v}_2$ . This situation is sketched in **Fig. 9.1**. The collision energy  $E$  of the system, calculated in a frame of reference that is moving with the velocity of the center-of-mass of the two particles, is given by:

$$E = \frac{\mu}{2} |\mathbf{v}_1 - \mathbf{v}_2|^2 = \frac{\mu}{2} (v_1^2 + v_2^2 - 2v_1v_2 \cos \phi), \quad (9.1)$$

where  $v_1$  and  $v_2$  are the magnitudes of the laboratory velocity vectors,  $\phi$  is the enclosed angle between  $\mathbf{v}_1$  and  $\mathbf{v}_2$ , and  $\mu = m_1m_2/(m_1+m_2)$  is the reduced mass of the system. This energy  $E$  is the total energy that is available for inelastic processes. Small changes in  $v_1$ ,  $v_2$  or  $\phi$  will cause an approximate change of  $E$  that is given by its differential:

$$\frac{dE}{\mu} = [v_1 - v_2 \cos \phi] dv_1 + [v_2 - v_1 \cos \phi] dv_2 + v_1 v_2 \sin \phi d\phi. \quad (9.2)$$

The geometric meaning of the partial derivatives is brought out more clearly if expressed directly by the velocity vectors:

$$\frac{dE}{\mu} = [v_1 - \hat{\mathbf{v}}_1 \cdot \mathbf{v}_2] dv_1 + [v_2 - \hat{\mathbf{v}}_2 \cdot \mathbf{v}_1] dv_2 + |\mathbf{v}_1 \times \mathbf{v}_2| d\phi \quad (9.3)$$

with the vectors of unit length  $\hat{\mathbf{v}}_1$  and  $\hat{\mathbf{v}}_2$ .

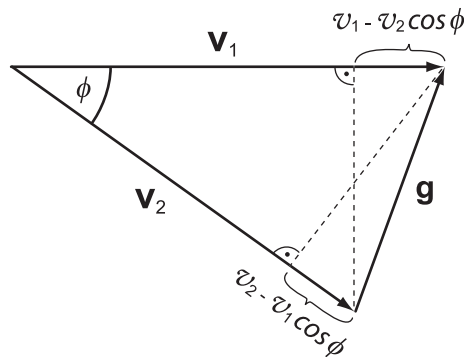


**Figure 9.1:** Laboratory velocity vectors  $\mathbf{v}_1$  and  $\mathbf{v}_2$  of two colliding particles. The relative velocity vector of the two particles is  $\mathbf{g} := \mathbf{v}_1 - \mathbf{v}_2$ .

Two important special cases can occur. If the beams are parallel on average ( $\phi = 0^\circ$  or  $180^\circ$ ), the influence of the angular spread of the beams becomes negligible. If the relative velocity vector  $\mathbf{g}$  is, on average, perpendicular to  $\mathbf{v}_1$  or  $\mathbf{v}_2$ ,  $E$  is almost unaffected by small changes in  $v_1$  or  $v_2$ , respectively. In this case the influence of the velocity spread of one of the beams becomes negligible. The collision energy resolution thus strongly depends on the geometry of the Newton diagram that describes the scattering process. For a suitable choice of the geometry, this can be exploited to optimize the collision energy resolution in the experiment. This is the main idea behind the method.

To make the discussion quantitative, an estimate of the collision energy distribution is required. This distribution is determined by the distributions of the vectors  $\mathbf{v}_1$  and  $\mathbf{v}_2$  and hence by six independent variables. This number can be reduced by changing to a more suitable coordinate system and by making appropriate approximations. If the vectors  $\mathbf{v}_1$  and  $\mathbf{v}_2$  are written as functions of spherical coordinates the collision energy becomes:

$$E(\mathbf{v}_1, \mathbf{v}_2) = E(\mathbf{v}_1(v_1, \varphi_1, \theta_1), \mathbf{v}_2(v_2, \varphi_2, \theta_2)) \quad (9.4)$$

where  $\theta_{1(2)}$  denotes the polar angle, i.e. the angle subtended by  $\mathbf{v}_{1(2)}$  and the z-axis and  $\varphi_{1(2)}$  denotes the azimuthal angle, i.e. the angle subtended by the orthogonal projection of  $\mathbf{v}_{1(2)}$  onto the xy-plane and the x-axis. If the averaged velocity vectors lie exactly within the xy-plane, the first order change of  $E$  with  $\theta_{1(2)}$  vanishes<sup>2</sup> so that we need to consider the projection of the velocity vectors onto the xy-plane only. For the experiment, this means that it is sufficient to collimate the beams by slits (rather than pinholes) that are oriented perpendicular to the xy-plane. We can now identify  $\phi$  in equation (9.1) with  $\phi = \varphi_1 - \varphi_2$ , and we only have to optimize the collision energy resolution with respect to the three scalar variables  $v_1$ ,  $v_2$ , and  $\phi$ .

---

<sup>2</sup>A derivation is given in the Appendix on p. 155.

		<sup>7</sup> LiH	OH/NH <sub>3</sub>	CO
$m_2 \backslash m_1$		8	17	28
1	H	0.88	0.94	0.97
2	D/H <sub>2</sub>	1.60	1.79	1.87
3	<sup>3</sup> He/HD	2.18	2.55	2.71
4	<sup>4</sup> He/D <sub>2</sub>	2.67	3.24	3.50
8	<sup>7</sup> LiH	4.00	5.44	6.22
17	OH/NH <sub>3</sub>	5.44	8.50	10.58
20	Ne/ND <sub>3</sub>	5.71	9.19	11.67
28	CO	6.22	10.57	14.00
40	Ar	6.67	11.93	16.47
83.8	Kr	7.30	14.13	20.99
131.3	Xe	7.54	15.05	23.08

**Table 9.1:** Reduced mass  $\mu = m_1 m_2 / (m_1 + m_2)$  (in atomic units) for a selection of collision systems.

In the experiment,  $v_1, v_2$  and  $\phi$  are distributed around their mean values; let the variance<sup>3</sup> of these variables be denoted by  $\sigma$ . Because  $\varphi_1$  and  $\varphi_2$  are independent, the variance  $\sigma_\phi$  of the distribution for  $\phi$  is given by  $\sigma_\phi^2 = \sigma_{\varphi_1}^2 + \sigma_{\varphi_2}^2$ . Hence the differential (9.2) can be used to estimate the width of the energy distribution, and the variance of the collision energy  $\sigma^2(E)$  is given to first order by:

$$\frac{\sigma^2(E)}{\mu^2} = [v_1 - v_2 \cos \phi]^2 \sigma_{v_1}^2 + [v_2 - v_1 \cos \phi]^2 \sigma_{v_2}^2 + [v_1 v_2 \sin \phi]^2 \sigma_\phi^2 \quad (9.5)$$

in which  $v_1, v_2$  and  $\phi$  now stand for the respective mean values. In the following,  $E$  will denote the *mean* collision energy which is to first order given by (9.1) when  $v_1, v_2$  and  $\phi$  are replaced by their mean values.

Because  $E$  as well as  $\sigma(E)$  is linear in  $\mu$ , it suffices to consider  $\sigma(E/\mu)$ . For convenience, the value of  $\mu$  is listed in Table 9.1 for a few selected collision systems. The molecules that are listed in the top row are typical molecules that are suitable candidates for Stark deceleration.

---

<sup>3</sup>The variance is defined as usual by  $\sigma^2 := \frac{1}{n} \sum_i (\bar{x} - x_i)^2$ , with the average value of  $x$  denoted by  $\bar{x}$ , and the summation over the total number of particles  $n$ .



## 9.3 Overview and applications

If one intends to conduct an experiment at a given mean energy  $E$  with the highest possible resolution, one has to optimize five parameters:  $\Delta v_1, \Delta v_2, \Delta \phi$  and the mean values of *two* of the three variables  $v_1, v_2, \phi$  – the third is always determined through equation (9.1). In the following sections, we will analyze how the resolution depends on the experimental parameters, using three different experimental approaches. In section 9.3.1 we discuss the situation in which the beam speeds are held constant, and the collision energy is tuned by variation of the beam intersection angle  $\phi$  alone. In section 9.3.2, we describe the situation for a fixed beam intersection angle and target beam speed; the collision energy is tuned by variation of  $v_1$ . Finally, in section 9.3.3 we discuss the most general case in which  $v_1, v_2$ , and  $\phi$  are allowed to vary to optimize the energy resolution.

The parameters that are used in the examples are chosen to represent the collision energy resolution as realistic as possible and that may be expected in an experiment. The molecular beam velocity spreads are assumed to be 10 % of the mean speed of the beam. In those cases where the velocity of the primary beam ( $v_1$ ) is varied, we assume that the beam is produced with a Stark decelerator. For a Stark-decelerated beam, the absolute velocity spread in the forward direction is (almost) constant and does not depend on the mean velocity; we will assume here a constant velocity spread of 10 m/s for all cases. The angular spread of a Stark-decelerated beam is generally smaller (typically  $1^\circ$ , or about 20 mrad) than the angular spread of a conventional molecular beam. To simplify the analysis, we assume a constant angular spread in the examples, but one should keep in mind that it actually depends on the forward velocity if a decelerator is used. Angular spreads are assumed to be 0, 20, 40 or 80 mrad.

For the following analysis, we assume Gaussian distributions for all variables. In this case the distribution for  $E$ , as approximated by the differential, becomes a well defined Gaussian with  $\sigma(E)$  given by equation (9.5). If we denote the full width at half maximum of the distribution of quantity  $x$  by  $\Delta(x) \equiv \Delta_x$ , we have  $\Delta(x) := 2.35\sigma(x)$  and

$$\Delta(E/\mu) = \left( [v_1 - v_2 \cos \phi]^2 \Delta_{v_1}^2 + [v_2 - v_1 \cos \phi]^2 \Delta_{v_2}^2 + [v_1 v_2 \sin \phi]^2 \Delta_\phi^2 \right)^{1/2}. \quad (9.6)$$

This expression is used for all calculations that are presented below.

### 9.3.1 $v_1$ and $v_2$ constant, $\phi$ variable

In this case, both beam speeds are assumed to be constant, and the beam intersection angle alone is used to change the energy. For the kinematic parameters we use  $v_1 = v_2 = 500$  m/s, and  $\Delta v_1 = \Delta v_2 = 50$  m/s. The resulting curves for the energy resolution  $\Delta(E/\mu)$  as a function of  $E/\mu$  are shown in **Fig. 9.2**. Two

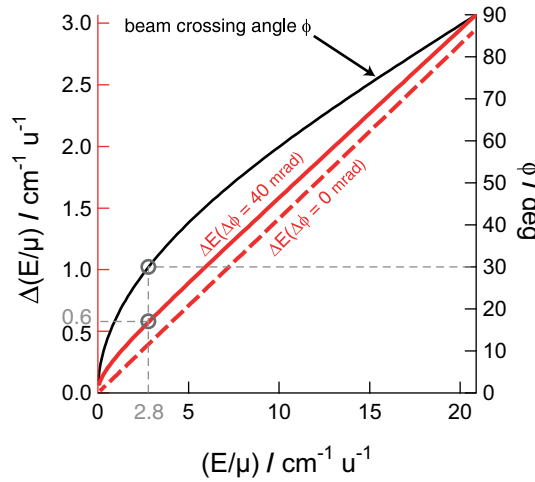


**Figure 9.2:** The dependence of the full width at half maximum  $\Delta(E/\mu)$  on  $E/\mu$  pertaining to the situation in which both beam velocities are constant, and the collision energy is tuned by variation of  $\phi$  (see section 9.3.1). Beam parameters:  $v_1 = v_2 = 500$  m/s,  $\Delta_{v_1} = \Delta_{v_2} = 50$  m/s and  $\Delta_\phi = 40$  mrad ( $2.3^\circ$ ) (solid red curve),  $\Delta_\phi = 0$  mrad (dashed red curve). The corresponding beam intersection angle is shown as the black curve with respect to the axis on the right side.

curves are shown that correspond to an angular spread of  $\Delta\phi = 0$  (red dashed curve), and  $\Delta\phi = 40$  mrad (red solid curve). The angle  $\phi$  that is needed to obtain a specific  $E/\mu$  is given by the black curve with respect to the right axis.

If small crossing angles can be realized, fairly low collision energies are accessible for systems with a small reduced mass. For example, the system  $\text{OH}/^4\text{He}$  has  $\mu = 3.2$  u, so that at  $30^\circ$  a collision energy of  $\approx 9$   $\text{cm}^{-1}$  is obtained with a resolution of  $\approx 1.9$   $\text{cm}^{-1}$ .

The energy resolution  $\Delta(E/\mu)$  depends approximately linearly on the energy  $E/\mu$ , resulting in a constant relative energy resolution  $\Delta E/E$ . This linear behavior is a consequence of the choice of equal velocities  $v_1 = v_2 = v$ . With the help of equations (9.6) and (9.1), the relative energy resolution  $\Delta E/E$  for this special case is given by:

$$\frac{\Delta E}{E} = \left( \frac{\Delta_{v_1}^2 + \Delta_{v_2}^2}{v^2} + \frac{1 + \cos \phi}{1 - \cos \phi} \Delta_\phi^2 \right)^{1/2}, \quad (9.7)$$

which is nearly independent of  $\phi$  for small values of  $\Delta\phi$ .

It is noted that the low collision energies and high energy resolutions that can be obtained for small beam intersection angles and systems with low reduced mass have been exploited in an experiment by Costes and coworkers, who have thereby been able to observe oscillations in the integral cross sections for the reactive scattering of S ( $^1D_2$ ) atoms with  $\text{H}_2$  molecules [167].

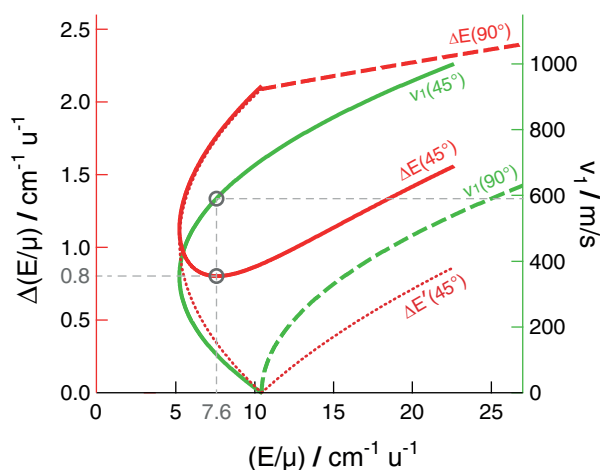


**Figure 9.3:** The dependence of  $\Delta(E/\mu)$  on  $E/\mu$  for the situation in which the beam intersection angle and the target beam velocity  $v_2$  is constant, while the collision energy is tuned by variation of  $v_1$  (see section 9.3.2). Beam intersection angles of  $\phi = 45^\circ$  (red solid curve), or  $\phi = 90^\circ$  (red dashed curve) are assumed. Beam parameters:  $v_2 = 500$  m/s,  $\Delta_{v_2} = 50$  m/s,  $\Delta_{v_1} = 10$  m/s, and  $\Delta_\phi = 40$  mrad ( $2.3^\circ$ ). The corresponding primary beam velocities  $v_1$  are shown as the green curves with respect to the axis on the right. Note that at low collision energies for  $45^\circ$  there are two possible values for  $v_1$  at a given energy with differing values for the resolution. The red dotted curve labeled  $\Delta E'(45^\circ)$  pertains to the hypothetical case in which  $\Delta_{v_1} = 0$  m/s,  $\Delta_\phi = 0$  mrad.

### 9.3.2 $v_2$ and $\phi$ constant, $v_1$ variable

In this case, the experimental geometry and the target beam velocity are fixed and the collision energy is tuned by varying the velocity  $v_1$ . This situation pertains, for instance, to a collision experiment in which a Stark-decelerated beam is collided with a conventional molecular beam at a fixed beam intersection angle. Hence we assume in the analysis for beam 2 the parameters  $v_2 = 500$  m/s, and  $\Delta_{v_2} = 50$  m/s; for beam 1 we assume a velocity spread of  $\Delta_{v_1} = 10$  m/s for all velocities. Further, we assume an angular spread  $\Delta_\phi = 40$  mrad ( $2.3^\circ$ ).

In **Fig. 9.3** the resulting values for  $\Delta(E/\mu)$  are shown for two different beam intersection angles. The red solid and red dashed curve (with respect to the axis on the left) shows the expected collision energy resolution as a function of the collision energy for  $\phi = 45^\circ$  and  $\phi = 90^\circ$ , respectively. The corresponding primary beam velocities  $v_1$  that are required to obtain this collision energy are shown as green curves with respect to the axis on the right.

From **Fig. 9.3** it is evident that beam crossing angles of  $\phi = 45^\circ$  result in lower collision energies and better energy resolutions. At low collision energies, there are actually two values for  $v_1$  that result in the same collision energy. The energy resolution, however, is quite different for both situations. The resolution shows a minimum at  $E/\mu = 7.6$  cm $^{-1}$  u $^{-1}$  and  $v_1 = 600$  m/s.

From the analysis given in section 9.2, one would expect that the best collision energy resolution is obtained when the relative velocity vector  $\mathbf{g}$  is perpendicular to  $\mathbf{v}_2$ ; this condition is fulfilled for  $E/\mu = 10.4 \text{ cm}^{-1} \text{ u}^{-1}$  and  $v_1 = 707 \text{ m/s}$ . The position of the minimum that is found in Fig. 9.3 deviates slightly from these values due to the nonzero angular spread  $\Delta_\phi$ , and the nonzero velocity spread of beam 1. This is illustrated by the red dotted curve in Fig. 9.3, labeled  $\Delta E'(45^\circ)$ , that shows the energy resolution that would be obtained for  $\Delta_{v_1} = \Delta_\phi = 0$ . In this hypothetical situation, the best collision energy resolution that can be obtained is indeed found for  $\mathbf{g} \perp \mathbf{v}_2$ , and becomes independent of the velocity spread of beam 2. To first order, the collision energy spread vanishes in this case.

### 9.3.3 Variation of $v_1$ , $v_2$ , and $\phi$ for a fixed energy

In this case the mean collision energy is specified while  $v_1$ ,  $v_2$ , and  $\phi$  are allowed to vary. For a given choice of  $E$ ,  $v_1$  and  $\phi$ , there are in general two possible values for  $v_2$  which yield this energy  $E$ . In calculations it is therefore advantageous to vary  $v_1$  and  $v_2$  and to let  $\phi$  be uniquely determined by equation (9.1). To search for a minimum in  $\Delta E$  then has the following geometrical significance: the vectors  $\mathbf{v}_1$ ,  $\mathbf{v}_2$  and the relative velocity  $\mathbf{g}$  define a triangle,  $\mathbf{g}$  is held fixed and the vertex opposite to  $\mathbf{g}$  is allowed to move over all points within the plane (excluding some areas which may not be accessible in the experiment).

Again, we calculate the expected energy resolution for an experiment in which a Stark-decelerated beam collides with a conventional molecular beam; i.e., we take the beam parameters  $\Delta_{v_1} = 10 \text{ m/s}$ ,  $\Delta_{v_2} = 0.10 \times v_2$  and  $\Delta_\phi = 40 \text{ mrad}$ . The collision energy resolution  $\Delta(E/\mu)$  is calculated on a suitable grid of values for  $v_1$  and  $v_2$ , where  $v_1 = 100 \dots 1000 \text{ m/s}$  and  $v_2 = 400 \dots 1000 \text{ m/s}$ . The subsidiary condition of constant (mean) energy is introduced by letting  $\phi$  be determined by equation 9.1. The surface  $\Delta(E/\mu)(v_1, v_2)$  for the fixed collision energy  $E/\mu = 10 \text{ cm}^{-1} \text{ u}^{-1}$  is shown in **Fig. 9.4**.

The optimal resolution with  $\Delta(E/\mu) = 0.73 \text{ cm}^{-1} \text{ u}^{-1}$  is obtained for  $v_1 = 627 \text{ m/s}$ ,  $v_2 = 400 \text{ m/s}$  and  $\phi = 51^\circ$ ; note that there is no local minimum, only a global one at the boundary (this seems to be the usual case, that is the minimum occurs at the boundary where  $v_2$  assumes the smallest value).

### 9.3.4 Applications

In a crossed beam collision experiment, one would like to tune the collision energy with the highest possible resolution for each value of the collision energy. As described in section 9.3.3, one would have to optimize the values for  $v_1$ ,  $v_2$ , and  $\phi$  to accomplish this. This is possible in theory, it is however not practical in an experiment. In this section we discuss to which extent satisfactory results can also be obtained by a variation of two parameters only. First, let us assume that the apparatus allows for a continuous variation of the crossing angle and

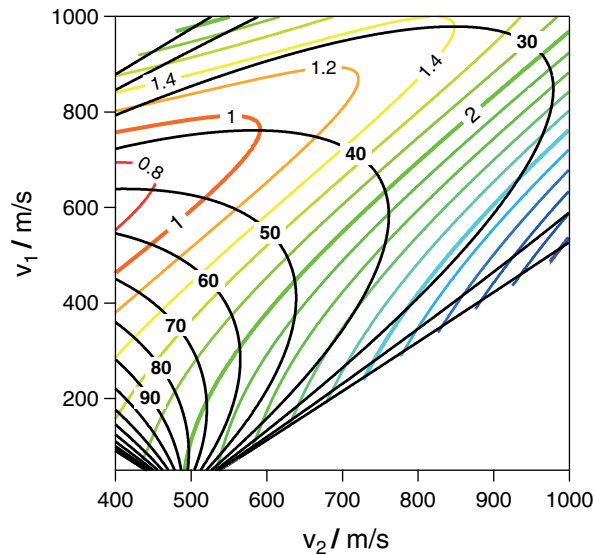


**Figure 9.4:** Contour plot of  $\Delta(E/\mu)$  for a fixed  $E/\mu$  of  $10 \text{ cm}^{-1} \text{ u}^{-1}$  pertaining to the situation where  $v_1$ ,  $v_2$ , and  $\phi$  are varied (see section 9.3.3). Beam parameters:  $\Delta v_1 = 10 \text{ m/s}$ ,  $\Delta v_2 = 0.10 \times v_2$ ,  $\Delta\phi = 40 \text{ mrad}$ . The contour lines for the beam intersection angles  $\phi$  are shown as black curves.

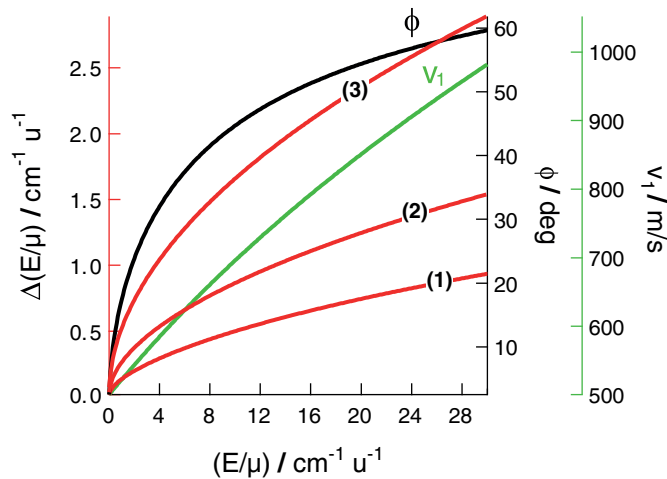


**Figure 9.5:** The minimized values for  $\Delta(E/\mu)$  (red curves with respect to the left axis) pertaining to the situation in which the target beam velocity  $v_2$  is kept constant, and both  $v_1$  and  $\phi$  are allowed to vary to tune the collision energy. Beam parameters:  $\Delta v_1 = 10 \text{ m/s}$ ,  $v_2 = 500 \text{ m/s}$  and  $\Delta v_2 = 50 \text{ m/s}$ . The assumed angular spreads are  $\Delta\phi = 20, 40, 80 \text{ mrad}$  corresponding to curves 1, 2 and 3 respectively. The values for  $v_1$  (green curve) and for  $\phi$  (black curve) that result in the optimal energy resolution are plotted with respect to the axes on the right.

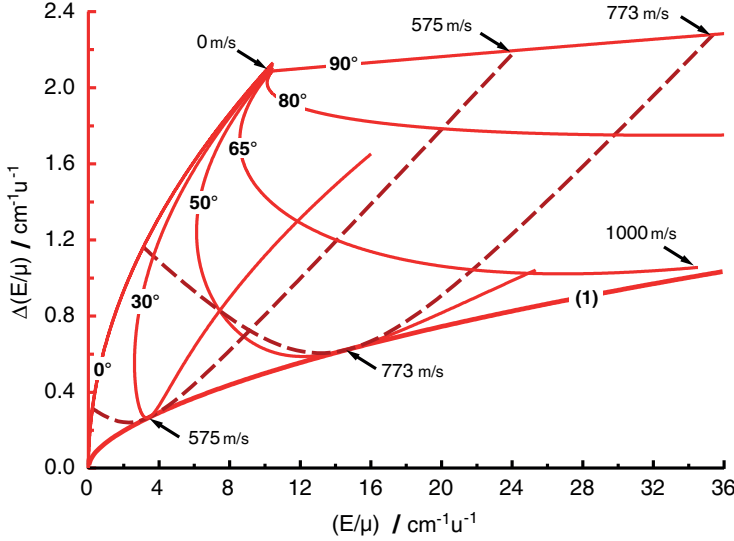


**Figure 9.6:** The expected energy resolution if only one parameter is continuously varied in an experiment to tune the collision energy. Beam parameters:  $\Delta v_1 = 10$  m/s,  $v_2 = 500$  m/s,  $\Delta v_2 = 50$  m/s, and  $\Delta\phi = 20$  mrad. Solid curves:  $v_1$  is continuously varied between 0 m/s and 1000 m/s for fixed beam intersection angles of  $0^\circ$ ,  $30^\circ$ ,  $50^\circ$ ,  $65^\circ$ ,  $80^\circ$  and  $90^\circ$ . Dashed curves:  $\phi$  is continuously varied between  $0^\circ$  and  $90^\circ$  for fixed primary beam speeds of  $v_1 = 575$  m/s and  $v_2 = 773$  m/s. The optimal energy resolution that is obtained if both  $v_1$  and  $\phi$  are tuned is shown as a comparison [curve (1); reproduced from Fig. 9.5].

the speed of beam one, while the speed of beam two is fixed. As before, we assume  $v_2 = 500$  m/s and  $\Delta v_2 = 50$  m/s. We calculate the values for  $v_1$  and  $\phi$  that result in an optimal energy resolution for the cases  $\Delta\phi = 20, 40, 80$  mrad (hereafter referred to as *case 1, 2* and *3*, respectively). In all cases and for all values for  $v_1$  we assume  $\Delta v_1 = 10$  m/s. The minimal value for  $\Delta(E/\mu)$  has been determined by numerically evaluating equation (9.6) on a sufficiently fine grid, subject to the condition of constant collision energy.

In **Fig. 9.5** the optimal values for  $\Delta(E/\mu)$  are shown (red curves) as a function of the collision energy for all three cases. The values for  $\phi$  (black curve) and  $v_1$  (green curve) for a given  $E/\mu$  are plotted with respect to the axes on the right.

To stay on the optimal curve,  $\phi$  and  $v_1$  have to be changed continuously. It is of practical interest to consider what happens if we move away from the optimal curve by either changing only  $v_1$  or only  $\phi$ . In **Fig. 9.6** such deviations are considered for *case 1*. The solid lines correspond to a change of  $v_1$  from 0 to 1000 m/s at fixed intersection angles (indicated on each curve). The two dashed lines correspond to fixed values for  $v_1$  with  $v_1 = 575$  or  $773$  m/s and variable  $\phi$  with  $\phi = 0 \dots 90^\circ$ .

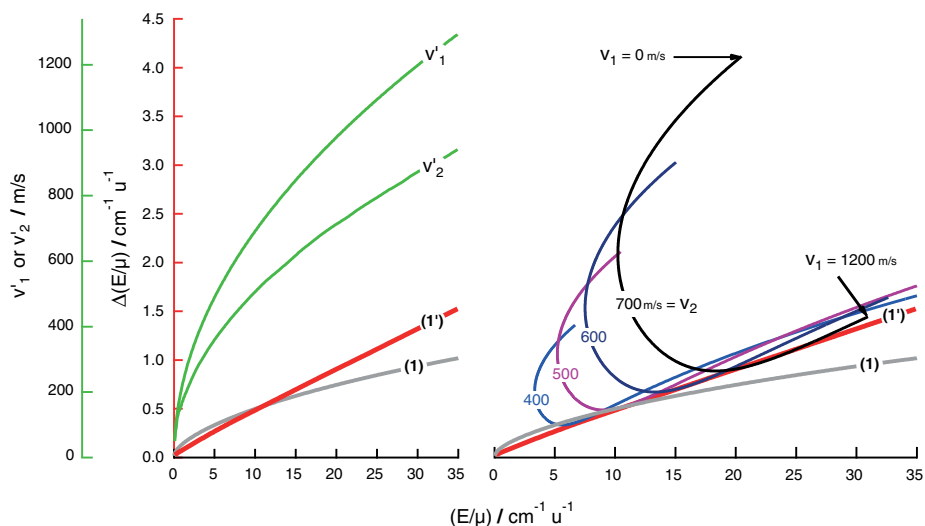


**Figure 9.7:** The minimized energy resolution for the situation in which both beam speeds  $v_1$  and  $v_2$  are varied for a fixed beam intersection angle  $\phi = 45^\circ$ . Beam parameters:  $\Delta v_1 = 10$  m/s for all values of  $v_1$ ,  $\Delta v_2 = 0.10 \times v_2$ , and  $\Delta\phi = 20$  mrad. Left panel: optimized energy resolution [curve (1')]. The values for  $v_1$  and  $v_2$  (green curves) that result in this energy resolution are shown with respect to the green axis on the left. Right panel: optimized energy resolution that is obtained if  $v_1$  is continuously varied between 0 and 1200 m/s for fixed values of  $v_2$  of 400, 500, 600, and 700 m/s. For comparison, curve (1) of Fig. 9.5 is shown in both panels.

All curves touch the optimal curve of *case 1*, as it should be. The energy range that can be scanned with a close to optimal resolution appears limited, both in the case where only  $v_1$  is varied and in the case where only  $\phi$  is varied. Note that by changing  $v_1$  alone, the energy range with a satisfactory energy resolution becomes more and more narrow as  $\phi$  decreases, finally vanishing at  $\phi = 0^\circ$ .

Let us now consider an apparatus in which the beam intersection angle is fixed, but both beam velocities are variable. We assume  $\phi = 45^\circ$ , as this beam intersection angle appears experimentally most feasible. Again, we assume the beam parameters pertaining to *case 1*, i.e.,  $\Delta v_1 = 10$  m/s for all values of  $v_1$ ,  $\Delta v_2 = 0.10 \times v_2$ , and  $\Delta\phi = 20$  mrad. In **Fig. 9.7** the optimal values for  $\Delta(E/\mu)$  are shown (red curve, labeled (1')), together with curve (1) that was shown in the preceding figures. On the left side of this figure, the corresponding values for  $v_1$  and  $v_2$  that are required to obtain the optimal value for the energy resolution are shown in green.

It is observed that by a proper variation of  $v_1$  and  $v_2$  at a fixed value of  $\phi = 45^\circ$  (curve (1')), energy resolutions are obtained that are very similar to the optimal resolution that result from a variation of  $v_1$  and  $\phi$  at a fixed value

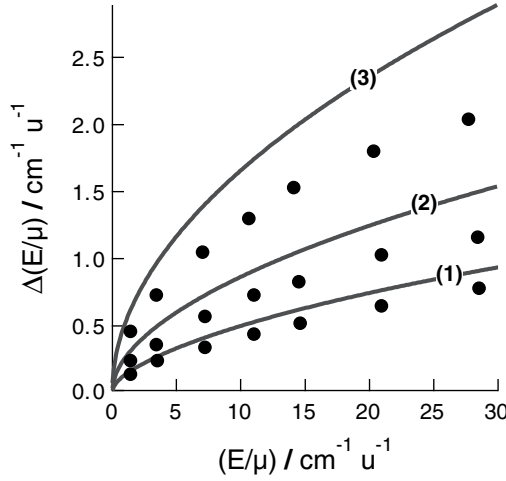


**Figure 9.8:** The minimized values of  $\Delta(E/\mu)$  pertaining to the three cases of Fig. 9.5. The values for  $\Delta(E/\mu)$  are calculated using the model (curves labeled (1), (2) and (3); identical to the curves in Fig. 9.5) and direct numerical evaluation using Gaussian beam distributions (dots).

of  $v_2$  (curve (1')). At low collision energies curve (1') is below curve (1). This is a consequence of the fixed value of  $v_2 = 500$  m/s that was assumed for curve (1); for curve (1')  $v_2$  may assume values below 500 m/s, improving the energy resolution.

Again, we may wonder what would happen if we move away from the optimal curve by either changing only  $v_1$  or  $v_2$ . This situation is addressed on the right hand side of **Fig. 9.7**. The energy resolution is shown that is obtained if  $v_1$  is varied between 0 m/s and 1200 m/s, while fixed values for  $v_2$  of 400, 500, 600 or 700 m/s are assumed. Again, we assume  $\Delta_{v_1} = 10$  m/s for all values of  $v_1$ ,  $\Delta_{v_2} = 0.10 \times v_2$ , and  $\Delta_\phi = 20$  mrad. It can be seen that as long as  $v_1$  can be tuned continuously, it is sufficient to change  $v_2$  in coarser steps in order to traverse the minimum curve (1'). This is of practical importance because the mean speed of a beam can easily be adjusted in larger steps by varying, for instance, the nozzle temperature.

It is also interesting to compare some of the above results to a direct numerical evaluation of  $\Delta E$ . To see whether the linear approximation is sufficiently accurate, we compare the calculations for the three cases shown in Fig. 9.5 to a direct numerical evaluation of  $\Delta(E/\mu)$ . For the latter we generate independent random numbers from Gaussian distributions for the angular and velocity spreads. All three cartesian velocity components of a beam are assumed to be independent, and the total angular spread is shared equally among both beams. The distributions for  $\Delta(E/\mu)$  are then not strictly Gaussian in shape, but can be reasonably well approximated by a Gaussian in all cases. The resulting val-



ues for a few sample points are plotted as dots in **Fig. 9.8**. It is seen that the linear approximation indeed describes the considered cases well, but that it actually overestimates the numerically calculated spread  $\Delta E/\mu$ .

## 9.4 Resonances in OH-He and OD-He collisions

In this section, we illustrate the benefits of the method to improve the energy resolution, using the scattering of Stark-decelerated OH and OD radicals with He atoms as an example. The scattering of OH with He is well-suited to be studied with high energy resolution, as this system is known to exhibit pronounced resonant structure in the inelastic scattering cross sections. The potential well for the OH-He van der Waals complex is shallow, and can only support a limited number of bound states [172, 145]. The well depth of  $\sim 25 \text{ cm}^{-1}$  is significantly smaller than the energy spacing between rotational levels of the OH radical, resulting in resonances in the inelastic cross sections that are grouped within rather narrow collision energy ranges. However, the energy resolution which is required to resolve these resonances is on the order of a wavenumber, as can be seen from the plots shown in **Fig. 9.9** on p. 154. In panel (a) of this figure, the optimized parameters for the highest energy resolution are shown for *case 1* and for a mean He beam velocity of  $v_2 = v_{\text{He}} = 500 \text{ m/s}$ . To the left of panel (a), calculated scattering cross sections [173] are shown for the three different scattering channels as a function of the collision energy. The cross sections pertain to the collision induced transitions  $F_1(3/2f) \rightarrow F_1(3/2e), F_1(5/2e), F_1(5/2f)$  (compare p.133). If these cross sections are convoluted with the energy resolution of panel (a), one obtains the red curves (vertically offset for reasons of clarity). It is seen that the resonances which occur at the energetic thresholds for scattering into the  $J = 5/2e, f$  levels can be partly resolved provided a sufficient signal to noise ratio can be obtained in the experiment. To resolve the resonances in all detail would require a resolution of  $< 1 \text{ cm}^{-1}$  which can only be obtained if the angular spread is further reduced. Whether this is experimentally feasible is currently unclear and the subject of future experiments. The resolution in the range  $E = 40 \dots 55 \text{ cm}^{-1}$  (OD-He) is higher than in the range  $75 \dots 90 \text{ cm}^{-1}$  (OH-He) but unfortunately the predicted resonances are also narrower in the former case. In panel (b) and (c) the energy resolution is shown for *case 1* but now the beam crossing angle is fixed to either  $\phi = 45^\circ$  (solid curves) or  $90^\circ$  (dashed curves) and only the velocity of the decelerated molecules ( $v_1 = v_{\text{OH/OD}}$ ) is varied as indicated by the green curves with respect to the axis on the right. In panel (b) the He beam velocity is  $v_{\text{He}} = 500 \text{ m/s}$  while in panel (c)  $v_{\text{He}} = 800 \text{ m/s}$ . To the left of both panels, the convolutions of the calculated cross sections are shown for both angles. We see that in the  $\phi = 45^\circ$  case, some of the structure can be resolved, which is hardly the case for  $\phi = 90^\circ$ .

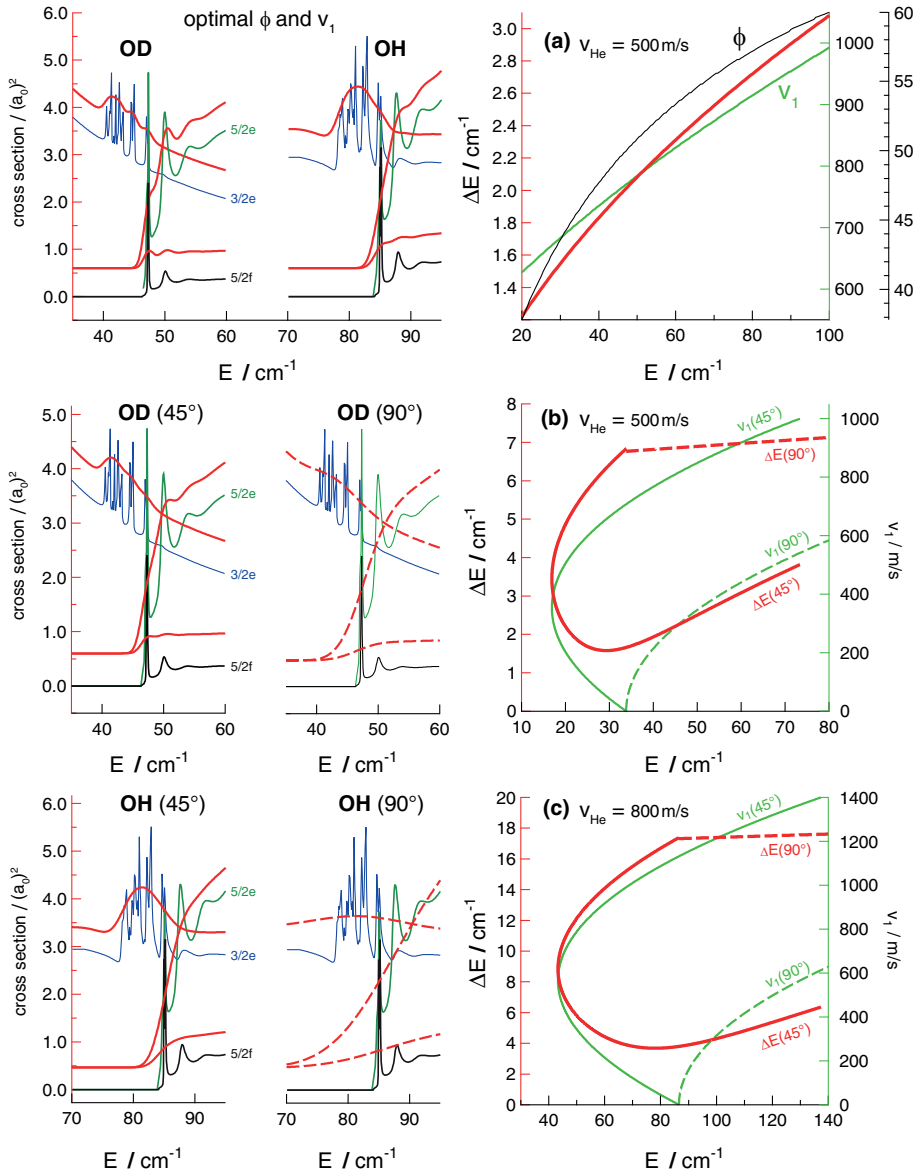


**Figure 9.9:** Panel (a) shows the optimized parameters for OH/OD - He collisions ( $v_{\text{OH/OD}} = v_1$ ,  $v_{\text{He}} = v_2 = 500$  m/s) for *case 1*, that is  $\Delta v_1 = 10$  m/s,  $\Delta v_2 = 0.10 \times v_2$  and  $\Delta \phi = 20$  mrad. To the left of this panel, the calculated cross sections [173] for three different scattering channels are shown:  $F_1(3/2f) \rightarrow F_1(3/2e)$ ,  $F_1(5/2e)$ ,  $F_1(5/2f)$  (compare p. 133). When the calculated cross sections are convoluted with the obtained energy resolution shown in panel (a), the solid red curves are obtained (vertically offset only for reasons of clarity). The data shown in panel (b) and (c) follows the same systematics but the beam crossing angle is fixed at  $45^\circ$  (solid red lines) or  $90^\circ$  (dashed red lines) and only  $v_{\text{OH}}$  is varied. For both panels, the parameters pertain to *case 1*, with  $v_{\text{He}} = 500$  m/s in (b) and  $v_{\text{He}} = 800$  m/s in (c).

## 9.5 Conclusion

We have presented a simple, yet effective method to optimize the collision energy resolution in crossed molecular beam scattering experiments. It is shown that for beam intersection angles smaller than  $90^\circ$ , kinematically favorable conditions can be found in which the beam with the largest velocity or angular spread contributes the least to the collision energy resolution. This allows for high collision energy resolutions, without the need for methods that reduce the velocity spread of the beam(s) and without greatly reducing the particle density in the beam(s). Via a systematic optimization of the beam velocities and beam intersection angle, we have analyzed the optimal value for the energy resolution that can be reached experimentally using a realistic set of beam parameters.

The method is particularly suitable if one of the molecular beam pulses already has a narrow angular and velocity spread, as is the case for Stark-decelerated beams, for instance. Stark decelerators offer molecular packets with a tunable velocity, an angular spread of typically  $1^\circ$ , and a narrow velocity spread that is typically in the  $5 - 20$  m/s range. Using additional electric field elements with which the phase-space distribution of the molecules is manipulated, velocity spreads below 1 m/s can be obtained [53]. Using a suitable beam intersection angle and velocity of the target beam, this narrow angular and velocity spread allows for exceptionally high collision energy resolutions. In particular for systems with a low reduced mass, absolute collision energy resolutions ranging from  $0.5 - 5$   $\text{cm}^{-1}$  appear feasible. This may well be exploited to experimentally observe and study scattering resonances.

## 9.6 Appendix (estimation of $\sigma_\phi$ )

Let the laboratory-frame velocity vector of beam 1(2) be denoted by  $\mathbf{v}_{1(2)} = v_{1(2)} \hat{\mathbf{v}}_{1(2)}$ . The orientation of the unit vectors  $\hat{\mathbf{v}}_{1(2)}$  can be specified in polar coordinates with the angles  $\theta_{1(2)}, \varphi_{1(2)}$  as defined above. We assume that the angular distributions in  $\theta$  and  $\varphi$  are symmetric with respect to their mean values  $\bar{\theta}$  and  $\bar{\varphi}$  and therefore we express the unit vectors by:

$$\hat{\mathbf{v}}_1 = \hat{\mathbf{v}}_1(\theta_1, \varphi_1) = \hat{\mathbf{v}}_1(\bar{\theta}_1 + \delta\theta_1, \bar{\varphi}_1 + \delta\varphi_1) \quad (9.8)$$

$$\hat{\mathbf{v}}_2 = \hat{\mathbf{v}}_2(\theta_2, \varphi_2) = \hat{\mathbf{v}}_2(\bar{\theta}_2 + \delta\theta_2, \bar{\varphi}_2 + \delta\varphi_2). \quad (9.9)$$

We choose  $\bar{\theta} = \pi/2$  by definition, so that the vectors lie in the xy-plane on average. We rewrite equation (9.1) as:

$$E = \frac{\mu}{2}(v_1^2 + v_2^2 - 2v_1v_2\hat{\mathbf{v}}_1 \cdot \hat{\mathbf{v}}_2) \quad (9.10)$$

$$= \frac{\mu}{2}(v_1^2 + v_2^2 - 2v_1v_2 \cos \alpha) \quad (9.11)$$

and evaluate  $\cos \alpha$  in terms of the angles  $\bar{\theta} + \delta\theta$  and  $\bar{\phi} + \delta\phi$  with the help of the transformation equations for the coordinates on the unit sphere:

$$\begin{aligned} x &= \sin \theta \cos \varphi \\ y &= \sin \theta \sin \varphi \\ z &= \cos \theta \\ \cos \alpha &= x_1 x_2 + y_1 y_2 + z_1 z_2. \end{aligned}$$

Using  $\bar{\theta}_{1(2)} = \pi/2$  and neglecting terms that are of second and higher order in  $\delta\theta_1 \delta\theta_2$  one obtains:

$$\begin{aligned} z_1 z_2 &= \cos(\bar{\theta}_1 + \delta\theta_1) \cos(\bar{\theta}_2 + \delta\theta_2) \\ &= \sin(\delta\theta_1) \sin(\delta\theta_2) \\ &\approx \delta\theta_1 \delta\theta_2 \\ &\approx 0. \end{aligned}$$

By an analogous argument we obtain:

$$\begin{aligned} y_1 y_2 &= \sin \theta_1 \sin \varphi_1 \sin \theta_2 \sin \varphi_2 \\ &\approx \sin(\bar{\varphi}_1 + \delta\varphi_1) \sin(\bar{\varphi}_2 + \delta\varphi_2) \\ x_1 x_2 &= \sin \theta_1 \cos \varphi_1 \sin \theta_2 \cos \varphi_2 \\ &\approx \cos(\bar{\varphi}_1 + \delta\varphi_1) \cos(\bar{\varphi}_2 + \delta\varphi_2). \end{aligned}$$

By using the trigonometric relation

$$\sin x \sin y + \cos x \cos y = \cos(x - y)$$

everything can be written more compactly as:

$$\cos \alpha = \cos(\bar{\varphi}_1 - \bar{\varphi}_2 + \delta\varphi_1 - \delta\varphi_2). \quad (9.12)$$

We now define the beam crossing angle  $\phi$  by  $\phi = \bar{\varphi}_1 - \bar{\varphi}_2$  and hence have:

$$\cos \alpha = \cos(\phi + \delta\varphi_1 - \delta\varphi_2). \quad (9.13)$$

The value of  $\cos \alpha$  is subject to fluctuations because  $\delta\varphi_{1(2)}$  can assume positive or negative values within some finite range. If these fluctuations are small, the mean value of  $\cos \alpha$  must be approximately equal to  $\cos \phi$  because the mean value of  $\delta\varphi_{1(2)}$  vanishes by assumption. To first order, the variance of  $\cos \alpha$  is hence given by:

$$\sigma^2(\cos \alpha) = \sin^2(\phi) \sigma^2(\phi + \delta\varphi_1 - \delta\varphi_2) \quad (9.14)$$

$$= \sin^2(\phi) (\sigma_{\varphi_1}^2 + \sigma_{\varphi_2}^2). \quad (9.15)$$

Therefore, the divergences of both beams as expressed by  $\sigma_{\varphi_{1(2)}}^2$  are added together to give the total variance in the collision angle. The spread in the variable  $\delta\theta_{1(2)}$  need not be taken into account.

# Bibliography

- [1] B. Friedrich and D. Herschbach, “Stern and Gerlach: How a bad cigar helped reorient atomic physics,” *Physics Today*, vol. 56, no. 12, pp. 53–59, 2003.
- [2] J. P. Toennies, H. Schmidt-Böcking, B. Friedrich, and J. C. A. Lower, “Otto Stern: The founding father of experimental atomic physics,” *Annalen der Physik*, vol. 523, no. 12, pp. 1045–1070, 2011.
- [3] S. Y. T. van de Meerakker, H. L. Bethlem, and G. Meijer, “Taming molecular beams,” *Nature Physics*, vol. 4, no. 8, pp. 595–602, 2008.
- [4] S. D. Hogan, M. Motsch, and F. Merkt, “Deceleration of supersonic beams using inhomogeneous electric and magnetic fields,” *Phys. Chem. Chem. Phys.*, vol. 13, pp. 18705–18723, 2011.
- [5] H. L. Bethlem, G. Berden, and G. Meijer, “Decelerating neutral dipolar molecules,” *Phys. Rev. Lett.*, vol. 83, no. 8, pp. 1558–1561, 1999.
- [6] S. Y. T. van de Meerakker, P. H. M. Smeets, N. Vanhaecke, R. T. Jongma, and G. Meijer, “Deceleration and electrostatic trapping of OH radicals,” *Phys. Rev. Lett.*, vol. 94, no. 2, p. 023004, 2005.
- [7] S. A. Meek, H. L. Bethlem, H. Conrad, and G. Meijer, “Trapping molecules on a chip in traveling potential wells,” *Phys. Rev. Lett.*, vol. 100, no. 15, p. 153003, 2008.
- [8] A. Marian, H. Haak, P. Geng, and G. Meijer, “Slowing polar molecules using a wire stark decelerator,” *Eur. Phys. J. D*, vol. 59, pp. 179–181, 2010.
- [9] A. Osterwalder, S. A. Meek, G. Hammer, H. Haak, and G. Meijer, “Deceleration of neutral molecules in macroscopic traveling traps,” *Phys. Rev. A*, vol. 81, no. 5, p. 051401, 2010.
- [10] G. Scoles, *Atomic and Molecular Beam Methods Vol. 1*. New York: Oxford University Press, 1988.

- [11] H. Bethlem, G. Berden, F. Cromptvoets, R. Jongma, A. van Roij, and G. Meijer, "Electrostatic trapping of ammonia molecules," *Nature*, vol. 406, no. 6795, pp. 491–494, 2000.
- [12] J. van Veldhoven, H. L. Bethlem, and G. Meijer, "AC electric trap for ground-state molecules," *Phys. Rev. Lett.*, vol. 94, p. 083001, 2005.
- [13] S. Y. T. van de Meerakker, N. Vanhaecke, M. P. J. van der Loo, G. C. Groenenboom, and G. Meijer, "Direct measurement of the radiative lifetime of vibrationally excited OH radicals," *Phys. Rev. Lett.*, vol. 95, no. 1, p. 013003, 2005.
- [14] B. C. Sawyer, B. L. Lev, E. R. Hudson, B. K. Stuhl, M. Lara, J. L. Bohn, and J. Ye, "Magnetoelectrostatic trapping of ground state OH molecules," *Phys. Rev. Lett.*, vol. 98, p. 253002, 2007.
- [15] J. J. Gilijamse, S. Hoekstra, S. A. Meek, M. Metsälä, S. Y. T. van de Meerakker, G. Meijer, and G. C. Groenenboom, "The radiative lifetime of metastable CO," *J. Chem. Phys.*, vol. 127, 2007.
- [16] S. Hoekstra, J. J. Gilijamse, B. Sartakov, N. Vanhaecke, L. Scharfenberg, S. Y. T. van de Meerakker, and G. Meijer, "Optical pumping of trapped neutral molecules by blackbody radiation," *Phys. Rev. Lett.*, vol. 98, no. 13, p. 133001, 2007.
- [17] S. Hoekstra, M. Metsälä, P. C. Zieger, L. Scharfenberg, J. J. Gilijamse, G. Meijer, and S. Y. T. van de Meerakker, "Electrostatic trapping of metastable NH molecules," *Phys. Rev. A*, vol. 76, p. 063408, Dec 2007.
- [18] J. J. Gilijamse, S. Hoekstra, S. Y. T. van de Meerakker, G. C. Groenenboom, and G. Meijer, "Near-threshold inelastic collisions using molecular beams with a tunable velocity," *Science*, vol. 313, no. 5793, pp. 1617–1620, 2006.
- [19] G. Scoles, *Atomic and Molecular Beam Methods Vol. 1*. New York: Oxford University Press, 1988. U. Buck, chapter 18, pp. 449.
- [20] O. Stern, "Zur Methode der Molekularstrahlen. I," *Z. Phys.*, vol. 39, pp. 751–763, 1926.
- [21] F. Knauer and O. Stern, "Zur Methode der Molekularstrahlen. II," *Z. Phys.*, vol. 39, pp. 764–779, 1926.
- [22] F. Knauer, "Über die Streuung von Molekularstrahlen in Gasen. I," *Zeitschrift für Physik A Hadrons and Nuclei*, vol. 80, pp. 80–99, 1933.

- [23] L. F. Broadway, "Experiments on molecular scattering in gases. II. The collision of sodium and potassium atoms with mercury," *Proceedings of the Royal Society of London. Series A*, vol. 141, no. 845, pp. 634–641, 1933.
- [24] W. H. Mais, "The scattering of a beam of potassium atoms in various gases," *Phys. Rev.*, vol. 45, pp. 773–780, Jun 1934.
- [25] S. Rosin and I. I. Rabi, "Effective collision cross sections of the alkali atoms in various gases," *Phys. Rev.*, vol. 48, pp. 373–379, Aug 1935.
- [26] P. Rosenberg, "Collision cross sections of K atoms and K<sub>2</sub> molecules in gases," *Phys. Rev.*, vol. 55, pp. 1267–1267, Jun 1939.
- [27] R. Feltgen, H. Kirst, K. A. Kohler, H. Pauly, and F. Torello, "Unique determination of the He<sub>2</sub> ground state potential from experiment by use of a reliable potential model," *J. Chem. Phys.*, vol. 76, no. 5, pp. 2360–2378, 1982.
- [28] M. N. R. Ashfold, N. H. Nahler, A. J. Orr-Ewing, O. P. J. Vieuxmaire, R. L. Toomes, T. N. Kitsopoulos, I. A. Garcia, D. A. Chestakov, S.-M. Wu, and D. H. Parker, "Imaging the dynamics of gas phase reactions," *Phys. Chem. Chem. Phys.*, vol. 8, pp. 26–53, 2006.
- [29] K. Liu, "Product pair correlation in bimolecular reactions," *Phys. Chem. Chem. Phys.*, vol. 9, pp. 17–30, 2007.
- [30] K. T. Lorenz, D. W. Chandler, J. W. Barr, W. Chen, G. L. Barnes, and J. I. Cline, "Direct measurement of the preferred sense of NO rotation after collision with argon," *Science*, vol. 293, no. 5537, pp. 2063–2066, 2001.
- [31] G. Hall, K. Liu, M. J. McAuliffe, C. F. Giese, and W. R. Gentry, "State-to-state vibrational excitation of I<sub>2</sub> in collisions with He," *J. Chem. Phys.*, vol. 81, no. 12, pp. 5577–5585, 1984.
- [32] P. R. Bunker and P. Jensen, *Molecular Symmetry and Spectroscopy*, 2nd Ed. NRC Press, 2006.
- [33] A. Lindner, *Drehimpulse in der Quantenmechanik*. Teubner, 1984.
- [34] L. C. Biedenharn and J. Louck, *Angular Momentum in Quantum Physics*. Cambridge University Press, 1985. see section 3.7 p.55.
- [35] K. Gottfried and T. M. Yan, *Quantum Mechanics Fundamentals*, 2nd Ed. Springer-Verlag, 2003. For integrals over rotation matrices see p. 297 (section 7.4), for the behaviour of states at potential level crossings see p. 166 (section 4.1).

- [36] D. Varshalovich, A. Moskalev, and V. Khersonskii, *Quantum Theory of Angular Momentum*. World Scientific Publishing, 1988. The relevant Clebsch-Gordon coefficients are listed on p. 271 (section 8.13); integrals over rotation matrices are given on p. 94 (section 4.10).
- [37] J. Brown and A. Carrington, *Rotational Spectroscopy of Diatomic Molecules*. Oxford University Press, 2003. For the parity of Hund's case (a) functions see p. 251 (section 6.9.4.), for a description of the case (a) basis set see p. 225.
- [38] G. Herzberg, *Molecular Spectra and Molecular Structure I. Spectra of Diatomic Molecules, 2nd Ed.* D. Van Nostrand, 1950. Several examples are given on p. 335 (ch. VI, section 3c).
- [39] R. N. Zare, *Angular Momentum*. Wiley Interscience, 1988. For the description of a  $^2\Pi$  state see p. 302 (section 6), for the parity classification see p. 305.
- [40] J. M. Brown, J. T. Hougen, K. P. Huber, J. W. C. Johns, I. Kopp, H. Lefebvrebrion, A. J. Merer, D. Ramsay, J. Rostas, and R. Zare, "Labeling of parity doublet levels in linear molecules," *J. Mol. Spectrosc.*, vol. 55, no. 1-3, pp. 500-503, 1975.
- [41] M. Larsson, "Phase conventions for rotating diatomic molecules," *Physica Scripta*, vol. 23, p. 835, 1981.
- [42] T. D. Hain, M. A. Weibel, K. M. Backstrand, and T. J. Curtiss, "Rotational state selection and orientation of OH and OD radicals by electric hexapole beam-focusing," *J. Phys. Chem. A*, vol. 101, pp. 7674-7683, 1997.
- [43] G. H. Dieke and H. M. Crosswhite, "The ultraviolet bands of OH - fundamental data," *Journal of Quantitative Spectroscopy and Radiative Transfer*, vol. 2, no. 2, pp. 97-199, 1962.
- [44] K.I.Peterson, G. Fraser, and W. Klemperer, "Electric dipole moment of OH and OD in several vibrational states," *Can. J. Phys.*, vol. 62, p. 1502, 1984.
- [45] J. Brown and A. Carrington, *Rotational Spectroscopy of Diatomic Molecules*. Oxford University Press, 2003. The OH  $\Lambda$ -doublet hyperfine transition frequencies are tabulated on p. 542.
- [46] W. Meerts and A. Dymanus, "Electric dipole moments of OH and OD by molecular beam electric resonance," *Chem. Phys. Lett.*, vol. 23, p. 45, 1973.



- [47] E. Anderson, Z. Bai, C. Bischof, S. Blackford, J. Demmel, J. Dongarra, J. Du Croz, A. Greenbaum, S. Hammarling, A. McKenney, and D. Sorensen, *LAPACK Users' Guide*. Philadelphia, PA: Society for Industrial and Applied Mathematics, third ed., 1999.
- [48] S. Y. T. van de Meerakker, *Deceleration and Electrostatic Trapping of OH radicals, Thesis*. Nijmegen: Radboud University, 2005.
- [49] E. A. Guggenheim, *Thermodynamics, 5th ed.* North-Holland Publishing Company Amsterdam, 1967. see page 120 for a derivation.
- [50] D. R. L. (Ed.), *CRC Handbook of Chemistry and Physics*. CRC Press, 2009.
- [51] J. Luque, "Lifbase 2.0." Database and Spectral simulation for diatomic molecules by Jorge Luque.
- [52] D. R. Yarkony, "A theoretical treatment of the predissociation of the individual rovibronic levels of OH/OD," *J. Chem. Phys.*, vol. 97, no. 3, pp. 1838–1849, 1992.
- [53] F. M. H. Cromptvoets, R. T. Jongma, H. L. Bethlem, A. J. A. van Roij, and G. Meijer, "Longitudinal focusing and cooling of a molecular beam," *Phys. Rev. Lett.*, vol. 89, no. 9, p. 093004, 2002.
- [54] H. L. Bethlem, G. Berden, A. J. A. van Roij, F. M. H. Cromptvoets, and G. Meijer, "Trapping neutral molecules in a traveling potential well," *Phys. Rev. Lett.*, vol. 84, no. 25, pp. 5744–5747, 2000.
- [55] S. Y. T. van de Meerakker, N. Vanhaecke, H. L. Bethlem, and G. Meijer, "Higher-order resonances in a Stark decelerator," *Phys. Rev. A*, vol. 71, no. 5, p. 053409, 2005.
- [56] K. B. Gubbels, G. Meijer, and B. Friedrich, "Analytic wave model of Stark deceleration dynamics," *Phys. Rev. A*, vol. 73, p. 063406, 2006.
- [57] H. L. Bethlem, F. M. H. Cromptvoets, R. T. Jongma, S. Y. T. van de Meerakker, and G. Meijer, "Deceleration and trapping of ammonia using time-varying electric fields," *Phys. Rev. A*, vol. 65, no. 5, p. 053416, 2002.
- [58] S. Y. T. van de Meerakker, N. Vanhaecke, H. L. Bethlem, and G. Meijer, "Transverse stability in a Stark decelerator," *Phys. Rev. A*, vol. 73, no. 2, p. 023401, 2006.
- [59] L. A. Pipes, "Matrix solutions of equations of the Mathieu-Hill type," *J. Appl. Phys.*, vol. 24, pp. 902 – 910, 1953.

- [60] N. V. Konenkov, M. Sudakov, and D. J. Douglas, "Matrix methods for the calculation of stability diagrams in quadrupole mass spectrometry," *J. Am. Soc. Mass Spectrom.*, vol. 13, pp. 597–613, 2002.
- [61] G. Paterson, S. Marinakis, J. Kłos, M. L. Costen, and K. G. McKendrick, "Depolarisation of rotational orientation and alignment in OH + Xe collisions," *Phys. Chem. Chem. Phys.*, vol. 11, pp. 8804–8812, 2009.
- [62] T. E. Wall, S. K. Tokunaga, E. A. Hinds, and M. R. Tarbutt, "Nonadiabatic transitions in a Stark decelerator," *Phys. Rev. A*, vol. 81, no. 3, p. 033414, 2010.
- [63] S. A. Meek, G. Santambrogio, B. G. Sartakov, H. Conrad, and G. Meijer, "Suppression of nonadiabatic losses of molecules from chip-based microtraps," *Phys. Rev. A*, vol. 83, p. 033413, 2011.
- [64] M. Kirste, B. G. Sartakov, M. Schnell, and G. Meijer, "Nonadiabatic transitions in electrostatically trapped ammonia molecules," *Phys. Rev. A*, vol. 79, p. 051401, 2009.
- [65] R. Latham, *High Voltage Vacuum Insulation*. Academic Press, 1995.
- [66] E. Kuffel, W. Zaengl, and J. Kuffel, *High Voltage Engineering: Fundamentals*. Newnes, 2000. The field strength between parallel cylinders is derived on page 218.
- [67] J. Küpper, H. Haak, K. Wohlfart, and G. Meijer, "Compact in-place gate valve for molecular-beam experiments," *Rev. Sci. Instr.*, vol. 77, no. 1, p. 016106, 2006.
- [68] J. van Veldhoven, J. Küpper, H. L. Bethlem, B. Sartakov, A. J. A. van Roij, and G. Meijer, "Decelerated molecular beams for high-resolution spectroscopy," *Eur. Phys. J. D*, vol. 31, pp. 337–349, 2004.
- [69] E. R. Hudson, H. J. Lewandowski, B. C. Sawyer, and J. Ye, "Cold molecule spectroscopy for constraining the evolution of the fine structure constant," *Phys. Rev. Lett.*, vol. 96, no. 14, p. 143004, 2006.
- [70] M. Baranov, L. Dobrek, K. Goral, L. Santos, and M. Lewenstein, "Ultracold dipolar gases - a challenge for experiments and theory," *Physica Scripta*, vol. T102, pp. 74–81, 2002.
- [71] J. Kalnins, G. Lambertson, and H. Gould, "Improved alternating gradient transport and focusing of neutral molecules," *Rev. Sci. Instr.*, vol. 73, no. 7, pp. 2557–2565, 2002.
- [72] B. C. Sawyer, B. K. Stuhl, B. L. Lev, J. Ye, and E. R. Hudson, "Mitigation of loss within a molecular Stark decelerator," *Eur. Phys. J. D*, vol. 48, pp. 197–209, 2008.

- [73] S. Y. Lee, *Accelerator Physics*. Singapore: World Scientific, 1999.
- [74] R. Wolfgang *Scientific American*, vol. 219, p. 44, 1968.
- [75] S. Y. T. van de Meerakker, N. Vanhaecke, and G. Meijer, "Higher-order resonances in a Stark decelerator," *Annu. Rev. Phys. Chem.*, vol. 57, p. 159, 2006.
- [76] R. Fulton, A. I. Bishop, M. N. Shneider, and P. F. Barker, "Controlling the motion of cold molecules with deep periodic optical potentials," *Nature Physics*, vol. 2, no. 7, pp. 465–468, 2006.
- [77] J. R. Taylor, *Scattering Theory*. Dover Publications, 2006. page 44, reprint of the 1983 edition.
- [78] C. Naulin, M. Costes, A. Benseddik, and G. Dorthé, "Kinematic effects on laser-induced fluorescence measurements performed in reactive crossed beam experiments," *Laser Chemistry*, vol. 8, no. 5-6, pp. 283–302, 1988. Density to flux transformation in reactive crossed beam scattering with LIF detection.
- [79] D. M. Sonnenfroh and K. Liu, "Number density-to-flux transformation revisited: kinematic effects in the use of laser-induced fluorescence for scattering experiments," *Chem. Phys. Lett.*, vol. 176, no. 2, pp. 183 – 190, 1991.
- [80] R. D. Levine and R. B. Bernstein, *Molecular Reaction Dynamics and Chemical Reactivity*. New York: Oxford University Press, 1987.
- [81] G. Hall, K. Liu, M. J. McAuliffe, C. F. Giese, and W. R. Gentry, "Pulsed molecular beam study of state-to-state vibrational excitation in He+I<sub>2</sub> collisions: Energy dependence of the  $v = 0$  to 1 cross section," *J. Chem. Phys.*, vol. 78, p. 5260, 1983.
- [82] D. M. Sonnenfroh, R. G. MacDonald, and K. Liu, "A crossed-beam study of the state-resolved integral cross sections for the inelastic scattering of OH with CO and N<sub>2</sub>," *J. Chem. Phys.*, vol. 94, p. 6508, 1991.
- [83] G. A. Raiche, J. B. Jeffries, K. J. Rensberger, and D. R. Crosley, "Vibrational energy transfer in OH  $v = 2$  and 1," *J. Chem. Phys.*, vol. 92, p. 7258, 1990.
- [84] J. Reuss, *Atomic and Molecular Beam Methods*, ed. G. Scoles. New York: Oxford University Press, 1988.
- [85] S. Stolte, *Atomic and Molecular Beam Methods*, ed. G. Scoles. New York: Oxford University Press, 1988.

- [86] C. J. N. van den Meijdenberg, *Atomic and Molecular Beam Methods*, ed. G. Scoles. New York: Oxford University Press, 1988.
- [87] M. Faubel, K.-H. Kohl, J. P. Toennies, K. T. Tang, and Y. Y. Yung, "The He – N<sub>2</sub> anisotropic van der waals potential - test of a simple model using state to state differential scattering cross sections," *Faraday Discuss. Chem. Soc.*, vol. 73, pp. 205–220, 1982.
- [88] S. Stolte, "Chemical physics - aiming the molecular arrow," *Nature*, vol. 353, no. 6343, pp. 391–392, 1991.
- [89] D. Watanabe, H. Ohoyama, T. Matsumura, and T. Kasai, "Effect of mutual configuration between molecular orientation and atomic orientation in the oriented Ar plus oriented CF<sub>3</sub>H reaction," *Phys. Rev. Lett.*, vol. 99, no. 4, p. 043201, 2007.
- [90] H. Kohguchi, T. Suzuki, and M. Alexander, "Fully state-resolved differential cross sections for the inelastic scattering of the open-shell NO molecule by Ar," *Science*, vol. 294, no. 5543, pp. 832–834, 2001.
- [91] N. E. Shafer-Ray, A. J. Orr-Ewing, and R. N. Zare, "Beyond state-to-state differential cross sections: Determination of product polarization in photoinitiated bimolecular reactions," *J. Phys. Chem.*, vol. 99, no. 19, pp. 7591–7603, 1995.
- [92] L. Che, Z. Ren, X. Wang, W. Dong, D. Wai, X. Wang, D. H. Zhang, X. Yang, L. Sheng, G. Li, H.-J. Werner, F. Lique, and M. H. Alexander, "Breakdown of the Born-Oppenheimer approximation in the F + D<sub>2</sub> → DF + D reaction," *Science*, vol. 317, no. 5841, pp. 1061–1064, 2007.
- [93] X. Wang, W. Dong, C. Xiao, L. Che, Z. Ren, D. Dai, X. Wang, P. Casavecchia, X. Yang, B. Jiang, D. Xie, Z. Sun, S.-Y. Lee, D. H. Zhang, H.-J. Werner, and M. H. Alexander, "The extent of non-Born-Oppenheimer coupling in the reaction of Cl with para-H<sub>2</sub>," *Science*, vol. 322, no. 5901, pp. 573–576, 2008.
- [94] J. J. Lin, J. Zhou, W. Shiu, and K. Liu, "State-specific correlation of coincident product pairs in the F + CD<sub>4</sub> reaction," *Science*, vol. 300, no. 5621, pp. 966–969, 2003.
- [95] H. Bethlem and G. Meijer, "Production and application of translationally cold molecules," *Int. Rev. Phys. Chem.*, vol. 22, no. 1, pp. 73–128, 2003.
- [96] S. Y. T. van de Meerakker and G. Meijer, "Collision experiments with Stark-decelerated beams," *Faraday Discussions*, vol. 142, pp. 113–126, 2009.

- [97] P. Andresen, D. Häusler, and H. W. Lülf, "Selective  $\Lambda$ -doublet population of OH in inelastic collisions with  $H_2$  - a possible pump mechanism for the astronomical OH maser," *J. Chem. Phys.*, vol. 81, no. 1, pp. 571–572, 1984.
- [98] P. Andresen, N. Aristov, V. Beushausen, D. Häusler, and H. W. Lülf, " $\Lambda$ -doublet substate specific investigation of rotational and fine structure transitions in collisions of OH with  $H_2$  and  $D_2$ ," *J. Chem. Phys.*, vol. 95, no. 8, pp. 5763–5774, 1991.
- [99] R. G. Macdonald and K. Liu, "State-to-state integral cross-sections for the inelastic scattering of  $CH + He$  - rotational rainbow and orbital alignment," *J. Chem. Phys.*, vol. 91, no. 2, pp. 821–838, 1989.
- [100] D. W. Chandler and S. Stolte, *Gas Phase Molecular Reaction and Photodissociation Dynamics*. Transworld Research Network, 2007. The NO-rare gas system.
- [101] K. Schreel, J. Schleipen, A. Eppink, and J. J. ter Meulen, "State-to-state cross sections for rotational excitation of OH by collisions with He and Ar," *J. Chem. Phys.*, vol. 99, no. 11, pp. 8713–8722, 1993.
- [102] M. C. van Beek, J. J. ter Meulen, and M. H. Alexander, "Rotationally inelastic collisions of OH + Ar. I. state-to-state cross sections," *J. Chem. Phys.*, vol. 113, no. 2, pp. 628–636, 2000.
- [103] M. H. Alexander, "Rotationally inelastic collisions between a diatomic molecule in a  $^2\Pi$  electronic state and a structureless target," *J. Chem. Phys.*, vol. 76, no. 12, pp. 5974–5988, 1982.
- [104] P. J. Dagdigian, M. H. Alexander, and K. Liu, "The inelastic scattering of  $^2\Pi$  [case (b)] molecules and an understanding of the differing  $\Lambda$ -doublet propensities for molecules of  $\pi$  vs  $\pi^3$  orbital occupancy," *J. Chem. Phys.*, vol. 91, no. 2, pp. 839–848, 1989.
- [105] M. C. van Beek, J. J. ter Meulen, and M. H. Alexander, "Rotationally inelastic collisions of OH + Ar. II. the effect of molecular orientation," *J. Chem. Phys.*, vol. 113, no. 2, pp. 637–646, 2000.
- [106] M. C. van Beek, G. Berden, H. L. Bethlem, and J. J. ter Meulen, "Molecular reorientation in collisions of OH+Ar," *Phys. Rev. Lett.*, vol. 86, no. 18, pp. 4001–4004, 2001.
- [107] G. Paterson, S. Marinakis, M. L. Costen, K. G. McKendrick, J. Klos, and R. Tobola, "Orientation and alignment depolarization in OH + Ar/He collisions," *J. Chem. Phys.*, vol. 129, no. 7, p. 074304, 2008.

- [108] P. J. Dagdigian and M. H. Alexander, "Tensor cross sections and the collisional evolution of state multipoles: OH( $X^2\Pi$ ) – Ar," *J. Chem. Phys.*, vol. 130, no. 9, p. 094303, 2009.
- [109] P. J. Dagdigian and M. H. Alexander, "Erratum: Tensor cross sections and the collisional evolution of state multipoles: OH( $X^2\Pi$ )–Ar [J. Chem. Phys. **130**, 094303 (2009)]," *J. Chem. Phys.*, vol. 131, no. 22, p. 229902, 2009.
- [110] R. T. Bonn, M. D. Wheeler, and M. I. Lester, "Infrared spectroscopy of Ar-OH: A direct probe of the Ar + OH potential energy surface," *J. Chem. Phys.*, vol. 112, no. 11, pp. 4942–4951, 2000.
- [111] M. C. Heaven, "Spectroscopy and dynamics of hydride radical van der Waals complexes," *Int. Rev. Phys. Chem.*, vol. 24, no. 3-4, pp. 375–420, 2005.
- [112] J. G. Choi, J. S. Hayden, M. T. O'Connor, and G. J. Diebold, "Direct detection of momentum flux in atomic and molecular beams," *J. Appl. Phys.*, vol. 52, no. 10, pp. 6016–6020, 1981.
- [113] J. A. Coxon, "Optimum molecular constants and term values for the  $X^2\Pi$  and  $A^2\Sigma^+$  states of OH," *Can. J. Phys.*, vol. 58, no. 7, pp. 933–949, 1980.
- [114] M. H. Alexander, "Quantum treatment of rotationally inelastic collisions involving molecules in  $\Pi$  electronic states: New derivation of the coupling potential," *Chem. Phys.*, vol. 92, no. 2-3, pp. 337 – 344, 1985.
- [115] G. Paterson, S. Marinakis, M. L. Costen, K. G. McKendrick, J. Klos, and R. Tobola, "Erratum: Orientation and alignment depolarization in OH + Ar/He collisions [J. Chem. Phys. **129**, 074304 (2008)]," *J. Chem. Phys.*, vol. 131, no. 15, p. 159901, 2009.
- [116] P. J. Knowles, C. Hampel, and H.-J. Werner, "Coupled cluster theory for high spin, open shell reference wave functions," *J. Chem. Phys.*, vol. 99, no. 7, pp. 5219–5227, 1993.
- [117] P. J. Knowles, C. Hampel, and H.-J. Werner, "Erratum: Coupled cluster theory for high spin, open shell reference wave functions [J. Chem. Phys. **99**, 5219 (1993)]," *J. Chem. Phys.*, vol. 112, no. 6, pp. 3106–3107, 2000.
- [118] J. Thom H. Dunning, "Gaussian basis sets for use in correlated molecular calculations. I. The atoms boron through neon and hydrogen," *J. Chem. Phys.*, vol. 90, no. 2, pp. 1007–1023, 1989.
- [119] R. A. Kendall, J. Thom H. Dunning, and R. J. Harrison, "Electron affinities of the first-row atoms revisited. Systematic basis sets and wave functions," *J. Chem. Phys.*, vol. 96, no. 9, pp. 6796–6806, 1992.

- [120] H.-J. Werner, P. J. Knowles, G. Knizia, F. R. Manby, M. Schütz, *et al.*, “Molpro, version 2008.1, a package of ab initio programs.” see <http://www.molpro.net>.
- [121] F.-M. Tao and Y.-K. Pan, “Møller–Plesset perturbation investigation of the  $\text{He}_2$  potential and the role of midbond basis functions,” *J. Chem. Phys.*, vol. 97, no. 7, pp. 4989–4995, 1992.
- [122] K. A. Peterson, D. E. Woon, and J. Thom H. Dunning, “Benchmark calculations with correlated molecular wave functions. IV. The classical barrier height of the  $H + H_2 \rightarrow H_2 + H$  reaction,” *J. Chem. Phys.*, vol. 100, no. 10, pp. 7410–7415, 1994.
- [123] D. Feller and J. A. Sordo, “A CCSDT study of the effects of higher order correlation on spectroscopic constants. I. First row diatomic hydrides,” *J. Chem. Phys.*, vol. 112, no. 13, pp. 5604–5610, 2000.
- [124] J. Kłos, G. Chalasinski, M. T. Berry, R. A. Kendall, R. Burel, M. M. Szczesniak, and S. M. Cybulski, “Ab initio potential energy surface for the  $\text{Ar} + \text{OH}$  interaction and bound rovibrational states,” *J. Chem. Phys.*, vol. 112, no. 11, pp. 4952–4958, 2000.
- [125] G. Herzberg, *Molecular Spectra and Molecular Structure I. Spectra of Diatomic Molecules*, 2nd Ed. D. van Nostrand, 1950.
- [126] J. P. Maillard, J. Chauville, and A. W. Mantz, “High-resolution emission spectrum of OH in an oxyacetylene flame from 3.7 to 0.9  $\mu\text{m}$ ,” *J. Mol. Spectrosc.*, vol. 63, no. 1, pp. 120 – 141, 1976.
- [127] HIBRIDON is a package of programs for the time-independent quantum treatment of inelastic collisions and photodissociation written by M. H. Alexander, D. E. Manolopoulos, H.-J. Werner and B. Follmeg, and others. More information and/or a copy of the code can be obtained from the website <http://www.chem.umd.edu/groups/alexander/hibridon/hib43>.
- [128] N. Vanhaecke, U. Meier, M. Andrist, B. H. Meier, and F. Merkt, “Multistage Zeeman deceleration of hydrogen atoms,” *Phys. Rev. A*, vol. 75, no. 3, p. 031402, 2007.
- [129] M. G. Raizen, “Comprehensive control of atomic motion,” *Science*, vol. 324, no. 5933, pp. 1403–1406, 2009.
- [130] R. C. Forrey, N. Balakrishnan, V. Kharchenko, and A. Dalgarno, “Feshbach resonances in ultracold atom-diatom scattering,” *Phys. Rev. A*, vol. 58, no. 4, pp. R2645–R2647, 1998.
- [131] N. Balakrishnan, A. Dalgarno, and R. C. Forrey, “Vibrational relaxation of CO by collisions with He at ultracold temperatures,” *J. Chem. Phys.*, vol. 113, no. 2, pp. 621–627, 2000.

- [132] C. E. Heiner, D. Carty, G. Meijer, and H. L. Bethlem, "A molecular synchrotron," *Nature Physics*, vol. 3, no. 2, pp. 115–118, 2007.
- [133] D. W. Chandler and A. Schiffman *Int. Rev. Phys. Chem.*, vol. 14, p. 371, 1995.
- [134] K. Liu, R. MacDonald, and A. Wagner *Int. Rev. Phys. Chem.*, vol. 9, p. 187, 1990.
- [135] J. Whitehead, "Molecular beam studies of free-radical processes: Photodissociation, inelastic and reactive collisions," *Rep. Prog. Phys.*, vol. 59, no. 8, pp. 993–1040, 1996.
- [136] H. Kohguchi and T. Suzuki, "State-to-state rotational inelastic scattering of free radicals," *Ann. Rep. Prog. Chem. Sect. C*, vol. 98, p. 421, 2002.
- [137] J. J. van Leuken, F. H. W. Van Amerom, J. Bulthuis, J. G. Snijders, and S. Stolte, "Parity-resolved rotationally inelastic collisions of hexapole state-selected NO with Ar," *J. Phys. Chem.*, vol. 99, no. 42, pp. 15573–15579, 1995.
- [138] A. Gijsbertsen, H. Linnartz, G. Rus, A. E. Wiskerke, S. Stolte, D. W. Chandler, and J. K. os, "Differential cross sections for collisions of hexapole state-selected NO with He," *J. Chem. Phys.*, vol. 123, no. 22, p. 224305, 2005.
- [139] M. C. Heaven, "Spectroscopy and dynamics of open-shell van der Waals molecules," *Ann. Rev. Phys. Chem.*, vol. 43, pp. 283–310, 1992.
- [140] M. Kirste, L. Scharfenberg, J. Klos, F. Lique, M. H. Alexander, G. Meijer, and S. Y. T. van de Meerakker, "Low-energy inelastic collisions of OH radicals with He atoms and D<sub>2</sub> molecules," *Phys. Rev. A*, vol. 82, no. 4, p. 042717, 2010.
- [141] M. Lara, J. L. Bohn, D. Potter, P. Soldán, and J. M. Hutson, "Ultracold Rb-OH collisions and prospects for sympathetic cooling," *Phys. Rev. Lett.*, vol. 97, no. 18, p. 183201, 2006.
- [142] L. González-Sánchez, E. Bodo, and F. A. Gianturco, "Quantum scattering of OH with He: Propensity features in rotational relaxation at ultralow energies," *Phys. Rev. A*, vol. 73, no. 2, p. 022703, 2006.
- [143] Z. Pavlovic, T. V. Tscherbul, H. R. Sadeghpour, G. C. Groenenboom, and A. Dalgarno, "Cold collisions of OH molecules with He atoms in external fields," *J. Phys. Chem. A*, vol. 113, no. 52, pp. 14670–14680, 2009.
- [144] T. V. Tscherbul, G. C. Groenenboom, R. V. Krems, and A. Dalgarno, "Dynamics of OH–He collisions in combined electric and magnetic fields," *Faraday Discuss.*, vol. 142, p. 127, 2010.



- [145] H.-S. Lee, A. B. McCoy, R. R. Toczyłowski, and S. M. Cybulski, "Theoretical studies of the He-OH and Ne-OH complexes," *J. Chem. Phys.*, vol. 113, no. 14, pp. 5736–5749, 2000.
- [146] Y. Sumiyoshi, I. Funahara, K. Sato, Y. Ohshima, and Y. Endo, "Microwave spectroscopy of the Ne-OH complex and three-dimensional intermolecular potentials," *Phys. Chem. Chem. Phys.*, vol. 12, pp. 8340–8349, 2010.
- [147] L. Scharfenberg, J. Kłos, P. J. Dagdigan, M. H. Alexander, G. Meijer, and S. Y. T. van de Meerakker, "State-to-state inelastic scattering of Stark-decelerated OH radicals with Ar atoms," *Phys. Chem. Chem. Phys.*, vol. 12, pp. 10660–10670, 2010.
- [148] Y. Sumiyoshi, I. Funahara, K. Sato, Y. Ohshima, and Y. Endo, "Three-dimensional intermolecular potential energy surfaces of the Kr-OH complex," *Mol. Phys.*, vol. 108, pp. 2207–2218, 2010.
- [149] S. Boys and F. Bernardi, "The calculation of small molecular interactions by the differences of separate total energies. Some procedures with reduced errors," *Molecular Physics*, vol. 19, no. 4, pp. 553–566, 1970.
- [150] B. Johnson, "Multichannel log-derivative method for scattering calculations," *J. Comput. Phys.*, vol. 13, no. 3, pp. 445–449, 1973.
- [151] M. S. Child, *Molecular Collision Theory*. London: Academic Press, 1974.
- [152] A. D. Esposti, A. Berning, and H.-J. Werner, "Quantum scattering studies of the lambda doublet resolved rotational energy transfer of OH in collisions with He and Ar," *J. Chem. Phys.*, vol. 103, no. 6, pp. 2067–2082, 1995.
- [153] A. Gijbbertsen, H. Linnartz, C. A. Taatjes, and S. Stolte, "Quantum interference as the source of steric asymmetry and parity propensity rules in NO-rare gas inelastic scattering," *J. Am. Chem. Soc.*, vol. 128, no. 27, pp. 8777–8789, 2006.
- [154] M. Leshchko and B. Friedrich, "An analytic model of rotationally inelastic collisions of polar molecules in electric fields," *J. Chem. Phys.*, vol. 129, no. 2, p. 024301, 2008.
- [155] X. Yang, "State-to-state dynamics of elementary bimolecular reactions," *Ann. Rev. Phys. Chem.*, vol. 58, pp. 433–459, 2007.
- [156] R. T. Skodje, D. Skouteris, D. E. Manolopoulos, S.-H. Lee, F. Dong, and K. Liu, "Resonance-mediated chemical reaction:  $F + HD \rightarrow HF + D$ ," *Phys. Rev. Lett.*, vol. 85, no. 6, pp. 1206–1209, 2000.

- [157] D. Skouteris, D. E. Manolopoulos, W. Bian, H.-J. Werner, L.-H. Lai, and K. Liu, "van der Waals interactions in the Cl + HD reaction," *Science*, vol. 286, no. 5445, pp. 1713–1716, 1999.
- [158] W. Erlewein, M. von Seggern, and J. P. Toennies, "Calculations of inelastic cross sections for rotational excitation," *Z. Phys. A*, vol. 211, pp. 35–50, 1968.
- [159] D. W. Chandler, "Cold and ultracold molecules: Spotlight on orbiting resonances," *J. Chem. Phys.*, vol. 132, no. 11, p. 110901, 2010.
- [160] M. von Seggern and J. P. Toennies, "Calculations of inelastic cross sections for rotational excitation," *Z. Phys. A*, vol. 218, pp. 341–351, 1969.
- [161] R. N. Zare, "Resonances in reaction dynamics," *Science*, vol. 311, no. 5766, pp. 1383–1385, 2006.
- [162] A. Schutte, D. Bassi, F. Tommasini, and G. Scoles, "Orbiting resonances in the scattering of H atoms by mercury at thermal energies," *Phys. Rev. Lett.*, vol. 29, no. 15, pp. 979–982, 1972.
- [163] A. Schutte, D. Bassi, F. Tommasini, and G. Scoles, "Energy dependence of high resolution integral collision cross section measurements for elastic scattering of H and D atoms by Hg at thermal energies," *J. Chem. Phys.*, vol. 62, no. 2, pp. 600–605, 1975.
- [164] J. P. Toennies, W. Welz, and G. Wolf, "Molecular beam scattering studies of orbiting resonances and the determination of van der waals potentials for H + Ne, Ar, Kr, and Xe and for H<sub>2</sub> + Ar, Kr, and Xe," *J. Chem. Phys.*, vol. 71, no. 2, pp. 614–642, 1979.
- [165] M. Qiu, Z. Ren, L. Che, D. Dai, S. A. Harich, X. Wang, X. Yang, C. Xu, D. Xie, M. Gustafsson, R. T. Skodje, Z. Sun, and D. H. Zhang, "Observation of Feshbach resonances in the F + H<sub>2</sub> → HF + H reaction," *Science*, vol. 311, no. 5766, pp. 1440–1443, 2006.
- [166] W. Dong, C. Xiao, T. Wang, D. Dai, X. Yang, and D. H. Zhang, "Transition-state spectroscopy of partial wave resonances in the F + HD reaction," *Science*, vol. 327, no. 5972, pp. 1501–1502, 2010.
- [167] C. Berteloite, M. Lara, A. Bergeat, S. D. Le Picard, F. Dayou, K. M. Hickson, A. Canosa, C. Naulin, J.-M. Launay, I. R. Sims, and M. Costes, "Kinetics and dynamics of the S + H<sub>2</sub> → SH + H reaction at very low temperatures and collision energies," *Phys. Rev. Lett.*, vol. 105, no. 20, p. 203201, 2010.
- [168] H. Pauly and J. Toennies, *Methods of Experimental Physics*, vol. 7a. New York and London: Academic Press, 1968.

- [169] R. Feltgen, *Weitere Messungen der Geschwindigkeitsabhängigkeit des totalen Streuquerschnittes an Systemen mit kleiner reduzierter Masse*. 1970. the PhD thesis is available *via* the library of the Bonn University.
- [170] M. S. Elioﬀ, J. J. Valentini, and D. W. Chandler, “Subkelvin cooling NO molecules via billiard-like collisions with argon,” *Science*, vol. 302, no. 5652, pp. 1940–1943, 2003.
- [171] M. S. Elioﬀ, J. J. Valentini, and D. W. Chandler, “Formation of molecules with sub-kelvin translational energy via molecular beam collisions with argon using the technique of molecular cooling by inelastic collisional energy-transfer,” *Eur. Phys. J. D*, vol. 31, pp. 385–393, 2004.
- [172] J. Han and M. C. Heaven, “Bound states and scattering resonances of OH-He,” *J. Chem. Phys.*, vol. 123, no. 6, p. 064307, 2005.
- [173] K. B. Gubbels, Q. Ma, M. H. Alexander, P. J. Dagdigian, D. Tanis, G. C. Groenenboom, A. van der Avoird, and S. Y. T. van de Meerakker, “Resonances in rotationally inelastic scattering of OH with helium and neon.” submitted to *J. Chem. Phys.*



# List of publications

1. Ludwig Scharfenberg, Koos B. Gubbels, Moritz Kirste, Gerrit C. Groenenboom, Ad van der Avoird, Gerard Meijer and Sebastiaan Y.T. van de Meerakker  
*Scattering of Stark-decelerated OH radicals with rare-gas atoms*  
Eur. Phys. J. D, **65**, 189-198 (2011)
2. Ludwig Scharfenberg, Sebastiaan Y.T. van de Meerakker and Gerard Meijer  
*Crossed beam scattering experiments with optimized energy resolution*  
Phys. Chem. Chem. Phys., **13**, 8448-8456 (2011)
3. Ludwig Scharfenberg, Jacek Kłos, Paul J. Dagdigian, Millard H. Alexander, Gerard Meijer and Sebastiaan Y.T. van de Meerakker  
*State-to-state inelastic scattering of Stark-decelerated OH radicals with Ar atoms*  
Phys. Chem. Chem. Phys., **12**, 10660-10670 (2010)
4. Moritz Kirste, Ludwig Scharfenberg, Jacek Kłos, Francois Lique, Millard H. Alexander, Gerard Meijer and Sebastiaan Y.T. van de Meerakker  
*Low-energy inelastic collisions of OH radicals with He atoms and D<sub>2</sub> molecules*  
Phys. Rev. A, **82**, 042717 (7 pp.) (2010)
5. Ludwig Scharfenberg, Henrik Haak, Gerard Meijer and Sebastiaan Y.T. van de Meerakker  
*Operation of a Stark decelerator with optimum acceptance*  
Phys. Rev. A, **79**, 023410 (11 pp.) (2009)

6. Steven Hoekstra, Markus Metsälä, Peter C. Zieger, Ludwig Scharfenberg, Joop J. Gilijamse, Gerard Meijer and Sebastiaan Y.T. van de Meerakker  
*Electrostatic trapping of metastable NH molecules*  
Phys. Rev. A, **76**, 063408 (6 pp.) (2007)
7. Steven Hoekstra, Joop J. Gilijamse, Boris Sartakov, Nicolas Vanhaecke, Ludwig Scharfenberg, Sebastiaan Y.T. van de Meerakker and Gerard Meijer  
*Optical Pumping of Trapped Neutral Molecules by Blackbody Radiation*  
Phys. Rev. Lett., **98**, 133001 (4 pp.) (2007)
8. Sandra Feyel, Ludwig Scharfenberg, Charles Daniel, Hans Hartl, Detlef Schröder and Helmut Schwarz  
*Dehydrogenation of Methanol by Vanadium Oxide and Hydroxide Cluster Cations in the Gas Phase*  
J. Phys. Chem. A, **111**, 3278-3286 (2007)
9. Maxim Dashtiev, Vladimir Azov, Vladimir Frankevich, Ludwig Scharfenberg and Renato Zenobi  
*Clear Evidence of Fluorescence Resonance Energy Transfer in Gas-Phase Ions*  
J. Am. Soc. Mass Spectrom., **16**, 1481-1487 (2005)

# Danksagung

Nach getaner Arbeit ist es immer interessant zu sehen, wie sich die Dinge zusammengefügt haben, was geklappt hat und was nicht. Bei dem beschriebenen Projekt funktionierte glücklicherweise das meiste. Zunächst danke ich Gerard Meijer herzlich für all seine Unterstützung sowie für sämtliche wissenschaftliche Expertise. Mein weiterer herzlicher Dank gilt Bas van de Meerakker, von dem ich einiges – insbesondere in der Anfangsphase unserer Zusammenarbeit – gelernt habe. Neben dem mehr technischen “Abbremsen”-Wissen betrifft dies auch seine organisatorischen Fähigkeiten.

Bei der Auswertung der Streuexperimente gab es mehrfach Gelegenheit zur Kooperation. Die Berechnungen zu den OH-Ar Messungen wurden von Millard Alexander, Jacek Klos und Paul Dagdigan gemacht. Zur Abwechslung konnte in diesem Fall auch mal die Theorie vom Experiment etwas lernen, und nicht nur umgekehrt. Den dreien sehr hiermit sehr für das letztlich sehr gute Resultat gedankt. Um die weiteren Messungen zur Edelgasreihe haben sich, mit großem Erfolg, Koos Gubbels, Ad van der Avoird und Gerrit Groenenboom gekümmert. Das Ergebnis kann weiter oben nachgesehen werden. Vielen Dank, besonders an Koos, für die ausgesprochen zügige Umsetzung der Rechnungen, sowie für zahlreiche Diskussionen.

Es liegt in der Natur der Sache, daß physikalische Experimente immer komplizierter werden und daß es immer schwieriger wird, sie allein oder in einer kleinen Gruppe aufzubauen und durchzuführen. Das hier vorliegende Experiment bildet keine Ausnahme und daher sei zunächst ein allgemeiner herzlicher Dank an die vielen Beteiligten gerichtet die es ermöglicht haben und von denen ich etwas lernen konnte.

Besonderer Dank gilt unserem Konstrukteur Henrik Haak, der ohne Zweifel das richtige Händchen für die meisten technischen Probleme hatte und mit dem die Zusammenarbeit wirklich Spaß gemacht hat. Ein mindestens ebenso großes Dankeschön sei an Georg Hammer gerichtet, der glücklicherweise die Einstellungstests seiner jetzigen Kollegen bestanden hatte und fortan am Abbremsen mitarbeitete. Georgs sorgfältiger Arbeitsstil hat erheblich zum reibungslosen

Verlauf der Experimente beigetragen<sup>4</sup>. Ebenso unentbehrlich bei allen Experimenten war die Hilfe unseres Lasertechnikers Sandy Gewinner. Die entlüfteten Madenschrauben (siehe weiter unten) waren nicht der einzige Beitrag von Manfred Erdmann zum Projekt, es war auch sonst sehr gut, daß er da war – nicht nur wegen der Mr. Toms (die man auch nachts noch in seiner Werkstatt antraf), auch wegen des angenehmen Umgangs und der Hilfe bei schnell benötigten Teilen.

Weiterer Dank gilt den Kollegen aus der Feinwerktechnik, die dafür Sorge trugen, daß der Stahl die richtige Form bekam; Adrian Kluge z.B. fräste – ganz entspannt – die 48 “Hirschgeweihe”, Klaus Grimm und Peter Schmidt drehten ziemlich flott, aber sehr genau, die z.T. sehr massiven Teile, Horst Schwäricke hörte aufmerksam zu, machte gute Vorschläge und koordinierte die Umsetzung der Aufträge. Wie üblich wurde die Elektrizität durch unser *E-Lab* auf die richtigen Bahnen geleitet. Neben allen, die irgendwie beteiligt waren, sei expliziter Dank gerichtet an Patrick Schlecht, Victor Platschkowski, Wilko Genz und Georg Heyne.

Für das ordnungsgemäße Funktionieren der Datenaufnahmesoftware “KouDa” sorgte Uwe Hoppe, dem hiermit herzlichst gedankt sei für die technische Hilfe, den guten Service und alles sonstige. Danke auch an Rolf für die Hilfe mit der Haustechnik und der Elektronik.

Meinen lieben Kollegen in der AG Meerakker – Joop, Steven, Peter, Christian und Moritz – sei hiermit herzlichst gedankt für die ausgesprochen angenehme Zusammenarbeit und alles andere. Ein spezieller Dank geht auch an meine zeitweiligen Zimmergenossen Amudha, Torsten und Stephan. Da die Abteilung groß ist, passiert es eher selten, dass man den Nachmittags Tee oder Kaffee allein zu sich nimmt. In diesem Zusammenhang sei hier Horst Conrad für lustige Unterhaltungen bei seinen gelegentlichen Zigarettenpausen gedankt. Danke auch an die bisher nicht erwähnten: Adela, Fabian, Jens, Janneke, Mikhail, Marko, Boris, Petrick, Frank, Dagmar, Cyndi, Peter K., Nadja, Frauke, Sophie, Stolli, Sam, Wieland, Knut, Jochen, Melanie, Simon, Hitoshi, Wolfgang, André, Gert, Philipp, Werner, Kirstin und Undine. Andreas Osterwalder sei insbesondere für die Organisation der berühmten Konferenz gedankt. Zumindest in der Besetzung wie ich sie kennengelernt habe, war die Abteilung MP ein sehr vielseitig talentierter Haufen – gute Schauspieler, Regisseure, Komödianten, Musiker, Fuß- und Volleyballer – alles da. Nur beim Sandburgenbauen tat man sich etwas schwer.

Bretislav danke ich aus zweierlei Gründen. Zum einen, daß er im Jahre 2005 eine Vorlesung über kalte Moleküle an der TU-Berlin hielt, zum anderen für die Organisation der Freitagsvorträge.

---

<sup>4</sup>Wer hat schonmal die Bedienungsanleitung für das General Valve befolgt wenn er das “Poppet” einbaut? Ja, man sollte eine Strom fließen lassen und damit den Eisenklotz nach unten ziehen, damit man das Poppet nicht gleich am Anfang zerkratzt wenn man die Düsenplatte draufschrubt. Das mag Hokus Pokus sein, aber man merkt dabei z.B. sofort, wenn einem die Werkstatt einen nicht magnetischen Stahl untergemogelt hat – wie in unserem Fall!!!



Schwer vorzustellen, daß alles so rund lief, wäre Inga nicht da und würde es organisieren. Ein herzliches Dankeschön an Dich. Ebenso danke an Andrea, für sämtliche Hilfe. Für das Korrekturlesen der Arbeit danke ich Gerard, Nicolas, Boris, Christian, Peter und Janneke.

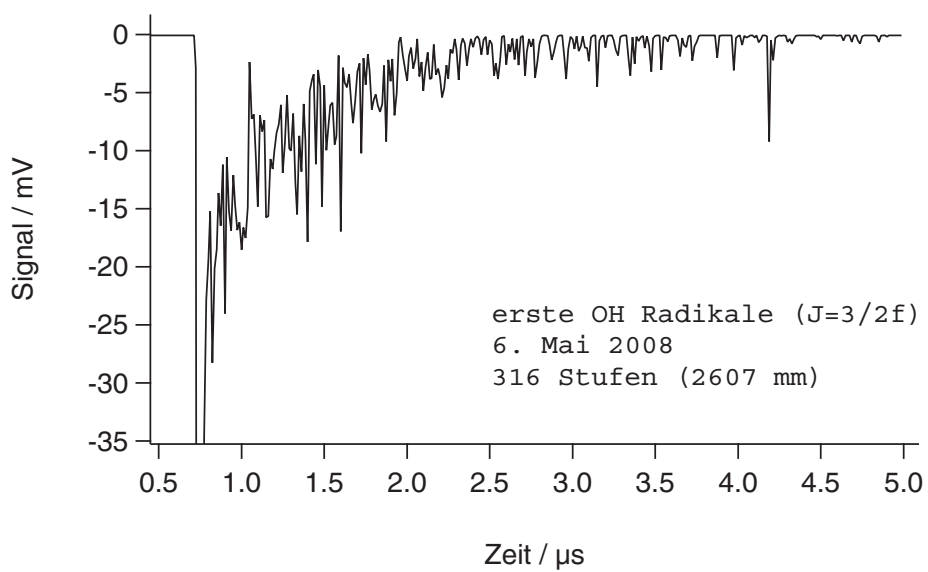
Nach dem offiziellen Teil, sei hier noch auszugsweise aus meinem Abbremsertagebuch berichtet – auf eigene Gefahr des Lesers, denn für den Unterhaltungswert übernehme ich keine Garantie!

Als ich im Februar 2006 am FHI anfang, hatten Henrik und Bas bereits die grundlegenden Entscheidungen über die mechanische Konstruktion getroffen und Henrik hatte einen Großteil auch schon gezeichnet. In der Halle waren Manfred und Jürgen dabei, das Gestell für die Kammern zusammenzubauen; Joop und Steven machten die Messungen für das später vielzitierte OH-Xe Stoßexperiment. Bas hielt die Abbremsersproduktion am laufen und bestellte beinahe täglich neues Zubehör. Die erste Zeit war ich nur damit beschäftigt, Bas beim Organisieren zu helfen und einen Überblick zu bekommen. Als langsam Routine eingekehrt war, bekam ich die Aufgabe, reine deuterierte Salpetersäure für das geplante Fallenexperiment herzustellen. Das war gut, denn ich konnte zur Abwechslung mal etwas tun, mit dem ich mich schon auskannte. Als ich fertig war, dauerte es nicht lange bis Joop, Steven und Bas zu mir kamen und mich fragten, ob ich sicher sei, daß es sich um  $\text{DNO}_3$  und nicht um  $\text{HNO}_3$  handelt. Man könne kein OD detektieren, lediglich kleinste Mengen OH. Da es schwierig ist, bei einer Reaktion die so einfach ist ( $\text{KNO}_3 + \text{D}_2\text{SO}_4 \rightarrow \text{DNO}_3 + \text{KDSO}_4$ ) etwas anderes als deuterierte Salpetersäure zu erhalten, war ich ernsthaft verwirrt. Natürlich war der Fehler schnell gefunden – man hatte die falsche Frequenz erwischt.

Nachdem die ersten Teile aus der Werkstatt kamen und wir auch Vakuum hatten, konnte das erste von drei Modulen in Betrieb genommen werden. Das ganze funktionierte! Am 22. Mai 2007 schafften die ersten OH-Radikale ein Drittel der geplanten Strecke. Später folgten ihnen metastabile NH-Radikale, deren Erzeugung allerdings etwas umständlicher war, aber aus Sicht des Chemikers mehr zu bieten hatte (Wer hantiert nicht gerne mit hochexplosiven Stoffen?).

Nachdem die ersten NH-Radikale abgremst waren, trudelten auch langsam die noch fehlenden Teile für den Rest der Maschine ein und wurden mit Georgs Hilfe zusammengebaut. Einen sehr wesentlichen Beitrag zum Erfolg leistete Manfred: 1268 *entlüftete* Madenschrauben. Später kamen nochmal so viele für die geplante zweite Strecke hinzu. Nachdem wir die Module installiert, ausgerichtet und konditioniert hatten war es soweit. Am Abend des 6. Mai 2008 traten die ersten OH-Radikale ihren Weg durch den 2.6 m langen Abbremsers an und erschienen auf der Bühne, wo sie noch ein paar Jahre ihr Tänzchen vollführten und sich durch Begegnungen mit Atomen der Reihe VIII – sowie ein, zwei Molekülen – zum Drehen animieren liessen ...

Ludwig Scharfenberg  
Berlin, Dezember 2011



# Lebenslauf

Ludwig Scharfenberg, geboren am 29. August 1980  
in Berlin

- |                   |   |
|-------------------|---|
| 1993 - 2000       | Besuch der Bühring Oberschule Berlin,<br>Abitur (22. Juni 2000)   |
| 10/2000 - 01/2006 | Chemiestudium an der TU-Berlin,<br>Diplom (25. Januar 2006)   |
| 10/2003 - 09/2004 | an der ETH Zürich, Schweiz, Erasmus Stipendium<br>Diplomarbeit bei Prof. Dr. Zenobi, zum Thema<br><i>Fluorescence detection and resonance energy transfer<br/>of trapped molecular ions</i>   |
| 02/2006 - derzeit | Doktorand am Fritz-Haber-Institut der<br>Max-Planck-Gesellschaft<br>Anfertigung der Dissertation unter Anleitung durch<br>Prof. Dr. Gerard Meijer zum Thema<br><i>Crossed beam scattering with a<br/>Stark-decelerated molecular beam</i> |

